Analyse et optimisation des interfaces dans les composites carbone / carbone à renfort fibreux

Béatrice Nguyen van Sang-Trouvat

N° d'ordre : 1635

THESE

PRESENTEE A

L'UNIVERSITE BORDEAUX I

ECOLE DOCTORALE DE SCIENCES CHIMIQUES

Par Mme **Béatrice NGUYEN VAN SANG-TROUVAT**

Ingénieur de l'ENSCP

POUR OBTENIR LE GRADE DE

DOCTEUR

SPECIALITE : SCIENCES DES MATERIAUX

Titre : ANALYSE ET OPTIMISATION DES INTERFACES DANS LES COMPOSITES CARBONE/CARBONE A RENFORT FIBREUX

Soutenue le : .....16 décembre 1996

Après avis de : MM	R.J. DIEFENDORF	Rapporteurs
	J.-P. FAVRE	

Devant la Commission d'examen formée de :

MM	R. NASLAIN	Président
	J.-M. QUENISSET	Rapporteur
	R.J. DIEFENDORF	Examinateurs
	J.-P. FAVRE	
	A. TRESSAUD	
	J.-M. JOUIN	
	X. BOURRAT	

-- 1996 --

N° d'ordre : 1635

THESE

PRESENTEE A

L'UNIVERSITE BORDEAUX I

ECOLE DOCTORALE DE SCIENCES CHIMIQUES

Par Mme **Béatrice NGUYEN VAN SANG-TROUVAT**

Ingénieur de l'ENSCP

POUR OBTENIR LE GRADE DE

DOCTEUR

SPECIALITE : SCIENCES DES MATERIAUX

Titre : ANALYSE ET OPTIMISATION DES INTERFACES DANS LES COMPOSITES CARBONE/CARBONE A RENFORT FIBREUX

Soutenue le : .....16 décembre 1996

Après avis de : MM	R.J. DIEFENDORF	Rapporteurs
	J.-P. FAVRE	

Devant la Commission d'examen formée de :

MM	R. NASLAIN	Président
	J.-M. QUENISSET	Rapporteur
	R.J. DIEFENDORF	Examinateurs
	J.-P. FAVRE	
	A. TRESSAUD	
	J.-M. JOUIN	
	X. BOURRAT	

-- 1996 --

Cette étude a été réalisée au Laboratoire des Composites Thermostructuraux (Unité Mixte de Recherche 47 CNRS-SEP-UBI) dont je remercie le Directeur, Monsieur le Professeur R. NASLAIN, pour son accueil, ses conseils, et pour avoir accepté la présidence de mon jury de thèse.

Monsieur le Professeur R.J. DIEFENDORF, de l'Université de Clemson (South Carolina), m'a fait le très grand honneur de juger mon travail. Je tiens à lui exprimer mes plus vifs remerciements, et ma profonde estime.

Monsieur J.-P. FAVRE, chef de division à l'ONERA (Direction des Matériaux), m'a fait l'honneur de juger mon travail. Je lui adresse mes sincères remerciements.

Monsieur le Professeur J.-M. QUENISSET, du Laboratoire de Génie mécanique de l'IUT et de l'ICMCB à Bordeaux I, a aimablement accepté de participer à mon jury de thèse. Je le remercie vivement de l'intérêt qu'il a porté à mon travail.

Monsieur le Professeur A. TRESSAUD, Directeur de Recherche à l'ICMCB à Bordeaux I, a aimablement accepté de participer à mon jury de thèse. Je lui adresse mes sincères remerciements.

Monsieur J.-M. JOUIN, ingénieur à Carbone Industrie, a suivi ces recherches lorsqu'il était à la SEP, et a bien voulu prendre part au jury de ma thèse. Qu'il trouve ici l'expression de ma sincère gratitude.

Monsieur X. BOURRAT, Chargé de Recherche au LCTS, a dirigé ce travail avec attention. Ses compétences scientifiques dans le domaine du carbone, et son soutien dans les moments difficiles m'ont permis de mener à bien cette étude. Je tiens à l'assurer de ma sincère reconnaissance, et de ma plus profonde estime.

Je remercie chaleureusement tous les membres du laboratoire pour la très bonne ambiance de travail, et l'esprit de groupe, qui a permis de partager de très bons moments et d'être soutenue pendant les périodes difficiles. Je soulignerais le travail, que je qualifierais de colossal, de Muriel ALRIVIE pour la préparation d'échantillons pour la microscopie électronique à transmission, ainsi que l'aide et les conseils techniques en CVD de Gilles BONDIEU qui s'est traduit par une chaleureuse collaboration.

J'aimerais également exprimer ma reconnaissance à X. BOURRAT et F. DOUX pour m'avoir fait partager leurs connaissances et leur savoir-faire dans le domaine de la microscopie électronique à transmission.

Je tiens enfin à remercier la Société Européenne de Propulsion et le CNRS qui m'ont permis de conduire cette étude en me faisant bénéficier d'une bourse de recherche.

ANALYSE ET OPTIMISATION DES INTERFACES DANS LES COMPOSITES CARBONE/CARBONE A RENFORT FIBREUX

INTRODUCTION GENERALE 1

1 - Les matériaux composites 1

1.1 - Généralités 1

1.2 - Les composites à matrice céramique (CMCs) 2

2 - Le carbone 2

2.1 - Structures cristallines 2

2.2 - Propriétés du graphite 3

2.3 - Carbones turbostratiques, les pyrocarbones 4

2.4 - Graphitation 5

3 - Fibres de carbone 6

4 - Matrice de carbone 7

4.1 - Voie liquide 7

4.2 - CVD / CVI 9

5 - Propriétés mécaniques 10

5.1 - Constituants 10

5.2 - Comportement mécanique des CMCs 11

5.2.1 - CMCs classiques (ex: SiC/SiC) 13

5.2.2 - Composites carbone/carbone 14

6 - Zone interfaciale 15

6.1 - Approche théorique 16

6.2 - Détermination de la contrainte de cisaillement interfaciale 17

6.2.1 - Par la mesure du pas de fissuration 17

6.2.2 - Par des cycles de charge-décharge lors d'un essai de traction 17

6.2.3 - Par essai de pull-out 18

6.2.4 - Par microindentation 18

7 - Conclusion **18**

8 - Objectifs et contenu du présent mémoire **19**

PROCEDURES EXPERIMENTALES-CONSTITUANTS **21**

1 - Procédures expérimentales **21**

1.1.- Elaboration CVD / CVI *21*

1.1.1- Microcomposites 21

1.1.2 - Minicomposites 22

1.2 - Essais de traction *22*

1.2.1 - Fibres, microcomposites 22

1.2.2 - Minicomposites 23

1.3 - Caractérisation structurale *23*

1.3.1 - Texture du pyrocarbone 23

1.3.2 - Structure de la zone interfaciale 25

1.3.3 - Endommagement-Rupture 25

1.3.4 - Faciès miroir des fibres 26

1.4 - Détermination de la différence entre coefficients de dilatation thermique axiaux de la fibre et de la matrice *26*

2 - Nature et caractéristiques mécaniques des constituants **27**

2.1 - Fibres *27*

2.2 - Matrice *28*

2.3 - Interphase *29*

SYNTHESE DES PRINCIPAUX RESULTATS **30**

1 - Comportement mécanique **30**

1.1 - Comportement inverse ($\varepsilon_{R,m} < \varepsilon_{R,f}$) *30*

1.2 - Comportement régulier ($\varepsilon_{R,m} > \varepsilon_{R,f}$) *32*

2 - La liaison interfaciale **33**

2.1 - Composante chimique *33*

2.2 - Composante physique 33

2.3 - Contraintes résiduelles 34

2.4 - Rôle de la zone interfaciale 35

3 - Mécanismes de ténacité dans les minicomposites C/C 36

3.1 - Comportement fragile 36

3.2 - Comportement tenace 36

3.2.1 - Mécanisme de ténacité par décohésion/frottement 37

3.2.2 - Mécanisme de ténacité par multifissuration matricielle 39

CONCLUSION GENERALE 42

REFERENCES BIBLIOGRAPHIQUES

ANNEXE 1

Fibre/matrix bonding in carbon/carbon microcomposites role of HTT and surface roughness of the fibre

1 - INTRODUCTION 2

2 - EXPERIMENTAL 4

2.1 - C/C microcomposites preparation 4

2.2 - Mechanical testing 4

2.3 - Structural characterisation 5

3 - RESULTS AND DISCUSSION 7

3.1 - Bare fibres 7

3.1.1 - Mechanical behaviour 7

3.1.2 - Microstructural characterisation 9

3.2 - Carbon/carbon microcomposites 10

3.2.1 - TEM cross-sections 10

3.2.2 - Mechanical behaviour 11

3.2.3 - SEM observations of the fracture surfaces 14

4 - CONCLUSIONS 15

REFERENCES

ANNEXE 2

Influence of a carbon interphase with a controlled microtexture on the mechanical properties of a single fibre C/C/C microcomposites

1 - INTRODUCTION 2

2 - EXPERIMENTAL 3

2.1 - C/C/C microcomposites preparation 3

2.2 - Mechanical testing 4

2.3 - Structural characterisation 5

3 - RESULTS AND DISCUSSION 7

3.1 - Microcomposites structure 7

3.1.1 - Texture of pyrocarbons 7

3.1.2 - TEM observation of interfaces 7

3.1.3 - SEM observation of polished transverse sections 8

3.2 - Mechanical behaviour 9

3.2.1 - Load-strain curves 9

3.2.2 - Fracture mirrors 10

3.2.3 - Interface and ultimate performances 11

3.3 - Microcomposites heat-treated to HTT2 13

3.3.1 - F/M and F/Ia/M microcomposites 13

3.3.2 - F/Ib/M and F/Ic/M microcomposites 16

4 - CONCLUSIONS 18

REFERENCES

ANNEXE 3

Toughening mechanisms in carbon/carbon minicomposites with interface control

1 - INTRODUCTION 2

2 - EXPERIMENTAL 3

2.1 - C/C minicomposites preparation 3

2.2 - Mechanical testing 4

2.3 - Structural characterisation 4

3 - RESULTS AND DISCUSSION 5

3.1 - Bare tows 5

3.1.1 - Non-heat-treated tow (A) 6

3.1.2 - Heat-treated tow (A-HTT) 7

3.2 - Carbon/carbon minicomposites 8

3.2.1 - Minicomposites structure 8

3.2.2 - Tensile behaviour 9

3.2.2.1 - Brittle behaviour with A tows: A/M 9

3.2.2.2 - Non-brittle behaviour with heat-treated tows: 9

A-HTT/M, A-HTT/I/M 9

3.3 - Modelling 14

3.3.1 - Interfacial shear stress measurement: τ 15

3.3.2 - Coefficient of thermal expansion (CTE) mismatch 15

3.3.3 - Matrix-multiple-cracking mode 17

CONCLUSION 20

REFERENCES

ANNEXE 4

Pyrocarbon anisotropy as measured by electron diffraction and polarised light

1 - INTRODUCTION 2

2 - EXPERIMENTAL 3

2.1 - Optical microscopy 3

2.2 - Transmission electron microscopy (TEM) 4

2.3 - Image Analysis (IA) 4

3 - RESULTS AND DISCUSSION 5

3.1 - Optical measurement of the anisotropy 5

3.1.1 - Fundamentals of the technique 5

3.1.2 - Measurements 9

3.2 - Pyrocarbon anisotropy as measured by electron diffraction 10

3.2.1 - Pyrocarbon diffraction and anisotropy 10

3.2.2 - Measurement procedure 11

3.2.3 - Results 12

3.2.3.1 - Anisotropy of interface pyrocarbon in C/C composites 12

3.2.3.2 - Comparative variation of anisotropy, OA, and d_{002} interlayer spacing 14

4 - DISCUSSION **16**

5 - CONCLUDING REMARKS **17**

REFERENCES

NOMENCLATURE

Ae	angle d'extinction
d	diamètre de la fibre
S_f	section de la fibre
S_m	section de la matrice
$S_{f,corr}$	section de la fibre corrigée
S_{fil}	section du fil
$S_{fil,corr}$	section du fil corrigée
V	volume soumis à la contrainte
V_f	fraction volumique de fibre
V_i	fraction volumique d'interphase
V_m	fraction volumique de matrice
F	charge appliquée
σ	contrainte appliquée
E	module d'Young du composite
E_f	module d'Young de la fibre
E_m	module d'Young de la matrice
R_m	rayon du miroir sur faciès miroir
$\mathcal{A}$	constante liant le rayon miroir à la contrainte à rupture de la fibre
$\sigma_{f,mirror}$	contrainte à rupture de la fibre déduite du faciès miroir
ε_{el}	déformation en fin de linéarité
ε_R	déformation à rupture
$\varepsilon_{R,f}$	déformation à rupture de la fibre
$\varepsilon_{R,m}$	déformation à rupture de la fibre
σ_{el}	contrainte en fin de linéarité
σ_R	contrainte à rupture
σ_f	contrainte à rupture de la fibre dans le microcomposite quand il n'y a pas de contrainte résiduelle: $\sigma_f = E_f.\varepsilon_R$

σ_f'	contrainte à rupture de la fibre dans le microcomposite quand elle supporte seule la charge: $\sigma_f' = F/S_f$
σ_0	facteur d'échelle dans la statistique de Weibull
m	module de Weibull
L_i	distance interfissure, déterminée pour une fissure i en faisant la moyenne des distances de cette fissure à la fissure (i-1), et à la fissure (i+1)
ℓ	longueur ineffective, définie comme la demi-longueur du domaine où l'interface est déliée de part et d'autre de la fissure
M_0	terme relié à la différence entre coefficients de dilatation thermique de la fibre (α_f) et de la matrice(α_m) : $M_0 = \int_{T_0}^{T_e} (\alpha_m - \alpha_f).dT$ avec T_0 la temperature ambiante, et T_e la temperature d'élaboration
u_0	ouverture de la fissure sous charge nulle
u(F)	ouverture de la fissure sous la charge F
c_f	raideur de la fibre $c_f=1/(E_f.S_f)$
τ	contrainte de cisaillement interfaciale

INTRODUCTION GENERALE

INTRODUCTION GENERALE

1 - Les matériaux composites

1.1 - Généralités

La recherche de matériaux, adaptés aux besoins de l'industrie aérospatiale (amélioration des performances mécaniques, allégement des structures), a conduit à la conception des matériaux composites. **Le principe de ces matériaux est d'associer différents constituants pour donner des propriétés originales, que n'ont pas les constituants pris isolément** [1]. Leur développement a été étendu à d'autres domaines tout aussi nombreux que divers (construction navale, automobile, équipement sportif, prothèses médicales, ...). Ils restent cependant des produits à forte valeur ajoutée.

Dans ce type de matériaux, la nature des constituants, leur disposition, leur fraction volumique sont choisies en fonction des propriétés souhaitées. Les matériaux composites, sont généralement constitués d'un renfort fibreux (fibres de verre, fibres céramiques, fibres de carbone, etc.), et d'une matrice (organique, métallique, céramique). Les fibres ont pour rôle de supporter la charge appliquée, et la matrice de répartir les efforts, et de protéger également les fibres de l'environnement extérieur.

Caractérisés par des **propriétés spécifiques (E/ρ, σ/ρ) élevées**, les matériaux composites concurrencent les matériaux usuels tels que les aciers pour les faibles températures d'utilisation (<300°C). Il s'agit des composites à **matrice organique**. Ils concurrencent les superalliages pour les moyennes températures (<800°C) avec une **matrice métallique**, et permettent des applications à haute température (>800°C) avec les **matrices céramiques**.

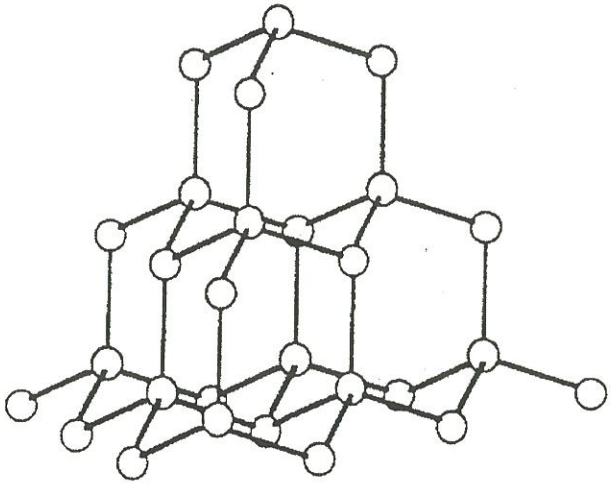

Figure 1: structure du diamant

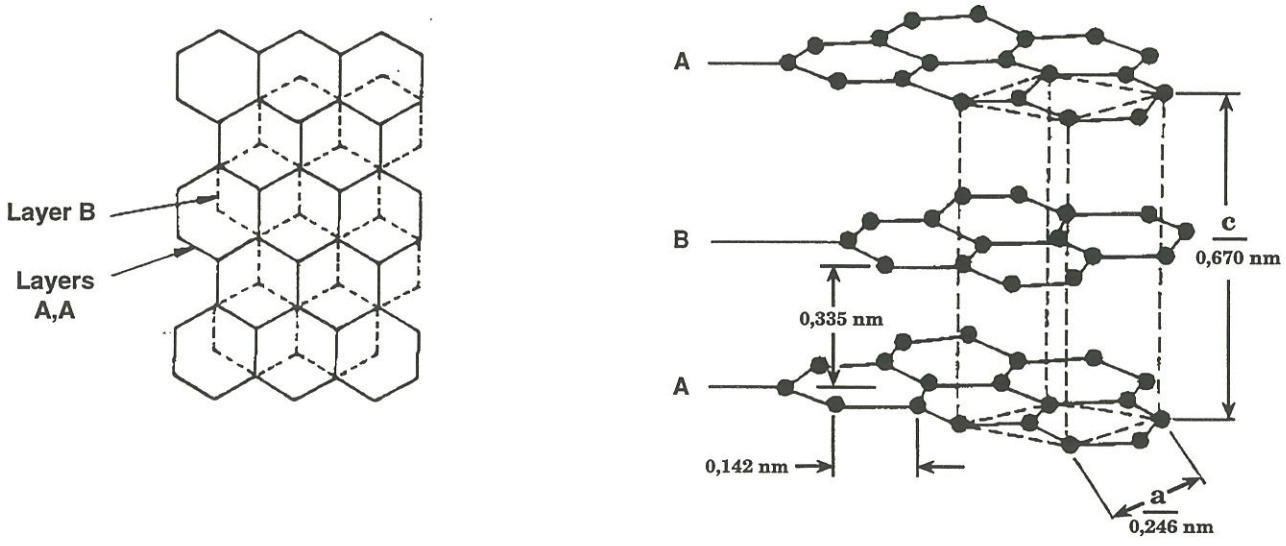

Figure 2: structure du graphite

1.2 - Les composites à matrice céramique (CMCs)

Les matrices céramiques sont réfractaires. Elles possèdent une dureté élevée, une bonne inertie chimique, et une faible masse volumique. Cependant, elles sont fragiles. Associées à des fibres céramiques ou des fibres de carbone, elles forment des **matériaux composites de type renfort fragile/matrice fragile**. Dans ce cas, le rôle des fibres n'est pas d'augmenter la rigidité, mais de permettre la discrétisation de la céramique, et d'accroître le travail de rupture.

Les premiers CMCs, ayant bénéficié d'un développement industriel, sont les **composites carbone/carbone**, du fait de leurs excellentes propriétés thermomécaniques en atmosphère neutre ou réductrice, et de leur légèreté. Ils furent développés pour les cols et divergents de tuyères de moteur de fusée, et les boucliers de corps de rentrée. Leur champ d'application fut ensuite étendu aux freins du fait de leur faible densité et de leurs propriétés thermiques, et aux prothèses médicales du fait de leur biocompatibilité. Cependant, leur emploi est limité par leur faible résistance à l'oxydation, qui débute dès 450°C à l'air.

2 - Le carbone

2.1 - Structures cristallines

Le carbone existe sous 3 formes cristallines ordonnées: le diamant, le graphite, et le fullerène.

La structure **diamant** consiste en un arrangement tridimensionnel de liaisons fortes σ (tétravalence de l'atome carbone: hybridation sp^3) comme le montre la figure 1. Sa densité est de 3,51g.cm^{-3}.

La forme **graphite** cristallise dans le système hexagonal (figure 2), ou rhomboédrique. Dans sa forme la plus stable, le graphite est caractérisé par une maille hexagonale avec $|\vec{a}|$=0,2461nm, et $|\vec{c}|$=0,6708nm (figure 2). Sa densité est de 2,25g.cm^{-3}. Les atomes de carbone se placent aux sommets d'hexagones

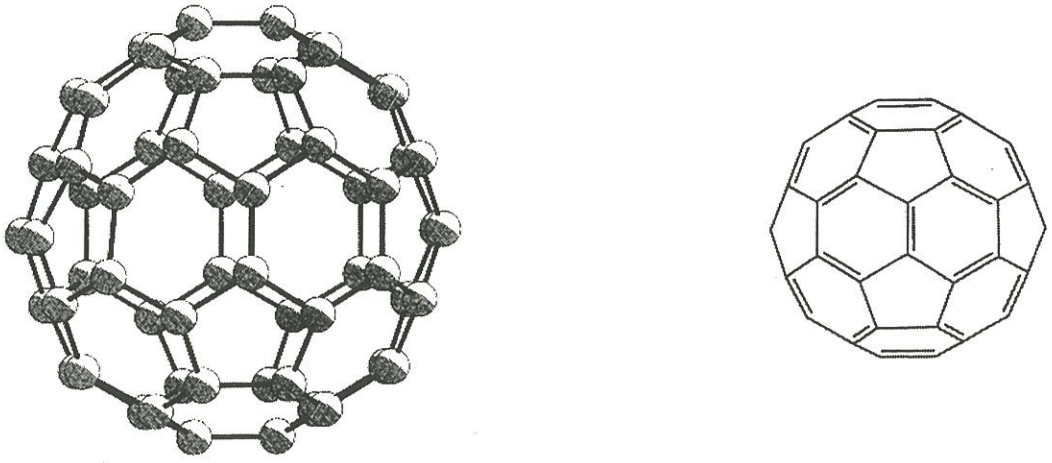

Figure 3: représentations schématiques du fullerène C_{60}

(trivalence de l'atome carbone: hybridation sp^2, d_{C-C}=0,142nm), formant des plans (plans 00ℓ dans la symétrie hexagonale), appelés couches graphitiques. Les atomes de carbone sont liés entre eux, dans ces plans, par des liaisons fortes de type covalentes, alors que les couches graphitiques sont reliées entre elles par des liaisons faibles (interaction π-π). Ces couches, distantes de 0,335nm (d_{002}), forment un empilement compact de séquence ABAB, de sorte que le centre de chaque hexagone du plan A est au-dessus d'un atome du plan B, et inversement.

Les **fullerènes** sont des formes stables du carbone pur. Les entités structurales de base sont sphériques. Il s'agit d'un assemblage de pentagones et d'hexagones, les pentagones permettant la courbure. Ce type de carbone est soluble dans une variété de solvants organiques. Le plus petit fullerène stable, et en même temps le plus abondamment obtenu par les méthodes de préparation utilisées, est le fullerène C_{60}, constitué de 60 atomes de carbone (figure 3).

2.2 - Propriétés du graphite

La structure lamellaire du graphite engendre des propriétés thermomécaniques et physiques anisotropes.

Le module d'élasticité ou **module d'Young** mesuré dans les plans de carbone (i.e. selon $\vec{a}$) est trente fois plus élevé (1060GPa) que celui mesuré selon l'axe $\vec{c}$ (36GPa). Au contraire, le module de cisaillement selon $\vec{a}$ est très faible (G=0,18GPa), et donne au graphite son clivage.

Le **coefficient de dilatation** α du graphite varie non seulement selon les axes $\vec{a}$ et $\vec{c}$, mais aussi avec la température [2]. Selon $\vec{a}$, il est négatif du zéro absolu ($-1{,}2.10^{-6}K^{-1}$) jusqu'à 656K où il s'annule, puis il devient positif pour des températures plus élevées ($0{,}8.10^{-6}K^{-1}$ à 1073K). Selon l'axe $\vec{c}$, le coefficient de dilatation est nul au zéro absolu, puis il croît avec la température ($25.10^{-6}K^{-1}$ à 273K, $28{,}5.10^{-6}K^{-1}$ à 1000K). Pellegrini [3] montre notamment que la distance intercouches (d_{002}) augmente lorsqu'on augmente la température. L'évolution

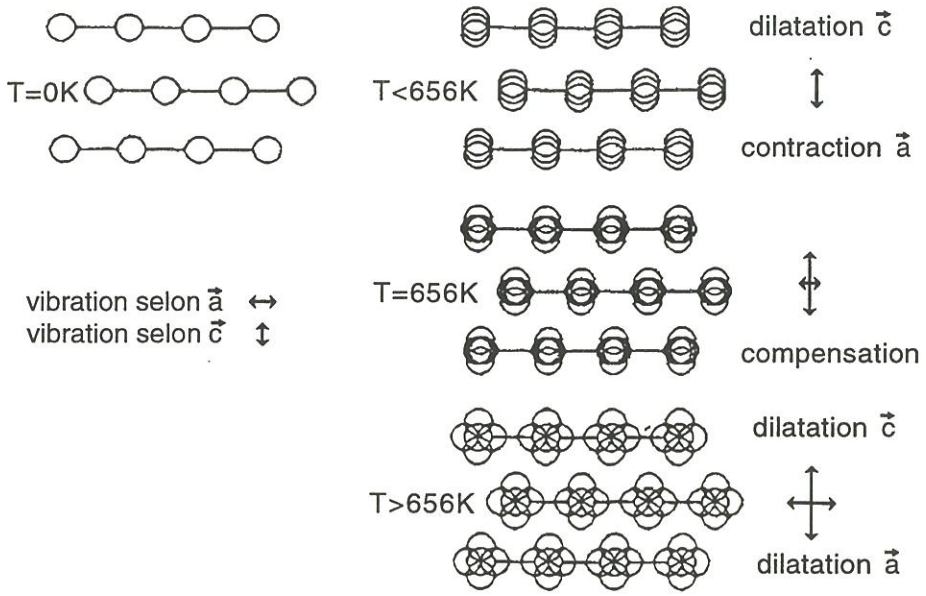

Figure 4: mécanismes expliquant la dilatation du graphite selon $\vec{a}$ et $\vec{c}$

différente des coefficients de dilatation avec la température peut s'expliquer en considérant les liaisons comme des systèmes d'oscillateurs constitués d'atomes reliés entre eux par des ressorts [4]. Les liaisons selon l'axe $\vec{c}$ sont les premières à "vibrer" dès que la température est supérieure au zéro absolu. En revanche, selon $\vec{a}$ les oscillations sont négligeables. De ce fait, le matériau, se dilatant selon $\vec{c}$, subit une contraction selon les directions perpendiculaires pour conserver son volume. Il en résulte une diminution de α_a. Mais avec la température, la dilatation naissante selon $\vec{a}$ annule dans un premier temps la contraction ($\alpha_a=0$), puis induit une baisse de la croissance de α_c ($\alpha_a\neq0$) (figure 4).

Les **conductivités électrique et thermique** sont largement supérieures au sein des plans de carbone, où les électrons et les phonons se propagent facilement, qu'entre ces mêmes plans.

Par ailleurs, le graphite est **biréfringent** (2 indices de réfraction selon 2 directions cristallographiques).

Cependant, sa **résistance à l'oxydation** est **faible**. Le graphite s'oxyde dès 450°C à l'air.

2.3 - Carbones turbostratiques, les pyrocarbones

Les carbones déposés par craquage pyrolytique (ou pyrocarbones) ont une structure turbostratique. Ils possèdent comme le graphite une **structure lamellaire**, mais les couches graphitiques, qui les composent, sont empilées parallèlement avec un **désordre de rotation**, qui est à l'origine du terme "turbostratique". Les couches graphitiques ne sont plus alors dans la configuration énergétique la plus stable, ce qui se traduit par **une distance d_{002} plus élevée** que celle du graphite. Par ailleurs, la présence de défauts structuraux dans ces carbones fait que les couches apparaissent distordues. Les couches ne sont rigoureusement parallèles qu'à courte distance. La structure des carbones turbostratiques est donc décrite à l'aide des longueurs de cohérence de l'ordre à courte distance. L'unité structurale de base (**USB**)

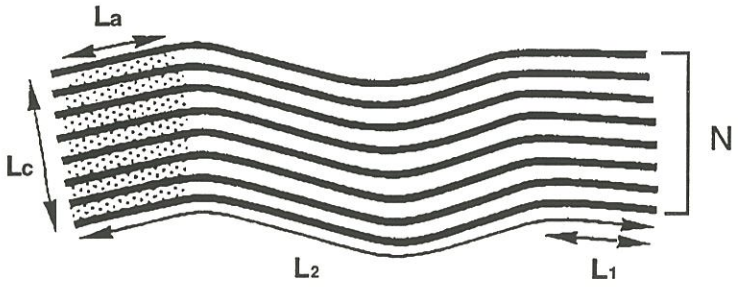

Figure 5: schéma d'un empilement de couches, où on distingue le domaine cohérent (pointillé) défini par L_a et L_c

constitue la forme la plus répandue. Elle est formée par l'empilement élémentaire de 2 ou 3 plans de carbone de quelques nanomètres de large, plus ou moins distordus et parallèles entre eux. Les caractéristiques associées à la structure turbostratique peuvent être déterminées sur les clichés en haute résolution au microscope électronique à transmission: L_2 (la longueur des franges distordues), L_1 (la longueur des franges parfaites au sein de cette unité de base), N (le nombre de couches empilées en cohérence) (figure 5). Les grandeurs $\mathbf{L_a}$ et $\mathbf{L_c}$, déduites des clichés de diffraction, représentent respectivement la largeur et la hauteur des cristallites (domaines cohérents). Ces grandeurs, ainsi que d_{002}, sont généralement utilisées pour caractériser la **structure** des carbones turbostratiques. L_a correspond en fait à L_1, et la distance L_c au nombre de couches N dans l'empilement (figure 5).

La **microtexture** des carbones turbostratiques est relative à l'orientation des domaines cohérents les uns par rapport aux autres (orientation préférentielle). Dans les pyrocarbones, la microtexture décrit le degré d'anisotropie du matériau. Une complète désorganisation résulte en un carbone isotrope. L'anisotropie de reflectance a permis de classer les pyrocarbones avec une anisotropie croissante de la manière suivante:

isotrope <laminaire sombre< laminaire lisse< laminaire rugueux

iso LS LL LR

Ces textures se caractérisent par un pouvoir réflecteur croissant en lumière polarisée. Elles sont associées, par ailleurs, à des densités qui varient de 1,5 pour l'isotrope à 2,2 pour le laminaire rugueux.

2.4 - Graphitation

Il s'agit d'un processus de cristallisation en phase solide activé thermiquement, à pression atmosphérique.

Le traitement thermique permet un réarrangement des plans de carbone. Vis-à-vis d'un traitement haute température (THT), les carbones turbostratiques peuvent être classés en deux catégories: les carbones "non

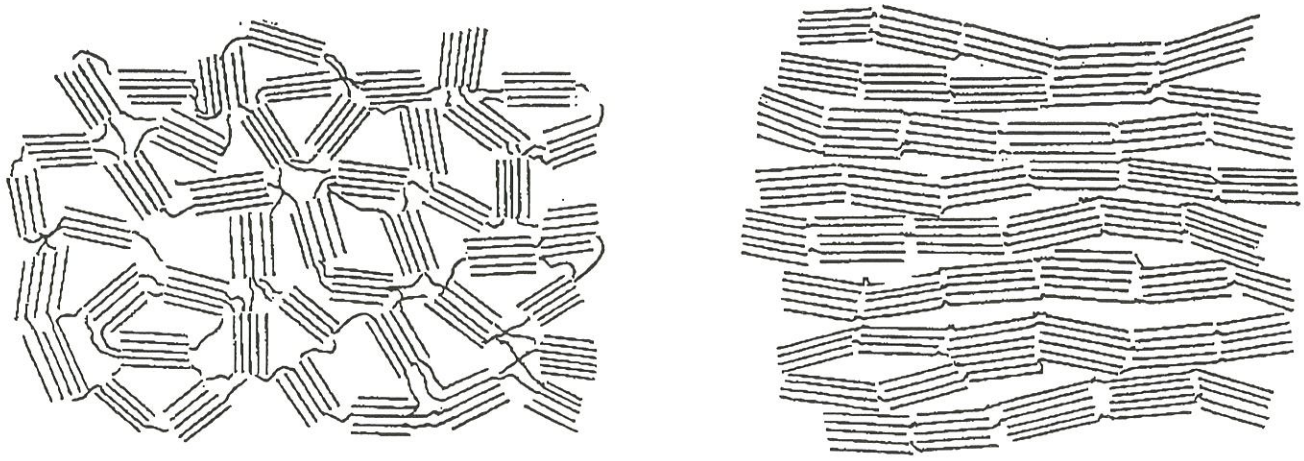

(a) (b)

Figure 6: représentation schématique de la microtexture d'un précurseur de carbone (a) non graphitable; (b) graphitable [5]

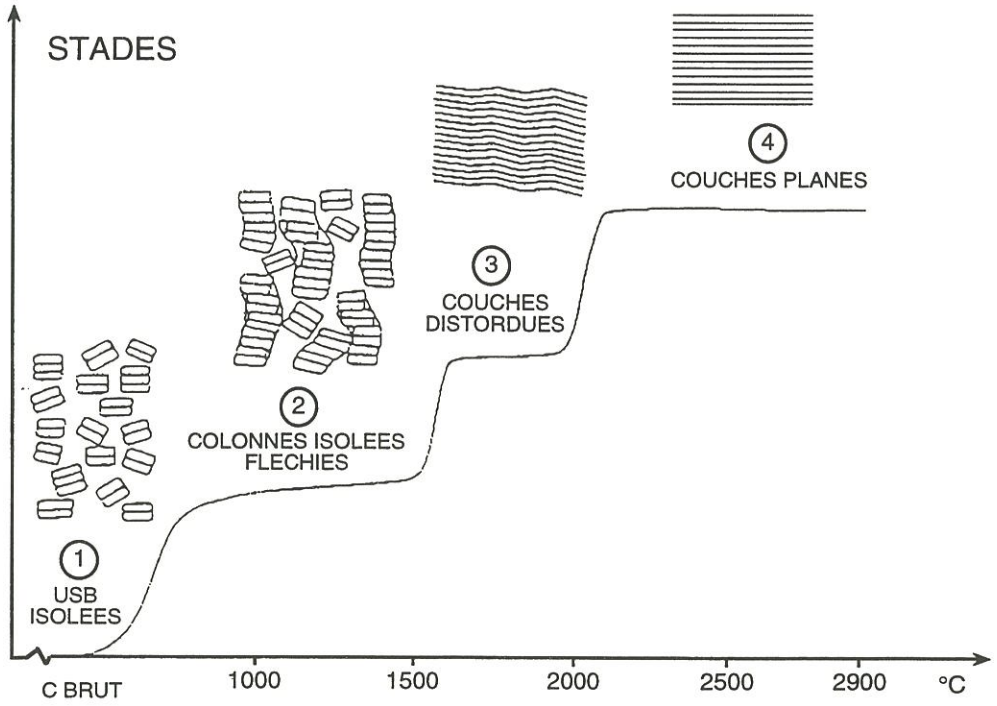

Figure 7: évolution de l'organisation d'un carbone graphitable [7]

graphitables" (ou "dur"), et les carbones "graphitables" (ou "tendres") [5], avec tous les intermédiaires partiellement graphitables [6].

Dans le cas d'un **carbone "non graphitable"** (figure 6.a), les changements d'orientation entre USBs sont trop importants pour permettre l'élimination des défauts structuraux par traitement thermique. L'oxygène, plus présent dans ces matériaux, joue un rôle réticulant du fait de sa bivalence, et fige le système avec une grande désorganisation des USBs. Cependant, l'obtention de l'anisotropie à longue distance peut être forcée par pressage isostatique de façon à faire acquérir aux USBs une orientation préférentielle.

Les **carbones "graphitables"** (figure 6.b) sont caractérisés par des zones étendues où les USBs ont des orientations proches (orientation moléculaire locale (OML)). L'évolution de l'organisation d'un carbone "graphitable" avec la température est décrit à la figure 7. Les USBs s'empilent sous forme de colonnes, qui par la suite fusionnent bord à bord donnant des couches distordues. Les défauts aux jonctions sont éliminés aux très hautes températures (1500-2000°C), élimination qui permet aux plans graphitiques d'acquérir l'ordre ABA du graphite entre 2000 et 3000°C.

3 - Fibres de carbone

L'intérêt pour les fibres de carbone a vraiment débuté au milieu des années 50. Il a porté tout d'abord sur l'étude de précurseurs cellulosiques de type **rayonne**, et l'optimisation des procédés de fabrication pour améliorer la rigidité et la résistance des fibres.

Puis, l'apparition d'un autre précurseur, le **polyacrylonitrile (PAN)**, a supplanté le précurseur rayonne dans la fabrication de fibres de carbone performantes. Différents types de fibres ex-PAN existent: les fibres haut module (HM ou fibres de type I), les fibres haute résistance (HT ou fibres de type II), et les fibres à grande déformation (A ou fibres de type III) développées plus spécialement pour les composites à matrice organique. La température

finale du processus d'élaboration de la fibre ex-PAN détermine le type de cette fibre. Ainsi des températures de 2500°C, voire plus, ou de l'ordre de 1000-1500°C, ou encore plus faibles donnent respectivement des fibres HM, des fibres HT, et des fibres A. Les fibres HT représentent la plus grande part du marché des fibres de carbone. Leur structure (figure 8.a) se différencie de celle des fibres HM (figure 8.b) par des plans de carbone beaucoup moins étendus et moins alignés selon l'axe de la fibre. Depuis ces dix dernières années, d'autres fibres (fibres IM) ont été développées avec une résistance équivalente aux fibres HT, mais un module amélioré (figure 9).

Un autre précurseur, n'appartenant pas au domaine du textile comme les précédents, le **brai**, sert pour la fabrication de fibres de carbone. Cette méthode a l'avantage de donner des fibres de haute qualité à moindre coût. Le brai est le résidu provenant de la carbonisation de la houille, ou du raffinage du pétrole. Le brai est soit utilisé sous forme isotrope, soit sous forme de brai de mésophase donnant lieu alors à des fibres très haut module (figure 9).

4 - Matrice de carbone

Le carbone, ne présentant pas de phase liquide à la pression atmosphérique, la matrice de carbone, qui enrobe les fibres dans les composites carbone/carbone, est obtenue soit par **pyrolyse de résines ou de brais**, infiltrés sous forme liquide dans la préforme fibreuse, soit par **dépôt chimique en phase gazeuse** (CVD/CVI: Chemical Vapour Deposition/Infiltration).

4.1 - Voie liquide

Deux types de précurseurs existent: les résines thermodurcissables, et les thermoplastiques [9].

Résines thermodurcissables.

La transformation de la résine en carbone s'effectue en trois étapes: (1) Stabilisation: oxydation ménagée à 200-300°C, pour rendre la résine infusible;

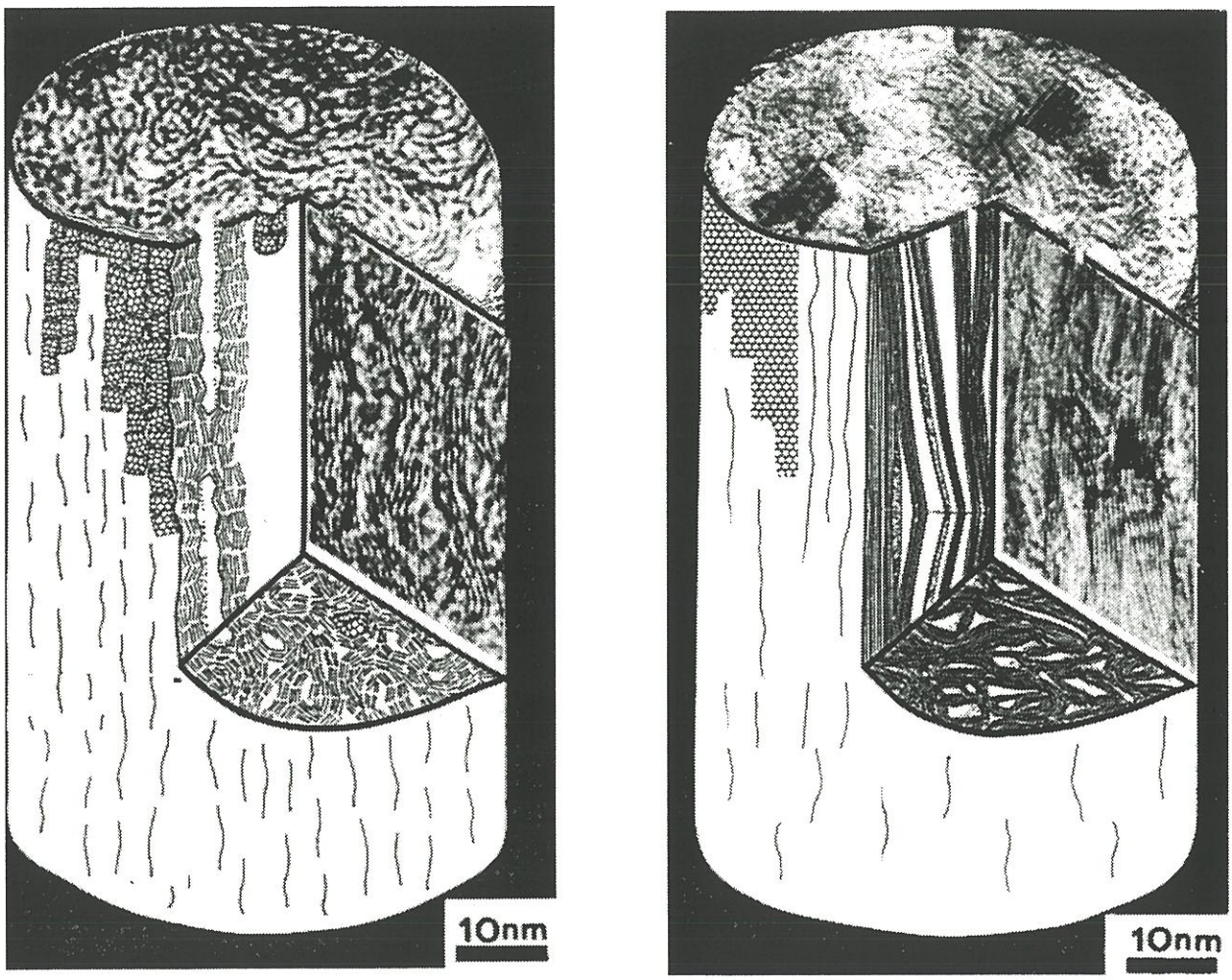

Figure 8: modèle de fibres ex-PAN de type (a) HT; (b) HM [7]

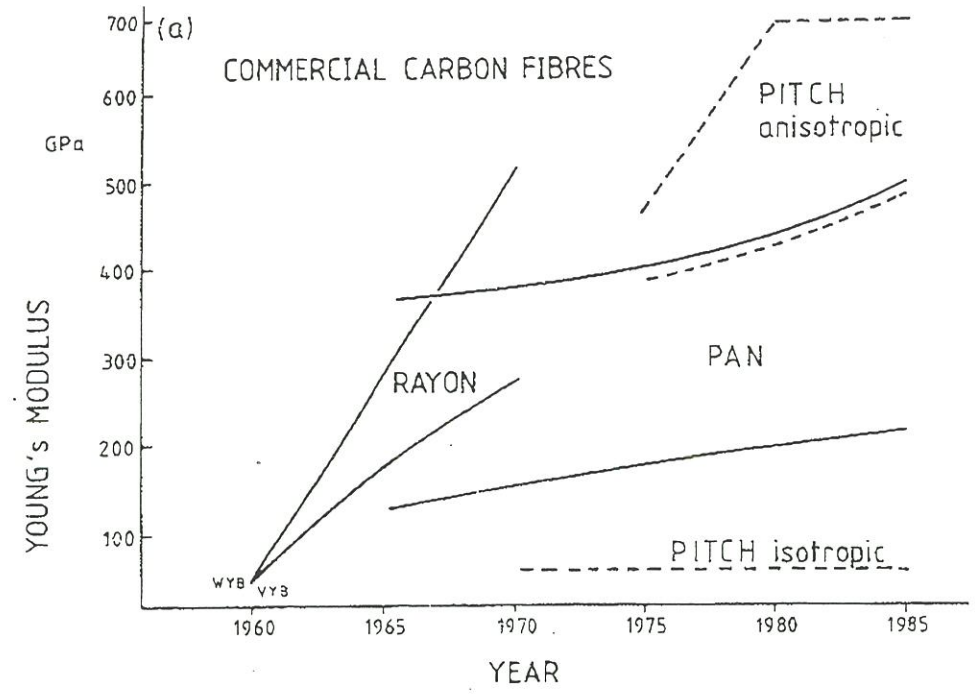

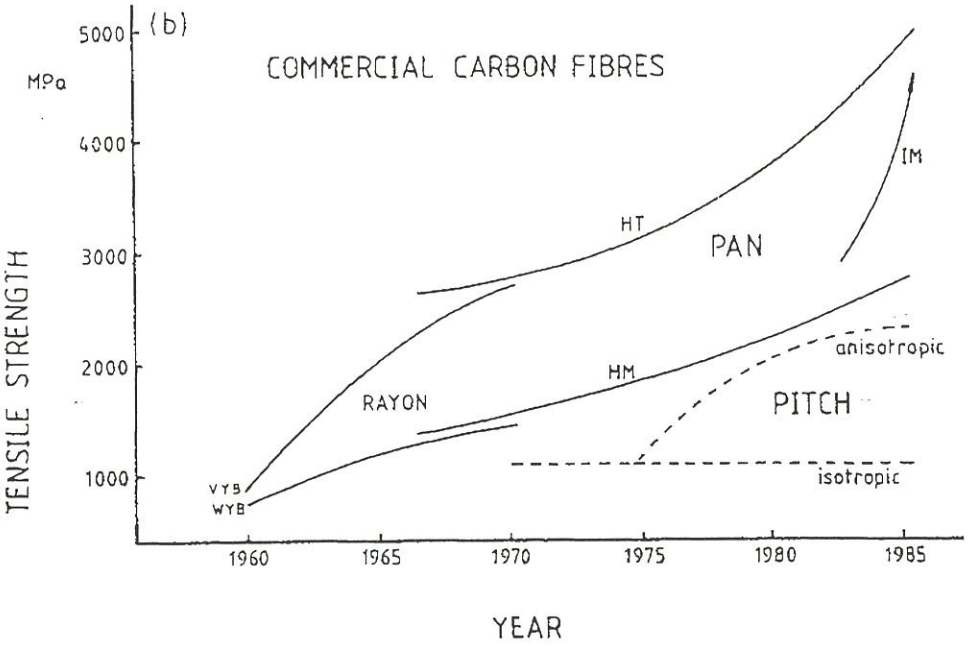

Figure 9: évolution (a) des modules et (b) des contraintes à rupture en tension des fibres de carbone [8]

(2) Carbonisation en atmosphère inerte, à 1000-1200°C; (3) Graphitation (facultatif) en atmosphère inerte, à 1600-2800°C.

Les résines se classent dans deux catégories. La première est constituée des résines **phénoliques** et **furfuryliques**. Ce sont les plus couramment utilisées. Elles présentent deux principaux inconvénients: (1) un faible rendement en carbone (50-60%), (2) un grand retrait lors de la carbonisation. Il en résulte un carbone poreux, de faible densité (1,5-1,6), avec de faibles propriétés mécaniques, d'où la nécessité de cycles de réimprégnation/recarbonisation pour améliorer densité et performance [10]. De ce fait, les temps d'élaboration sont longs.

La seconde catégorie comprend des résines "exotiques" telles que les **polyimides**, et des oligomères contenant des groupes **acétylèniques** (-C≡C-). Elles donnent de hauts rendements en carbone (≥75%), et produisent des composites résistants après seulement un cycle d'imprégnation-carbonisation. Cependant, leurs propriétés mécaniques ne peuvent pas être améliorées par des cycles de densification car ils développent généralement des porosités fermées.

Thermoplastiques.

Contrairement aux résines, le **brai** est un matériau "précarbonisé". Il est constitué, en effet, d'entités polyaromatiques. La carbonisation consiste en une croissance aromatique et une polymérisation, accompagnées d'une élimination des atomes d'hydrogène. Ce dégazage se produit en phase plus ou moins visqueuse. Le rendement en carbone dépend de la composition du brai précurseur, et des conditions de carbonisation. La diminution de la vitesse de chauffe, l'application d'une pression (Hot Isostatic Pressing (HIP)), ou l'utilisation d'additifs chimiques avant la décomposition thermique du brai accroît le rendement en carbone. La technologie HIP nécessite la présence d'une capsule autour de l'échantillon. Le brai permet d'obtenir des carbones de haute densité (d=2) par imprégnations successives.

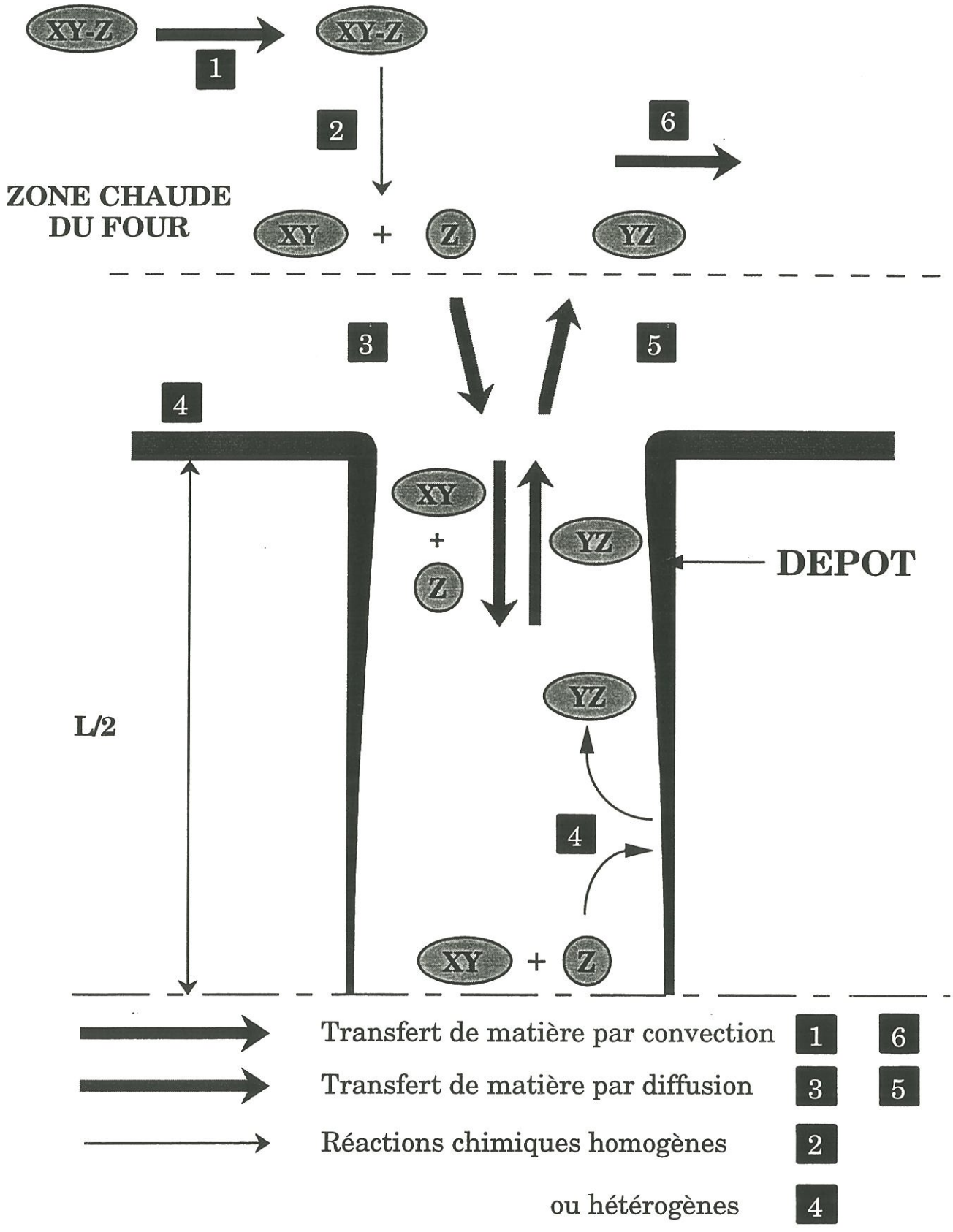

Figure 10: schéma de principe du processus de dépôt dans un pore de dimension L d'un solide X à partir de l'espèce gazeuse source XYZ

$$XYZ_{(g)} \longrightarrow X_{(s)} + YZ_{(g)}$$

Il existe également des polymères thermoplastiques comme précurseurs potentiels, qui utilisent la technologie HIP sans la nécessité d'encapsulation comme pour le brai (**PEI,PEEK**). Ils sont cependant chers, mais les carbones dérivés possèdent des propriétés supérieures aux composites avec une matrice ex-résine phénolique après plusieurs cycles de densification.

Dans l'industrie la plupart des précurseurs pour la densification sont mixtes: résine/brai. La co-carbonisation permet d'améliorer le rendement en carbone.

4.2 - CVD/CVI

Le dépôt chimique en phase vapeur (CVD) est un processus dans lequel une phase solide se forme par réaction chimique à partir d'une ou plusieurs espèces gazeuses généralement au contact d'un substrat maintenu en température. Dans le cas de la densification de préformes fibreuses, le terme de CVI est plus approprié car un dépôt en profondeur s'effectue en parallèle au dépôt de surface. Dans ce cas précis, le rapport entre la vitesse de dépôt et la vitesse des transferts de masse dans la phase gazeuse (figure 10) est un paramètre essentiel, qui détermine le caractère diffusionnel ou chimique du régime de dépôt. Le régime chimique permet d'éviter la fermeture prématurée de la porosité ouverte. Il est favorisé, en CVI isotherme et isobare (ICVI), dans des conditions de basses pression (<50kPa) et température (<1200°C). Des procédés, autres que la ICVI, ont été envisagés pour ne pas subir cette limitation due aux vitesses de diffusion et de surface: procédé (1) par gradient thermique (gradient thermique au sein du substrat), (2) par gradient de pression, (3) par CVI pulsée (cycles de dépôt-mise sous vide: renouvellement de la phase gazeuse). Cependant, ils ne sont pas adaptés à la production industrielle en grande quantité, dans l'état actuel de la technologie.

La chambre de dépôt est une enceinte ouverte aux deux extrémités, parcourue par le flux gazeux constitué d'un gaz vecteur entraînant le ou les

gaz précurseurs du solide. Dans le cas des réacteurs à parois froides, seul le substrat est chauffé directement par exemple par induction, ce qui limite les réactions en phase homogène et les dépôts sur les parois du réacteur, mais provoque de forts gradients de température, et donc de fort courants de convection. Dans le cas des réacteurs à parois chaudes, le chauffage est obtenu par rayonnement ce qui porte les parois et le substrat à des températures voisines, élevées. Ce type de réacteur permet d'obtenir une phase gazeuse homogène mais le dépôt simultané sur les parois provoque une consommation accrue des gaz.

Le dépôt de **pyrocarbone**, par craquage d'hydrocarbures gazeux (méthane, propane, ...), est un processus particulièrement complexe. Il met en jeu toute une série de réactions de déshydrogénation/polymérisation, et fait ainsi intervenir de nombreuses espèces intermédiaires (acétylène, éthylène, benzène, aromatiques à haut poids moléculaires,...) [11]. Leurs proportions relatives dans la phase gazeuse, différentes selon le ou les gaz précurseurs et les conditions opératoires, déterminent la microtexture du carbone déposé [12,13]. Des études menées sur les relations liant conditions expérimentales et microtexture du carbone ont abouti à des tendances [12-16]. Mais les mécanismes restent encore mal connus.

5 - Propriétés mécaniques

5.1 - Constituants

Fibre et matrice sont fragiles: elles sont sensibles aux défauts (défauts intrinsèques, défauts de surface...). Or, à chaque taille de défaut, a_c, est associée une contrainte à rupture σ_R différente [17,18], selon la relation suivante:

$$\sigma_R = \frac{K_{Ic}}{Y}\frac{1}{\sqrt{\pi a_c}} \qquad (1)$$

avec K_{Ic} la ténacité à rupture, et Y, un facteur de forme.

Une dispersion des contraintes à rupture est ainsi observée: aspect statistique de la rupture. La probabilité de trouver un défaut de taille critique a_c dans un volume V, soumis à la contrainte σ, est le plus souvent formulée par la statistique de Weibull [19] dans le cas des fibres de carbone. La probabilité de rupture est exprimée de la manière suivante:

$$P = 1 - exp\left(-\frac{V}{V_0}\left(\frac{\sigma - \sigma_u}{\sigma_0} \right)^m \right) \qquad (2)$$

avec

σ: la contrainte appliquée

σ_u: la contrainte en dessous de laquelle P=0 (σ_u est supposée égale à zéro)

V: le volume soumis à la contrainte

V_0: un volume de normalisation

σ_0: le facteur d'échelle en unité de contrainte

m: le module de Weibull; il rend compte de la dispersion des contraintes à rupture.

L'équation (2), établie pour les contraintes à rupture, peut être appliquée aux déformations de la même manière.

Divers estimateurs sont utilisés pour définir la probabilité de rupture, P. Celui, choisi par la suite, est le suivant:

$$P = \frac{i - 0,5}{N} \qquad (3)$$

avec N, le nombre d'échantillons testés, et i le rang de la $i^{ème}$ contrainte à rupture, celles-ci étant classées par ordre croissant.

5.2 - Comportement mécanique des CMCs

Lors d'une sollicitation mécanique, quand la déformation à rupture du constituant le plus fragile est atteinte, la première fissure apparaît au sein de ce constituant. Si cette première rupture ne conduit pas immédiatement à la rupture globale du matériau (surcharge de l'autre constituant), il y a **rupture multiple** dans le constituant au sein duquel s'est amorcée la rupture. Les conditions de multifissuration, au sein d'un composite unidirectionnel, sont

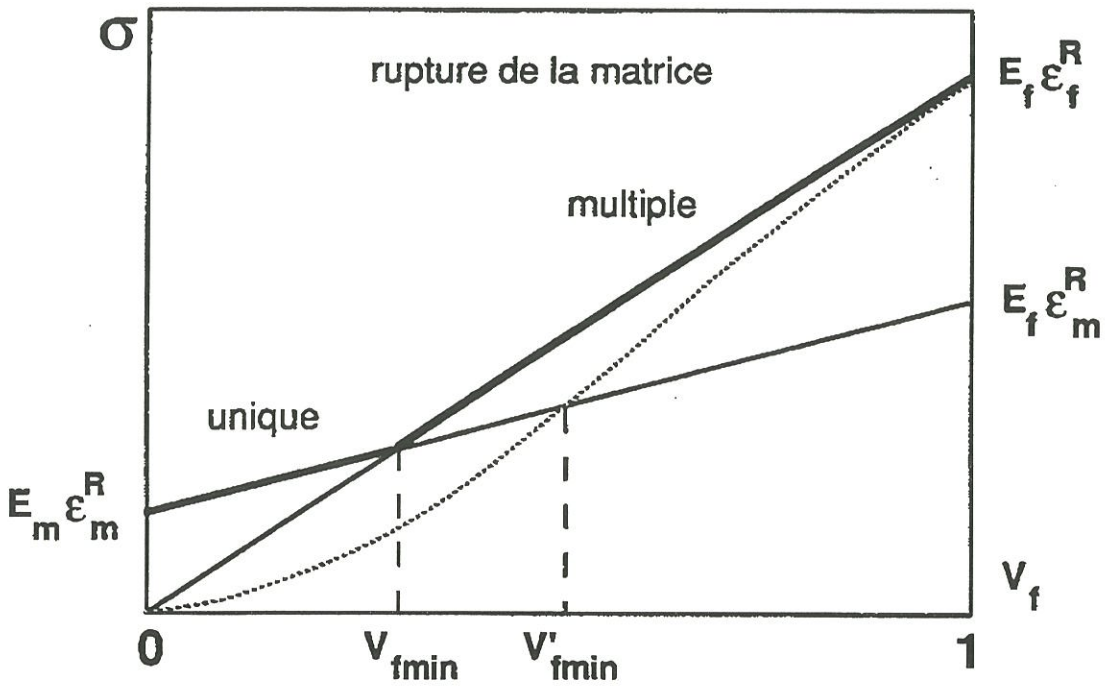

(a)

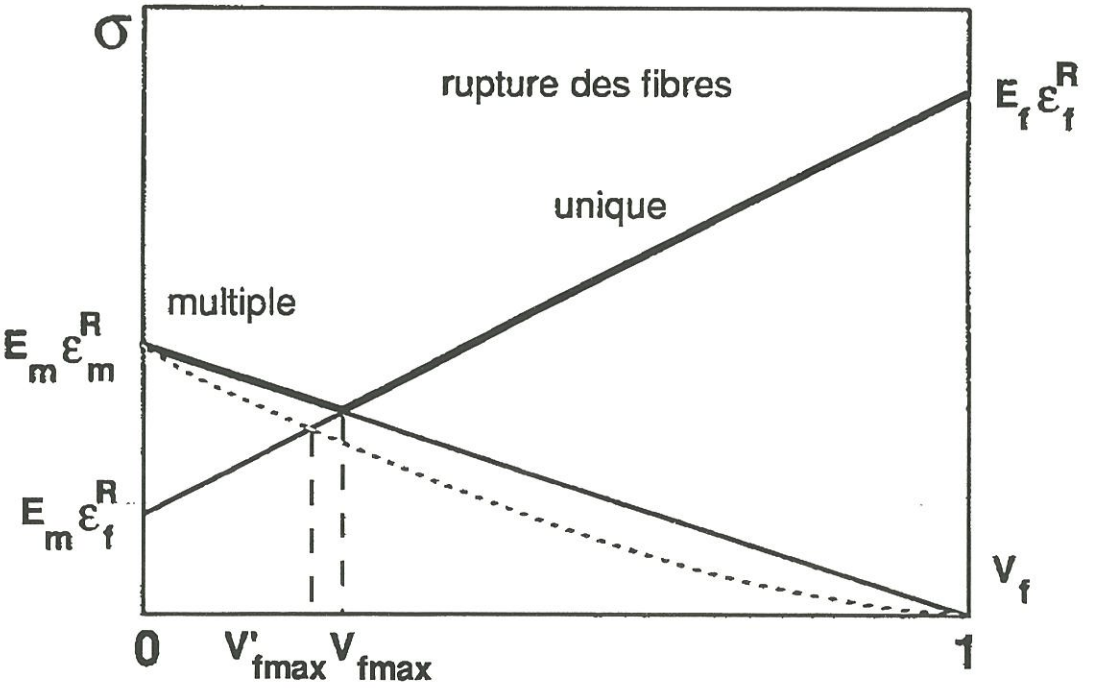

(b)

Figure 11: représentation schématique des conditions de rupture unique ou multiple dans les composites unidirectionnels fragile-fragile [20]
(a) $\varepsilon_{R,m}<\varepsilon_{R,f}$; (b) $\varepsilon_{R,m}>\varepsilon_{R,f}$

illustrées par les courbes en trait plein de la figure 11, suivant que la matrice est plus ou moins fragile que les fibres [20]. Les comportements mécaniques de différents types de matériaux composites unidirectionnels, sollicités en traction et ayant un V_f amenant à la rupture multiple, sont représentés schématiquement à la figure 12. Ils peuvent se subdiviser en deux groupes: les **composites inverses** (figure 12.a,b) pour lesquels $\varepsilon_{R,m}<\varepsilon_{R,f}$, et les **composites réguliers** (figure 12.c,d) pour lesquels $\varepsilon_{R,m}>\varepsilon_{R,f}$.

Les valeurs critiques de fraction volumique de fibres (V_{fmin}, V_{fmax}), déduites des courbes de la figure 11 et conduisant à la distinction rupture unique ou multiple, ne tiennent pas compte des **effets d'entaille** liés à la rupture du constituant le plus fragile. Ceux-ci sont susceptibles de diminuer le niveau de contrainte à rupture de l'autre constituant, et donc de modifier les valeurs de taux de fibre critique (courbes en trait pointillé de la figure 11, auxquelles sont associées des taux critiques différents: $V_{f'min}$ et $V_{f'max}$).

Par ailleurs, des **mécanismes de dissipation d'énergie**, tels que la décohésion à l'interface fibre/matrice et/ou le glissement avec frottement lorsque la fissure arrive à une interface, rendent possible par exemple la multifissuration de la matrice pour des $V_f<V_{f'min}$. Dans ce cas, la comparaison entre l'énergie, pouvant être dissipée à l'interface (par exemple l'énergie de décohésion par cisaillement $\mathcal{G}_{IId}$), et l'énergie de rupture de la fibre ($\mathcal{G}_{If}$) permet de prédire si il y aura rupture de la fibre, et donc celle du composite, ou décohésion interfaciale [21]. D'où l'intérêt d'**affaiblir la liaison interfaciale** afin de disposer d'un domaine d'endommagement dans le comportement du composite (augmentation du travail de rupture du composite).

Les mécanismes de dissipation d'énergie à l'échelle de la micromécanique, dans le cas d'une matrice plus fragile que la fibre, sont les suivants:

- la fissure matricielle
- la décohésion fibre/matrice

- le pontage des fissures par les fibres, et la résistance par frottement des fibres intactes
- la rupture de fibres en arrière du front de fissure
- l'extraction de fibre en arrière du front de fissure, après rupture de la fibre.

5.2.1 - CMCs classiques (ex: SiC/SiC)

Dans le cas des SiC/SiC, à fibres Si-C-O ($E_f \approx 200GPa$) et à matrice SiC-CVI ($E_m \approx 400GPa$), la fibre est moins fragile que la matrice ($\varepsilon_{R,f} > \varepsilon_{R,m}$), mais elle est beaucoup moins rigide ($E_f < E_m$). Lorsque le composite est sollicité mécaniquement, la matrice commence à se fissurer avant les fibres.

Si la **liaison entre fibre et matrice** est **trop forte**, les toutes premières fissures matricielles se propagent en mode I à travers les fibres ($V_f < V_{f'min}$), entraînant la rupture prématurée des fibres, et donc du composite. Les fibres n'assurent pas leur rôle de renfort, et le comportement du composite reste **fragile** (figure 13.a).

Si la **liaison entre fibre et matrice** est **faible**, les fissures provenant de la matrice sont déviées en mode II à l'interface fibre/matrice, préservant les fibres, mais provoquant des décohésions entre les deux matériaux. La multifissuration de la matrice (plateau de la courbe de la figure 13.b) se poursuit jusqu'à l'endommagement complet de la matrice (fin du plateau ou saturation). Le transfert des efforts n'est plus assuré entre la fibre et la matrice (décohésion totale entre fibre et matrice). La déformation à rupture du composite tends vers celle plus importante de la fibre (figure 13.b). Dans ce type de matériau, la dissipation de l'énergie de rupture est principalement assurée par les décohésions fibre/matrice et les frottements qu'elles engendrent, d'où un **mécanisme de ténacité par décohésion de l'interface et frottement** [22].

Le cas d'une **liaison intermédiaire** a été obtenue pour des matériaux SiC/SiC élaborés avec une interphase séquencée $(C/SiC)_n$ [23]. Elle est associée

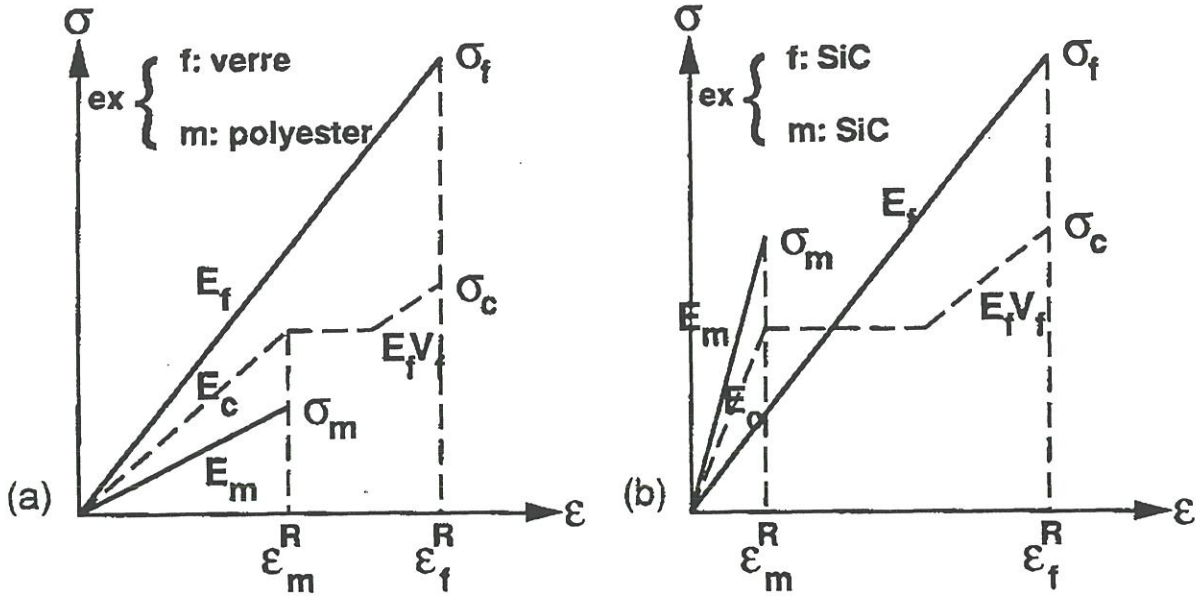

subdivision de la matrice ($V_f > V_{fmin}$)

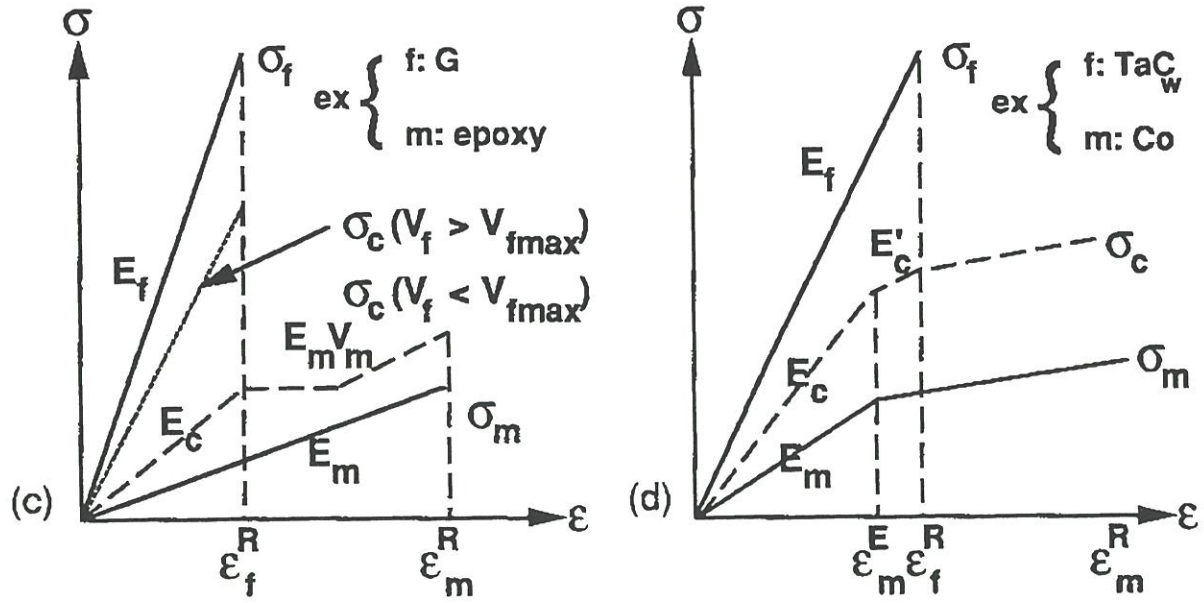

subdivision des fibres ($V_f < V_{fmax}$)

Figure 12: représentation schématique du comportement endommageable de matériaux composites unidirectionnels [20]

(a), (b) $\varepsilon_{R,m}<\varepsilon_{R,f}$; (c), (d) $\varepsilon_{R,m}>\varepsilon_{R,f}$

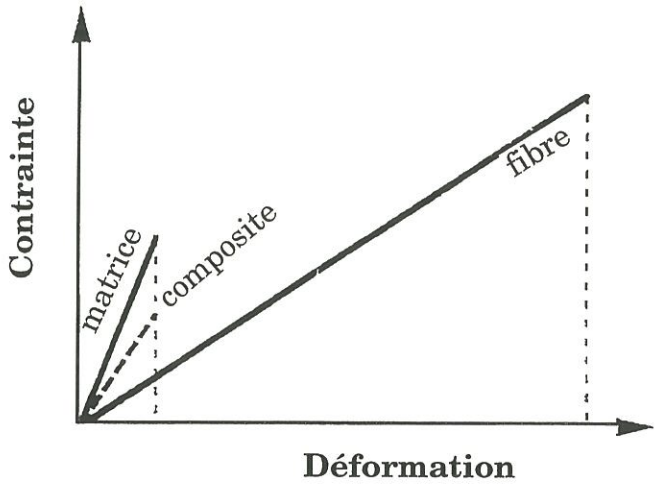

(a)

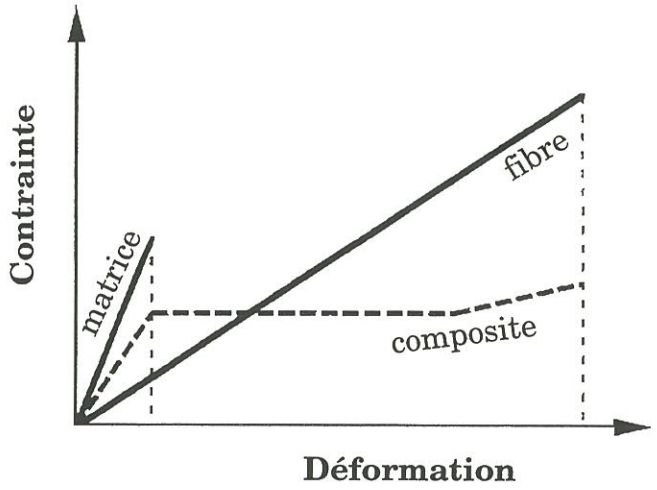

(b)

Figure 13: représentation schématique des courbes contrainte-déformation en traction de matériaux composites du type SiC/SiC selon la force de la liaison fibre/matrice: (a) forte; (b) faible

lors des déviations de fissure en mode II à de plus faibles longueurs de décohésion (2ℓ), et à une **contrainte de cisaillement interfaciale (τ) plus élevée**, qui permet de recharger rapidement la matrice déliée de la fibre. Il en résulte un pas de fissuration matricielle plus faible par rapport au cas précédent. La dissipation de l'énergie de rupture est alors assurée essentiellement par la rupture matricielle: **mécanisme de ténacité par multifissuration de la matrice**. Ce comportement mécanique ne présente pas de plateau, et permet d'atteindre des contraintes à rupture plus élevée (figure 14).

5.2.2 - Composites carbone/carbone

La matrice de carbone est en général plus fragile et moins rigide que les fibres carbone ($\varepsilon_{R,f}>\varepsilon_{R,m}$, $E_f>E_m$). Le rapport des modules est inversé par rapport aux SiC/SiC: ce sont les fibres qui contrôlent la rigidité du matériau. Les comportements en traction, attendus pour les composites carbone/carbone, devraient être du même type que ceux, précédemment décrits, selon que la liaison fibre/matrice est très forte ou faible.

Une **forte liaison fibre/matrice** est obtenue en utilisant des fibres traitées en surface (oxydation), et un précurseur liquide pour la matrice [24-27]. Il en résulte un **comportement** mécanique de type **fragile** (courbe (a) de la figure 15). D'une manière générale, lorsque la fibre présente à sa surface un nombre suffisant de sites actifs une forte liaison est assurée. Par exemple, la fibre HM présente moins de sites actifs (moins de plans de carbone débouchent sur leur tranche en surface de fibre), que la fibre HT, qui elle-même en présente moins que la fibre A. La liaison fibre/matrice augmente donc en passant de la fibre HM à la fibre HT, puis à la fibre A [24].

Une **faible liaison fibre/matrice** peut être obtenue en utilisant des matrices élaborées par voie liquide, et des fibres non traitées en surface, et présentant très peu de sites actifs en surface [24-27]. Le moyen le plus utilisé pour affaiblir la liaison interfaciale est le traitement thermique, car il induit

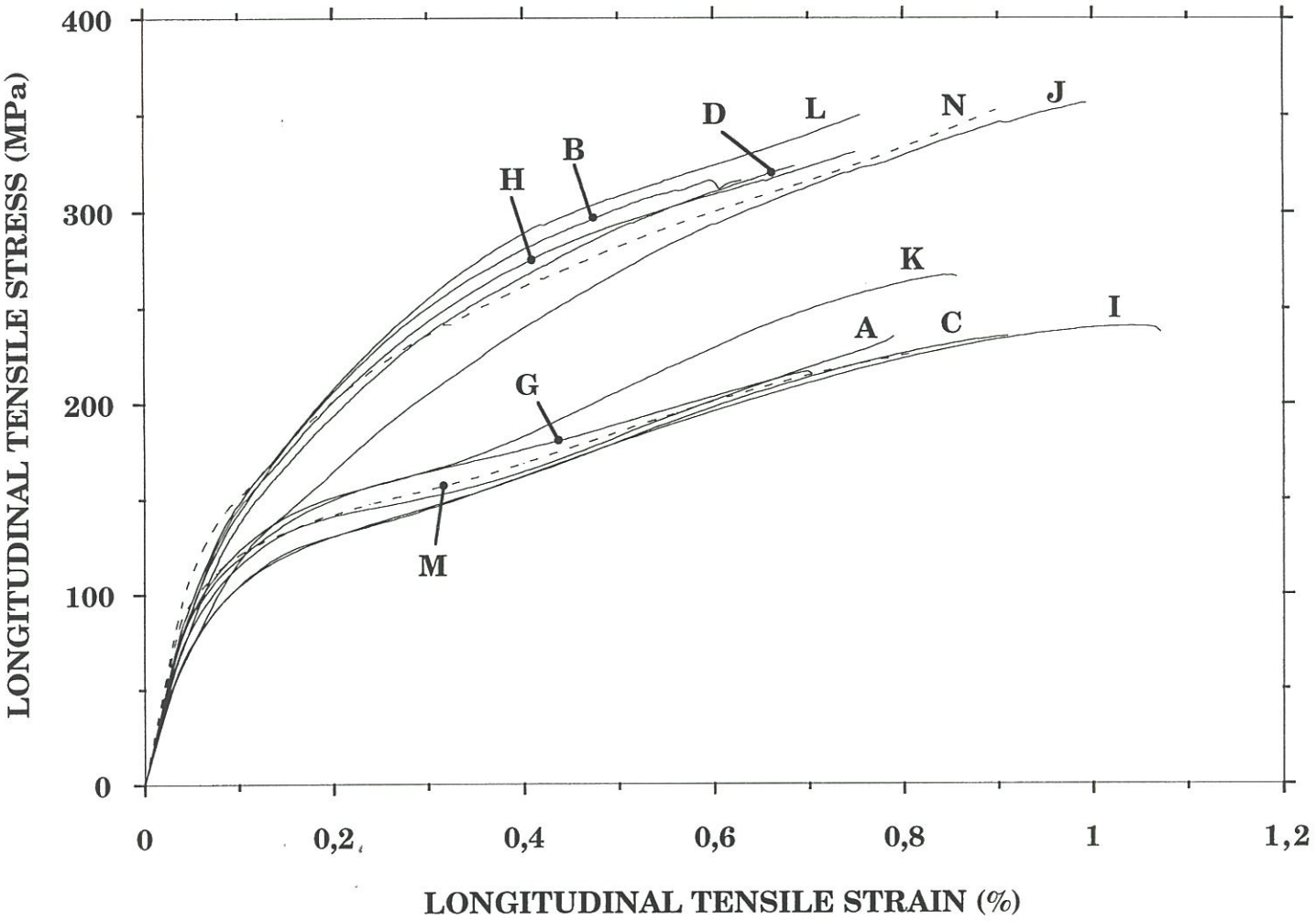

Figure 14: courbes contrainte-déformation de composites 2D SiC/SiC [23] avec deux mécanismes de ténacité à rupture différents:
courbes A, C, G, I, K, M: décohésion fibre/matrice et frottement
courbes B, D, H, J, L, N: fissuration matricielle

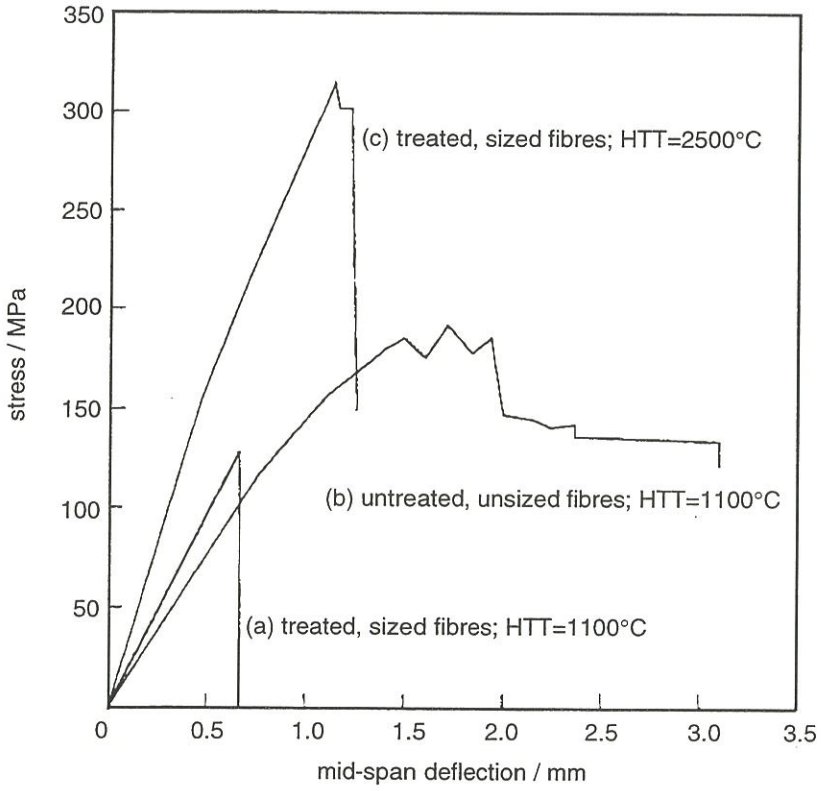

Figure 15: effet du traitement de surface et du THT sur les courbes de contrainte-déformation en flexion de composites carbone/carbone unidirectionnels [28]

des changements dans une matrice élaborée par voie liquide (retrait, réorientation des plans de carbone parallèlement à la surface des fibres à l'interface ("stress-graphitization")) [29-30]. Une autre alternative possible est l'oxydation des composites [31], car elle s'effectue préférentiellement à l'interface fibre/matrice. La figure 15 montre l'effet d'une fibre, non traitée en surface, et du THT sur les courbes en flexion de composites C/C unidirectionnels (**non linéarité**). Il y a une **augmentation de la ténacité** de ces C/C par les mécanismes de dissipation d'énergie, décrits précédemment, dans le plan de la fissure matricielle. Si τ est trop faible (courbe (b) de la figure 15), de grandes longueurs de fibres extraites sont observées sur le faciès de rupture, et les contraintes restent faibles du fait d'un mauvais transfert de charge entre fibre et matrice.

Dans le cas des **matrices de pyrocarbone**, la **microtexture de la matrice** à l'interface **conditionne la force de la liaison fibre/matrice** [15,32]. Kimura et al. [15] ont montré qu'un pyrocarbone isotrope adhère aux fibres, et qu'une structure iso+LR pour la matrice donne une rupture fragile, alors que la structure LR+LL engendre de la délamination parallèlement aux fibres. Ceci a été attribué à une contrainte de cisaillement interfaciale plus faible, due à des fissures dans la structure laminaire lisse. Oh et Lee [32] ont montré qu'en augmentant la concentration de propane lors de la CVI, une plus grande orientation de la matrice vis-à-vis de la surface de la fibre est obtenue. Ceci résulte en une liaison fibre/matrice plus faible, et ainsi à un comportement non linéaire en flexion.

6 - Zone interfaciale

Le rôle de la zone interfaciale apparaît donc primordial dans le comportement mécanique des CMCs. Il faut noter, cependant, que d'autres paramètres influencent les propriétés mécaniques de ces matériaux, tels que l'architecture fibreuse, et les porosités. De ce fait, les modèles théoriques se

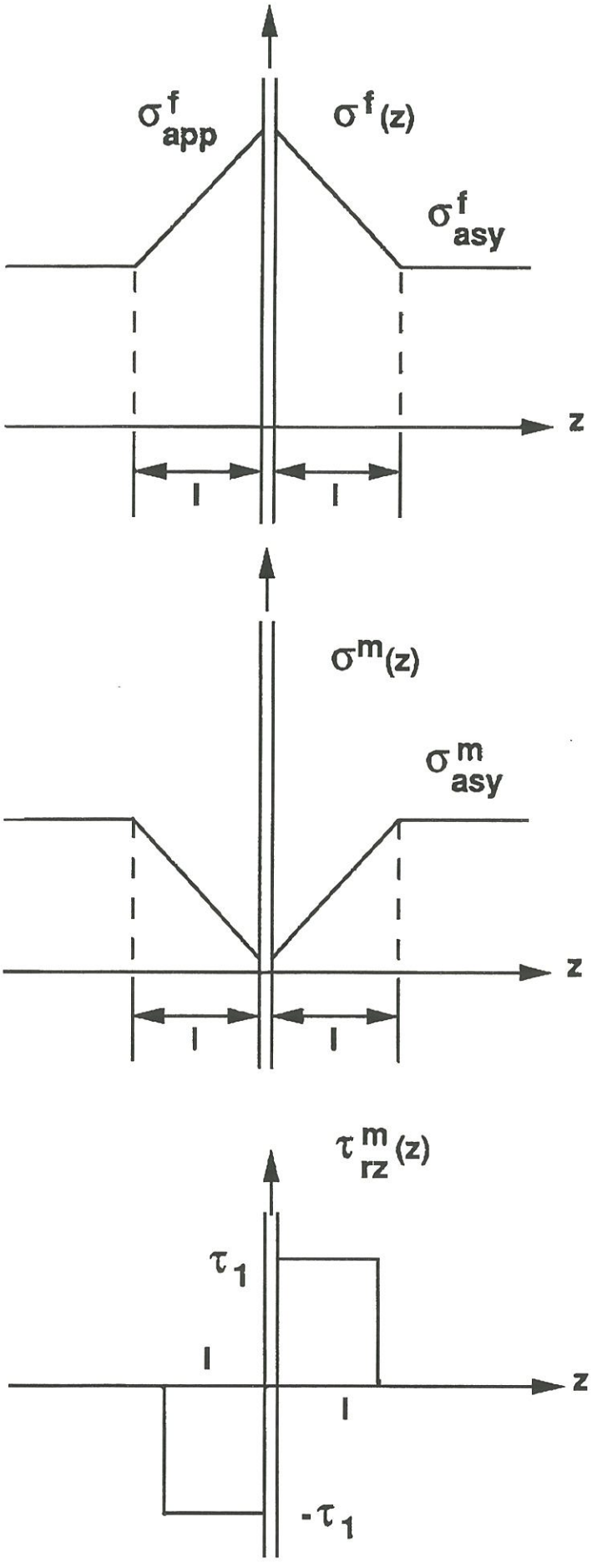

Figure 16: représentation schématique des états de contraintes au droit d'une fissure transverse lors d'un glissement interfacial à seuil fixe

rapportent à des systèmes plus simples tels que les composites unidirectionnels, ou les microcomposites (une fibre unique enrobée dans une matrice) pour isoler le rôle de la zone interfaciale.

6.1 - Approche théorique

L'observation au microscope des matériaux après rupture renseigne sur les faciès de rupture, les longueurs de décohésion fibre/matrice (2ℓ), le pas de fissuration ou distance moyenne entre fissures matricielles, l'ouverture résiduelle des fissures, la zone de la déviation des fissures, etc.

L'endommagement du matériau a fait l'objet de modèles théoriques pour prédire les comportements mécaniques des CMCs. Ces modèles concernent pour la plupart les CMCs unidirectionnels.

Le seuil de début d'endommagement a été ainsi modélisé par Aveston, Cooper, et Kelly (ACK) [33]. Ils se sont intéressés à la propagation d'une fissure, perpendiculaire à l'axe des fibres, en introduisant la possibilité d'un glissement entre la fibre et la matrice. Les états de contraintes au droit d'une fissure transverse, lors d'un glissement interfacial à seuil fixe, sont représentés à la figure 16. Des contraintes seuil de début d'endommagement ont été déterminées dans les 3 cas suivants: (1) pas de glissement fibre/matrice; (2) glissement fibre/matrice; (3) décohésion fibre/matrice sans frottement. Bundiansky, Hutchinson et Evans (BHE) [34] ont généralisé l'approche d'ACK en considérant différents phénomènes interfaciaux possibles: (1) liaison fibre/matrice parfaite; (2) fibres non liées à la matrice et possibilité de glissement avec frottement; (3) fibres liées à la matrice et susceptibles d'être déliées par une tension normale à l'interface fibre/matrice.

Des critères de propagation de la fissure dans le matériau (K_{Ic}) [35,36], et de déviation interfaciale de la fissure [37] ont également été établis.

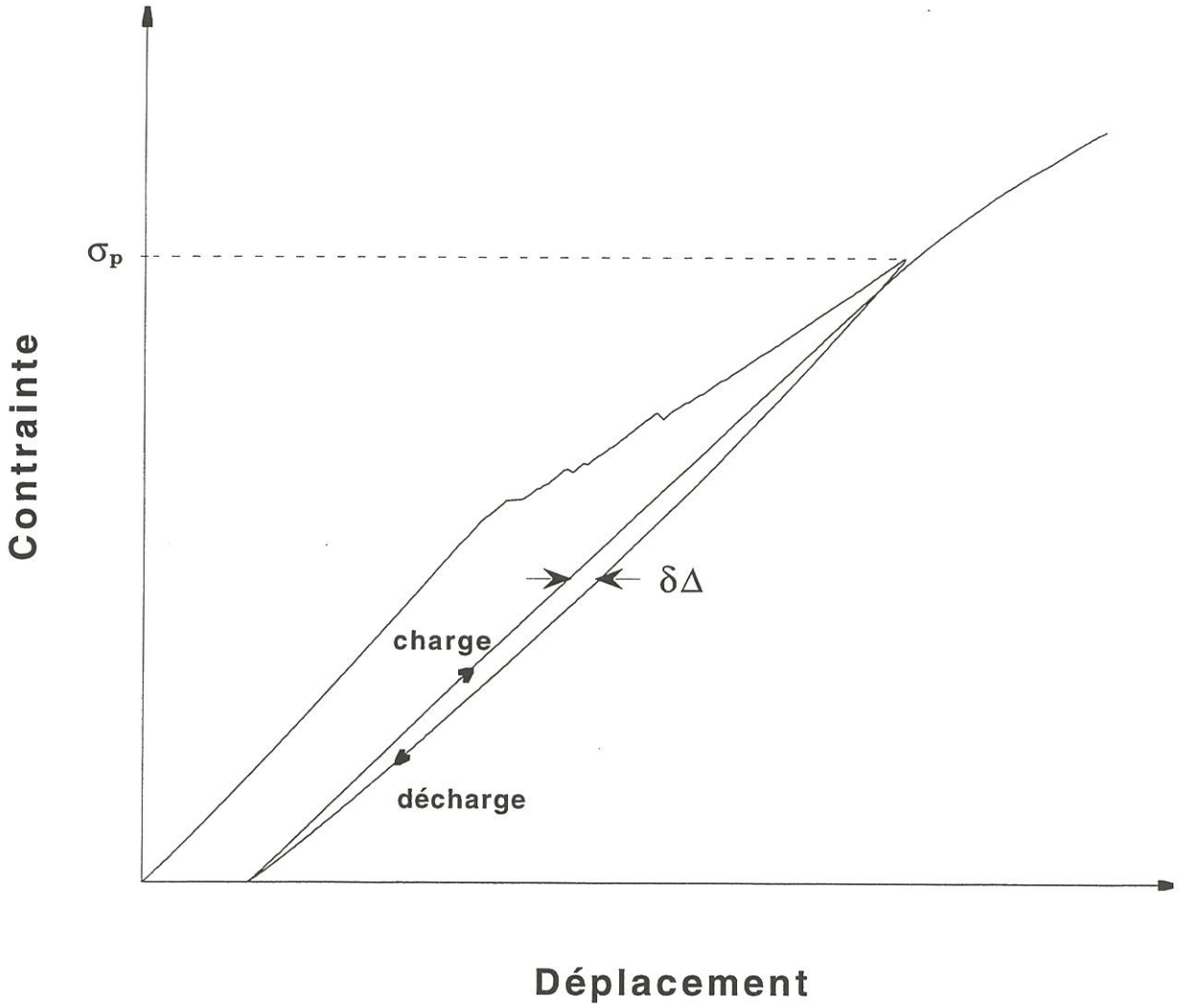

Figure 17: représentation schématique d'un cycle de charge-décharge

6.2 - Détermination de la contrainte de cisaillement interfaciale

6.2.1 - Par la mesure du pas de fissuration

Marshall et al. [38] propose une estimation de τ par la mesure du pas de fissuration à saturation ($2\ell^*$) après essai de traction:

$$\tau = \frac{\sigma_c \cdot R}{2V_f \cdot 2\ell^* \cdot \left(1 + \frac{E_f V_f}{E_m V_m}\right)} \quad (4)$$

avec σ_c la contrainte appliquée au composite, R le rayon de la fibre, E le module d'Young, V la fraction volumique (l'indice f se rapportant à la fibre, m à la matrice).

6.2.2 - Par des cycles de charge-décharge lors d'un essai de traction

La méthode utilisée pour déterminer la contrainte de cisaillement interfaciale a été développée pour les microcomposites (fibre unique revêtue de la matrice) [39]. Dans ce modèle, τ est supposé constant le long de l'interface déliée. Des cycles de charge-décharge sont effectués pendant l'essai de traction. Il y a formation de boucles d'hysteresis, dont la largeur $\delta\Delta$ (figure 17) est reliée à τ et à la contrainte appliquée σ correspondante par la relation:

$$\frac{\delta\Delta}{\sigma_p^2} = \frac{b_2 \cdot \left(1 - a_1 \cdot V_f\right)^2 \cdot R \cdot N}{2 \cdot E_m \cdot V_f^2} \cdot \frac{1}{\tau} \cdot \left(\frac{\sigma}{\sigma_p} \cdot \left(1 - \frac{\sigma}{\sigma_p}\right)\right) \quad (5)$$

où σ_p, est la contrainte maximale du cycle, a_1 et b_2 les coefficients de Hutchinson [40] définis pour des coefficients de Poisson identiques pour la fibre et la matrice (ν=0,4), R, le rayon de la fibre, et N le nombre de fissures matricielles.

τ est déterminé en traçant $\delta\Delta/\sigma_p^2$ en fonction de $(\sigma/\sigma_p.(1-\sigma/\sigma_p))$. Pour cela, le nombre de fissures à la contrainte σ_p doit être connu.

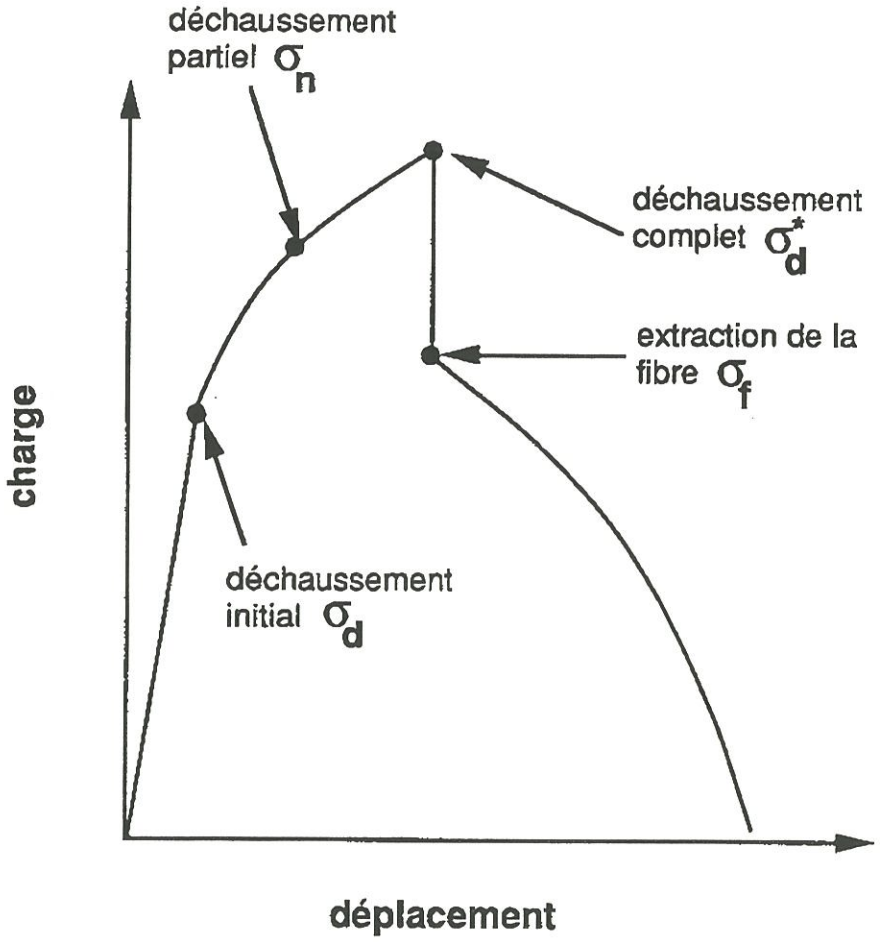

Figure 18: représentation schématique de la courbe charge-déplacement d'un essai de pull-out

6.2.3 - Par essai de pull-out

Le principe de cet essai consiste à soumettre une fibre, dont une partie est enchâssée dans une gaine de matrice, à une contrainte de traction uniaxiale, jusqu'à provoquer la décohésion à l'interface, puis l'extraction complète du filament. La courbe charge-déplacement d'un essai de pull-out est représentée schématiquement à la figure 18 [41]. L'exploitation de la partie finale du graphe, correspondant au déchaussement de la fibre, permet de déterminer la contrainte interfaciale de frottement τ avec :

$$\tau = \frac{dF/dL}{2\pi R} \tag{6}$$

avec R, le rayon de la fibre.

6.2.4 - Par microindentation

L'essai de microindentation a été développé à l'origine par Marshall [42]. Une charge ponctuelle est appliquée au centre d'une fibre au moyen d'un indenteur. Il en résulte un déplacement de la fibre dans sa gaine de matrice, fonction de la charge appliquée, des propriétés des constituants, et de l'interface. Les mesures de la charge et du déplacement permettent d'accéder à une ou des caractéristiques interfaciales selon les hypothèses faites.

Des essais ont été récemment menés sur des composites carbone/carbone par Hamada et al. [43].

7 - Conclusion

L'interface fibre/matrice joue un rôle déterminant dans le comportement mécanique tant pour les carbone/carbone que pour les CMCs en général. Il est donc nécessaire de pouvoir contrôler la liaison interfaciale afin d'optimiser les propriétés mécaniques des carbone/carbone.

L'ajout d'une interphase de carbone entre fibre et matrice, de microtexture donnée, apparaît comme un moyen de contrôler la zone

interfaciale. Ce concept est différent de ceux, qui ont jusque-là été utilisés pour faire varier la force de la liaison fibre/matrice (traitement de surface de la fibre, THT).

Le passage d'un comportement fragile, où les fibres ne jouent pas leur rôle de renfort, à un comportement tenace avec décohésion fibre/matrice est recherché. Toutefois, la liaison fibre/matrice ne doit pas être trop faible pour éviter de trop fortes décohésions (délamination), et un transfert de charge insuffisant.

8 - Objectifs et contenu du présent mémoire

Ce travail a eu comme objectifs (i) d'étudier et d'optimiser la zone interfaciale fibre/matrice de matériaux carbone/carbone modèles, que sont les microcomposites (fibre revêtue de la matrice), et (ii) d'étudier la ténacité de minicomposites carbone/carbone (fil infiltré) en relation avec la zone interfaciale.

La première partie de cette étude traite de l'influence de la modification de la liaison fibre/matrice de pyrocarbone sur les propriétés mécaniques en traction des microcomposites. Ces modifications portent sur (i) la *liaison physique* par l'emploi d'une même fibre avec 2 états de surface différents, (ii) les *contraintes résiduelles* à l'interface par le traitement thermique préalable à haute température de la fibre, (iii) la *liaison chimique* par l'ajout d'une interphase de pyrocarbone, de microtexture variable, entre fibre et matrice. La zone interfaciale est caractérisée par des observations en microscopie optique et électronique (à balayage et à transmission).

Dans une seconde partie, la liaison interfaciale fibre/matrice est modifiée au sein de minicomposites carbone/carbone. L'étude est recentrée autour des paramètres importants, identifiés dans la partie précédente. Le comportement mécanique de ces minicomposites est alors relié aux

caractéristiques interfaciales, et notamment à la contrainte de cisaillement interfaciale τ.

Les principaux résultats sont présentés dans un chapitre de synthèse, suivi d'annexes plus détaillées, consistant en des projets de publication dans des revues internationales.

PROCEDURES EXPERIMENTALES CONSTITUANTS

PROCEDURES EXPERIMENTALES-CONSTITUANTS

1 - Procédures expérimentales

1.1.- Elaboration CVD/CVI

Les dépôts de pyrocarbone sont effectués dans un four ICVI, décrit à la figure 19. La pression est maintenue constante à l'aide d'un régulateur relié au système de pompage. La chambre de dépôt est verticale, et constituée d'un suscepteur en graphite. Le chauffage se fait par induction.

1.1.1- Microcomposites

Un microcomposite représente la cellule élémentaire d'un composite, une fibre unique revêtue de matrice. Pour l'élaboration de ces matériaux, les fibres sont tendues une à une sur un cadre en Papiex[1], et fixées à l'aide d'une colle à base de carbone. Les cadres, ainsi préparés, sont placés à l'intérieur de l'enceinte du four. Deux types de microcomposites sont alors élaborés: les références constituées de la fibre et de la matrice de pyrocarbone (F/M), et les microcomposites pour lesquels une interphase de pyrocarbone est insérée entre la fibre et la matrice (F/I/M) (figure 20). Pour ces derniers, le dépôt de l'interphase et celui de la matrice s'effectuent dans le même cycle de chauffe. L'épaisseur totale de pyrocarbone est gardée constante ($V_f \approx 45\%$), avec $V_i \approx 12\%$ et $V_m \approx 43\%$ (V_f, V_i, et V_m étant respectivement les fractions volumiques de la fibre, de l'interphase, et de la matrice). Différentes conditions opératoires sont appliquées pour l'interphase afin d'obtenir des interphases de microtexture différente.

---

[1] Papiex™: feuilles de graphite expansé et recompressé, Le Carbone Lorraine, France

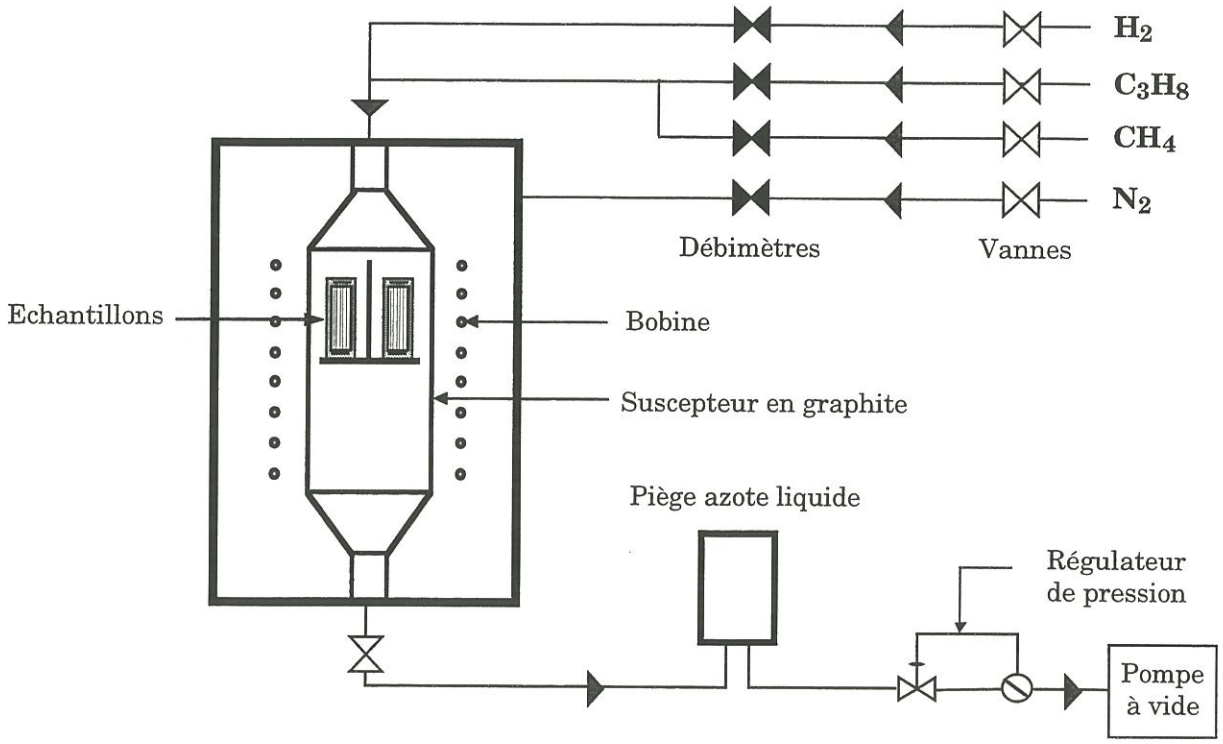

Figure 19: schéma du four CVD/CVI

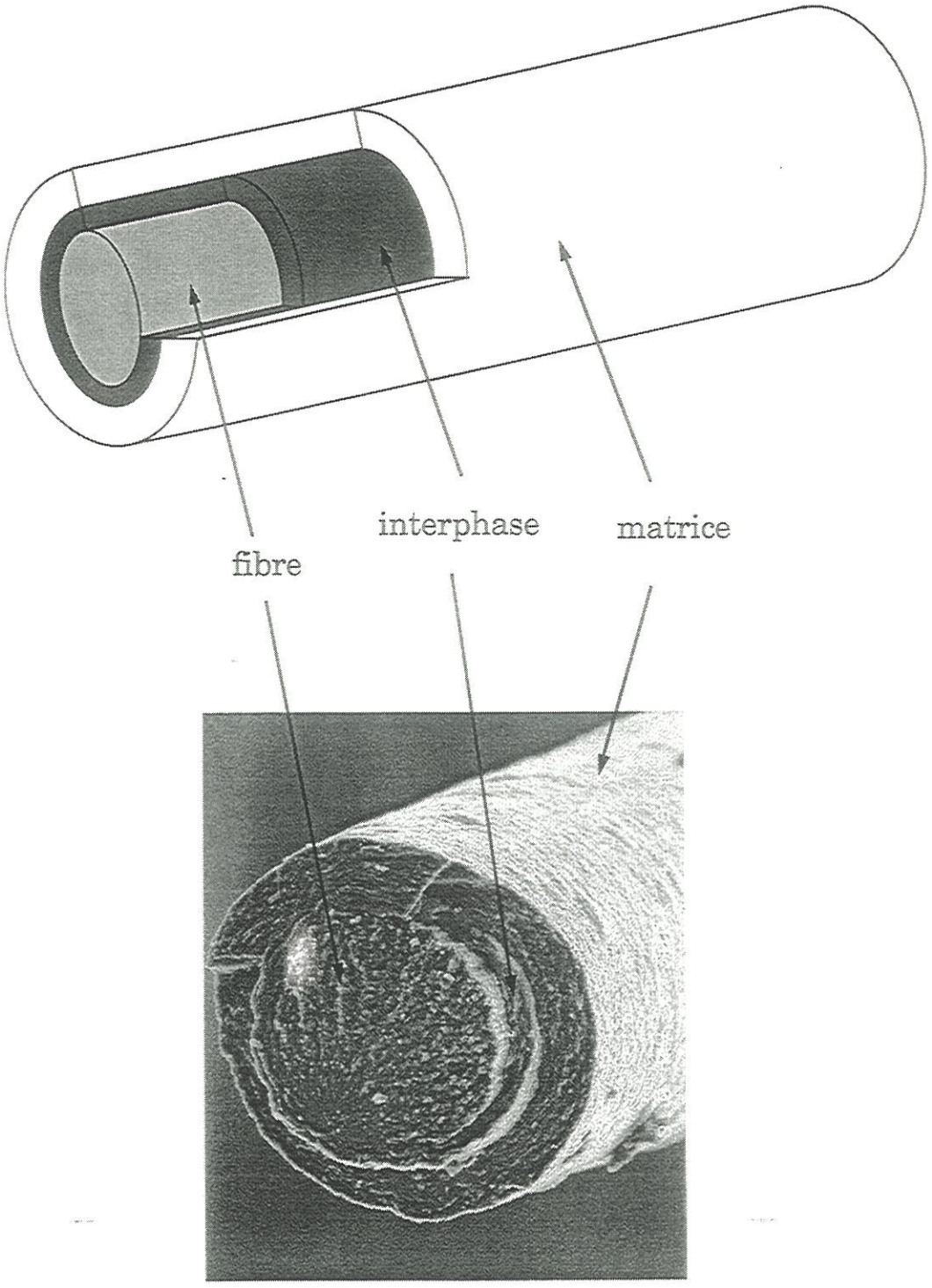

Figure 20: représentation schématique d'un microcomposite C/C/C
et le microcomposite réel associé

1.1.2 - Minicomposites

Un minicomposite est un fil densifié. Les fils, utilisés dans ce travail, sont constitués de 3000 fibres. Pour l'élaboration de ces minicomposites, les fils sont préalablement désensimés avec de l'acétone, qui sert également à homogénéiser la forme de tous les matériaux. Ils sont ensuite enroulés autour d'un cadre en graphite, fixés avec de la colle à base de carbone, et placés dans l'enceinte du four. La matrice de pyrocarbone est élaborée dans les mêmes conditions opératoires que pour les microcomposites. Cependant, des conditions CVI vont s'appliquer à l'intérieur du fil, alors que des conditions CVD vont s'appliquer à la surface du fil. Différentes microtextures caractérisent donc le pyrocarbone interne et externe au minicomposite, de même que des épaisseurs plus importantes sont observées en surface (figure 21). Les conditions opératoires utilisées pour l'interphase ont été choisies en fonction de la microtexture voulue pour le pyrocarbone à l'intérieur du fil, et pour des épaisseurs d'environ 0,1µm.

1.2 - Essais de traction

1.2.1 - Fibres, microcomposites

Pour les tests en traction, les fibres et les microcomposites sont collés sur des cadres en papier. Un banc de traction monofilamentaire est utilisé, comprenant un capteur de force de capacité 0-2N, et un dispositif de déplacement à vitesse constante (1%/min). Les propriétés en tension sont mesurées sur des longueurs de jauge de 10mm. Pour chaque type de matériaux, un lot de 15 à 20 échantillons est testé afin d'obtenir une population statistique.

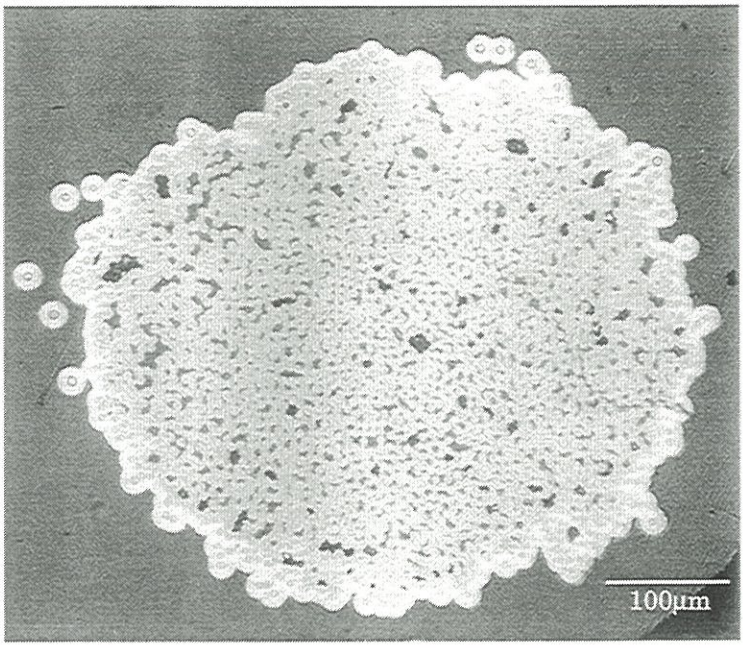

Figure 21: coupe transverse polie d'un minicomposite vue en microscopie optique

1.2.2 - Minicomposites

Les essais mécaniques sont effectués sur des longueurs de jauge de 50mm. Les échantillons sont collés aux deux extrémités dans des tiges support en acier par une colle structurale[1]. L'alignement des minicomposites vis-à-vis des tiges support est assuré à l'aide d'un outillage spécialement conçu à cet effet. Dans le cas des fils bruts (non infiltrés), l'ensimage est préalablement éliminé. Des lots de 5 échantillons ont été testés pour chaque type de minicomposites.

Les minicomposites sont testés sur une machine de traction pour fils, développée au laboratoire. Elle est constituée d'un capteur de force de 500N, et permet une mesure indirecte des déformations par les 2 capteurs de déplacement, de capacité 1mm, placés symétriquement sur le bâti. Un moteur pas à pas assure le déplacement, et une acquisition sur micro-ordinateur est effectuée, avec une visualisation de l'essai de traction en parallèle sur table traçante.

1.3 - Caractérisation structurale

1.3.1 - Texture du pyrocarbone

Microscopie optique: mesure de l'angle d'extinction (Ae)

L'anisotropie des pyrocarbones a été déterminée en lumière polarisée[2] sur des sections transverses d'échantillons polis. Cette caractérisation s'appuie sur la mesure de l'anisotropie de reflectance Ro/Re du pyrocarbone. Elle consiste à déterminer l'angle d'extinction (Ae) par rotation de l'analyseur, nécessaire pour que les 2 branches opposées de la croix de Malte, observée en lumière polarisée, s'éteignent (figure 22) [44, Annexe 4]. Dans la gamme des

---

[1] Scotch-Weld 9323 B/A, Scotch 3M

[2] microscope MeF_3 Reichert-Jung

pyrocarbones de basse température et basse pression, ces angles d'extinction sont reliés à la texture optique de manière empirique:

isotrope	0<Ae<4°
laminaire sombre	4<Ae<12°
laminaire lisse	12<Ae<18°
laminaire rugueux	Ae>18°

Microscopie électronique à transmission (MET): mesure de l'angle d'ouverture azimutale (OA)

Les mesures sont effectuées sur des clichés de diffraction électronique à aire sélectionnée réalisés au MET[1]. Ces clichés sont étudiés par analyse d'image à l'aide d'un programme informatique développé sur le logiciel LabView™ [44, Annexe 4].

Le diagramme de diffraction électronique se présente sous la forme d'une tâche centrale (faisceau direct), et d'anneaux concentriques représentant les réflexions 00ℓ (ℓ pair), et les bandes 10, et 11, relatives à la structure interne bidimensionnelle des couches graphitiques. La mesure de la distance entre l'arc 002 et la tâche centrale permet tout d'abord de déterminer la distance interréticulaire d_{002}, qui diminue avec l'amélioration du mode d'empilement des couches graphitiques.

Les anneaux 00ℓ sont continus pour les fibres HT ex-PAN utilisées (figure 23). Pour ces dernières, les plans de carbone ont, en effet, leur axe c orienté aléatoirement dans le plan perpendiculaire à l'axe de la fibre.

Dans le pyrocarbone, l'anisotropie de la texture induit des arcs symétriques (figure 23). Ces arcs sont caractérisés d'une part par leur largeur à mi-hauteur, qui permet de déterminer la grandeur L_c à l'aide de l'équation de Scherrer, et d'autre part, par leur angle d'ouverture azimutale OA, qui est relié à la désorientation des plans de carbone par rapport au plan d'anisotropie (plus OA est élevé, plus la désorientation est grande).

---

[1] microscope CM-30 ST Philips, avec une haute tension de 300kV

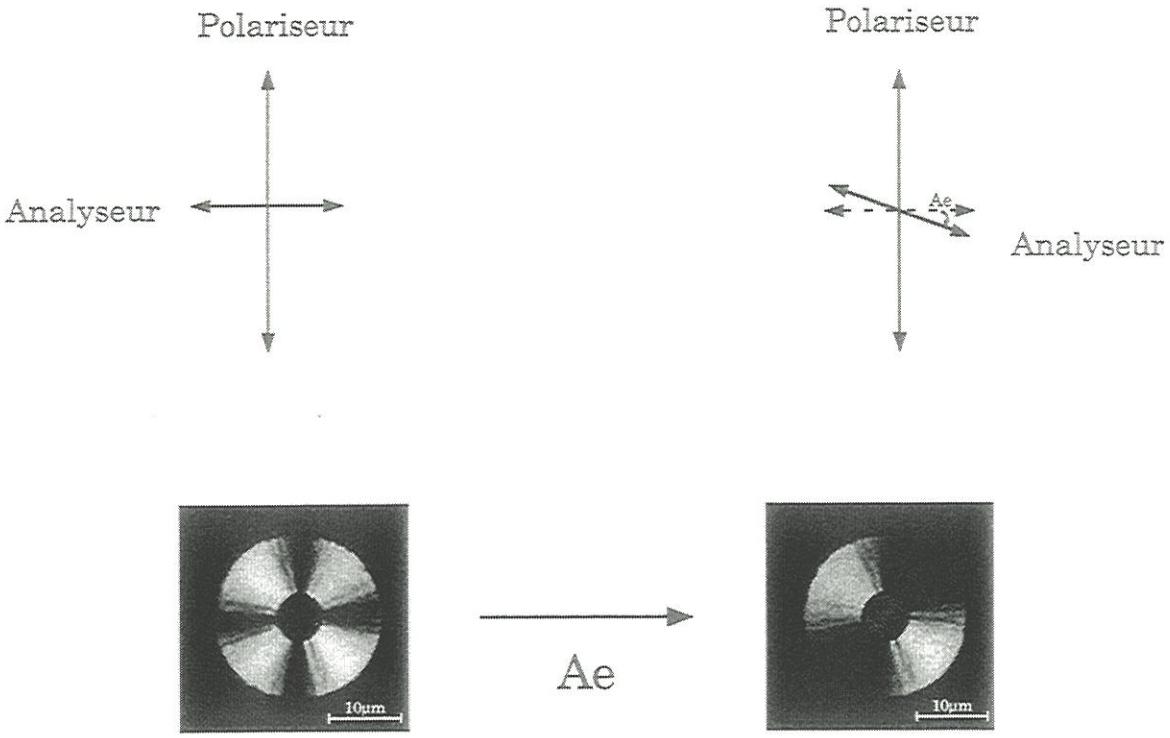

Figure 22: schéma de principe de la mesure de l'angle d'extinction (Ae) en lumière polarisée

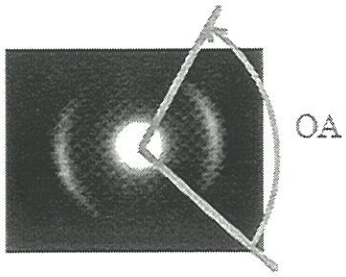

(a)

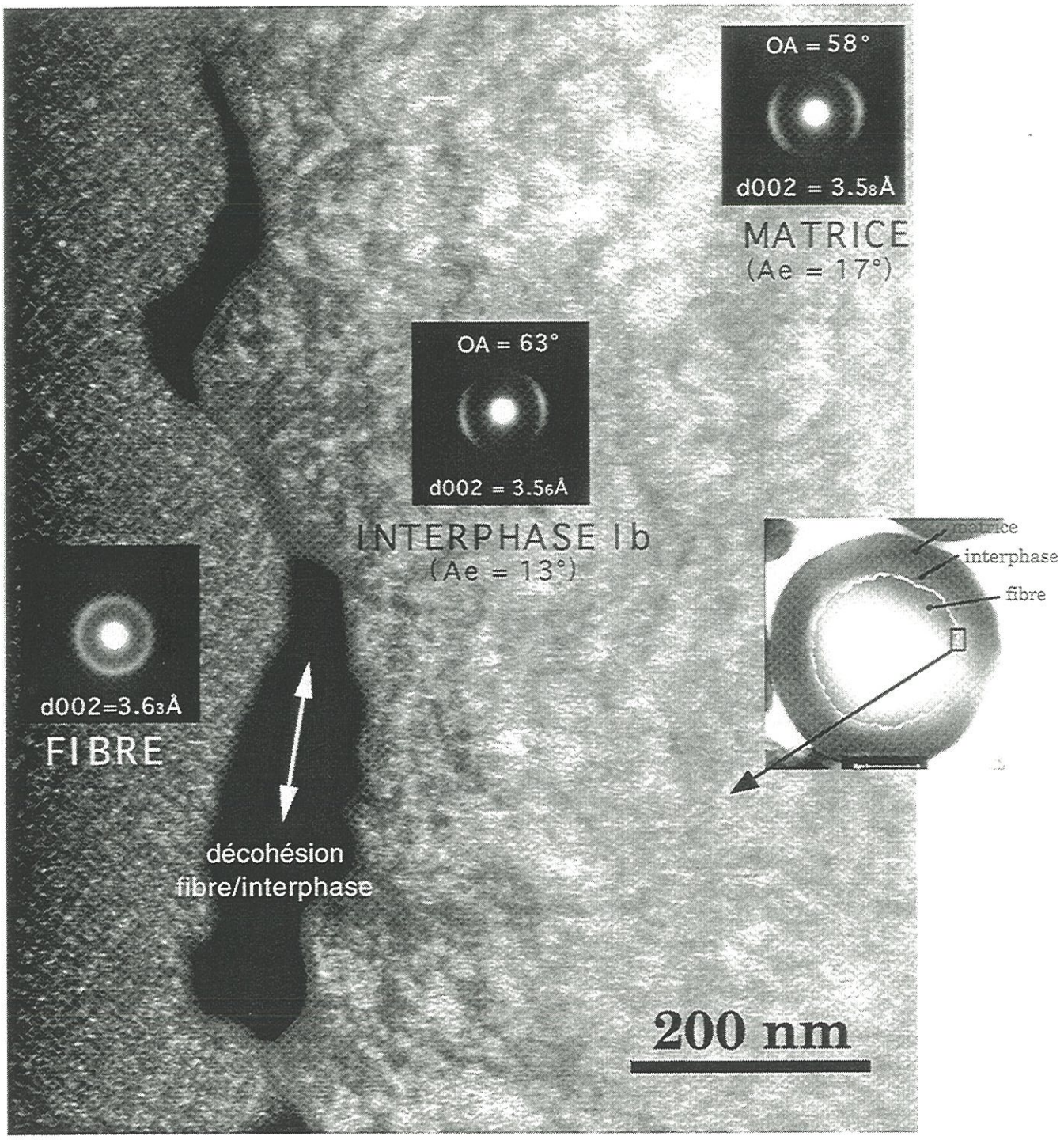

(b)

Figure 23: mesure des angles d'ouverture azimutale (OA) sur les clichés DEAS (Diffraction Electronique à Aire Sélectionnée) obtenus en MET
(a) principe de la mesure
(b) exemple sur le microcomposite A-HTT/Ib/M

1.3.2 - Structure de la zone interfaciale

L'observation au MET de la zone interfaciale après élaboration des matériaux nécessite la préparation de lames minces. Pour cela, un groupe de microcomposites (figure 24) ou un minicomposite est imprégné dans de la colle époxyde, puis enrobé dans de la colle à base d'alumine. Des tranches sont ensuite découpées, dans lesquelles une pastille est prélevée avec l'échantillon au centre. Cette dernière est polie mécaniquement jusqu'à environ 80µm, et une cuvette est ensuite creusée à l'aide d'un Dimpler jusqu'à une épaisseur d'environ 30µm en fond de cuvette. Finalement, un amincissement ionique est effectué à froid [45, Annexe 1].

1.3.3 - Endommagement-Rupture

Les faciès de rupture ont été étudiés en microscopie électronique à balayage (MEB[1]), de même que l'endommagement des matériaux après rupture.

Le polissage de sections longitudinales de minicomposites, après rupture, a permis d'étudier l'endommagement au sein du matériau en microscopie optique et à balayage.

Des essais de traction sous MEB[2] ont pu être effectués à l'aide d'un microscope muni d'une platine. Dans ce dispositif, un moteur pas à pas permet le déplacement, et la force est mesurée par un capteur de capacité 0-200N. L'endommagement peut être ainsi étudié in-situ (apparition des fissures, ouverture des fissures).

---

[1] microscope HITACHI S-4500 à champs proche

[2] microscope JEOL JSM-840A équipé d'une platine Oxford

1.3.4 - Faciès miroir des fibres

Les faciès de rupture présentent systématiquement un faciès miroir (figure 25). La constante $\mathcal{A}$, caractéristique à chaque type de fibre, relie le rayon du miroir (R_m) à la contrainte appliquée (σ) par la relation:

$$\sigma = \frac{\mathcal{A}}{\sqrt{R_m}} \qquad (2)$$

Cette constante $\mathcal{A}$ a été déterminée pour les fibres A et A-HTT en évaluant la pente de la courbe σ en fonction de $1/\sqrt{R_m}$: $\mathcal{A}$(A)=2,6MPa.m$^{1/2}$; $\mathcal{A}$(A-HTT)=2,2MPa.m$^{1/2}$. Ces valeurs sont proches de celle obtenue pour une fibre T300 ($\mathcal{A}$=1,7MPa.m$^{1/2}$) [46].

Connaissant la constante $\mathcal{A}$, il est donc possible de déterminer la contrainte à rupture de la fibre dans le composite. Ceci a été réalisé sur les microcomposites. Il est à noter que la mesure déduite des faciès miroir, sur les faciès de rupture de type fragile (plat), est directement comparable à la contrainte de la fibre dans le microcomposite, σ_f, calculée dans le cas où il n'existe pas de contrainte résiduelle (σ_f=Ef.ε_R). En revanche, pour les faciès de rupture, présentant une extraction de la fibre, la relaxation partielle (frottement) ou totale des contraintes résiduelles sur la fibre à l'endroit de la rupture, due à la fissure matricielle, ne permet pas de remonter à l'état de contrainte initial de la fibre (avant rupture de la matrice) dans le matériau par cette méthode.

1.4 - Détermination de la différence entre coefficients de dilatation thermique axiaux de la fibre et de la matrice

L'ouverture des fissures à charge nulle, u_0, est fonction de la longueur sur laquelle les contraintes résiduelles axiales sont relaxées. Ces contraintes proviennent de la différence entre les coefficients de dilatation axiaux de la fibre et de la matrice. En négligeant les contraintes radiales résiduelles, l'effet Poisson, et les frottements, qui peuvent intervenir à l'encontre d'une complète relaxation le long de la décohésion fibre/matrice, et en négligeant la

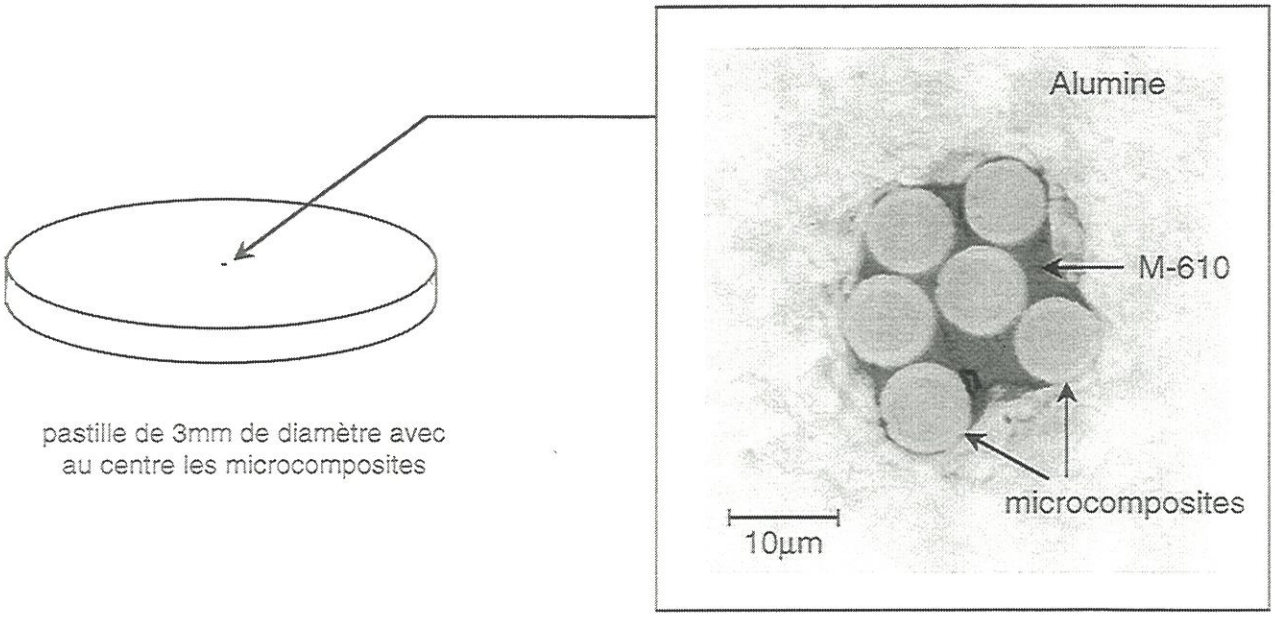

a - enrobage des échantillons dans une colle alumine
(encadré: section polie vue en microscopie optique)

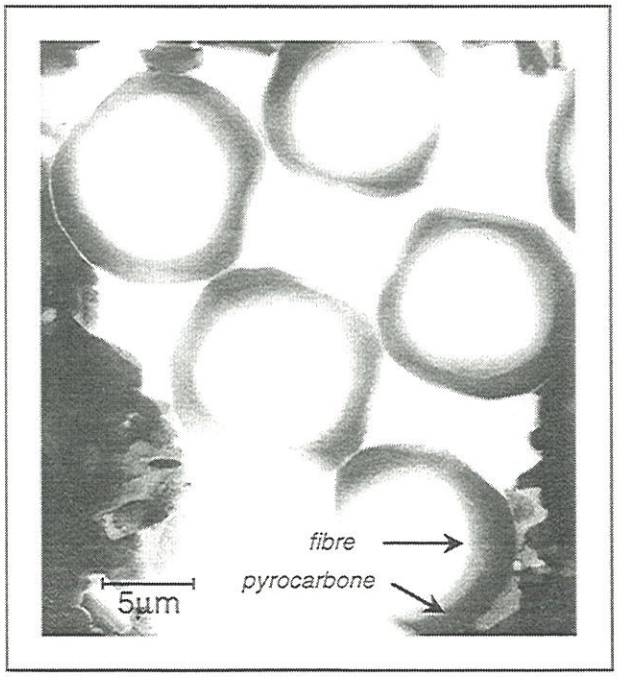

b - preparation MET après amincissement ionique
(image MET à faible gradissement)

Figure 24: preparation MET

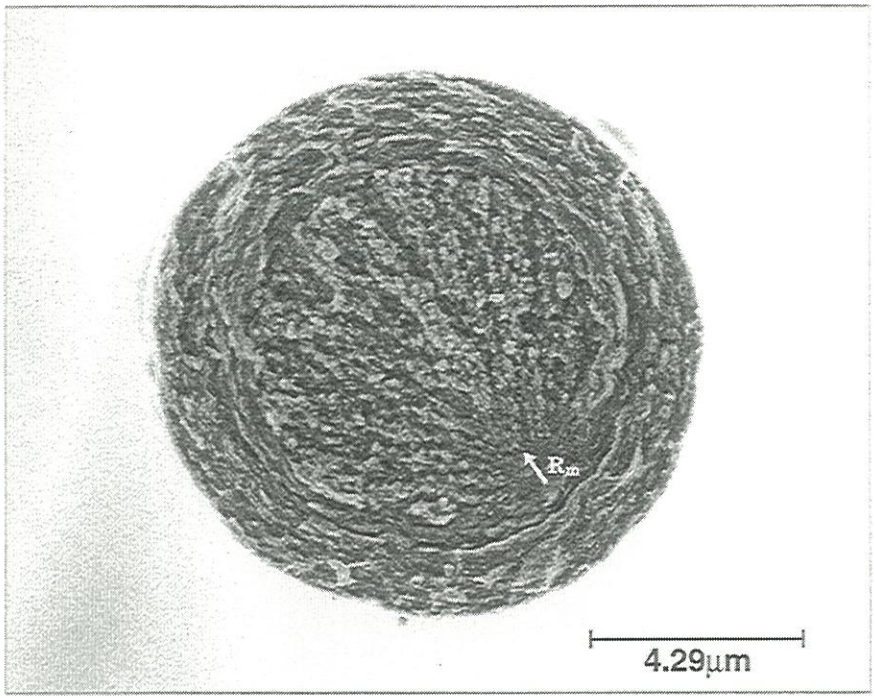

Figure 25: observation au MEB d'un faciès de rupture d'un microcomposite A-HTT/Ic/M après traction, montrant l'existence du faciès miroir dans la fibre

contribution du coefficient de dilatation du cadre support, l'ouverture u_0 d'une fissure i à saturation peut être reliée à la distance moyenne L_i, qui sépare cette fissure de la suivante, par une relation simple [47] (figure 26.b):

$$u_0 = M_0 . L_i \tag{3}$$

avec $M_0 = \int_{T_0}^{T_e} (\alpha_m - \alpha_f).dT$, où T_0 est la température ambiante, T_e la température d'élaboration, α_m and α_f les coefficients de dilatation thermique axiaux de la matrice et de la fibre.

Pour les matériaux, n'ayant pas atteint l'état de saturation, l'ouverture de la fissure est indépendante de la distance interfissure. La longueur ineffective, ℓ, définie comme la demi-longueur caractérisant le domaine où la fibre est déliée de la matrice de part et d'autre de la fissure, est identique pour chaque fissure ($\ell=\ell_0$) (figure 26.a): $u_0 = M_0 . 2\ell = M_0 . 2\ell_0$ (4)

Une seconde mesure de M_0 peut être déduite des ouvertures de fissures sous charge. L'ouverture de la fissure, u, est reliée à la force appliquée F en ajoutant à l'équation (4) le déplacement induit par la force:

$$u = 2.\ell . (c_f . F + M_0) \tag{5}$$

avec $c_f=1/(E_f.S_{f,corr})$.

or, $u_0=2.\ell.M_0$, d'où $$\frac{du}{dF} = 2.\ell . c_f = \frac{c_f}{M_0} . u_0 \tag{6}$$

M_0 est alors déduit de la pente de la courbe du/dF en fonction de u_0.

2 - Nature et caractéristiques mécaniques des constituants

2.1 - Fibres

Les fibres utilisées sont des fibres de carbone ex-PAN HT (haute résistance), avec deux états de surface différents: fibres A et B, avec B ayant une rugosité de surface plus importante. Les caractéristiques mécaniques de ces fibres ont été déterminées sur des lots de 20 échantillons [45, Annexe 1]. Elles sont réunies dans le tableau 1, ainsi que celles de ces mêmes fibres

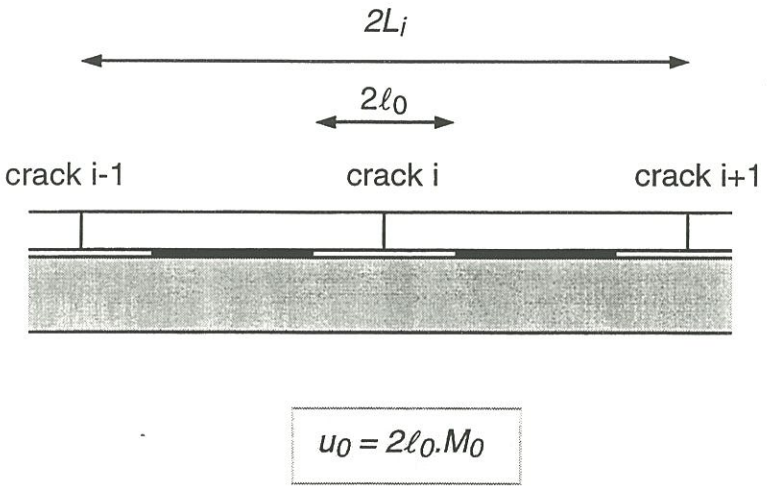

a.

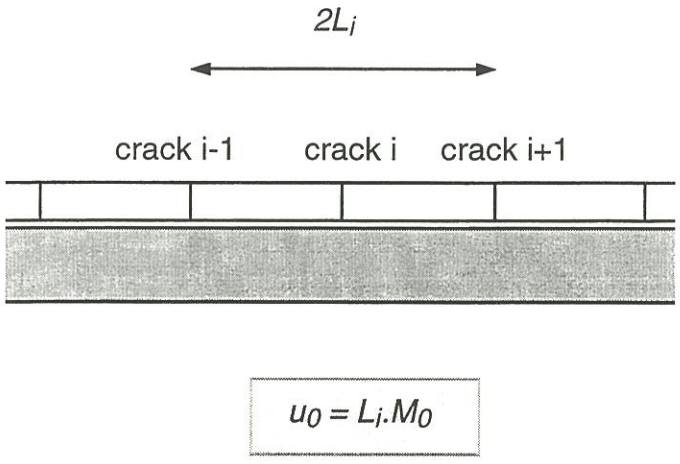

b.

Figure 26: endommagement du minicomposite [47]
(a) matériau non saturé, et (b) matériau saturé

traitées à haute température (THT), à la température T1 (A-HTT, B-HTT), ou à la température T2 (A-HTT2, B-HTT2). La température T2 est supérieure à T1, qui est elle-même supérieure à la température d'élaboration de la fibre.

Le module d'Young augmente avec le THT dû au réarrangement des plans de carbone selon l'axe de la fibre [48], et couvre un domaine allant de 250GPa à 450GPa.

La déformation et la contrainte à rupture diminuent avec le THT. La déformation à rupture couvre ainsi un domaine assez large: 0,6-1,6%. Les déformations plus faibles, observées pour les fibres B, et dérivées de B, sont reliées à des défauts de surface plus gros que pour les fibres A, et dérivées de A. Ceci est en accord avec la rugosité de surface plus élevée des fibres B, et très probablement des fibres dérivées de B. L'observation de clichés en microscopie à effet tunnel[1] de fibres A-HTT2 et B-HTT2 irait dans ce sens: une rugosité plus marquée à très courte distance pour la fibre B-HTT2 (figure 27).

2.2 - Matrice

La matrice CVD (M) est un pyrocarbone de type laminaire lisse, dont les conditions élaboratoires sont données dans le diagramme température-pression de la figure 28.a. Les caractéristiques texturales (Ae, OA, d_{002} (§1.3.1)) associées à ce pyrocarbone sont réunies à la figure 28.b.

Les propriétés mécaniques de cette matrice ont été mesurées de manière indirecte en appliquant la loi des mélanges[2] ($E=V_m.E_m+V_f.E_f$) (figure 29), ou par la caractérisation de microcomposites avec un V_m élevé (96%) (Tableau 2). Il ressort que le module d'Young de la matrice est au moins quatre fois plus

---

[1] avec la collaboration de H. Saadoui, J.C. Roux, et S. Flandrois du Centre de Recherche Paul Pascal, Pessac, France

[2] Il est à noter que la loi des mélanges n'est strictement vérifiée que dans le cas d'une liaison parfaite entre fibre et matrice, avec fibre et matrice considérées comme isotrope, et caractérisées par un coefficient de Poisson identique.

Tableau 1. Résultats mécaniques moyens obtenus après traction de fibres carbone HT ex-PAN [45]

	d (μm)	E (GPa)	ε_R (%)	σ_R (MPa)
A	6,9	255	1,58	3992
	(0,3)*	(36)	(0,22)	(630)
A-HTT	6,7	316	1,27	3995
	(0,3)	(34)	(0,24)	(889)
A-HTT2	6,5	398	0,84	3336
	(0,3)	(13)	(0,13)	(471)
B	6,7	247	1,44	3538
	(0,3)	(28)	(0,29)	(742)
B-HTT	6,7	336	0,78	2630
	(0,4)	(30)	(0,18)	(633)
B-HTT2	6,5	412	0,64	2607
	(0,2)	(17)	(0,19)	(732)

* entre parenthèses: écart type

N.B.: A: fibre de carbone ex-PAN

B: même fibre que A, mais avec une rugosité de surface plus élevée

HTT, HTT2: traitement thermique à T1 et T2 respectivement (T2>T1)

faible que celui de la fibre ($E_m \approx 70GPa$), avec une déformation à rupture de l'ordre de 1,1%.

Cette même matrice, traitée à HTT2, a pu être caractérisée isolément mais seulement sur 2 échantillons, après extraction de la fibre lors d'essais de traction sur microcomposites traités à HTT2. Les résultats sont les suivants:

$$Em=36GPa \qquad \varepsilon_{R,m}=1,23\% \qquad \sigma_{R,m}=449MPa$$

soit une déformation à rupture similaire à celle de la matrice non traitée en température, mais un module d'Young plus faible. Or, la valeur de ce module devrait augmenter avec le THT. Une dégradation probable de la matrice lors du THT serait due à la présence de la fibre.

2.3 - Interphase

L'ajout de différentes interphases de pyrocarbone a permis d'obtenir différents micro- et minicomposites. Les conditions opératoires et les textures de ces interphases sont présentées à la figure 28 pour les microcomposites, et à la figure 30 pour les minicomposites.

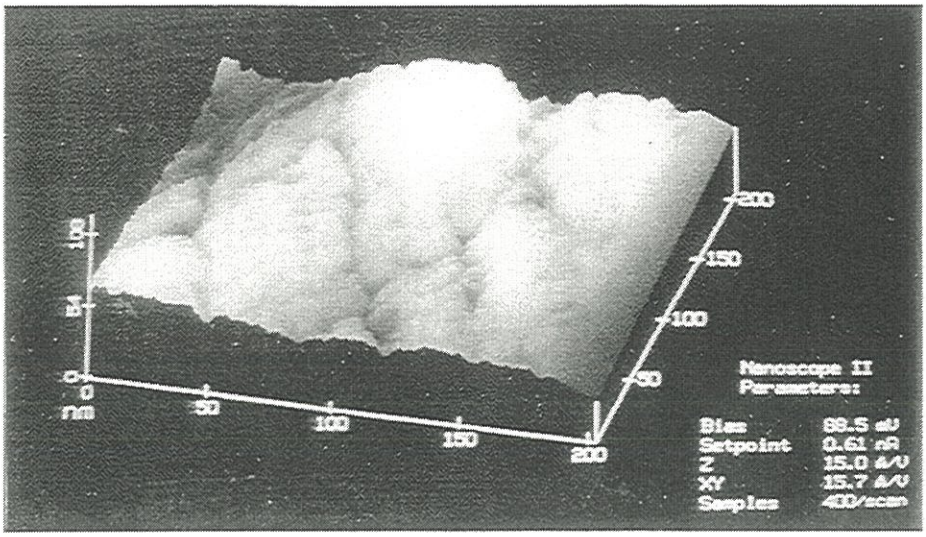

(a)

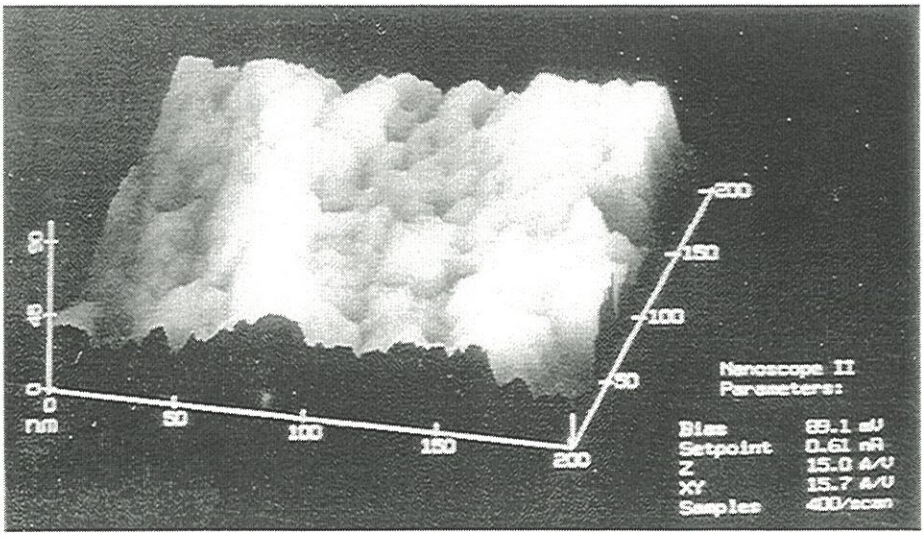

(b)

Figure 27: image par microscopie à effet tunnel de la surface de la fibre (a) A-HTT2, et de la fibre (b) B-HTT2 (200x200nm)

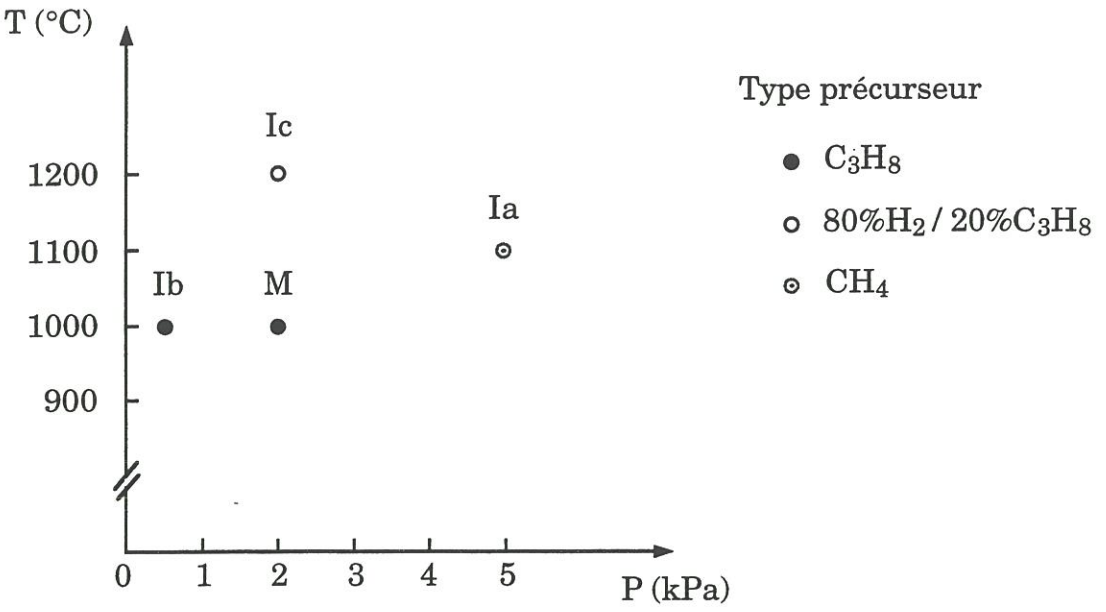

(a)

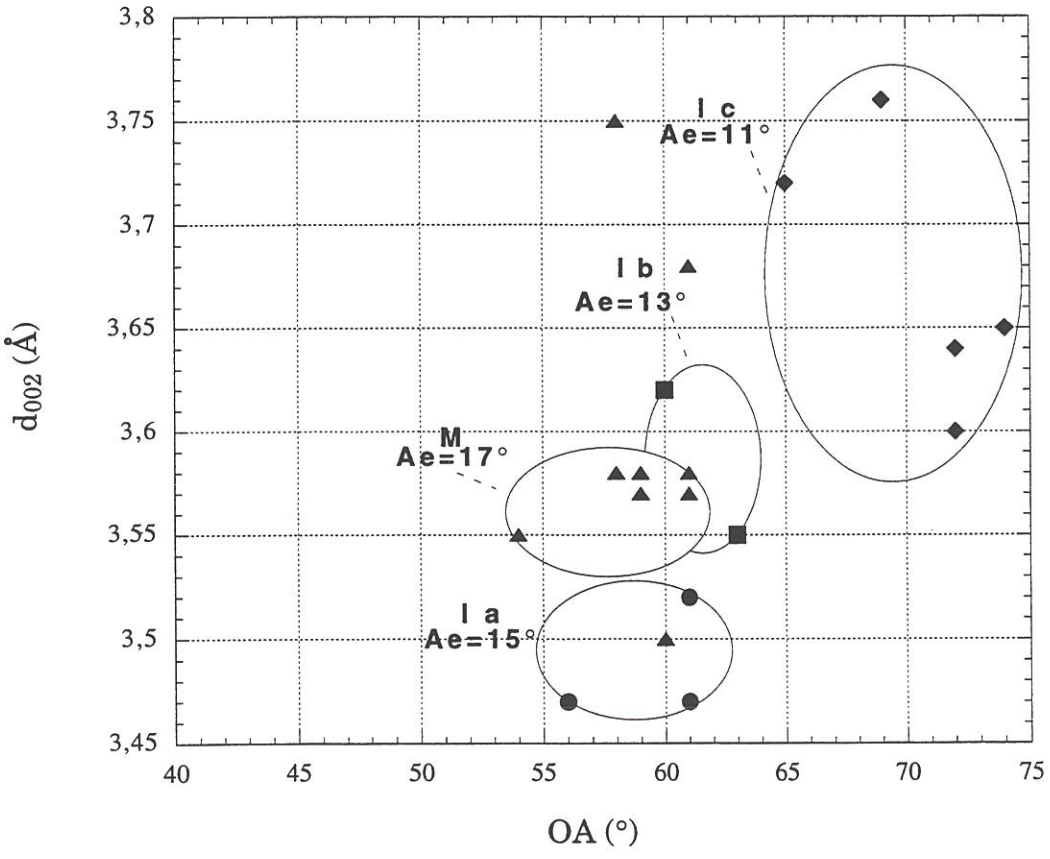

(b)

Figure 28: caractéristiques des pyrocarbones déposés pour l'élaboration des microcomposites (a) conditions opératoires, (b) microtexture (Ae, OA) et distance interréticulaire (d_{002}) [44, Annexe 4]

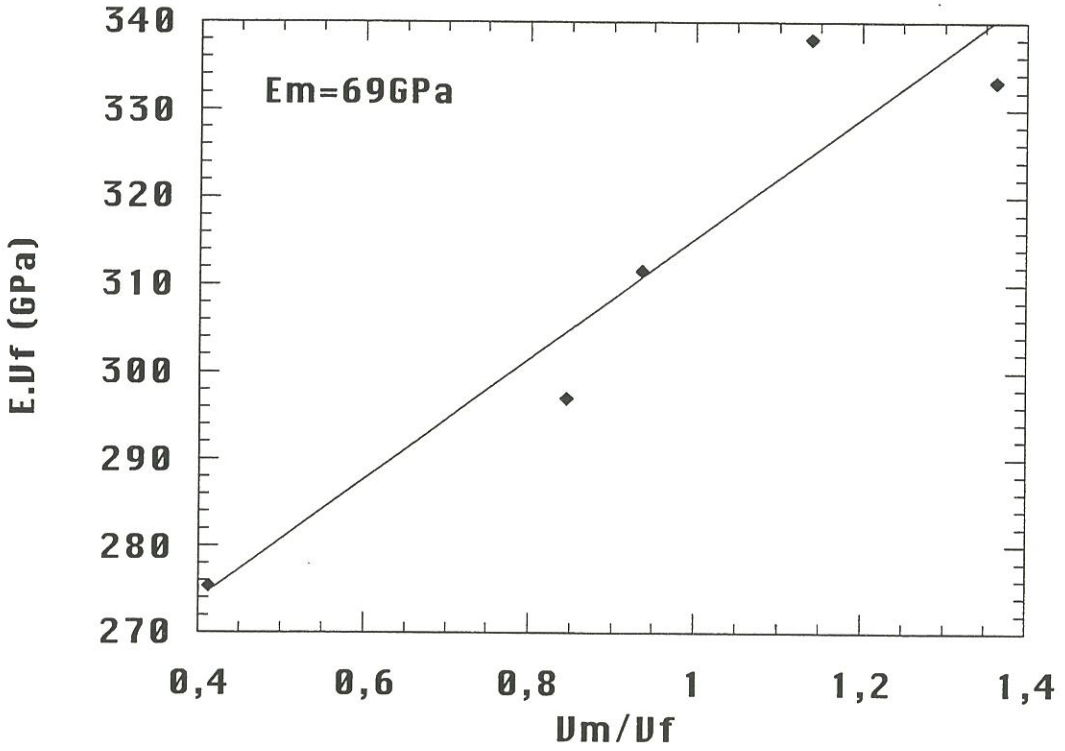

Figure 29: détermination du module d'Young de la matrice par la loi des mélanges appliquée à des microcomposites B/M de fraction volumique de matrice, V_m, différente

Tableau 2. Propriétés mécaniques en tension de A-HTT/M (V_m=96%)

	V_f (%)	E (GPa)	ε_R (%)	σ_R (MPa)	σ_m (MPa)	σ_f (MPa)	σ_f' (MPa)	E_m (GPa)
A-HTT/M	4	62 (6)*	1,11 (0,34)	702 (201)	599	3520	19914	53

* entre parenthèses: écart type

avec $\sigma_m=E_m.\varepsilon_R$

$\sigma_f=E_f.\varepsilon_R$

$\sigma_f'=F/S_f$

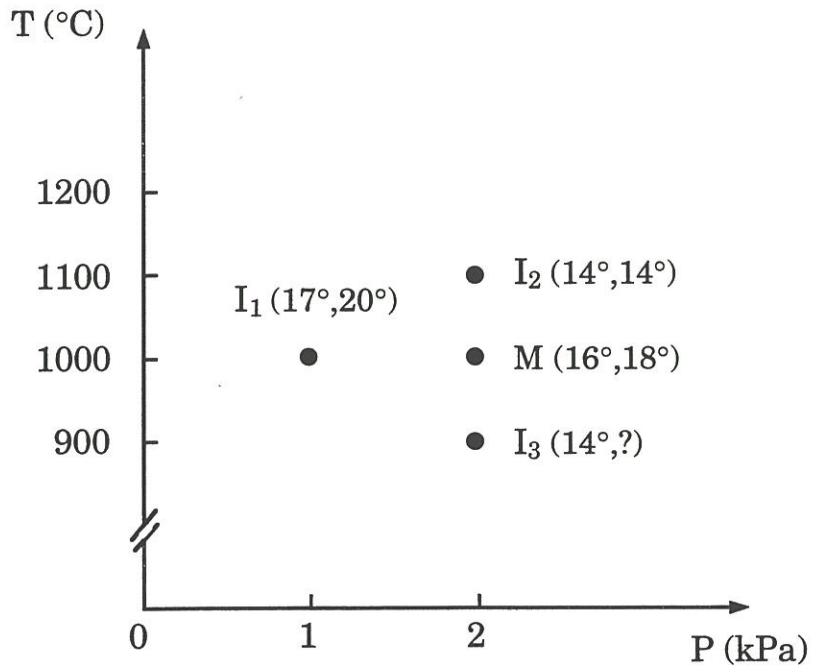

Figure 30: conditions opératoires des pyrocarbones déposés à partir du propane pour l'élaboration des minicomposites,
avec entre parenthèse les valeurs des angles d'extinction (Ae(CVD), Ae(CVI))

SYNTHESE DES PRINCIPAUX RESULTATS

SYNTHESE DES PRINCIPAUX RESULTATS

1 - Comportement mécanique

Si on considère les déformations à rupture des fibres (0,6-1,6%), et celle de la matrice (≈1%), les 2 comportements inverse et régulier peuvent être observés dans les composites carbone/carbone.

1.1 - Comportement inverse ($\varepsilon_{R,m}<\varepsilon_{R,f}$)

Le comportement inverse est observé pour les microcomposites non traités à HTT2, élaborés avec les fibres A, B, et ces mêmes fibres traitées à HTT (figures 31.a,b). En effet, les fibres ont des déformations à rupture supérieures à 1%. Ceci s'applique aussi à la fibre B-HTT, dont la déformation à l'origine est de 0,78%, et qui acquiert **une déformation plus élevée à l'intérieur du microcomposite**, au vu des caractéristiques à rupture qui sont rattachées au microcomposite.

Microcomposites et minicomposites sont des composites inverses dans la mesure où ils n'ont pas subi de HTT2. Ce comportement similaire à celui des SiC/SiC n'est clairement mis en évidence que pour les minicomposites, pour lesquels une multifissuration matricielle se produit (cf. §3.2). Dans le cas des microcomposites, une seule fissure matricielle est observée, donnant lieu soit à un faciès plat (figure 25), soit à un faciès de rupture avec extraction de fibre (figure 32) créant peu ou pas de perturbation des courbes de traction [45, Annexe 1].

Le changement de comportement entre micro et minicomposites peut s'expliquer par les contraintes axiales résiduelles, engendrées par les différences entre coefficients de dilatation thermique, et qui influent sur les déformations à rupture des constituants. Une contrainte axiale résiduelle de compression augmente la déformation à rupture, et inversement pour une

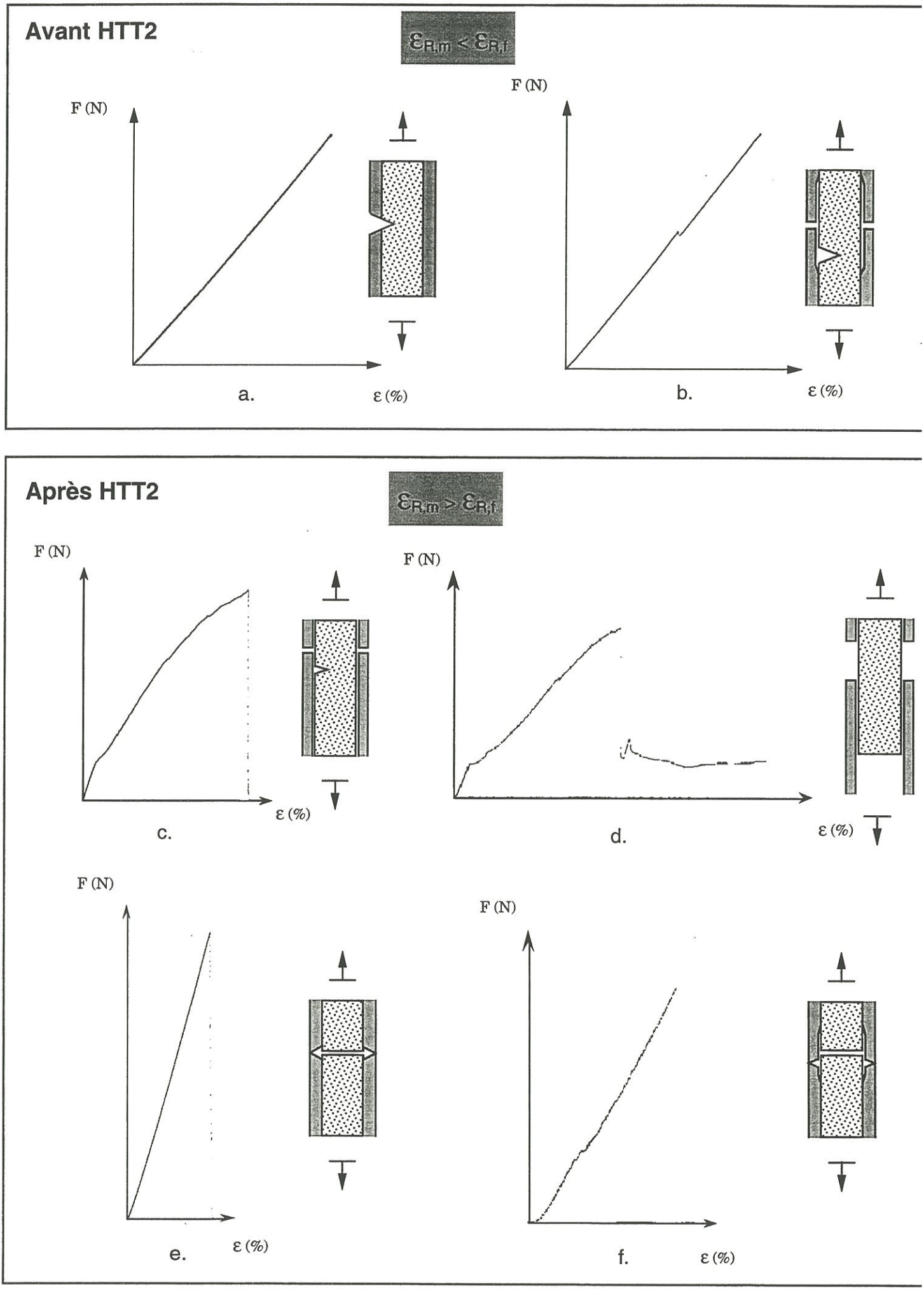

Figure 31: comportements mécaniques typiques des microcomposites

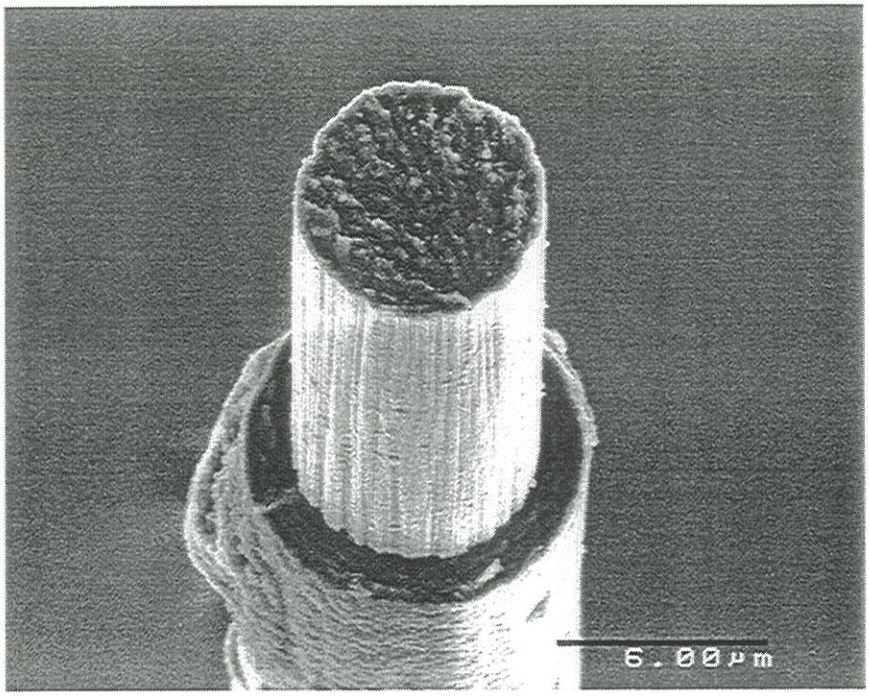

Figure 32: faciès de rupture avec extraction de la fibre
après traction d'un microcomposite C/C

contrainte axiale de tension. Une **contrainte axiale en compression dans la matrice** a été mise en évidence **dans les microcomposites** [45, Annexe 1; 49, Annexe 2] de différentes manières:

- Par observation au MEB de 2 faciès de rupture complémentaires comme le montre la figure 33: de part et d'autre, la relaxation des contraintes résiduelles provoque un retrait de la fibre par rapport à la matrice.
- L'analyse des faciès miroir sur faciès plat montrent que les fibres sont en tension axiale ($\sigma_{f,mirror}>\sigma_f$) ou quelque fois proche de l'équilibre (Tableau 3).

En revanche, les **minicomposites** sont caractérisés par une **contrainte résiduelle axiale en tension dans la matrice**. En effet, les courbes liant l'ouverture de fissure u_0 à la distance interfissure L_i (cf. p.26, §1.4) pour les minicomposites A-HTT/M, et ceux à interphase I_1 ou I_3 forment une même droite (figure 34) de pente positive M_0=0,007, soit $\alpha_{//PyC}>\alpha_{//f}$. L'étude de l'ouverture de la fissure en fonction de la charge appliquée (traction sous MEB, figure 35) donne une valeur similaire (0,006 à 0,008). Cependant, cette valeur de M_0 correspond à une valeur trop forte de la différence entre coefficients de dilatation ($7.10^{-6}°C^{-1}$), comparée aux coefficients de dilatation thermiques axiaux attribués dans la littérature à des fibres similaires ex-PAN (T300: $\alpha_{//}$=-0.5+3.2.10^{-3}.T [50]), et à des pyrocarbones ($\alpha_{//(0°C)}$=-1.2.$10^{-6}°C^{-1}$, $\alpha_{//(1000°C)}$=-0.8.$10^{-6}°C^{-1}$ [51]). Il faut convenir que les paramètres, négligés dans ce modèle, interviennent dans la relation linéaire liant u_0 à L_i par une constante non nulle, et une pente M_0 plus complexe que celle explicitée. Cependant, le signe de la pente ($M_0>0$) indique que $\alpha_{PyC}>\alpha_f$, c'est-à-dire que la matrice est en tension et la fibre en compression dans le minicomposite.

Au regard de ce résultat, les premières ruptures de la matrice, observées vers 0,3-0,4%, sous-estiment la déformation à rupture réelle de la matrice de pyrocarbone. Ceci est en accord avec les valeurs de l'ordre de 1%, déterminées sur microcomposites, et non pas avec les valeurs à rupture données généralement dans la littérature pour les pyrocarbones basse température (0,3-0,5% [52]).

Tableau 3. Comparaison des données mécaniques de microcomposites et des données déduites des faciès miroir (faciès de type fragile seulement pris en compte)

Matériau	Propriétés mécaniques			Faciès miroir	
	ε_R (%)	σ_R (MPa)	σ_f (MPa)	R_m (μm)	$\sigma_{fmirror}$ (MPa)
A/M	1,46	2467	3716	0,483	3739
	1,54	2452	3931	0,388	4171
	1,47	2147	3739	0,522	3597
A/Ic/M	0,79	1400	2010	0,738	3026
	0,96	1553	2436	1,10	2473
	1,06	1917	2699	0,651	3222
	0,77	1251	1969	1,11	2463
	0,95	1396	2424	1,01	2591
	1,47	2325	3750	0,428	3974
	1,13	1801	2871	0,694	3121
	1,11	1756	2841	0,836	2874
A-HTT/Ic/M	1,18	2196	3009	0,691	3127
	1,01	1692	3197	0,450	3279
	1,29	2100	4067	0,222	4659
	1,12	1917	3536	0,364	3646
	0,89	1543	2804	0,536	3005

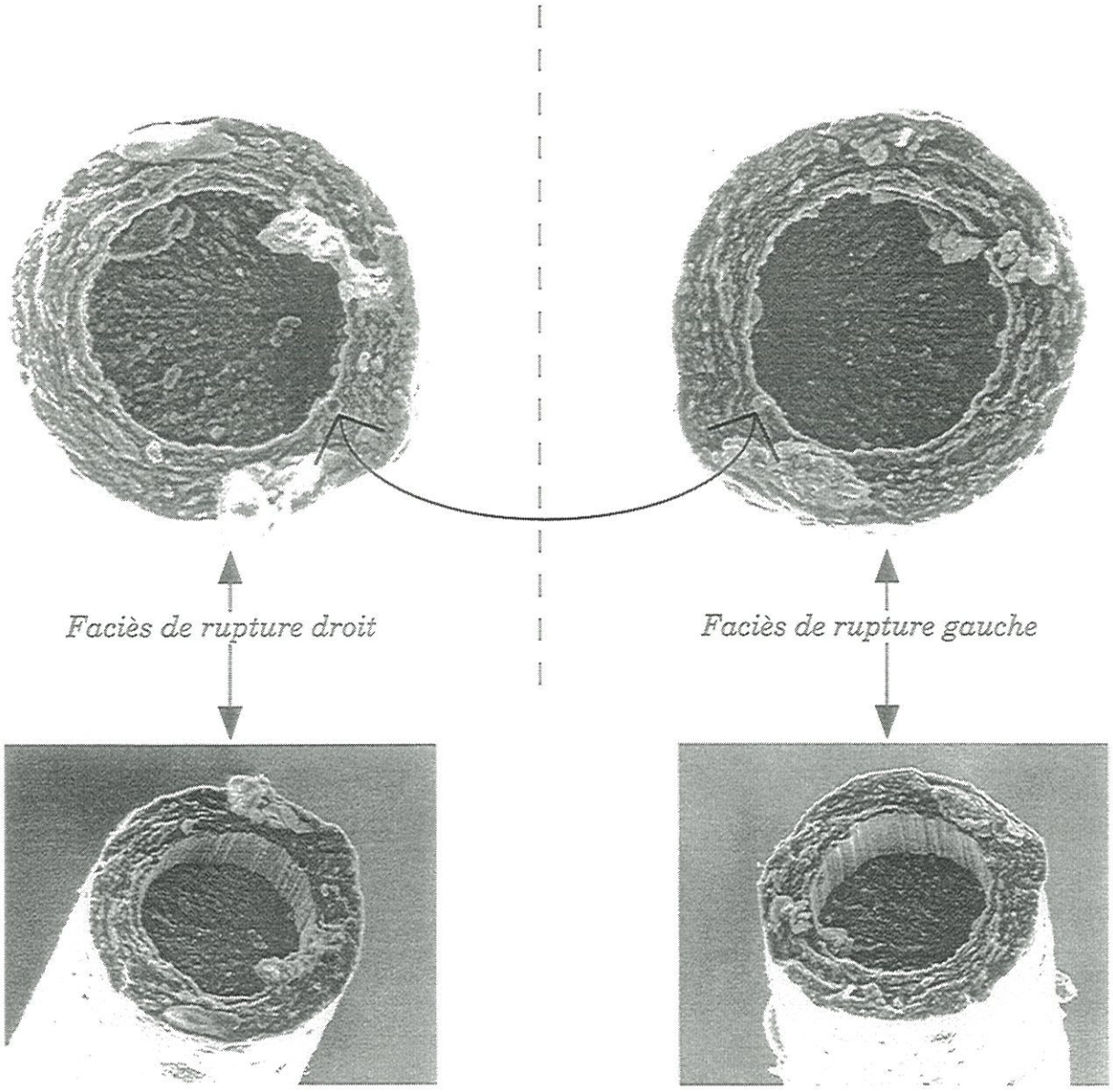

fibre en retrait par rapport à la surface de rupture

Figure 33: observation au MEB de 2 faciès de rupture complémentaires
d'un microcomposite B-HTT/M testé en traction,
qui prouve que la fibre est en tension axiale dans le microcomposite

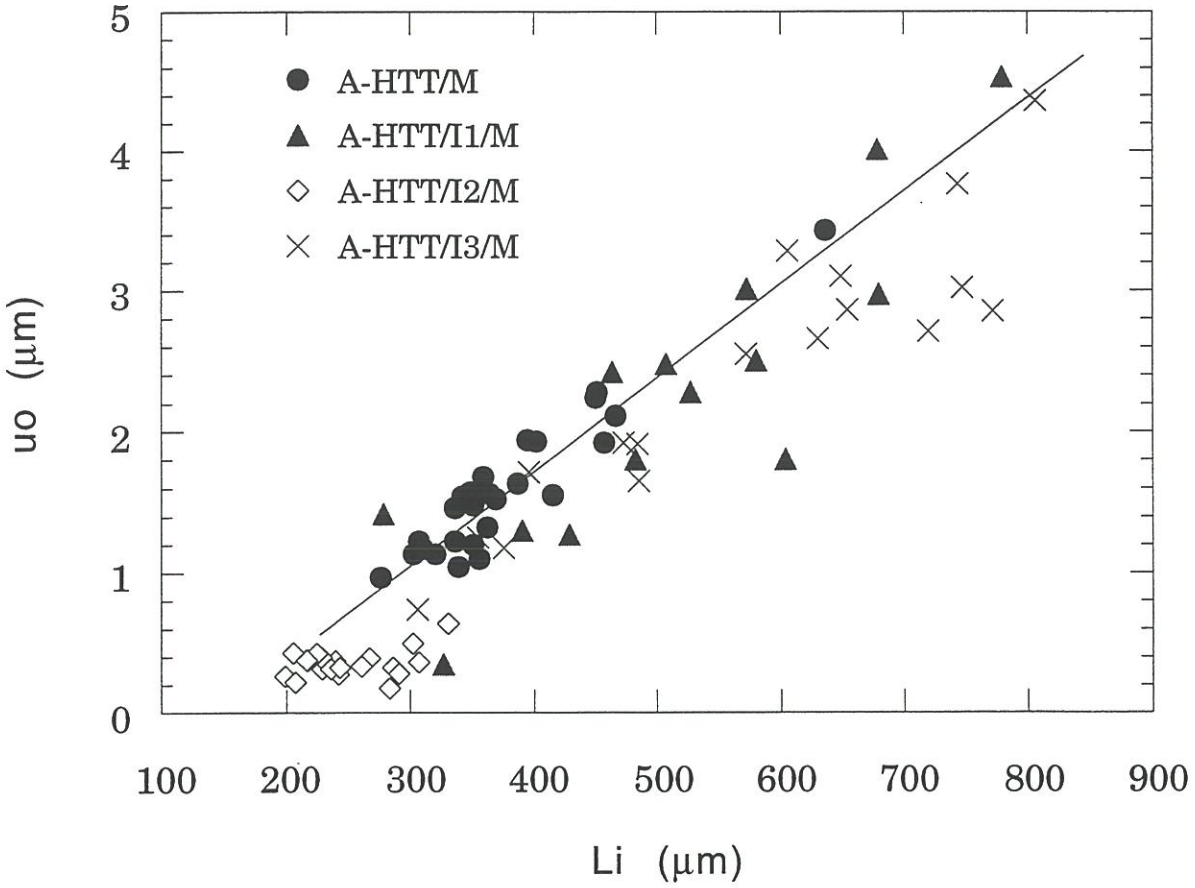

Figure 34: courbes u_0 en fonction de L_i pour les minicomposites A-HTT/M and A-HTT/I/M

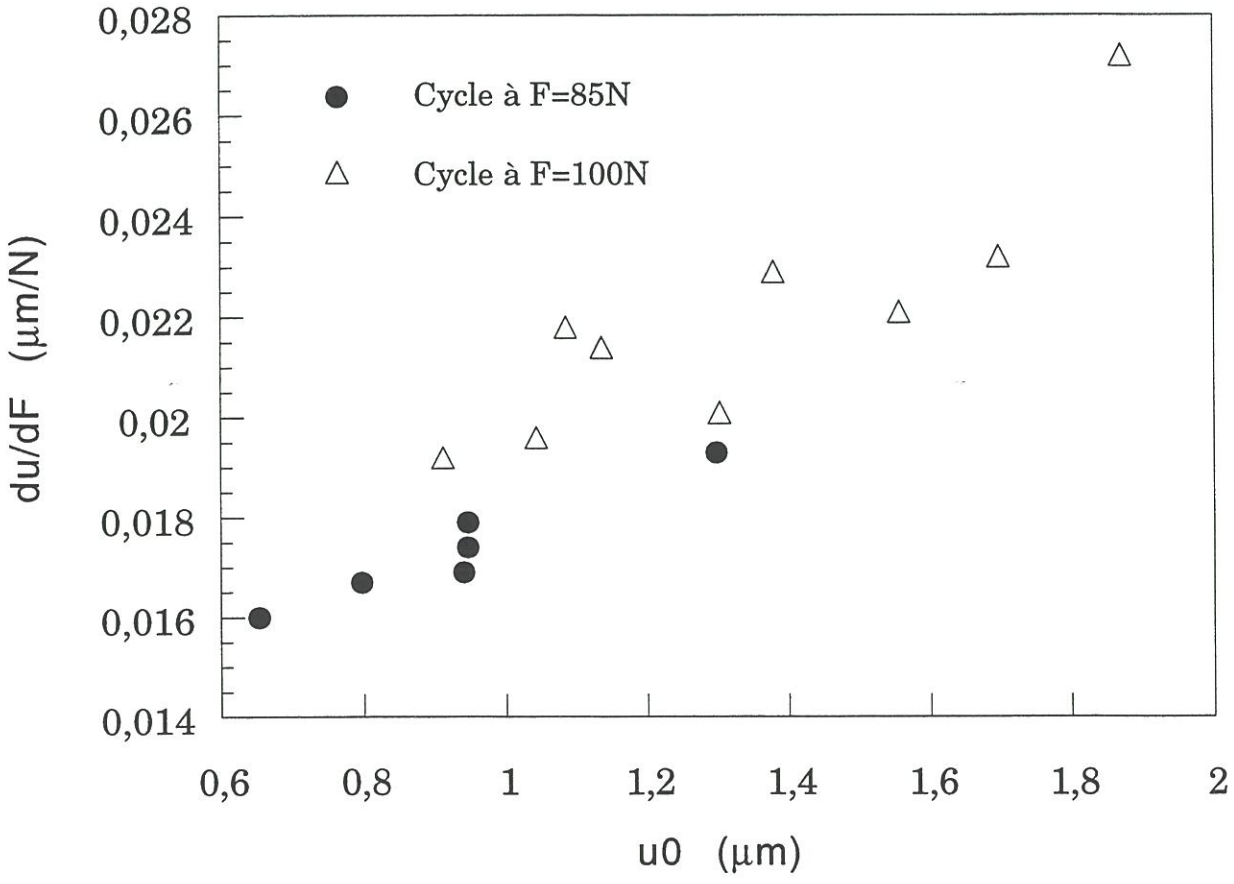

Figure 35: courbes du/dF en fonction de u_0, obtenues par des cycles de charge-décharge sur A-HTT/M testé en traction sous MEB (chaque point correspond à l'étude d'une fissure)

Les données u_0-L_i, peu dispersées (figure 34) pour le minicomposite à interphase I_2, ne permettent pas de tirer de conclusions. Cependant, comme les premières ruptures de la matrice se produisent pour des déformations du même ordre que pour les autres minicomposites étudiés, l'état de tension de la matrice et de compression des fibres est également vrai pour A-HTT/I_2/M.

Un écart plus marqué est donc obtenu entre déformations à rupture des fibres et de la matrice pour les minicomposites, donnant la possibilité d'observer **le comportement inverse avec multifissuration de la matrice** [53, Annexe 3]. L'inversion des états de contrainte résiduelle entre micro et minicomposites est attribuée à la contribution inévitable des coefficients de dilatation des cadres carbone (Papiex et graphite), sur lesquels les échantillons sont fixés lors de l'élaboration (micro- et mini-composite, respectivement).

1.2 - Comportement régulier ($\varepsilon_{R,m}>\varepsilon_{R,f}$)

Le comportement régulier est observé pour les **microcomposites traités à HTT2** (figures 31.c à 31.f), dans lesquels la fibre, la matrice, et l'interphase ont subi un changement de structure lors du THT. La fibre diminue fortement de diamètre par rapport à la matrice. Par ailleurs, des mesures réalisées sur des fibres A, extraites après THT [49, Annexe 2], montre qu'elles possèdent des performances dégradées ($\varepsilon_{R,f}$=0,5%) par rapport aux fibres A-HTT2 ($\varepsilon_{R,f}$=0,84%) (Tableau 1).

Pour certains microcomposites, une décohésion importante entre fibre et matrice s'étend tout le long du microcomposite après le THT (figures 36.a,b). Les courbes de traction correspondantes (figures 31.c,d) n'ont donc pas de réalité physique, car elles sont le résultat du pincement du microcomposite au niveau des mors engendrant une liaison artificielle à cet endroit. Pour les autres matériaux, grâce à l'interphase (Ib ou Ic) la liaison fibre/matrice résiste au THT (figures 36.c,d), et un comportement régulier est observé. Cependant, la rupture de la fibre entraîne celle du microcomposite à cause de la surcharge

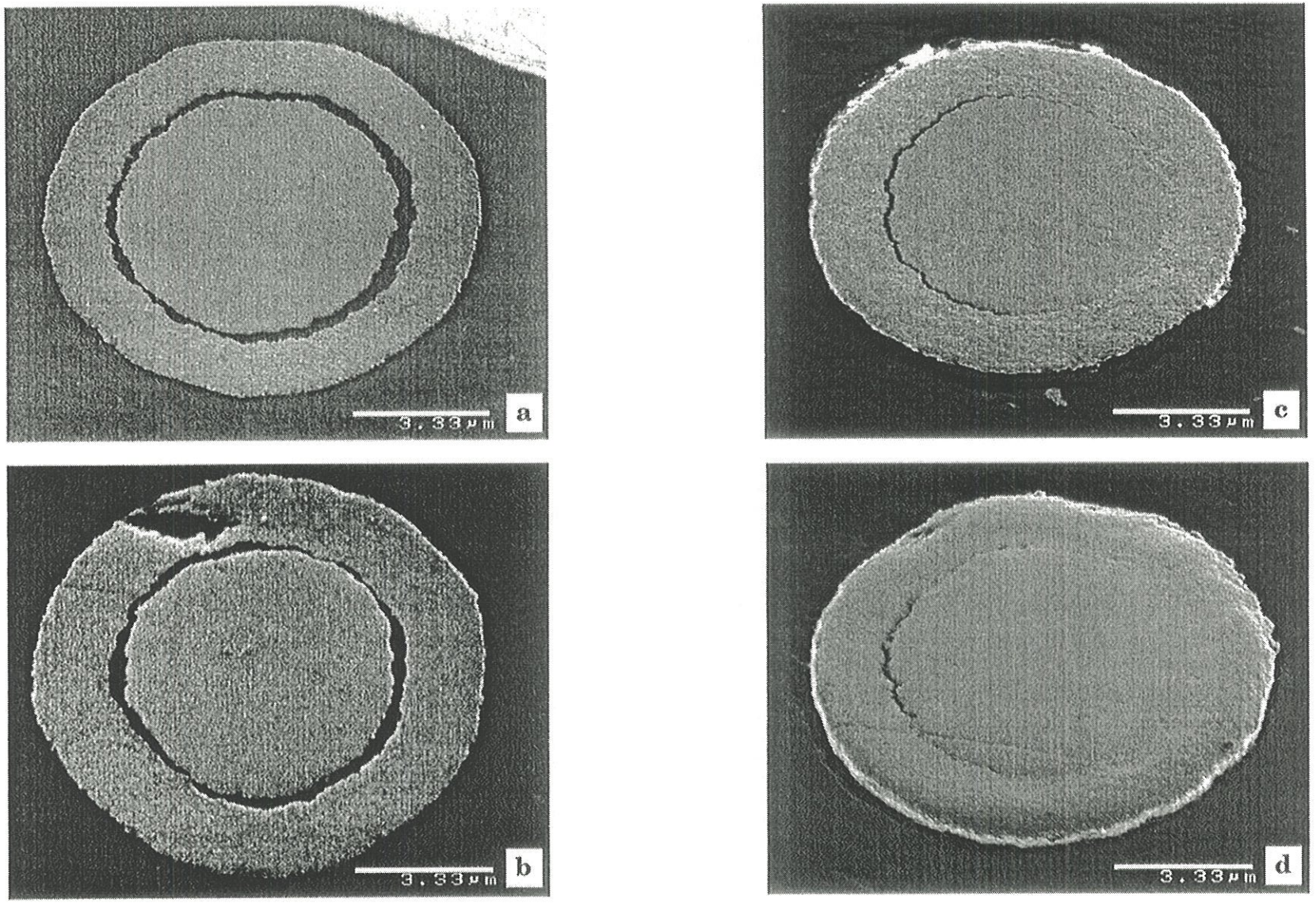

Figure 36: images MEB de sections transverses polies de microcomposites traités à HTT2 montrant:

- une décohésion fibre/matrice importante: (a) A/M; (b) A/Ia/M
- une faible décohésion partielle fibre/matrice: (c) A/Ib/M; (d) A/Ic/M

de la matrice qui s'ensuit. Les courbes sont donc de type linéaire élastique (figure 31.e), sauf lorsqu'il se produit des décohésions fibre/matrice et des glissements locaux et limités qui peuvent entraîner des singularités sur les courbes (figure 31.f).

Dans un C/C comme dans les autres CMCs, une interphase, d'anisotropie plus faible que la matrice, joue un rôle de compliance en absorbant les dilatations différentielles entre fibre et matrice, et les retraits irréversibles, et en maintenant la liaison fibre/matrice.

2 - La liaison interfaciale

Trois composantes contrôlent la liaison interfaciale: la composante chimique, la composante physique, et les contraintes résiduelles d'origine thermique qui s'exercent sur l'interface en modifiant la contrainte locale appliquée.

2.1 - Composante chimique

La contribution chimique à la force de la liaison fibre/matrice est mise en évidence par le microcomposite avec une interphase Ic de type laminaire sombre. Pour ce matériau, seules des ruptures fragiles sont observées quelle que soit la fibre utilisée (figure 25), ce qui n'est pas le cas des autres microcomposites. L'interphase Ic, du fait de sa texture désorganisée (figure 28), permet de développer des liaisons chimiques avec les bords de plans de carbone qui débouchent en surface de fibre.

2.2 - Composante physique

Ce type de liaison fait référence à un accrochage mécanique entre les 2 constituants lié à la rugosité à l'interface. Les microcomposites, élaborés avec les fibres B et B-HTT, dont la rugosité de surface est plus élevée que pour les

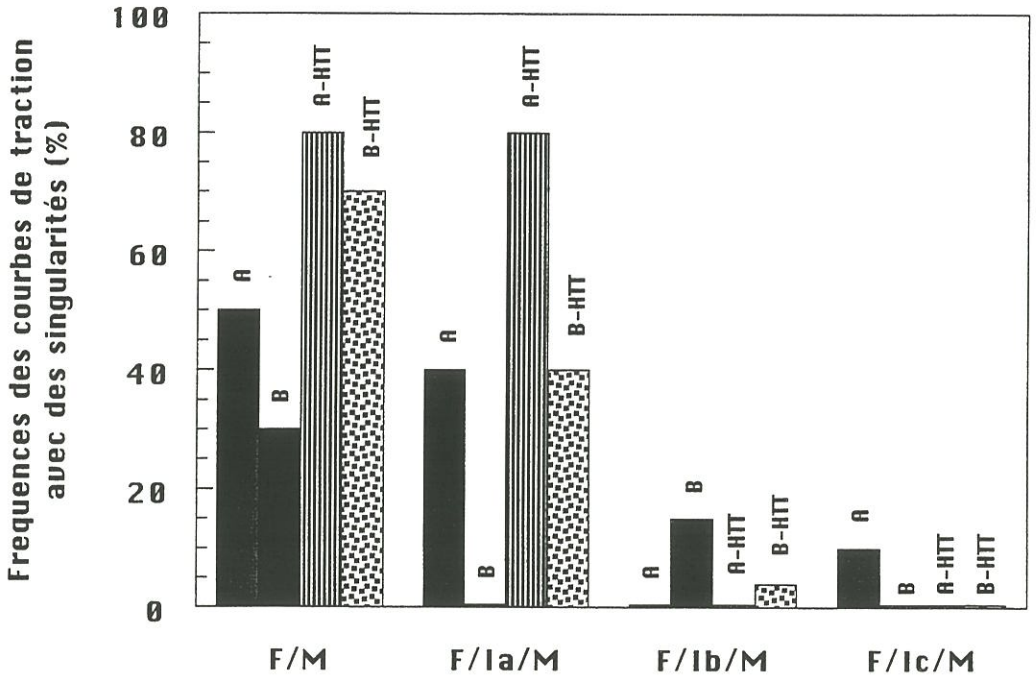

Figure 37: fréquences des courbes en traction avec des singularités selon le type de la fibre et l'interphase

fibres A et A-HTT, sont caractérisés par des courbes de traction qui tendent plus vers un comportement de type fragile: les courbes, présentant des singularités (figure 31.b), reliées à la rupture probable de la matrice, sont généralement moins fréquentes (figure 37). Il semblerait donc que la composante physique joue également un rôle dans la liaison entre fibre de carbone et pyrocarbone.

2.3 - Contraintes résiduelles

Alors que **les contraintes résiduelles axiales jouent sur les caractéristiques à rupture des constituants, les contraintes résiduelles radiales influencent la force de la liaison interfaciale**. En effet, une interface en tension radiale favorise la décohésion fibre/matrice, alors qu'une interface en compression radiale favorise une rupture de type fragile (propagation de la fissure à travers l'interface).

La différence entre coefficients de dilatation transverses de la fibre et du pyrocarbone engendre de telles contraintes résiduelles radiales à l'interface.

Seules des observations indirectes sur les décohésions interfaciales permettent de montrer que les fibres A-HTT et B-HTT ont un coefficient de dilatation transverse supérieur à A et B. Une relaxation des contraintes résiduelles dans le matériau peut se produire lors de la préparation de lames minces pour le MET pour une certaine épaisseur critique. Ainsi, des décohésions fibre/matrice sont observées en section transverse pour les microcomposites A-HTT/M (figure 38.d), et ceux avec une interphase Ia ou Ib (figure 23) [44, Annexe 4], ce qui dénotent une interface en tension radiale, qui ne serait pas contrebalancée par une forte liaison chimique comme pour le matériau avec une interphase Ic, pour qui la liaison interfaciale reste intacte (figure 38.f). Dans le cas de A/M, la fibre reste liée à la matrice (figure 38.b). Donc, la fibre stabilisée (A-HTT), engendre un retrait plus important que la fibre non stabilisée (A). La décohésion plus importante pour la fibre A-HTT s'expliquerait par le réarrangement des plans de carbone parallèlement entre

eux et parallèlement à la surface de la fibre. Du fait de l'anisotropie des coefficients de dilatation (α_a,α_c), plus les plans de carbones sont orientés, plus la dilatation est grande perpendiculairement à ces plans, soit un coefficient de dilatation thermique transverse plus élevé a priori pour la fibre traitée en température.

Le traitement thermique HTT2 des microcomposites provoque un retrait radial supplémentaire de la fibre au refroidissement. Ce traitement montre que **seules les interphases Ib et Ic arrivent à accommoder la différence de coefficients de dilatation entre fibre et matrice** (figure 36). Ce comportement est dû très certainement à une forte liaison chimique pour Ic, mais également à un coefficient de dilatation thermique radial de l'interphase adapté, car l'interphase Ib crée une liaison chimique relativement faible (MET).

2.4 - Rôle de la zone interfaciale

Les expériences sur microcomposites montrent très clairement que les deux paramètres essentiels, qui contrôlent la liaison interfaciale sont **la liaison chimique et les contraintes résiduelles radiales**, et que celle-ci joue un rôle essentiel dans les propriétés mécaniques.

Considérons les résultats mécaniques résumés dans les graphes de la figure 39. Ces graphes portent les performances moyennes en tension (contrainte, et déformation à rupture) en fonction de la texture optique (angle d'extinction Ae) de l'interphase. La référence est constituée de la fibre avec la matrice sans interphase. Ils montrent que la liaison interfaciale doit être optimisée, en terme de liaison chimique et contraintes résiduelles (Ib), afin d'utiliser les fibres jusqu'à 100% de leurs propriétés. Les fibres A et B engendrent des liaisons déjà trop fortes sans interphase, et ceci n'est que renforcé avec l'ajout des interphases choisies. Au contraire, les fibres stabilisées (HTT) donnent une liaison plutôt faible avec la matrice. Celle-ci peut être alors augmentée (Ib, Ic) et optimisée (Ib) par l'ajout de ces interphases. Le résultat le plus remarquable est obtenu avec la fibre stabilisée (A-HTT), qui

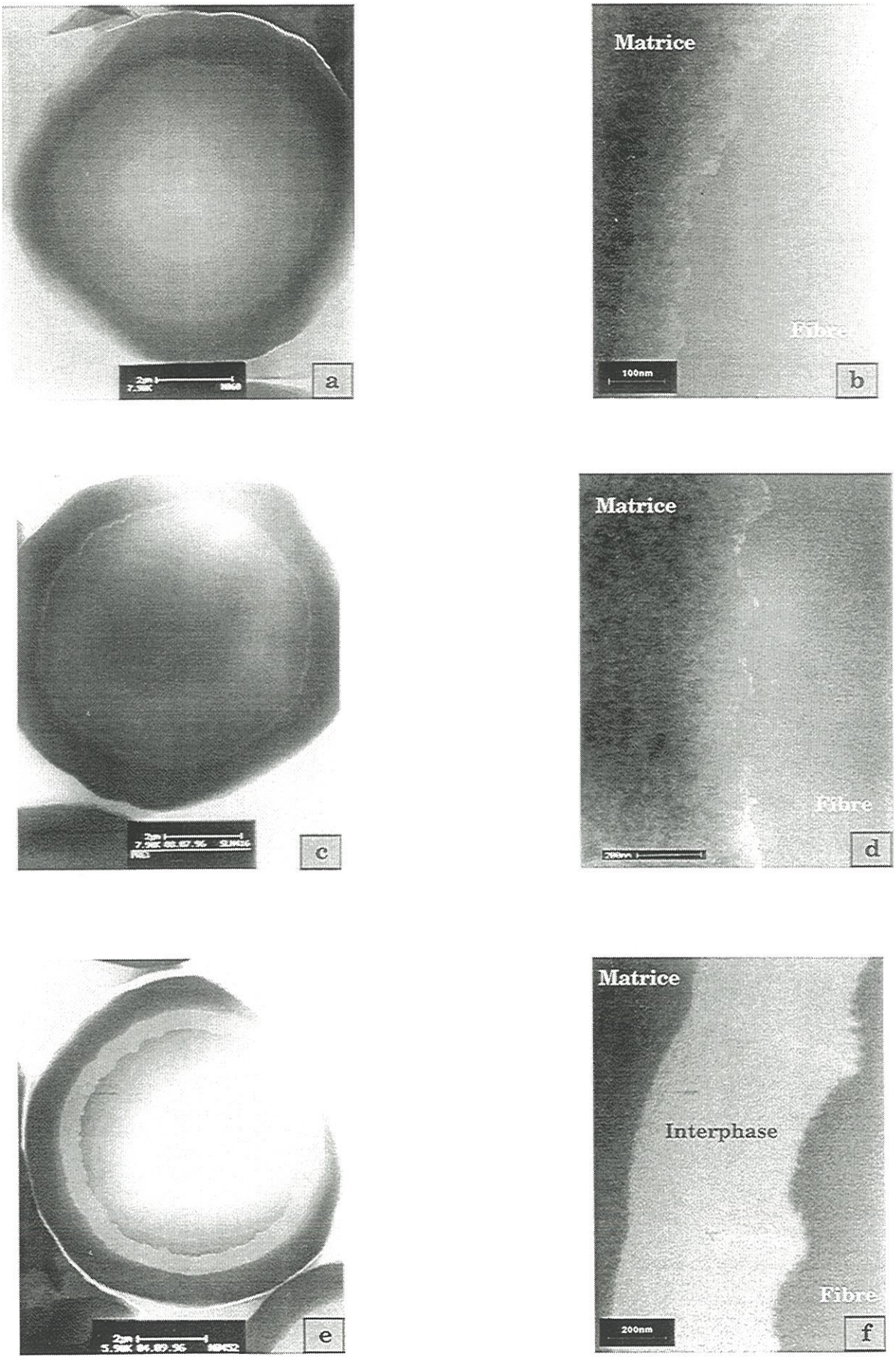

Figure 38: images MET en fond clair contrasté d'une vue globale du microcomposite et de la région interfaciale pour
(a), (b) A/M; (c),(d) A-HTT/M; (e),(f) A-HTT/Ic/M

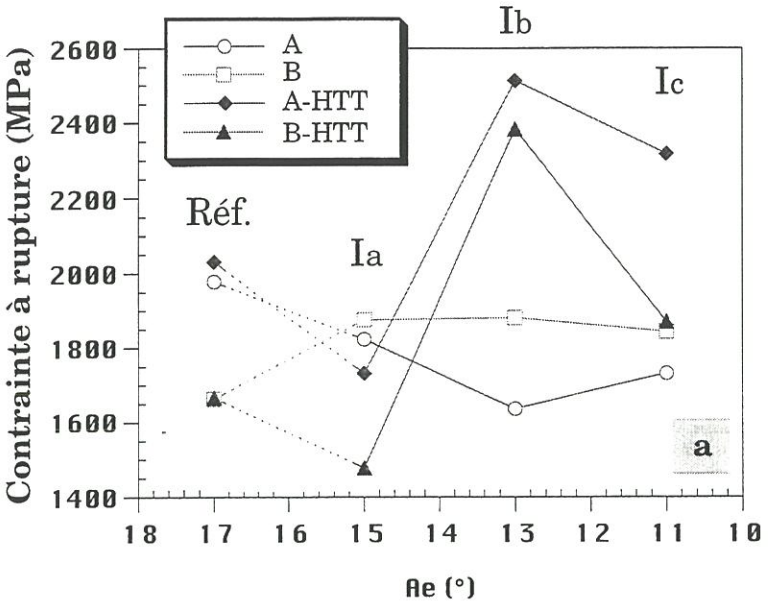

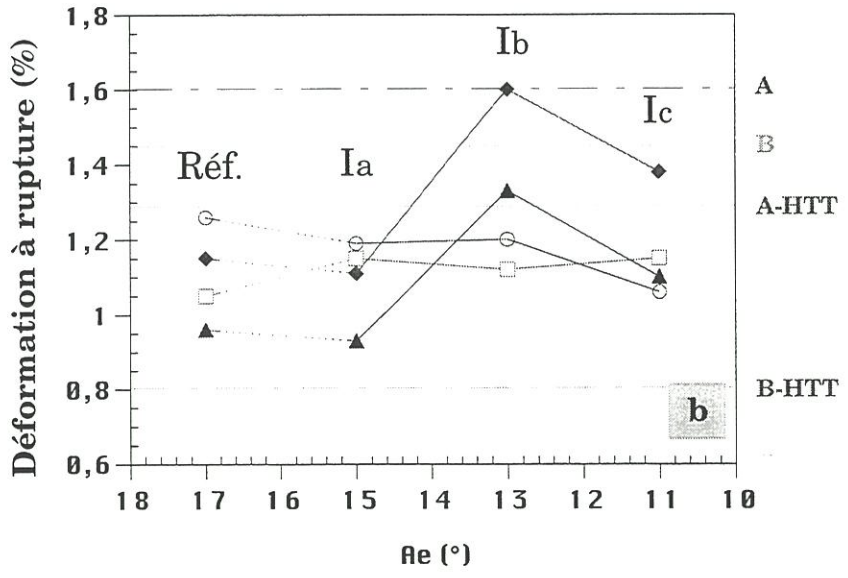

Figure 39: influence de la microtexture de l'interphase sur les propriétés mécaniques de microcomposites C/C/C : (a) contrainte et (b) déformation à rupture

retrouve à l'intérieur du microcomposite ses propriétés mécaniques (ε_R,σ_R) antérieures au THT, et est utilisée à 100% de ses capacités à condition d'introduire une interphase Ib plus désorganisée. **Les propriétés mécaniques sont alors supérieures à celles des microcomposites élaborés avec les fibres brutes.**

3 - Mécanismes de ténacité dans les minicomposites C/C

3.1 - Comportement fragile

La liaison entre la fibre A et la matrice est forte, et entraîne une rupture catastrophique du matériau dès que la première fissure matricielle se produit à 0,57% de déformation (Tableau 4). Ceci se traduit par une courbe en traction linéaire (figure 40), associée à un faciès de rupture plat, sans extraction de fibre (figure 41). La rupture des fibres survient prématurément (déformation à rupture des premières fibres dans le fil brut à 0,70%), et ne jouent pas leur rôle de renfort.

3.2 - Comportement tenace

Il a été montré sur microcomposites que la liaison entre la fibre stabilisée (A-HTT) et la matrice est plus faible qu'avec la fibre A. Ceci est également mis en évidence par les comportements mécaniques des minicomposites: comportement fragile pour A/M, mais tenace pour A-HTT/M par déviation de la fissure à l'interface fibre/matrice. Dans la littérature, la non linéarité en flexion des C/C unidirectionnels est due aux décohésions fibre/matrice et frottements dans le plan de la fissure interfaciale, donnant des faciès de rupture avec extraction de fibres importante [24-30]. Ce mécanisme de dissipation d'énergie est celui observé pour les CMCs classiques (ex:SiC/SiC), mais la multifissuration matricielle, qui se produit pour ces derniers, n'a pas

Tableau 4. Caractéristiques des minicomposites C/C

Fil	Données mécaniques											Données endommagement	
	S_{fil} (mm^2)	V_f (%)	ε_{el} (%)	σ_{el} (MPa)	E_c (GPa)	$S_{fil,corr}$ (mm^2)	ε_R (%)	σ_R (1) (MPa)	$S_{f,corr}$ (mm^2)	E_f (2) (GPa)	$\sigma_{R,f}$ (3) (MPa)	L_i (µm)	u_0 (µm)
A	0,109	100	0,70 (0,06)*	1455 (162)	209 (9)	0,085	1,03 (0,11)	2587 (258)					
A-HTT	0,104	100	0,55 (0,10)	1297 (274)	237 (10)	0,067	0,77 (0,03)	2429 (93)					
A/M	0,168	65	0,57 (0,05)	992 (58)	177 (4)	0,168	0,57 (0,05)	992 (58)					
A-HTT/M	0,198	52	0,38 (0,02)	701 (35)	186 (7)	0,149	1,02 (0,08)	1872 (62)	0,078	288	3576	376	1,6
A-HTT/I1/M	0,211	49	0,33 (0,01)	578 (49)	175 (9)	0,158	1,04 (0,04)	1818 (170)	0,078	322	3683	521	2,3
A-HTT/I3/M	0,203	51	0,30 (0,03)	532 (76)	177 (11)	0,152	1,02 (0,17)	1810 (226)	0,078	320	3527	575	2,4
A-HTT/I2/M	0,221	47	0,45 (0,02)	766 (23)	173 (9)	0,161	0,79 (0,07)	1665 (116)	0,078	382	3437	251	0,355

* entre parenthèse: écart type

(1) $\sigma_R = \dfrac{F}{S_{fil,corr}}$ avec $S_{fil,corr} = S_{fil}(1-\gamma)(1-\alpha_c)$ pour fils bruts, ou $S_{fil,corr} = S_{fil}(1-\gamma)$ pour minicomposites, avec γ est le pourcentage de fibres rompues avant l'essai de traction, et α_c le taux de fibres rompues avant la rupture du fil brut

(2) E_f est la pente de la dernière partie de la courbe de traction, en prenant $S_{f,corr}$

(3) $\sigma_{R,f} = \dfrac{F}{S_{f,corr}}$ avec $S_{f,corr} = S_{filbrut}.(1-\gamma)$

lieu. Seuls Thomas [54] et Zaldivar [55] ont reporté l'existence d'un tel endommagement dans les C/C unidirectionnels.

Dans cette étude, les minicomposites, élaborés avec la fibre stabilisée A-HTT, présentent tous de la multifissuration matricielle. La mécanique de l'endommagement des CMCs peut donc s'appliquer ici. Par ailleurs, il apparaît possible d'optimiser l'interface en favorisant un mécanisme de ténacité par multifissuration matricielle, identifié pour les SiC/SiC [23], plutôt qu'un mécanisme par décohésion/frottement. L'ajout d'une interphase entre fibre et matrice, de microtexture variée, est le moyen choisi pour modifier la liaison interfaciale. Dans le cas de A-HTT/M et des minicomposites avec une interphase I_1 ou I_3, un même comportement est observé: mécanisme de ténacité par décohésion/frottement. En revanche, pour le matériau avec une interphase I_2, le mécanisme de multifissuration matricielle se substitue au mécanisme de décohésion/frottement.

3.2.1 - Mécanisme de ténacité par décohésion/frottement

Courbes de traction.

Elles se présentent en 3 parties: (1) une partie linéaire jusqu'à 0,3-0,4% de déformation; (2) une partie présentant plus ou moins d'accidents; (3) une partie linéaire si la seconde partie est très accidentée, ou légèrement convexe si la seconde partie n'a que peu d'accidents (figure 42). La seconde partie est associée en émission acoustique à une augmentation brutale du signal. Les accidents observés sont donc reliés à un endommagement du matériau. Cet endommagement est attribué à de la fissuration matricielle (figure 43), un essai de traction sous MEB d'un minicomposite A-HTT/M ayant montré l'apparition simultanée d'une grande part des fissures matricielles. Par ailleurs, une seconde partie plus accidentée est associée à une augmentation plus abrupte de l'émission acoustique, et donc correspond à un endommagement plus grand.

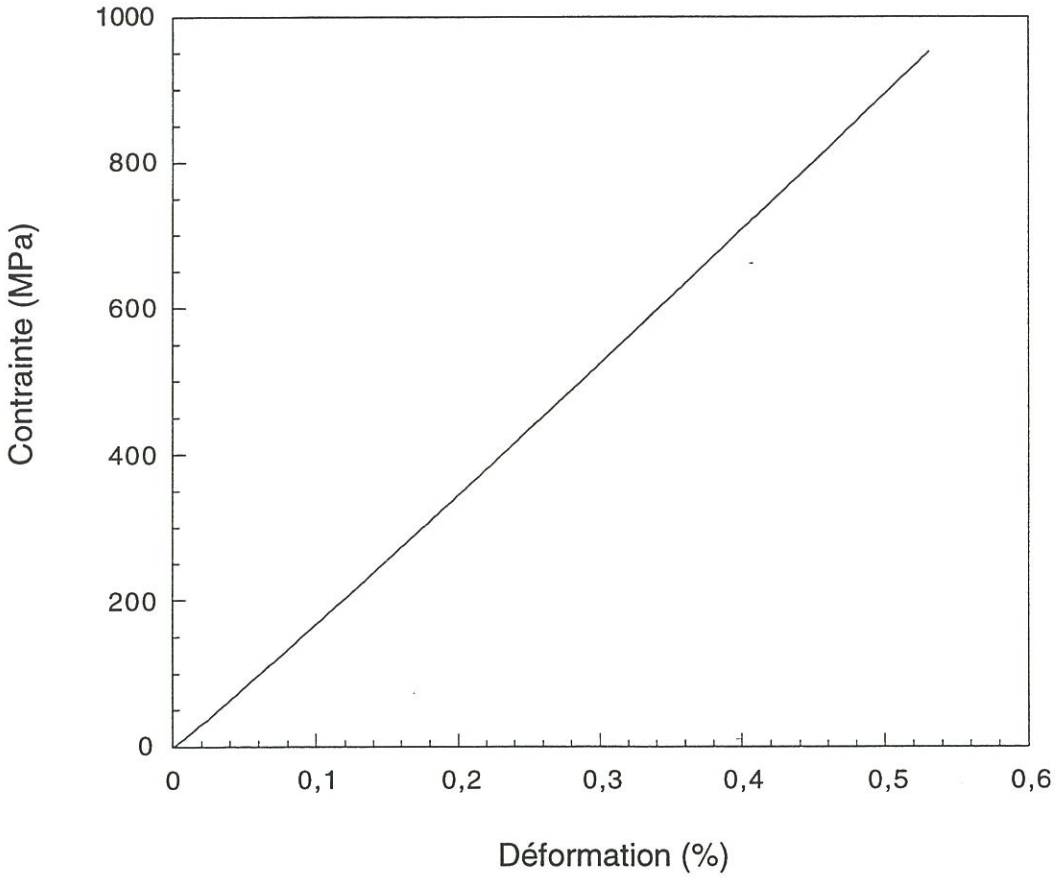

Figure 40: courbe de traction du minicomposite A/M (comportement fragile)

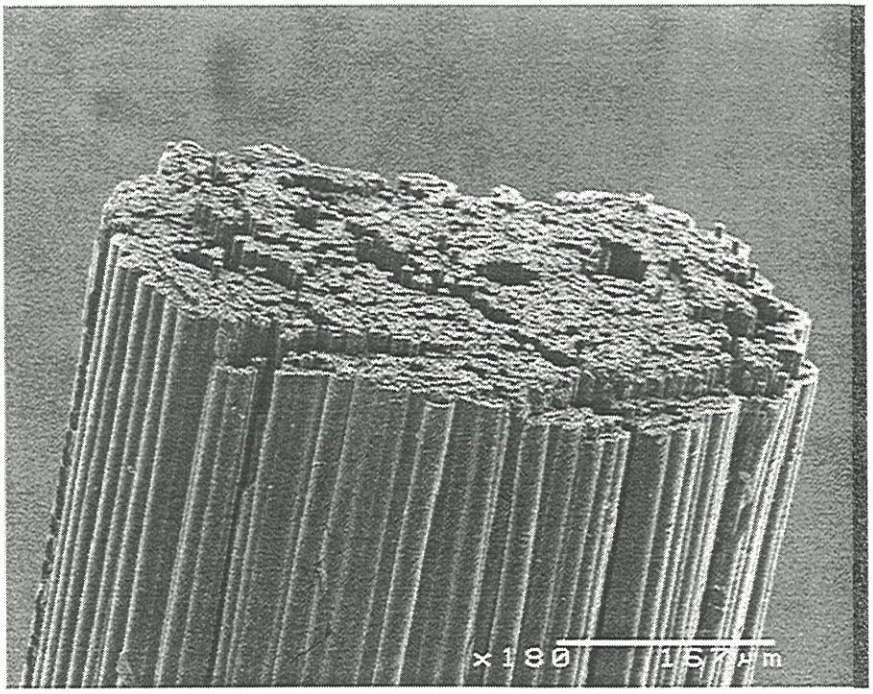

Figure 41: faciès de rupture plat pour le minicomposite A/M

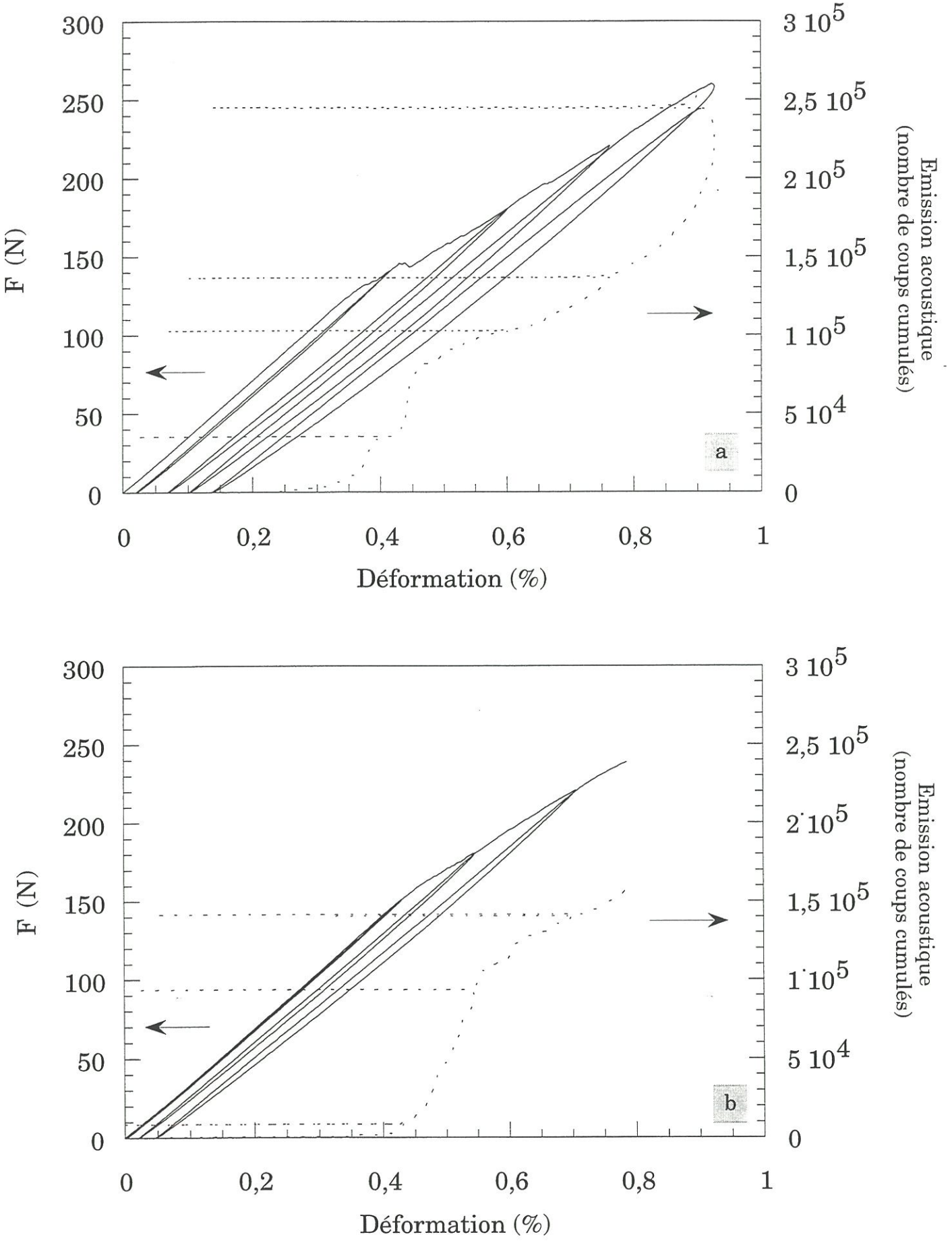

Figure 42: courbe force-déplacement avec cycles de charge-décharge et émission acoustique pour (a) A-HTT/I_3/M dans le cas d'une seconde partie très accidentée et pour (b) A-HTT/M dans le cas d'une seconde partie peu accidentée

La linéarité en fin de courbe de traction désigne une absence d'endommagement supplémentaire. La pente, évaluée dans ce cas, correspond à la seule contribution des fibres. La matrice est donc complètement endommagée: la fissuration est arrivée à saturation. Les propriétés mécaniques à rupture sont ainsi identiques pour les A-HTT/M et les minicomposites avec une interphase I_1 ou I_3: ε_R=1%, σ_R=1800MPa.

Endommagement.

Des pas de fissuration d'environ 400µm pour A-HTT/M, et d'environ 500µm pour A-HTT/I_1/M et A-HTT/I_3/M ont été déterminés au MEB, avec une ouverture de fissure respectivement de 1,6 et 2,3µm (Tableau 4). Ces fissures sont traversantes, et sont déviées à l'interface fibre/matrice (figure 44.a). Il en résulte un pontage des fissures par les fibres intactes (figure 44.b). Il n'y a pas d'évidence de rupture de fibre hors de la zone de rupture.

Faciès de rupture.

La rupture s'effectue à différents niveaux (figure 45). Des régions sont caractérisées par peu ou pas d'extraction de fibres (figure 45.b), alors que d'autres sont caractérisées par des extractions de fibre importantes (figure 45.c), en particulier en périphérie du minicomposite où la fraction volumique locale de matrice est plus élevée.

Contrainte de cisaillement interfaciale τ

La contrainte τ a été déterminée à partir de cycles de charge-décharge effectués lors des essais de traction (figure 42) [53, Annexe 3]. Le nombre de fissures, N, pris en compte dans les calculs correspond aux fissures créées avant la décharge. Ici, on a considéré N égal au nombre de fissures observées après rupture du matériau pour le cycle le plus proche de la rupture. L'erreur sur N est faible compte tenu du fait de l'apparition de la plupart des fissures matricielles dans la partie II de la courbe de traction, qui entraîne très rapidement l'état de saturation de la fissuration matricielle. τ est évalué à 1MPa pour A-HTT/M, et légèrement inférieur pour A-HTT/I_1/M et A-HTT/I_3/M

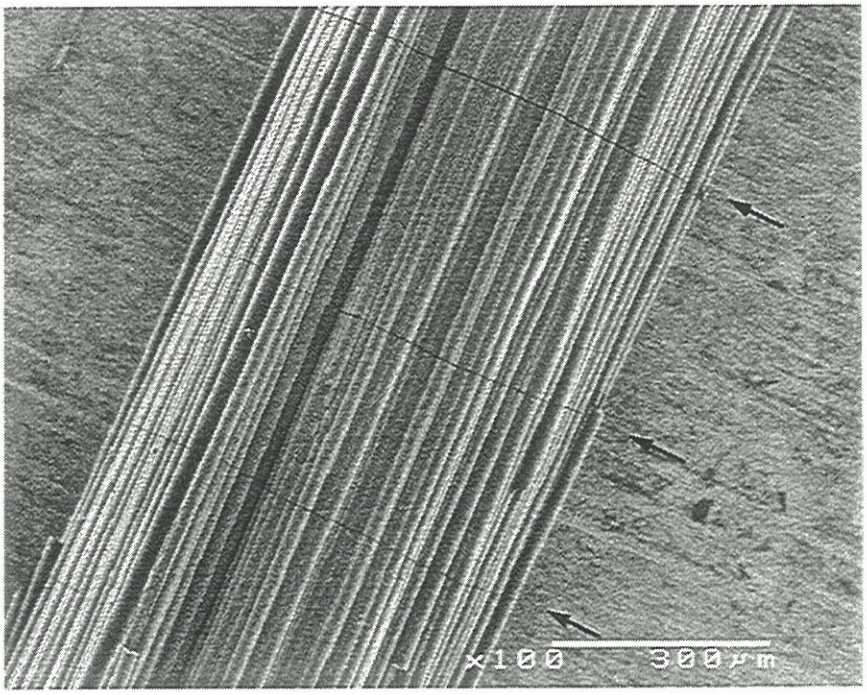

Figure 43: multifissuration matricielle observée pour un minicomposite A-HTT/M

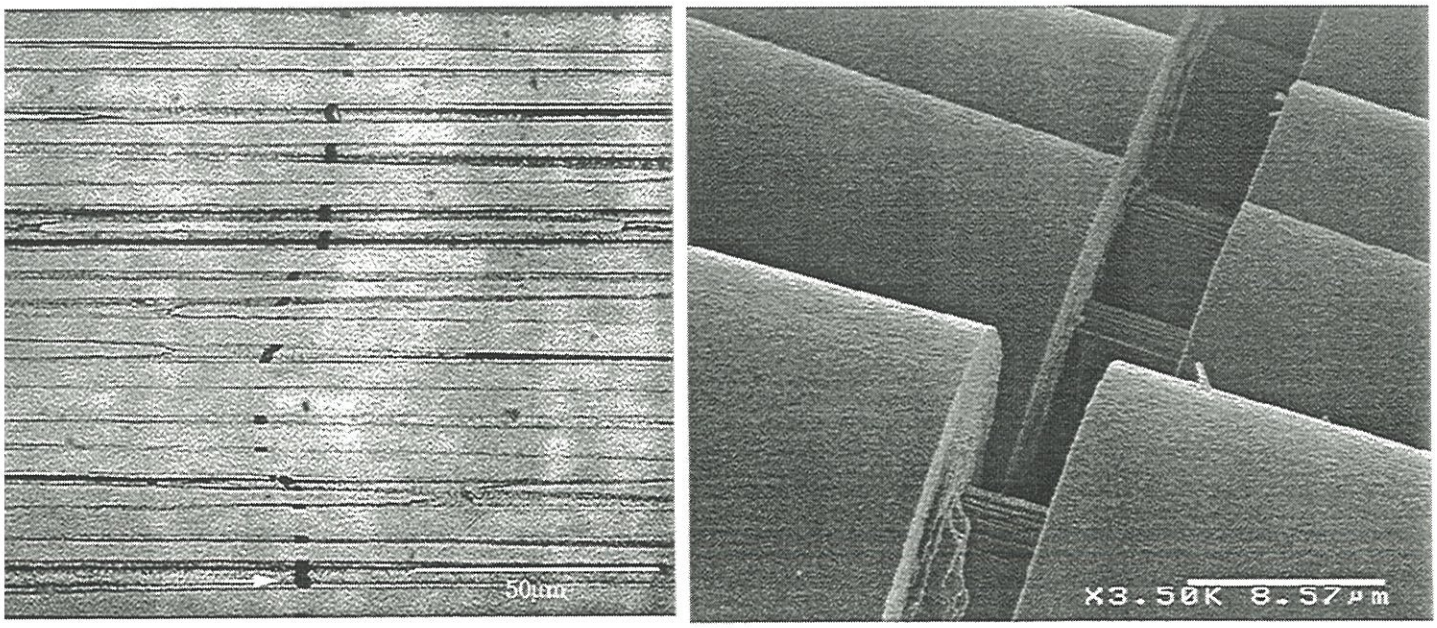

(a) (b)

Figure 44: fissuration matricielle (a) vue en microscopie optique d'un minicomposite A-HTT/M en coupe longitudinale polie (déviation de la fissure à l'interface fibre/matrice); (b) d'un minicomposite A-HTT/I_1/M vu au MEB à plus fort grandissement (pontage des fissures par les fibres)

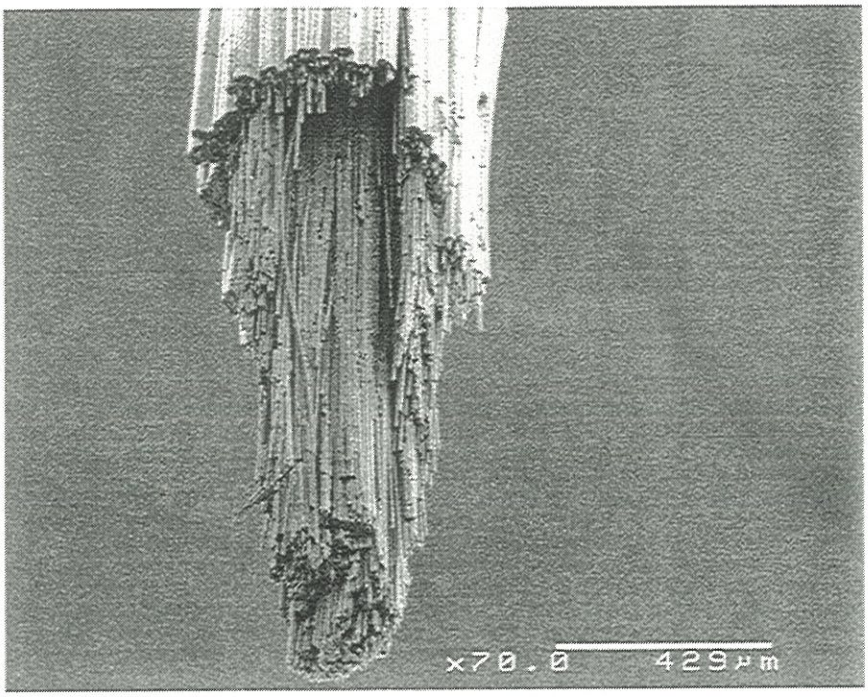

(a)

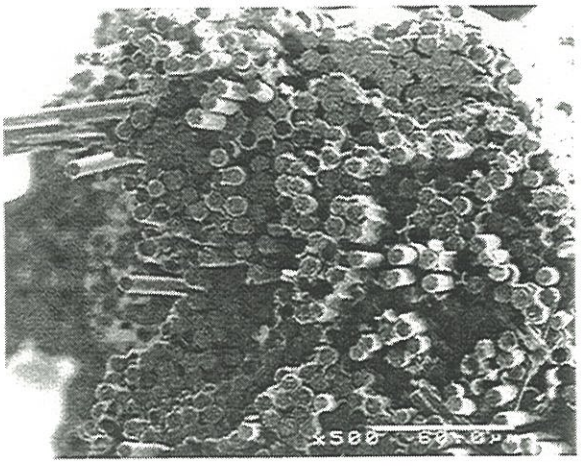

(b)

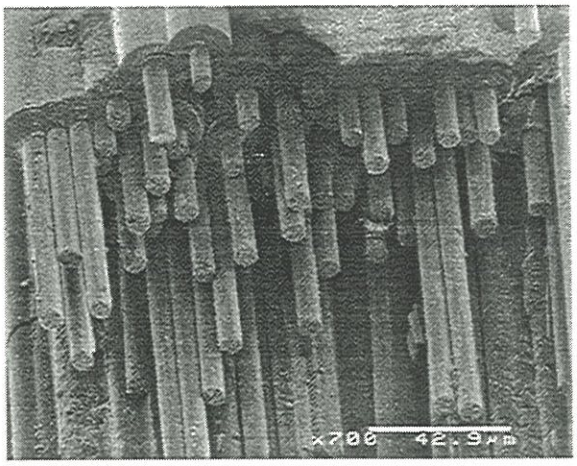

(c)

Figure 45: faciès rupture d'un minicomposite A-HTT/M observé au MEB
(a) vue d'ensemble, régions avec (b) peu ou pas d'extraction, et (c) des extractions importantes

(Tableau 5). Peu de différence existe entre ces minicomposites ce qui explique leurs comportements similaires.

Une faible liaison fibre/matrice, associée à un faible τ, donne de grandes longueurs de décohésion, et un faible rechargement de la matrice. De ce fait, l'ouverture de fissure, fonction de la longueur relaxée, est grande, et le pas de fissuration est important (figure 46.a).

La relaxation des contraintes résiduelles sur de grandes longueurs perpendiculairement aux fissures entraîne des fissures ouvertes sous charge nulle (figure 46.b).

3.2.2 - Mécanisme de ténacité par multifissuration matricielle

Courbes de traction.

Le minicomposite avec une interphase I_2, A-HTT/I_2/M, ne présente pas le domaine intermédiaire accidenté, observé auparavant (figure 47). Cependant, la première partie linéaire prend fin vers ε_{el}=0,45% (Tableau 4), soit une valeur similaire aux précédents minicomposites, et marque également le début d'une montée brutale de l'émission acoustique (figure 47.b). Ceci est attribué à la multifissuration matricielle. La seconde partie de la courbe est caractérisée par des contraintes plus élevées que pour les autres minicomposites à déformation identique (figure 47.a), et par une pente légèrement plus forte (E_f dans le Tableau 4), . Les fibres ne supportent donc pas seules la charge jusqu'à la rupture. La matrice reste partiellement chargée. La faible différence de pente entre les deux courbes s'explique par le fait que le module de la matrice est faible, environ 4 fois plus faible que celui de la fibre. Le module reste élevé même pour un endommagement complet de la matrice (référence, A-HTT/I_1/M, A-HTT/I_3/M). Il s'agit là d'une différence importante avec d'autres matrices comme le SiC, pour lequel la contrainte à rupture augmente d'environ 40% dans les SiC/SiC (module de la matrice deux fois plus élevé que celui de la fibre) [23] en passant d'un mécanisme de ténacité par décohésion/frottement à celui par multifissuration matricielle.

Tableau 5. Contraintes de cisaillement interfaciales τ déduites des cycles de charge-décharge effectués sur des courbes de traction de minicomposites

	A-HTT/M	A-HTT/I1/M	A-HTT/I3/M	A-HTT/I2/M
τ (MPa)	1,1	0,73	0,63	6,8

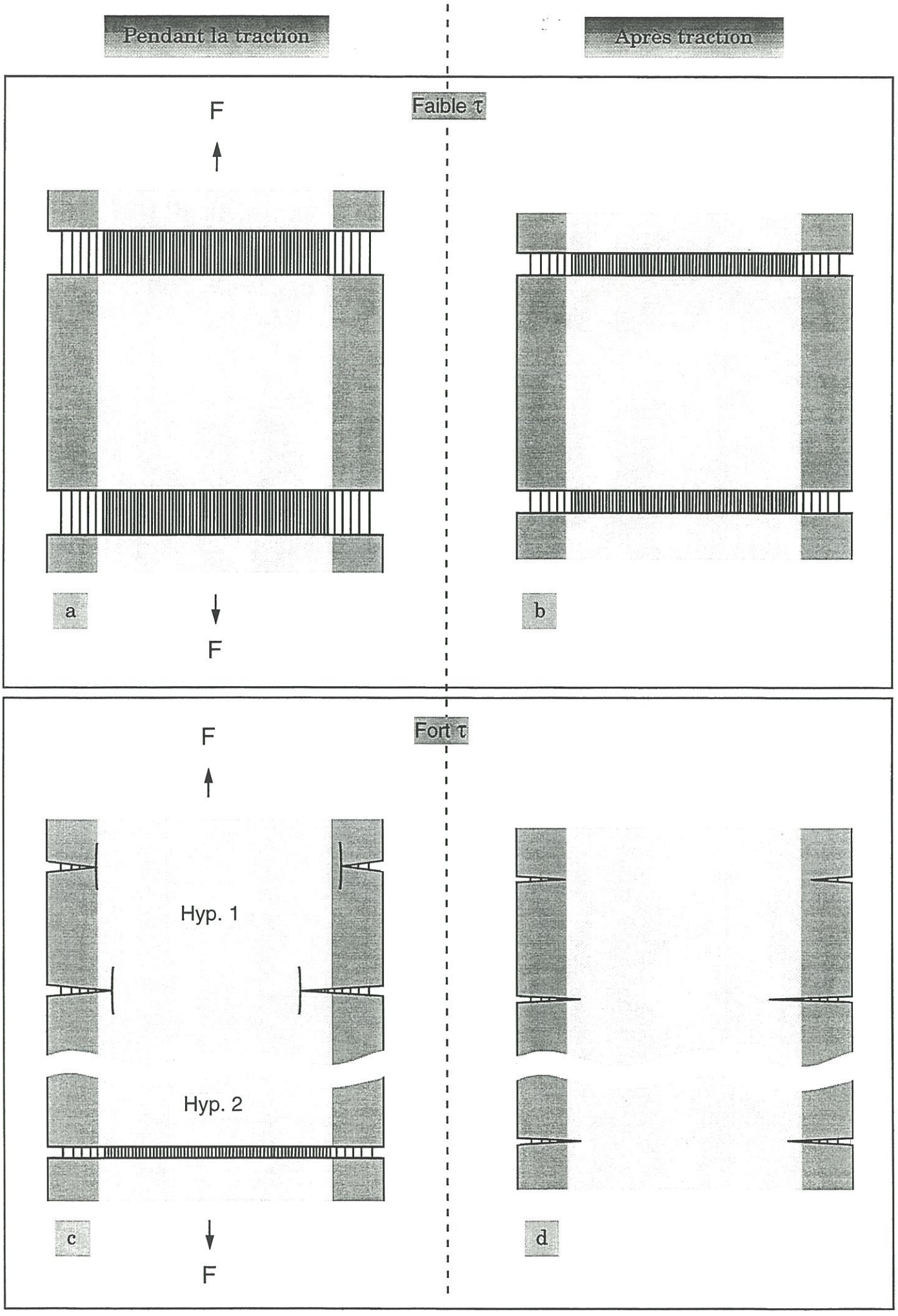

Figure 46: représentation schématique des modes d'endommagement dans les minicomposites selon τ

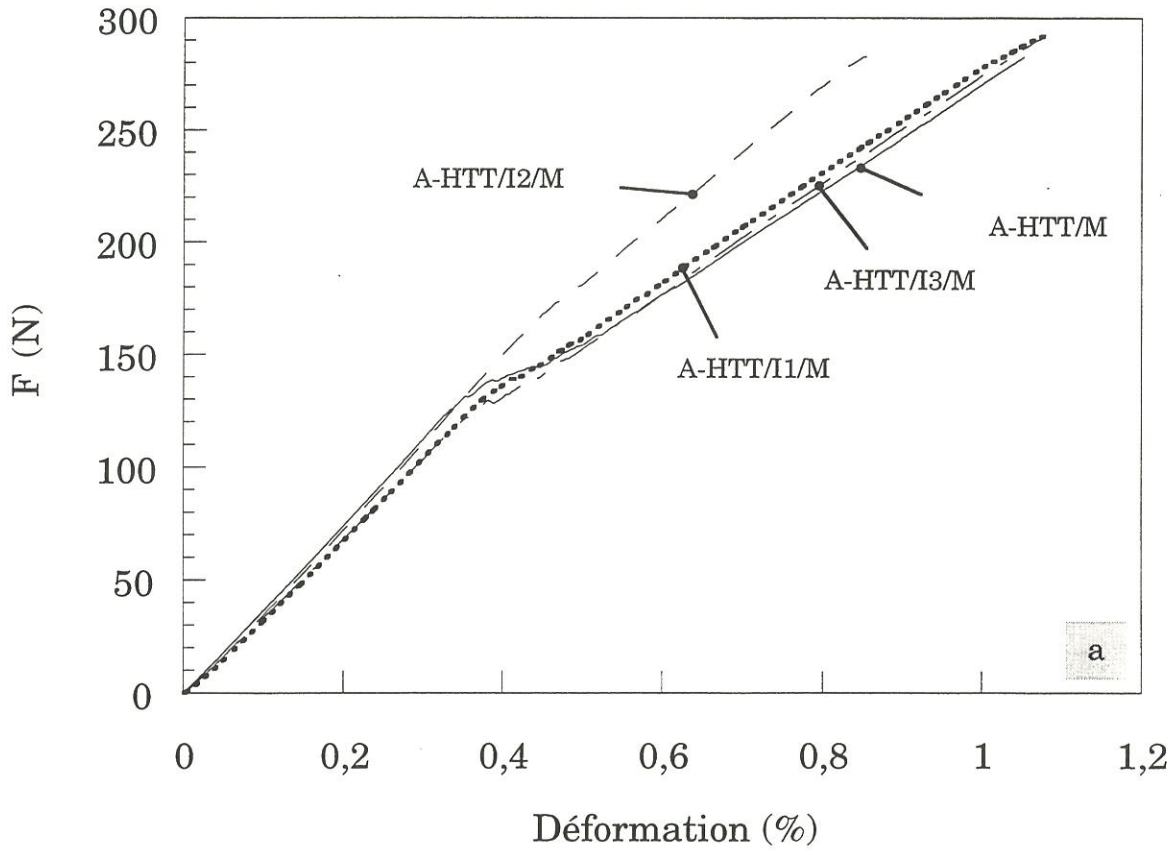

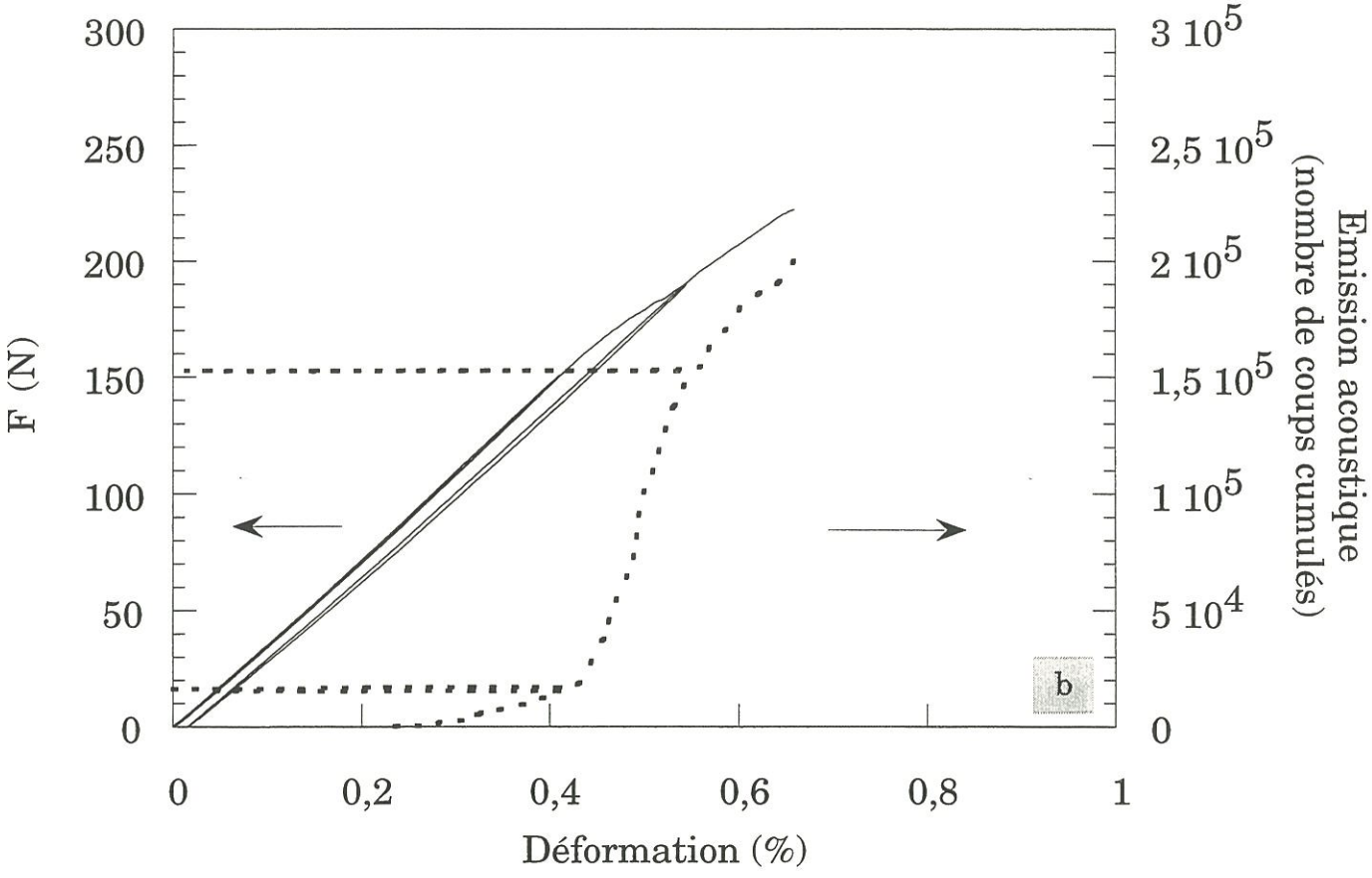

Figure 47: courbe force-déplacement en traction d'un minicomposite A-HTT/I_2/M
(a) comparée aux courbes de traction des autres minicomposites
(b) avec un cycle charge-décharge, associé à une mesure de l'émission acoustique
(N.B.: ce test n'a pas été conduit jusqu'à la rupture)

Endommagement.

Un pas de fissuration de 250µm est mesuré après rupture, avec une ouverture de fissure estimée à 0,355µm en moyenne (figure 48), soit un pas 2 fois plus faible, et une ouverture de fissure au moins 4 fois plus petite que ceux précédemment observés. De ce fait, une longueur de décohésion fibre/matrice plus faible, associée à une contrainte de cisaillement interfaciale plus élevée caractérise A-HTT/I_2/M. Le calcul de τ donne, en effet, une valeur bien supérieure à 1MPa: τ=6,8MPa (Tableau 5). Le mécanisme de dissipation de l'énergie par multifissuration matricielle est alors favorisé par rapport au mécanisme de décohésion/frottement.

L'examen plus approfondi des fissures au sein du minicomposite montre des fissures a priori non traversantes, et des déviations de ces fissures à l'**interface matrice/interphase** (figure 49.b). L'ajout de l'interphase I_2 engendre une liaison interphase/fibre plus forte que la liaison matrice/interphase, contrairement aux autres interphases et notamment à l'interphase I_3, qui possède la même texture optique dans la couche périphérique du minicomposite (Ae=14° (figure 30)).

Deux hypothèses peuvent être envisagées pour expliquer l'observation de fissures non traversantes après rupture (schéma figure 46.d): (1) les fissures matricielles initiées à l'extérieur du minicomposite sont arrêtées en périphérie du minicomposite; (2) les fissures sont traversantes et se referment au coeur du minicomposite sous charge nulle.

Dans la première hypothèse (figure 46.c,d, hyp.1), le minicomposite se comporte comme un "gros microcomposite", la fraction volumique de matrice à l'intérieur du minicomposite étant très faible ($V_m \approx 10\%$) alors qu'elle est de 85% en périphérie. On peut donc considérer les deux entités homogènes suivantes: l'enveloppe externe, constituée principalement de la matrice, en tension axiale résiduelle, et le coeur, constitué principalement des fibres, en compression axiale. La fissuration matricielle s'arrête vers la frontière coeur-peau du minicomposite, l'énergie de rupture, subsistant après la déviation de

la fissure à l'interface matrice/interphase, n'étant plus suffisante pour rompre la matrice interne, qui possède une déformation à rupture supérieure à celle de la matrice externe.

Dans la seconde hypothèse (figure 46.c,d, hyp.2), les fissures se propagent à travers le minicomposite. Mais comme τ est élevé, la longueur de décohésion est faible et la matrice reste en partie chargée jusqu'à la rupture. A charge nulle, la relaxation incomplète des contraintes résiduelles dans le coeur du minicomposite se traduit par la refermeture des fissures à coeur.

Le minicomposite A-HTT/I_2/M a un faciès de rupture du même type que pour les autres minicomposites (figure 49). Ce faciès peut aussi bien représenter la rupture dans le cas de l'hypothèse 1 d'endommagement que dans le cas de l'hypothèse 2.

Paramètres responsables d'un τ élevé.

Deux paramètres peuvent être à l'origine des changements survenus dans les liaisons interfaciales compte tenu des conditions opératoires: la texture plus désordonnée de I_2, et son élaboration à une température plus élevée (1100°C (figure 30)). En fait, une combinaison des 2 effets doit être plus probable car I_3, qui présente la même texture optique à l'extérieur pour le pyrocarbone d'interphase (Ae=14°) que I_2, n'engendre pas de déviation à l'interface matrice/interphase. L'élaboration de I_3 à 900°C, soit une température inférieure à celle du dépôt de la matrice, n'aboutit pas aux mêmes contraintes résiduelles radiales que I_2, élaborée à une température supérieure à celle de la matrice.

En résumé, selon la force de la liaison fibre/matrice on change de comportement mécanique pour les minicomposites carbone/carbone à l'image des SiC/SiC (figure 50). En diminuant τ, on passe d'un comportement fragile à un comportement tenace par un mécanisme de multifissuration matricielle, puis par un mécanisme de décohésion/frottement.

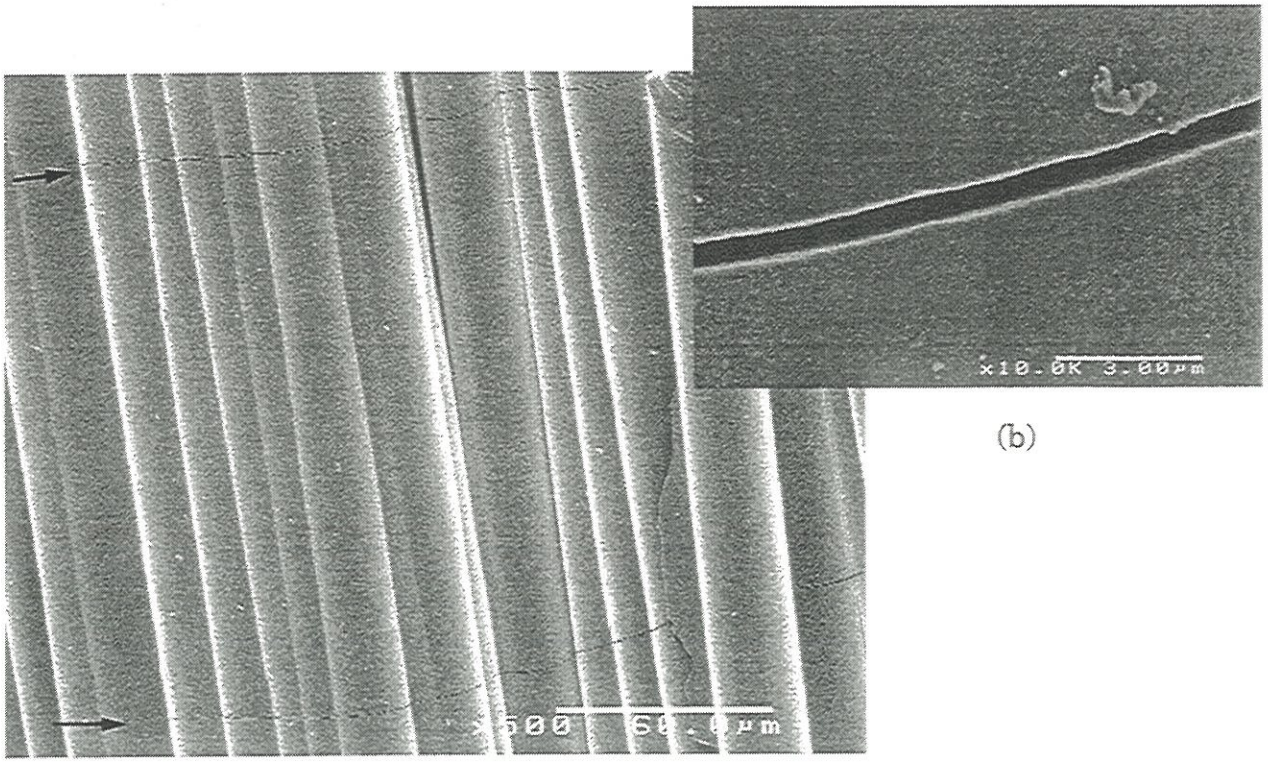

(b)

(a)

Figure 48: observation au MEB d'un minicomposite A-HTT/I_2/M après rupture montrant (a) de la multifissuration matricielle; (b) vue à plus fort grandissement d'une fissure

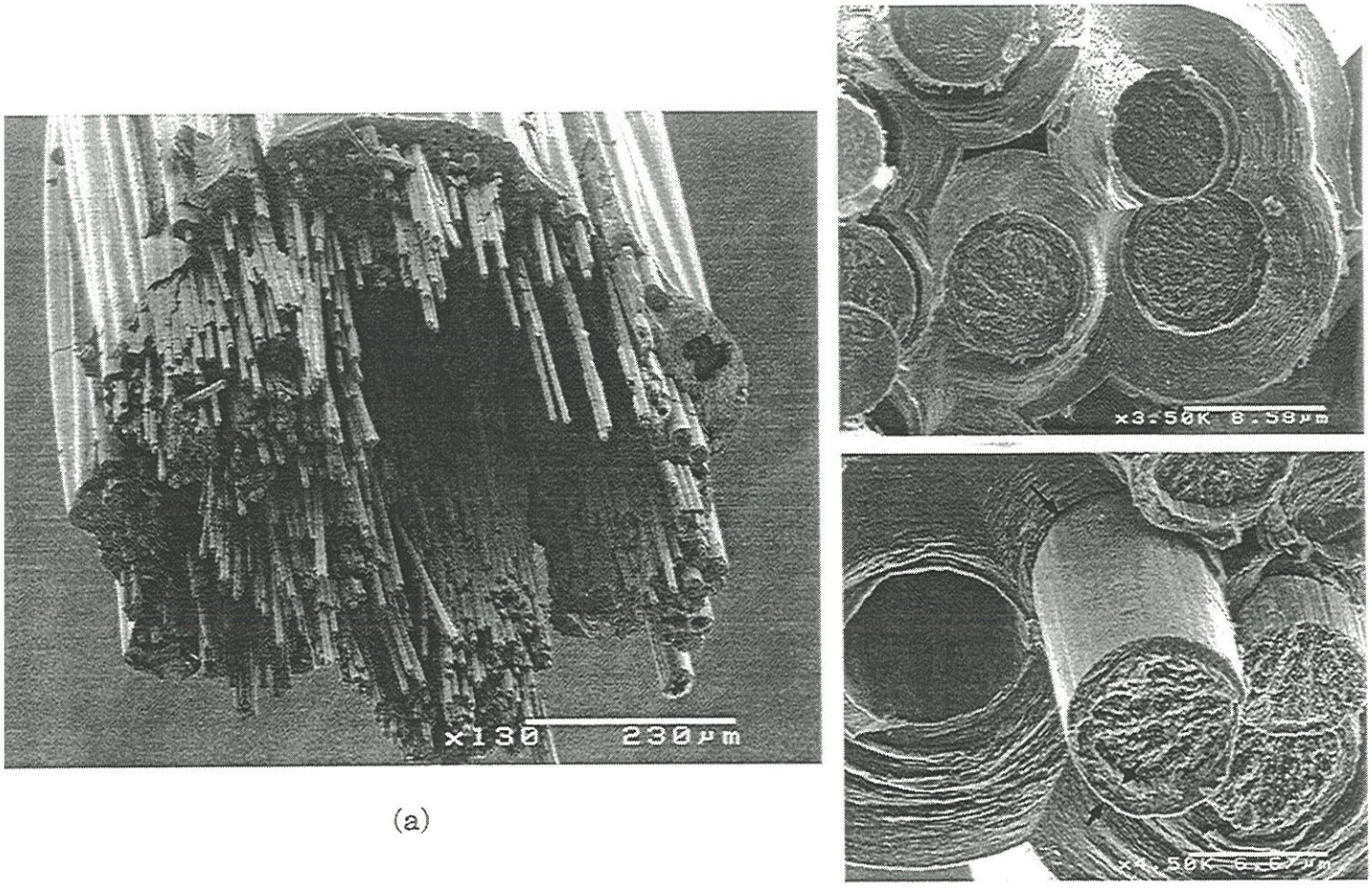

(a)

(b)

Figure 49: faciès de rupture d'un minicomposite A-HTT/I_2/M
(a) vue d'ensemble, et (b) regions montrant la déviation de la fissure

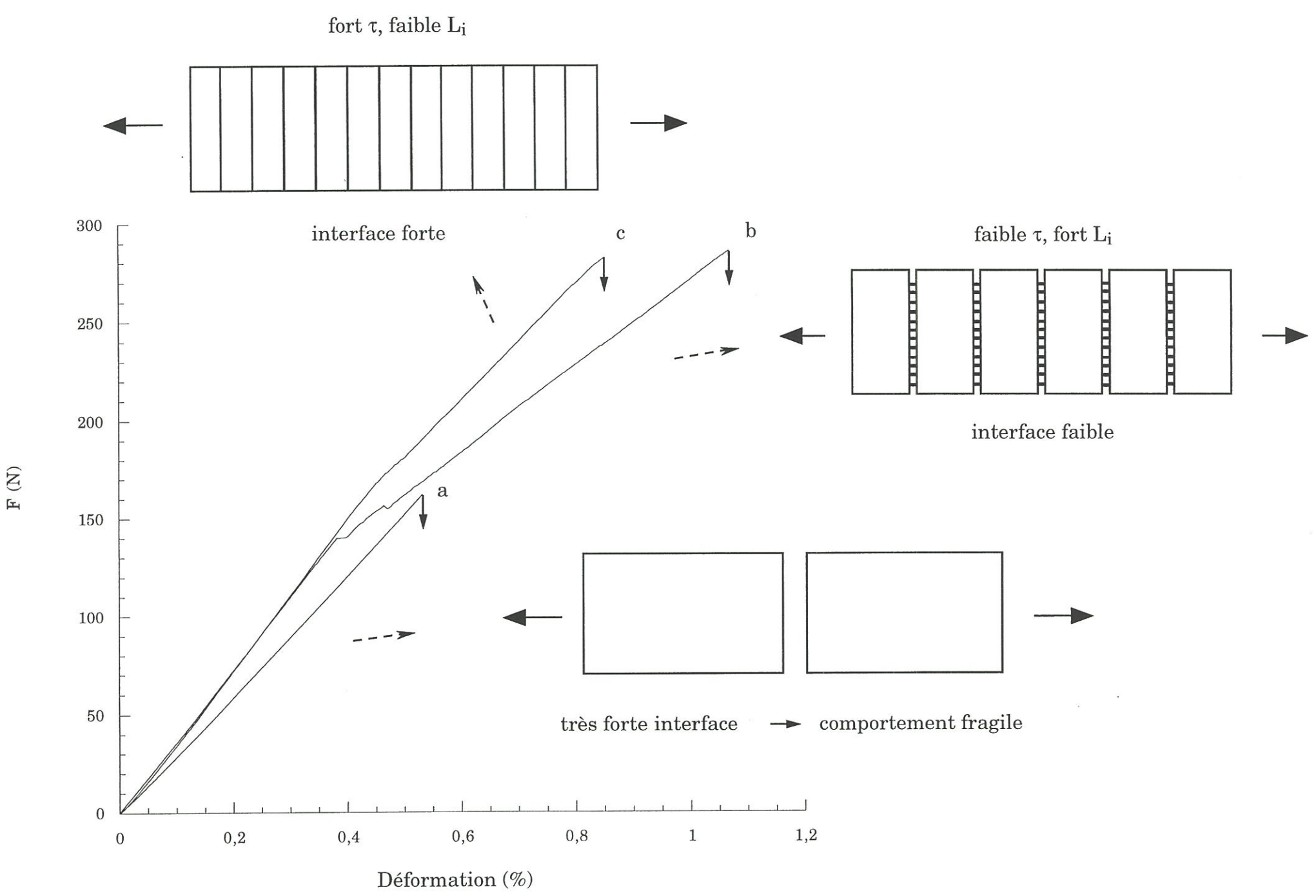

Figure 50: courbes de traction typiques, et endommagement associé, obtenus pour les minicomposites C/C selon la force de la liaison interfaciale

CONCLUSION GENERALE

CONCLUSION GENERALE

Le rôle de l'interface dans les carbone/carbones a été étudié à l'aide de matériaux modèles: le **microcomposite** (fibre revêtue d'une matrice), et le **minicomposite** (fil infiltré). L'originalité de ce travail a consisté à modifier les caractéristiques interfaciales par l'interposition d'une **interphase de carbone**, de microtexture variable, entre fibre et matrice de carbone. Interphase et matrice ont été élaborées de manière reproductible par CVD/CVI.

Les **composites carbone/carbone, non traités à HTT2**, sont des **composites inverses** comme les autres CMCs. Selon les contraintes résiduelles axiales dans le matériau, la multifissuration sera visible ou non: une compression de la matrice amène sa déformation à rupture proche de celle de la fibre, une seule fissure matricielle se produit alors avant la rupture du matériau (cas des microcomposites); une tension résiduelle de la matrice accentue l'écart entre la fibre et la matrice (cas des minicomposites), et permet la multifissuration matricielle.

Dans le cas particulier des **microcomposites traités à HTT2**, le **comportement** devient **régulier**, la fibre ayant une déformation à rupture plus faible que la matrice. La courbe de traction contrainte-déformation est linéaire (liaison fibre/matrice forte), ou présente des singularités (liaison fibre/matrice faible).

L'**étude sur microcomposites** a permis de mettre en évidence les 3 facteurs jouant sur la force de la liaison interfaciale. Tout d'abord, l'utilisation de fibres, avec une rugosité de surface plus élevée, a montré qu'une **adhésion physique** peut apporter une augmentation substantielle de l'adhésion entre fibre et pyrocarbone.

D'autre part, la stabilisation de la fibre (A-HTT) engendre une liaison fibre/matrice plus faible que pour la fibre brute. Ceci s'explique par un retrait plus grand de la fibre A-HTT, c'est-à-dire une interface plus en tension. La **contribution des contraintes résiduelles** est essentiel.

Enfin, l'ajout d'une **interphase de texture plus désordonnée** (Ib (Ae=13°), Ic (Ae=11°)) que la matrice (Ae=17°) crée une **liaison chimique plus forte** entre la fibre et le pyrocarbone d'interphase. Son influence a été mise en évidence pour les fibres stabilisées, car pour les fibres brutes la liaison interfaciale est déjà forte.

Les C/C sont des CMCs où le module de la fibre est très supérieur à celui de la matrice. Les performances ultimes, in-situ, de la fibre sont primordiales surtout lorsqu'elle subit des traitements ou post-traitements thermiques. Cette étude montre qu'un pyrocarbone, de texture plus désordonnée, **"cicatrise" les défauts de surface de la fibre, créés par le traitement thermique**. La fibre A-HTT retrouve alors à l'intérieur du microcomposite ses propriétés mécaniques (ε_R,σ_R) antérieures au THT. Par ailleurs, ce type de pyrocarbone **permet une meilleure utilisation des capacités de la fibre** jusqu'à 100% pour une interphase de type Ib, mais beaucoup moins pour l'interphase Ic moins orientée (laminaire sombre), car cette dernière engendre une liaison chimique trop forte sans possibilité de déviation de la fissure à l'interface (faciès de rupture de type fragile quel que soit le type de la fibre). L'interphase Ib crée donc une liaison fibre/pyrocarbone optimale avec un juste équilibre entre liaison chimique et contraintes résiduelles. La préparation de lames minces pour le MET montre notamment que la composante chimique de la liaison est plus faible que la composante représentée par les contraintes résiduelles de tension à l'interface: une décohésion fibre/pyrocarbone est en effet créée à partir d'une certaine épaisseur critique, ce qui n'est pas le cas pour l'interphase Ic.

L'**étude sur minicomposites** a permis de mettre en évidence, pour la première fois, l'existence et le contrôle d'une **multifissuration matricielle dans**

les composites carbone/carbone. Ce phénomène, classique pour les autres CMCs (ex: SiC/SiC), est contrôlé, comme pour les CMCs, par la force de la liaison fibre/matrice. Il est montré que la **liaison forte**, qui caractérise la liaison entre la fibre A et la matrice, entraîne un effet d'entaille après rupture de la matrice, qui conduit à la **rupture catastrophique du matériau**. En revanche, l'utilisation de la fibre stabilisée (A-HTT) entraîne une **liaison interfaciale plus faible**, comme cela a été démontré précédemment, et conduit à une **déviation de la fissure matricielle à l'interface fibre/matrice**. Un **comportement tenace** est alors observé pour ce minicomposite, caractérisé en traction par un domaine de fort endommagement après la linéarité initiale, et une reprise des efforts par les fibres en fin d'essai. La matrice est complètement endommagée, avec un pas de fissuration (400µm) et une ouverture de fissure (1,6µm) importants, résultant d'une **faible contrainte de cisaillement interfaciale** τ (1MPa). Dans ce cas, la dissipation de l'énergie de rupture est assurée essentiellement par la décohésion fibre/matrice, et les frottements au niveau des interfaces déliées: **mécanisme de ténacité par décohésion/frottement**.

L'**ajout d'une interphase de texture plus désordonnée** (I_2, Ae=14°) que la matrice a donné un comportement différent: une **déviation de la fissure à l'interface matrice/interphase**, et une **contrainte de cisaillement interfaciale associée plus élevée** (τ=6,8MPa). Dans ce cas, la courbe de traction ne présente pas comme précédemment un domaine intermédiaire accidenté, mais seulement un changement de pente. La matrice reste partiellement chargée jusqu'à la rupture, ce qui conduit à des contraintes plus élevées que pour A-HTT/M à déformation identique après la linéarité. Ceci s'explique par le τ élevé, qui implique une faible longueur de décohésion interfaciale et un rechargement de la matrice sur de petites distances. L'ouverture des fissures et le pas de fissuration sont donc faibles. Ce comportement s'apparente à celui observé pour les SiC/SiC, caractérisés par un τ élevé (quelques centaines de MPa), une déviation de la fissure dans l'interphase par branchements, et

attribué à un **mécanisme de ténacité par multifissuration matricielle**. Il est à noter que, contrairement aux SiC/SiC, le passage d'un mécanisme de ténacité à l'autre dans les minicomposites C/C couvre un domaine restreint de la contrainte de cisaillement interfaciale.

Le changement des caractéristiques interfaciales par l'ajout d'une interphase I_2 est probablement due à sa texture moins orientée (liaison chimique fibre/pyrocarbone plus forte), couplée aux contraintes résiduelles radiales en tension. Ces contraintes résiduelles résultent de l'élaboration de l'interphase à une température plus élevée que celle du dépôt de la matrice, et aux caractéristiques thermomécaniques des différents constituants.

REFERENCES BIBLIOGRAPHIQUES

[1] R. Naslain, Introduction aux matériaux composites. 2-Matrices métalliques et céramiques, ed. CNRS/IMC, Bordeaux (1985)

[2] J. Rappeneau, A.M. Barrachin, dans Les Carbones, ed. Groupe Français d'Etude des Carbones, **2**, p.642 (1965)

[3] G. Pellegrini, Carbon, **10**, pp.487-490 (1972)

[4] J.B. Nelson, D.P. Riley, Proc. Phys. Soc., **57**, 477, (1945)

[5] R.E. Franklin, Acta Cryst., **3**, 107 (1950)

[6] A. Oberlin, Carbon, **22**, pp.521-541 (1984)

[7] A. Oberlin, dans Chemistry and Physics of Carbon, ed. P. A. Thrower, **22**, pp. 1-143 (1989)

[8] E. Fitzer, M. Heine, dans Fiber reinforcement for composite materials, ed. A.R. Bunsell, Elsevier, Amsterdam, pp. 73-148 (1988)

[9] G. Savage, Carbon-carbon composites, ed. Chapman and Hall (1992)

[10] E. Fitzer, B.Terwiesch, Carbon, **10**, pp.383-390 (1972)

[11] F. Fau-Canillac, F. Carrere, A. Reynes, C. Vahlas, et F. Maury, Journal de physique, C5, 5, pp.89-96 (1995)

[12] M.L. Lieberman, H.O. Pierson, Carbon, **12**, pp.233-241 (1974)

[13] H.O. Pierson, M.L. Lieberman, Carbon, **13**, pp.159-166 (1975)

[14] P. Loll, Préparation et propriétés physiques de composites carbone-carbone déposés en phase vapeur, Thèse de docteur-ingénieur, Université de Bordeaux I, n° 240, Juin (1976)

[15] S. Kimura, E. Yasuda, N. Takase, S. Kasuya, High Temp. High Press., **13**, pp.193-199 (1981)

[16] S.M. Oh, J.Y. Lee, Carbon, **26**, N°6, pp.763-768 (1988)

[17] A.A. Griffith, Phil. Tran. Roy. Soc., **A221**, p.163 (1921)

[18] G.R. Irwin, J. Appl. Mech., **24**, p.361 (1957)

[19] W. Weibull, J. Appl. Mech., **18**, pp.293-297 (1951)

[20] J.M. Quenisset, Conf. Générale, 23e colloque du groupe français de rhéologie, Bordeaux, eds. LMP-CERMUB, pp.1-41 (1988)

[21] J.O. Outwater, M.C. Murphy, 26th Ann. Tech. Conf. on reinforced plastics: Composites Division of Soc. of Plastics Industry paper 11-C-1 (1969)

[22] A.G. Evans, F.W. Zok, J. Davis, Comp. Sci. Technol., **42**, 3 (1991)

[23] C. Droillard, J. Lamon, X. Bourrat, Mat. Res. Symp. Proc., **365**, pp.371-375 (1995)

[24] C.R. Thomas, E.J. Walker, Proceedings 5th Conf. on Industrial Carbon and Graphite, Soc. Cem. Ind. London, **1**, pp. 520-531 (1978)

[25] E. Fitzer, K.H. Geigl, W. Hüttner, Carbon, **18**, pp. 265-270 (1980)

[26] L.M. Manocha, O.P. Bahl, Y.K. Singh, Carbon, **27**, N°3, pp.381-387 (1989)

[27] W. Kowbell, C.H. Shan, Carbon, **28**, N°2/3, pp.287-299 (1990)

[28] L. Pardini, B. McEnaney, dans Extended Abstracts of the 21st Conference on Carbon, American Carbon Society, Buffalo, pp.30-31 (1993)

[29] R.J. Zaldivar, G.S. Rellick, J.M. Yang, J. Mater. Res., **8**, N°3, pp.501-511 (1993)

[30] S. Takano, T. Uruno, T. Kinjo, P. Tlomak, C.P. Ju, Journal of Materials Science, **28** , pp. 5610-5619 (1993)

[31] C. Ahearn, B. Rand, Carbon, **34**, N°2, pp. 239-249 (1996)

[32] S.M. Oh, J.Y. Lee, Carbon, **27**, p.423 (1989)

[33] J. Aveston, G.A. Cooper, and A. Kelly, dans The properties of fiber composites, Conference Proceedings of the National Physical Laboratory, IPC Science and Technology Press, Surrey, England, pp.15-26 (1971)

[34] B. Budiansky, J.W. Hutchinson, A.G. Evans, J. Mech. Phys. Solids, **34**, n°2, pp.167-189 (1986)

[35] D.B. Marshall, Cox, A.G. Evans, Acta Met., **33**, n°11, pp.2013-2021 (1985)

[36] L.N. McCartney, Proc. R. Soc. Lond., A409, pp.329-350 (1987)

[37] A.G. Evans, D.B. Marshall, Acta Met., **37**, n°10, pp.2567-2584 (1989)

[38] D.B. Marshall, A.G. Evans, J. Am. Ceram. Soc., **68**, n°5, pp.225-231 (1985)

[39] J. Lamon, F. Rebillat, J. Am. Ceram. Soc., **78** [2], pp. 401-405 (1995)

[40] J.W. Hutchinson, H.M. Jenson, **9**, pp. 139-163 (1990)

[41] P. Lawrence, J. Mat. Sci., **7**, n°1, pp.1-6 (1972)

[42] D.B. Marshall, Mat. Sci. Res., **21**, Ceramic Microstructures '86: Role of Interfaces, J.A. Pask, A.G. Evans, Plenum Press, New-York-London, pp.859-868 (1986)

[43] K. Hamada, S. Sato, H. Tsunakawa, A. Kohyama, Proceedings of ICCM-10, Whistler, B.C., Canada, August, Vol.VI: Microstructure, Degradation, and Design, pp. 423-430 (1995)

[44] X. Bourrat, B. Trouvat, G. Limousin, G. Vignoles, Pyrocarbon anisotropy as measured by electron diffraction and polarized light, to be submitted in Journal of Materials Research

[45] B. Trouvat, X. Bourrat, R. Naslain, Fibre-matrix bonding in carbon/carbon microcomposites: role of HTT and surface roughness of the fibre, to be submitted in Carbon

[46] J.B. Barr, dans Extended Abstracts and Program of the 21st Biennial conference on carbon, American Carbon Society, June 13-18, Buffalo, pp.118-119 (1993)

[47] G.-A. Lebrun, Comportement thermomécanique et durée de vie de composites à matrice céramique: théorie et expérience, Thèse, Université de Bordeaux I, N° d'ordre:1606, 30 novembre (1996)

[48] W. Ruland, Appl. Symp., **9**, p.285 (1969)

[49] B. Trouvat, X. Bourrat, R. Naslain, Influence of a carbon interphase with a controlled microtexture on the mechanical properties of single fibre C/C/C/ composites, to be submitted in Carbon

[50] E. Yasuda, Y. Tanabe, H. Machino, S. Kimura, 18th Biennal Conference on Carbon (1987) pp.30-31, Tanso (1988) [N°132] 3

[51] B.T. Kelly, Physics of graphite, Applied Science Publishers (1981)

[52] B. Rand, dans Essentials of carbon-carbon composites, C.R. Thomas ed., Royal society of chemistry, pp.67-102 (1993)

[53] B. Trouvat, X. Bourrat, F. Rebillat, G.-A. Lebrun, R. Naslain, Toughening mechanisms in carbon/carbon minicomposites with interface control, to be submitted in Journal of the American Ceramic Society

[54] C.R. Thomas, E.J. Walker, High Temp. High Press.,**10**, pp.79-86 (1978)

[55] R.J. Zaldivar, G.S. Rellick, J.M. Yang, 21st Biennal Conference on Carbon, American Carbon Society, June 13-18, Buffalo pp.52-53 (1993)

ANNEXE 1

Fibre/matrix bonding in carbon/carbon microcomposites role of HTT and surface roughness of the fibre

ANNEXE 1

Fibre/matrix bonding in carbon/carbon microcomposites: role of HTT and surface roughness of the fibre

1 - INTRODUCTION 2

2 - EXPERIMENTAL 4

2.1 - C/C microcomposites preparation 4

2.2 - Mechanical testing 4

2.3 - Structural characterisation 5

3 - RESULTS AND DISCUSSION 7

3.1 - Bare fibres 7

3.1.1 - Mechanical behaviour 7

3.1.2 - Microstructural characterisation 9

3.2 - Carbon/carbon microcomposites 10

3.2.1 - TEM cross-sections 10

3.2.2 - Mechanical behaviour 11

3.2.3 - SEM observations of the fracture surfaces 14

4 - CONCLUSIONS 15

REFERENCES

NOMENCLATURE

Q	gas flow
T	temperature
P	pressure
Ae	extinction angle
d	fibre diameter
F	tensile load
V	volume submitted to the stress
V_f	fibre volume fraction
S_f	fibre section
V_m	matrix volume fraction
S_m	matrix section
E	Young elastic modulus
E_f	fibre Young modulus
E_m	matrix Young modulus
R_m	fracture mirror radius
$\mathcal{A}$	constant relating mirror radius to fibre stress-to-failure
$\sigma_{f,mirror}$	fibre stress-to-failure deduced from mirror radius
ε_R	strain-to-failure
$\varepsilon_{R,f}$	fibre strain-to-failure
$\varepsilon_{R,m}$	matrix strain-to-failure
σ	applied stress
σ_R	stress-to-failure
σ_f	fibre stress-to-failure in the microcomposite such as $\sigma_f = E_f \cdot \varepsilon_R$
σ_f'	fibre stress-to-failure in the microcomposite such as $\sigma_f' = F/S_f$
σ_0	scale parameter in Weibull model
m	Weibull modulus

Fibre/matrix bonding in carbon/carbon microcomposites: role of HTT and surface roughness of the fibre

Submitted in Carbon

B. TROUVAT, X. BOURRAT, and R. NASLAIN

Laboratoire des Composites Thermostructuraux

UMR 47 CNRS-SEP-UBI, Université Bordeaux I

3, allée de la Boëtie, 33600 Pessac, France

SUMMARY

Tensile test on single fibre, or microcomposite, was used to study the interfacial behaviour of carbon/carbon composites (C/C). Two identical HT PAN-based fibres, A and B, but with a different surface roughness, were used as substrates for a pyrocarbon deposit, as well as the same fibres previously treated to high temperature. Tensile mechanical tests and electron microscopy have shown that C/C microcomposites are inverse composites : matrix strain-to-failure is lower than that of the fibre ($\varepsilon_{R,m}<\varepsilon_{R,f}$). Only one matrix crack occurs before failure of the microcomposite when fibre and matrix are characterised by similar strains-to-failure ($\varepsilon_{R,m}\approx 1\%$). Contribution of a physical interaction was shown by the influence of fibre surface roughness on mechanical behaviour. However, this contribution is low compared to those of the chemical bonding, and residual stresses at the interface. Composites made with heat-treated fibres have weak interfaces. Most fracture surfaces exhibit pull-out features, and fibre/matrix debonding by relaxation of residual stresses when samples are prepared for transmission microscopy is observed.

1 - INTRODUCTION

Although carbon/carbon composites have been quite developed and utilised much sooner than other ceramic matrix composites, the lack of understanding of their mechanical behaviour still motivates a lot of studies. Sensitivity of carbon/carbon mechanical properties to interface strength is well known. Most works dealing with this subject have preferred liquid precursor for the carbon matrix [1,7], which permits to modify easily the fibre/matrix bonding by fibre surface treatment and composite graphitization [1,5]. Oxidation was also used to decrease the interface strength of carbon/carbon composites [6]. The aim of all these studies was to change a catastrophic failure (strong fibre/matrix bonding) in a non brittle behaviour with fibre pull-out. Recently, Beindorn et al. reported the positive effect on unidirectional (1D) carbon/carbon composites mechanical properties, of coating fibre with a cured phenolic resin [7], before resin phenolic impregnation for matrix. The fibre/cured resin phenolic bonding is supposed to be stronger than the cured resin/resin phenolic bonding. Otherwise, interfacial sliding strength in 1D C/C composites has been investigated by Hamada et al. [8] with a microindentation test technique. The aim of the following work was to study the interfacial properties of carbon/carbon composites.

For that purpose the single fibre mechanical test specimen was used. It is known as "microcomposite" test. Very few works dealt with such carbon coated carbon fibres in literature [9,10]. First, Butler et al. [9] have used these model materials for checking the application of the rule of mixture. However, they did not study their mechanical behaviour (tensile tests stopped before failure). More recently, Schinazi and Diefendorf [10] have investigated the mechanical behaviour of T-1000 carbon fibres coated with pyrolytic carbon. They show a non brittle failure with matrix failure occurring first. Conversely, the microcomposite approachs has been extensively used in other systems (e.g.: ceramic fibres reinforced silicon carbide) and with various types of interlayers

such as boron nitride or carbon [11]. More recently it has been recognised as a very efficient way to test and improve new interfacial materials as multilayers [12] or boron-doped pyrocarbon interfaces [13]. With the recent development of TEM sampling preparations, longitudinal sections of microcomposites (silicon carbide reinforced silicon carbide) were observed by TEM in high resolution [13]. The interfacial microstructure and its chemical analysis (EELS) are now accessible. It is of prime interest for the analysis of the micromechanical fracture processes: when performed on specimen loaded to failure, it is possible to relate directly the stress-strain curve and the mechanical performances with the damaging mode : debonding, matrix cracks deflection, etc. [12,13].

In no case, microcomposite does simulate the whole 3D composite, but microcomposite is very efficient to assess rapidly the relationship between the nano-structure and the mechanical behaviour of the composite interface.

A HT (High Tensile) PAN-based carbon fibre was used in this study. CVD (Chemical Vapour Deposition) pyrocarbon matrix was preferred for its reproducibility. Tensile tests were conducted on the bare fibre as well as on the corresponding microcomposites. Fibre surface state, fibre annealing as well as relevant processing conditions controlling the interfacial behaviours were addressed.

A companion paper [14] emphasises the improvement obtained by intercalating a carbon interphase in-between the fibre and the matrix, and controlling its microtexture (carbon/interphase/carbon).

Table 1. Pyrocarbon matrix characteristics

Experimental conditions				Deposit rate	Extinction angle Ae	Microtexture
Gas	Q (sccm)	T (°C)	P (kPa)	(μm/h)	(°)	
C_3H_8	2500	1000	2	0.23	17	Smooth Laminar

2 - EXPERIMENTAL

2.1 - C/C microcomposites preparation

Same HT PAN-based carbon fibres[1], with a different surface state, referred to as A and B, were used. A rougher surface characterised B fibre. Some fibres were subjected to a final heat treatment up to a temperature T1 (HTT) or T2 (HTT2), with T2 higher than T1, and T1 higher than fibre processing temperature. These fibres are referred to respectively as A-HTT, B-HTT, and A-HTT2, B-HTT2. Microcomposites (Fibre/M), consisting of a single fibre in a pyrocarbon sheath, were made with above types of carbon fibres, except A-HTT2, and B-HTT2 fibres. For that purpose, fibres were mounted on a carbon frame made of Papiex®[2]. Pyrocarbon was deposited in a CVD/CVI furnace, using constant pressure and temperature, with propane as hydrocarbon precursor (Table 1).

2.2 - Mechanical testing

For tensile testing, a microtensile device was used [15]. It consists of a 0-2N load cell, and a straining device[3], driven at constant speed (1%/min) with a d.c. motor. Tensile properties were measured at 10mm gauge length (paper frame). For each sample a set of 15 to 20 specimens was prepared and tested in order to get a statistical population.

Weibull statistics (weakest link model) were used to analyse the failure of these brittle materials. This approach is the most common technique employed for carbon fibres. The failure probability is expressed as follows:

---

[1] from SEP, Le Haillan, France

[2] Papiex: graphite sheet from Le Carbone Lorraine, France

[3] model UT 100CC, from Microcontrole

$$P = 1 - exp\left(-\frac{V}{V_0}\left(\frac{\sigma - \sigma_u}{\sigma_0} \right)^m \right) \quad \text{for stresses} \qquad (1)$$

where

V: volume submitted to the stress, V_0 a reference volume (V_0=1m^3)

σ: applied stress

σ_u: value of stress below which P is zero

σ_0: scale parameter (in stress unit)

m: Weibull modulus which characterises the scatter in strength; slope of the plot lnln(1/(1-P)) against ln(σ)

with the failure probability estimator taken as $P = \frac{i - 0,5}{N}$ where N is the number of tested specimens. In this study, σ_u was assumed to be zero.

As already mentioned by other authors for carbon fibres [16,17], stiffening under load was also identified for carbon fibres with the non-linear concave-up strength-strain curve. Different values could be measured corresponding to the initial, final and tangent moduli. Only tangent modulus was taken into account in this study.

2.3 - Structural characterisation

Optical measurement was used to characterise pyrocarbon texture by measuring the extinction angle, Ae, on polished cross-sections of microcomposites [18]. This measurement is achieved with cross polars by rotating the analyser of the microscope as for a compensator. The larger the angle Ae, the higher the anisotropy. This technique has been adopted by the laboratory to characterise pyrocarbon. The classification, for low pressure and low temperature pyrocarbons, for the optical microscope[1] used is the following: the extinction angle Ae ranges from 0 to 4° for isotropic pyrocarbon, from 4 to 12° for dark-laminar, from 12 to 18° for smooth laminar, and finally 18° and

[1] MeF_3 Reichert-Jung microscope

more for rough laminar pyrocarbon. Matrix was then identified as smooth laminar pyrocarbon (Table 1).

A scanning tunnelling microscope (STM)[1] was used to study the surface morphology of A-HTT2 and B-HTT2 fibres[2]. The measurement parameters were bias voltage 89mV and setpoint current 0.6nA. A platinum/iridium tunnelling tip was used.

TEM preparation: Some microcomposites were close-packed with an epoxy bond (M-610)[3]. After the resin was cured (2h-160°C), the fibres were embedded in alumina cement, and heat treated. Thin transverse sections (700µm) of the sample were cut with a diamond saw[4], and 3-mm diameter specimens were drilled from these slices with microcomposites in the centre (figure 1.a). The discs were mechanically thinned to approximately 80µm with a 3µm finish on one face. An impregnation with M-610 was then done on one face, the resin was cured, and this face was polished. Samples were dimpled with a bare steel wheel with 3µm diamond paste to a thickness of about 30µm. The samples were then ion milled[5] (7kV/1mA-6kV/0,8mA) at liquid-nitrogen temperature and low angle (13°-12°). This method allows coated fibres to be thinned from centre of fibres (figure 1.b). If not, pyrocarbon is first attacked by ion beam and cliff-like thinning takes place. In this case, neither pyrocarbon nor interface regions can be observed by means of lattice-fringes technique (002 LF). The close-packing of fibres is one of the key points which avoids this phenomenon. A low thickness, before ion milling, is the other one but not the least, to obtain a good thinning behaviour of fibres. However, as alumina thins

---

[1] Nanoscope II STM manufactured by Digital Instruments of Santa Barbara, CA

[2] with the collaboration of H. Saadoui, J.C. Roux, and S. Flandrois, Centre de Recherche Paul Pascal, Pessac, France

[3] M-610 from M-line accessories, Measurements group, inc.

[4] Escil, Switzerland

[5] Dual ion mill, Gatan, model 600 Pleasanlon, CA

at a faster rate than carbon, although slower than resin, the probability for fibres to collapse is very high. This last problem was solved by the M-610 impregnation of the thinned discs, which hardens alumina.
TEM preparations were observed with a high voltage microscope[1] (300kV).

Scanning Electron Microscopy (SEM)[2] was used to observe microcomposite fracture surfaces, obtained by collecting the broken ends after tensile tests. Carbon-carbon microcomposites smashed to fragments on failure due to vibrations caused by the initial fracture, as do carbon fibres. To recover the fracture surface, paraffin oil was used on samples, but it remained difficult to collect them. So, only few fracture surfaces could be examined by SEM.

3 - RESULTS AND DISCUSSION

3.1 - Bare fibres

3.1.1 - Mechanical behaviour

Mechanical properties of the different carbon fibres under study are listed in Table 2.

For these HT PAN-based carbon fibres, Young modulus increases with HTT, whereas stress- and strain-to-failure tend to decrease. The alignment of carbon planes along the fibre axis with temperature is well known and involves the increase of Young modulus. Heat treatment also removes nitrogen atoms, remaining in PAN-based carbon fibres after processing. Decrease in stress could then be explained by the evolution of nitrogen atoms, which creates defects in fibre structure [19]. For HTT2, another phenomenon can take place:

---

[1] CM-30 ST Philips microscope

[2] using a JEOL JSM-840A microscope, and a HITACHI S-4500 microscope equipped with a field emission gun

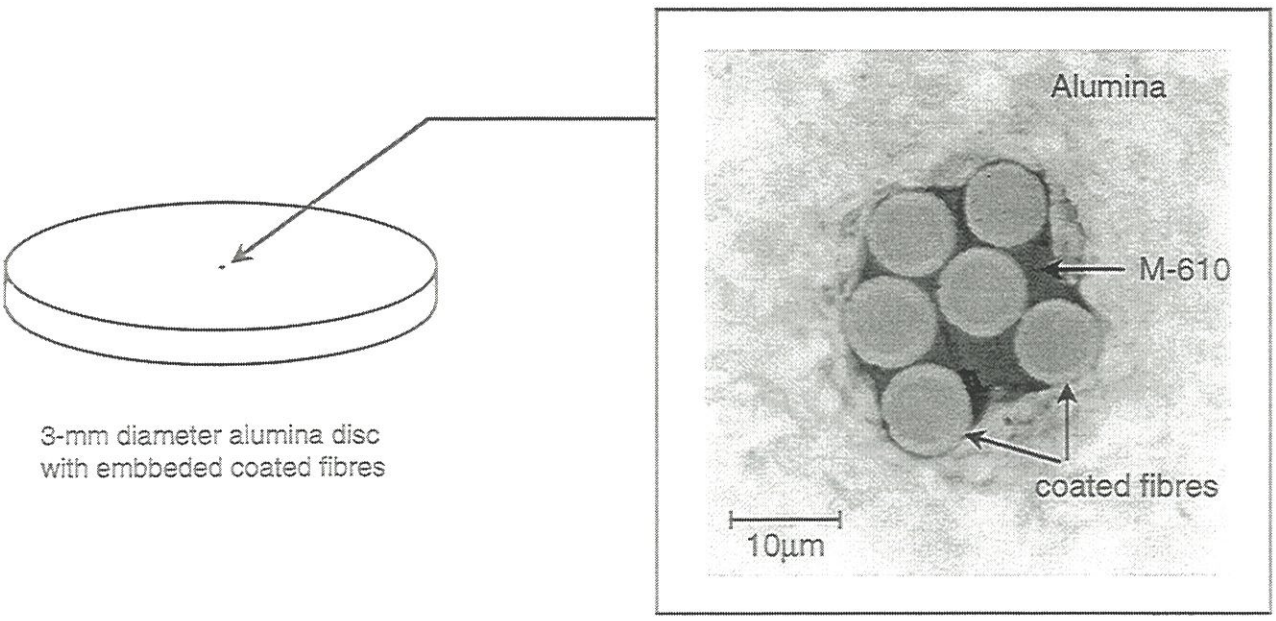

a - Embedding of samples in alumina-based cement
(inset: optical microscopy on polished section)

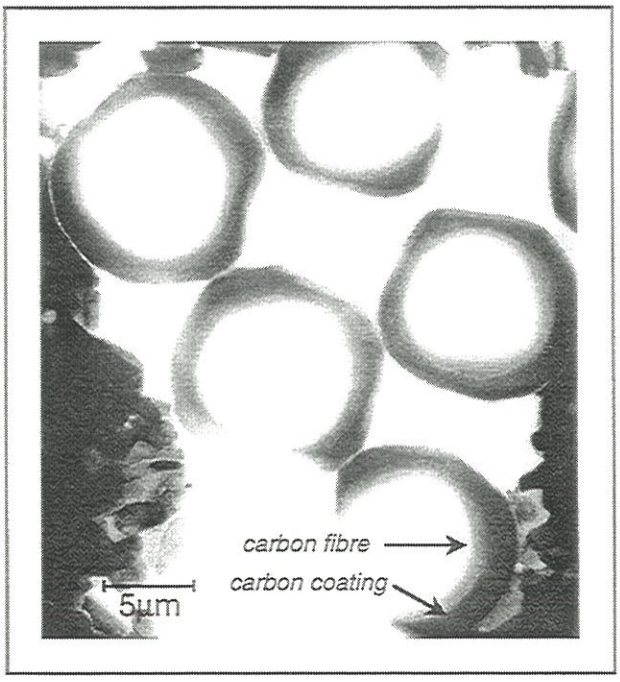

b - TEM preparation after ion-milling
(TEM low magnification)

Figure 1: TEM sample preparation

Table 2. Mechanical data for HT PAN-based fibres

	d (μm)	E (GPa)	ε_R (%)	σ_R (MPa)
A	6.9	255	1.58	3992
	(0.3)*	(36)	(0.22)	(630)
A-HTT	6.7	316	1.27	3995
	(0.3)	(34)	(0.24)	(889)
A-HTT2	6.5	398	0.84	3336
	(0.3)	(13)	(0.13)	(471)
B	6.7	247	1.44	3538
	(0.3)	(28)	(0.29)	(742)
B-HTT	6.7	336	0.78	2630
	(0.4)	(30)	(0.18)	(633)
B-HTT2	6.5	412	0.64	2607
	(0.2)	(17)	(0.19)	(732)

* standard deviation in brackets

N.B.:
A-HTT, B-HTT: A and B fibres heat-treated to T_1
A-HTT2, B-HTT2: A and B fibres heat-treated to T_2 ($T_2 > T_1$)
gauge length: 10mm

Table 3. Results of Weibull analysis for fibres

	m	σ_0 (MPa)
A	7.7	1469
A-HTT	5.7	1007
A-HTT2	8.3	1390
B	5.6	972
B-HTT	4.6	545
B-HTT2	4.4	440

Table 4. Mechanical results for fibres treated under deposit pyrocarbon conditions

	d (μm)	E (GPa)	ε_R (%)	σ_R (MPa)
A	6.7	252	1.16	2929
	(0.3)*	(8)	(0.17)	(459)
A-HTT	6.7	317	1.12	3569
	(0.3)	(14)	(0.17)	(597)

* standard deviation in brackets

boiling of inorganic inclusions [20], which leads to bubbles in fibres. In this case, the defect remains but changes in nature.

Stress- and strain-to-failure of B fibre are lightly lower than those of A fibre, whereas Young modulus remains unchanged. Difference is more pronounced if a final heat treatment is performed. Lower stresses-to-failure, associated to higher defect sizes, might be involved by the rougher surface of B-based fibres.

Weibull statistics were applied to carbon fibres. Weibull parameters are listed in Table 3. These results can be compared with results from the literature related to PAN-based carbon fibres. For example, Moreton [21] reported that heat treatment affects the strength, but not the type nor the distribution of defects. More recently, Tanabe et al. [22] have shown that there is no effect of HTT on the Weibull distribution of failure stresses for PAN-based T-300 fibre, which is not the case for pitch-based carbon fibres. They found for the T-300 fibre heat-treated to 1500, 2000, and 2500°C, Weibull moduli respectively equal to 6.0, 7.6, and 6.0. Similar results were obtained in this work for A-HTT and A-HTT2 fibres. However, B-based fibres have lower Weibull moduli, or, in other words, a higher scattering in strength.

In order to compare bare and coated fibres, it was first necessary to check that no fibre degradation actually takes place during microcomposite processing at a temperature of ≈1000°C. For verification, treatments of A and A-HTT fibres were conducted under conditions as close as those for pyrocarbon deposit: same temperature, pressure, and experiment duration (8 hours). It is to note however that this test does not respect the partial pressure of hydrocarbons. As soon as the first coating layers are deposited on the fibre, fibre is protected. So, 8 hours under low pressure (2kPa) appears very severe. As a matter of fact, results have shown (Table 4) that A fibre might be degraded by a so long exposure to very low pressure even at 1000°C, and in a less extent so would A-HTT fibre. Young modulus remained unchanged, but stress-, and so

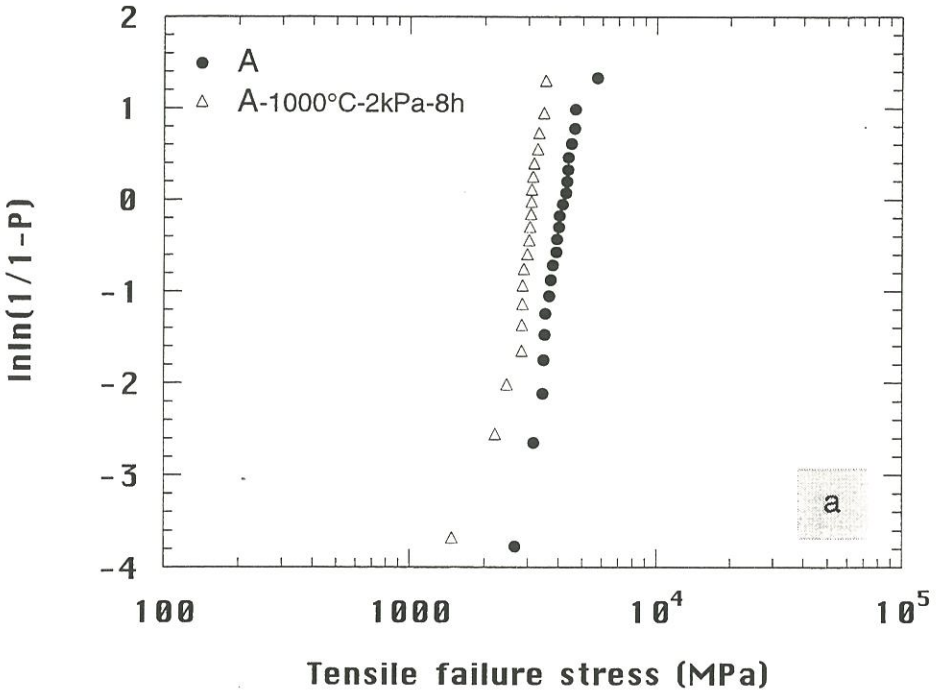

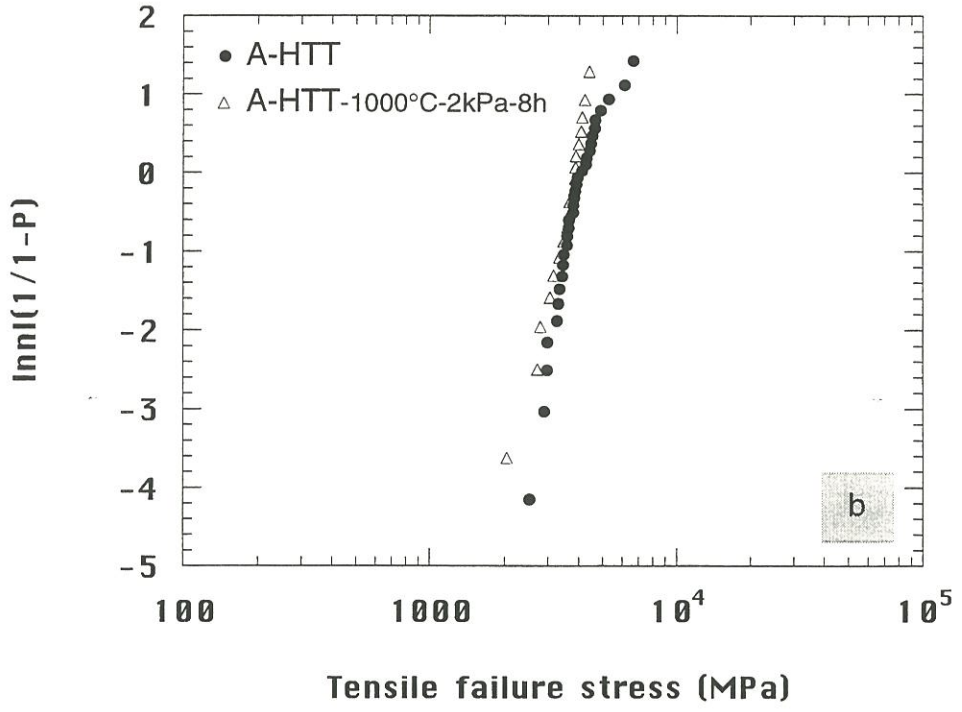

Figure 2: Weibull plots for (a) A and (b) A-HTT and same fibres treated under conditions close to those used for pyrocarbon deposition

strain-to-failure might decrease. This degradation could be due to an extra evolution of nitrogen atoms. Weibull plots (figure 2) evidence the decrease in strength of A fibres compare to A-HTT fibres. However, strength distribution is not affected by the 1000°C-2kPa-8h treatment.

3.1.2 - Microstructural characterisation

Fibre surface analysis

SEM observations have revealed the spinning-related striations along the fibre axis, but did not show any difference in surface topography between A- and B-based fibres (figure 3), as could be expected for heat-treated fibres considering mechanical properties. A surface study at greater scale was needed.

Views of surface morphology of A-HTT2 and B-HTT2 at nanometer scale were made with a STM microscope. Some STM studies of PAN-based fibres surface are available in literature [23,24]. STM micrographs of A-HTT2 (figure 4) and B-HTT2 (figure 5) fibres suggest that B-HTT2 fibre have a more fractured surface: a more marked roughness was observed at short range. However, a more statistical study of fibres would be necessary to know features representative of fibre surfaces. The lower mechanical properties (ε_R, σ_R) obtained for B-HTT2 fibre, compared to A-HTT2 fibre ones, could then be explained by an increase of surface defects. It is assumed to be the same for B-HTT, and may be for B fibre.

SEM fracture surface analysis

Fractured surfaces, examined by SEM, reveal mirror patterns (figure 6) as for SiC fibres. Barr [25] also reported the existence of mirror-mist-hackle features (figure 7) on carbon fibre fracture surface. These features are created by the crack propagation through the fibre. The mirror is smooth, whereas mist and hackle regions are characterised by an increasing roughness. It is worthy of note that such a fracture shows that carbon fibre fails at defects

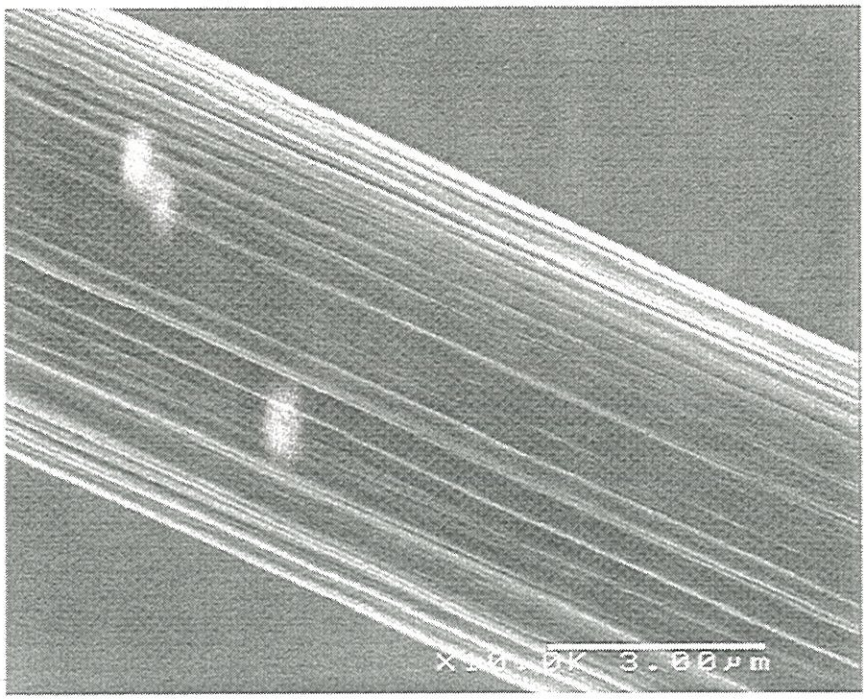

(a)

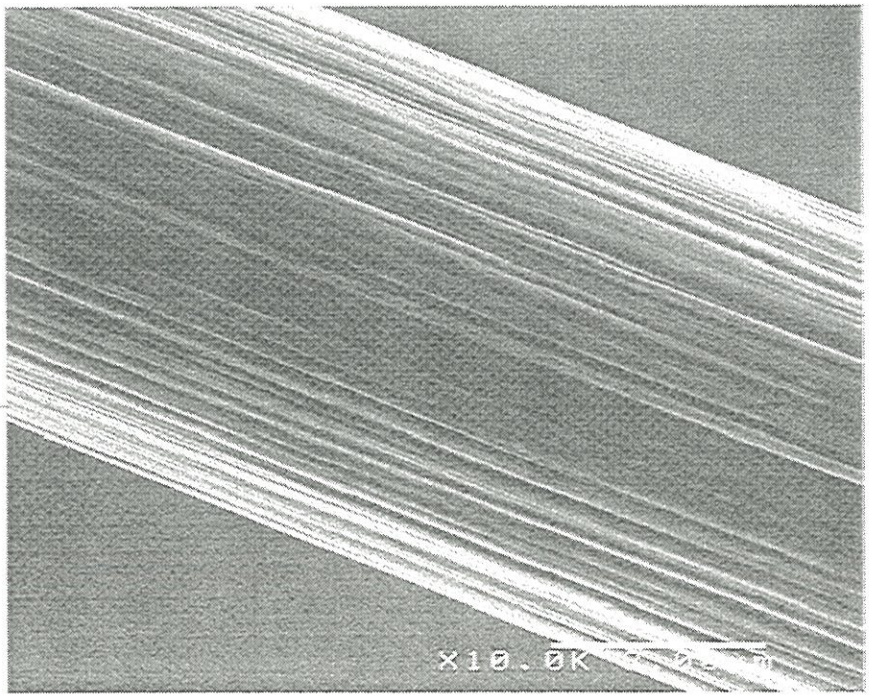

(b)

Figure 3: SEM micrographs of suface of fibres heat-treated to temperature T2
(a) A-HTT2 and (b) B-HTT2 fibres

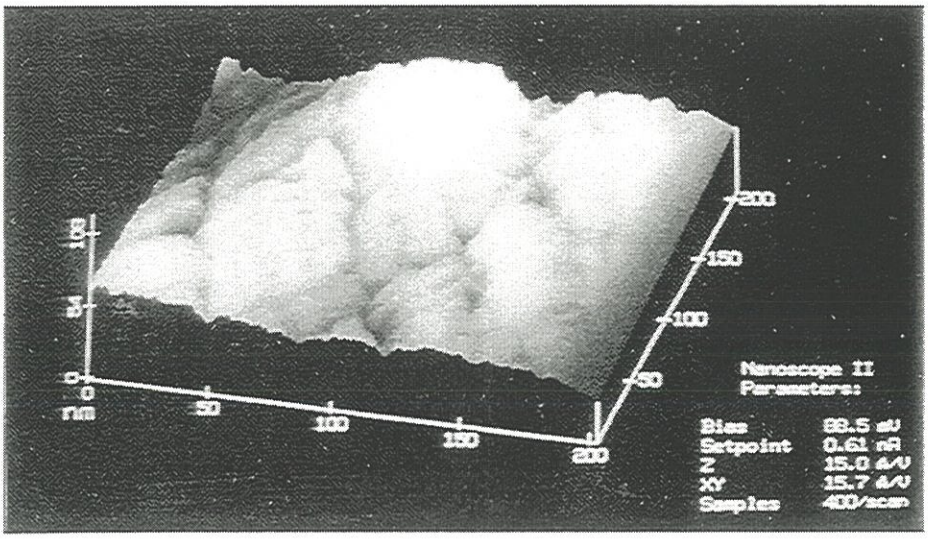

Figure 4: STM micrograph of A-HTT2 fibre
(200x200nm)

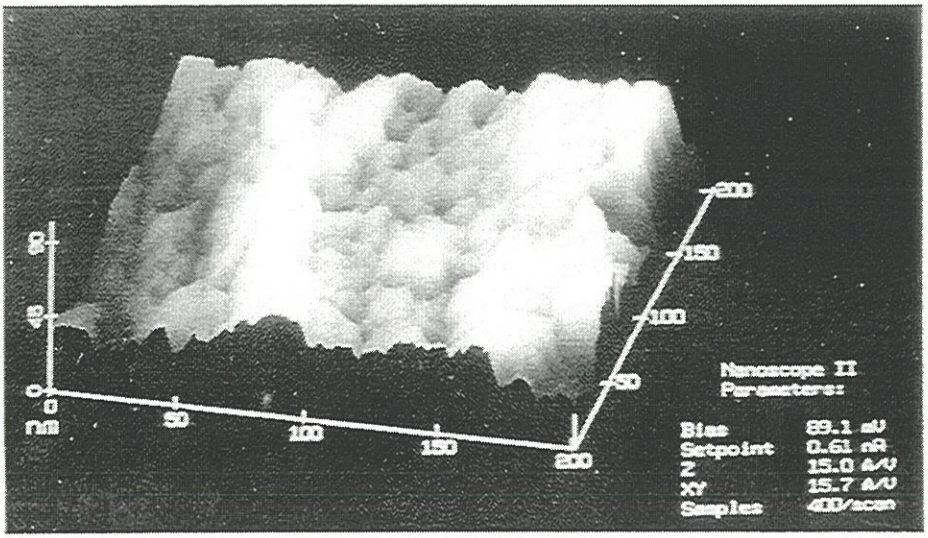

Figure 5: STM micrograph of B-HTT2 fibre
(200x200nm)

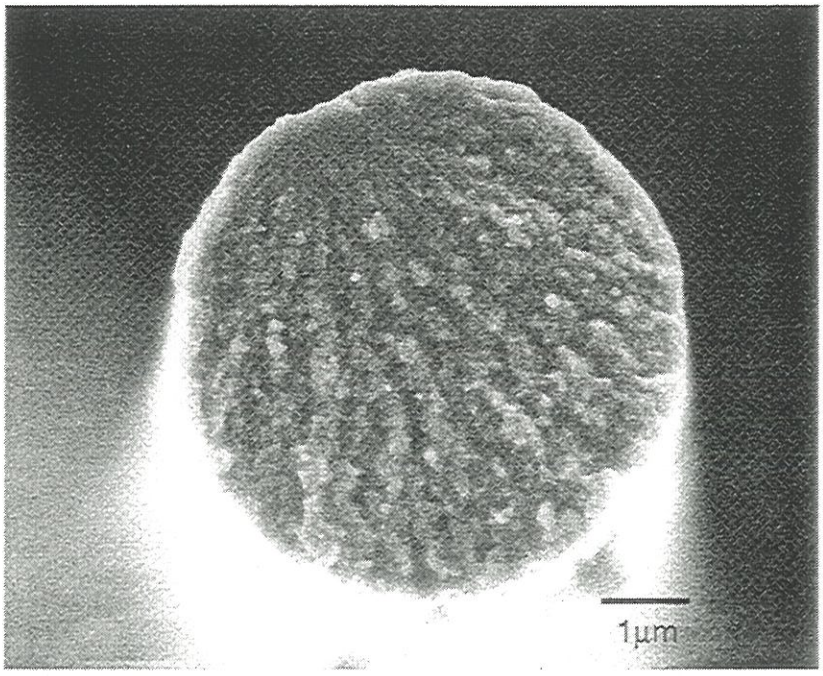

Figure 6: Mirror pattern on A-HTT fibre failure surface

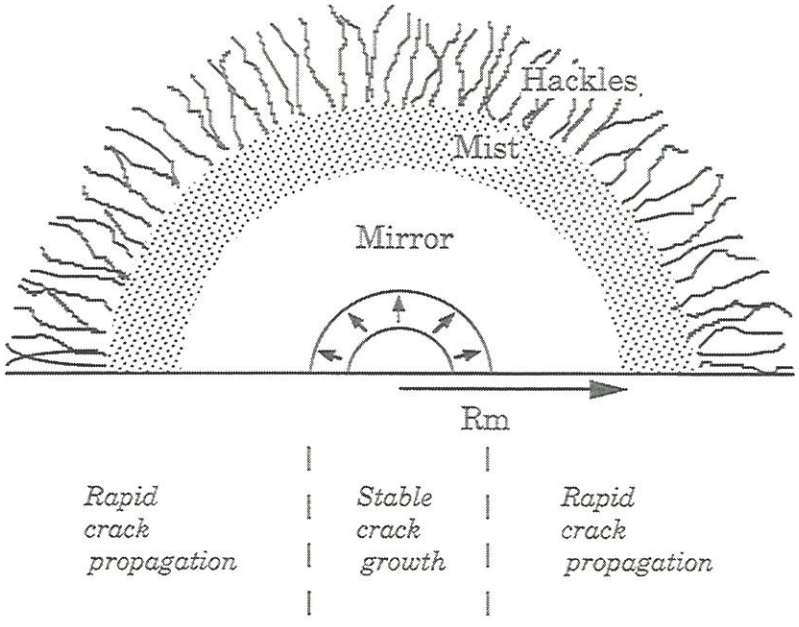

Figure 7: fracture surface of a brittle material (schematic)

which can be actually identified. Boundaries between the different regions were difficult to locate, which can lead to mirror measurement errors. It has been established that square root of the mirror radius (R_m) is inversely proportional to the fracture stress (σ) [26,27] according to the relation:

$$\sigma = \frac{\mathcal{A}}{\sqrt{R_m}} \qquad (2)$$

The constant, $\mathcal{A}$, was estimated from the plot σ against $R_m^{-1/2}$, the values of σ being assessed from tensile tests on monofilamentary samples (gauge length: 10mm). For A fibres, $\mathcal{A}$ is 2.6MPa.m$^{1/2}$ (figure 8.a), and for A-HTT fibres, $\mathcal{A}$ is 2.2MPa.m$^{1/2}$ (figure 8.b). These values are similar to, or of same order than, the mirror constant for SiC fibre (2-3.5MPa.m$^{1/2}$) [28] and T-300 fibre (1.7MPa.m$^{1/2}$) respectively [25].

3.2 - Carbon/carbon microcomposites

3.2.1 - TEM cross-sections

During the thinning of TEM samples, residual stresses are released if the interlaminar shear strength is not too high. This is clearly visible in figure 9 obtained after polishing the thin foil just before the ion-milling stage. In this case, B-HTT/M exhibits fibre axial shrinkage (arrows). This means that the fibre acquires axial tensile residual stress while cooling down after the CVD process. Matrix is therefore in axial compression.

Transverse coefficient of thermal expansion (CTE) mismatch can occur as well. TEM thin foil preparation can helpfully evidence those residual stresses in the same fashion. If interfacial debonding occurs during thinning, it means that tensile transverse residual stress was present across the

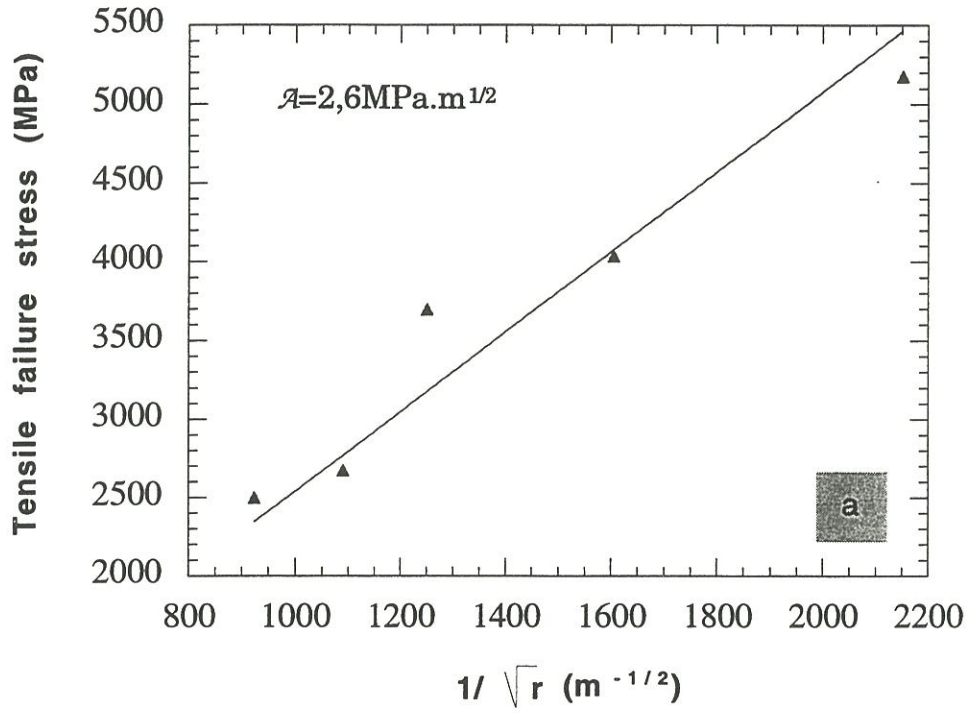

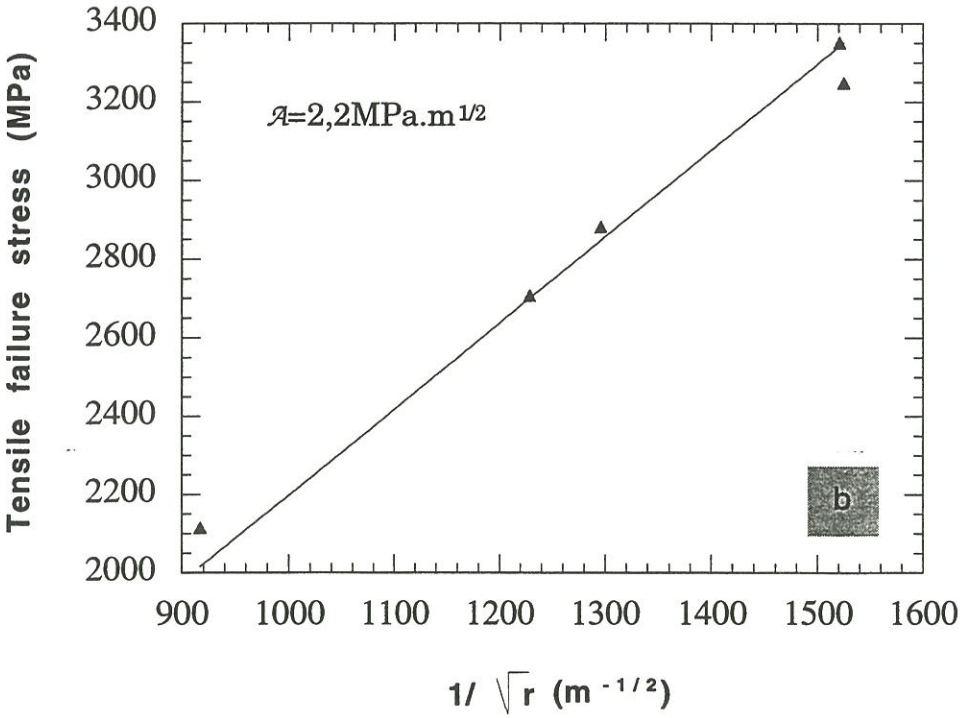

Figure 8: determination of constant A from mirror radii observed on (a) A and (b) A-HTT fibres

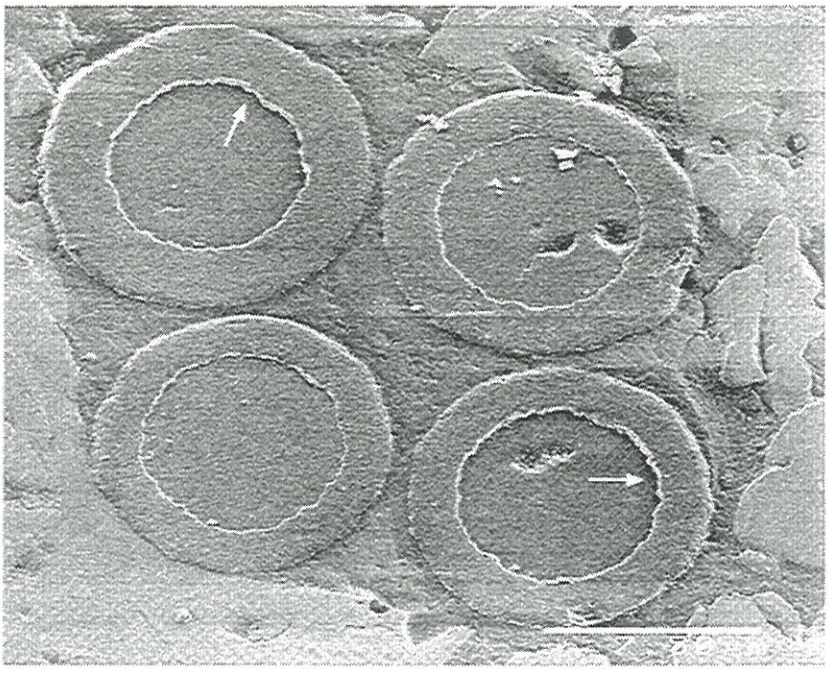

Figure 9: SEM observation of the thin foil of B-HTT/M TEM sample before the ion-milling
(arrows: fibre shrinkage)

interface[1]. It also supposes that no strong chemical bonding balances that lateral shrinkage. Figure 10a and b show two different sets of microcomposites as seen by contrasted bright field TEM at low magnification. A/M (figure 10.a) presents practically no debonding, whereas A-HTT/M interfaces (figure 10.b) are systematically debonded.

Lattice fringes images of A/M interface show a strong bonding (figure 11). A thick sheath of highly oriented carbon is sometimes described onto fibre surface in literature. In the microcomposite obtained in this work this effect is limited to the very first nanometers. The high magnification of A-HTT/M interface shows the debonded interface: adhesive failure at the fibre surface (figure 12).

A-HTT/M interface is thereafter weaker. HTT involves carbon planes alignment along fibre axis, and thus a higher transverse CTE. For A fibre, shrinkage is not so important, and/or the fibre/matrix chemical bonding is stronger.

3.2.2 - Mechanical behaviour

Load-strain curves.

Two types of tensile curves were observed.

- The first one is similar to a bare fibre curve. It is represented in figure 13. Microcomposites with such a tensile behaviour are linear elastic. As for carbon fibres, stress stiffening is clearly seen in the case of carbon/carbon microcomposites.

---

[1] It must be said that sometimes, interfacial debonding can be produced by ion-milling, which can amorphise the interface, and then creates holes (artefact). HR-SEM was used, before ion-milling the sample, to verify that the debonding is pre-existing. So it can be safely asserted that debonding, as observed by TEM, in these sampling conditions does represent tensile residual stresses.

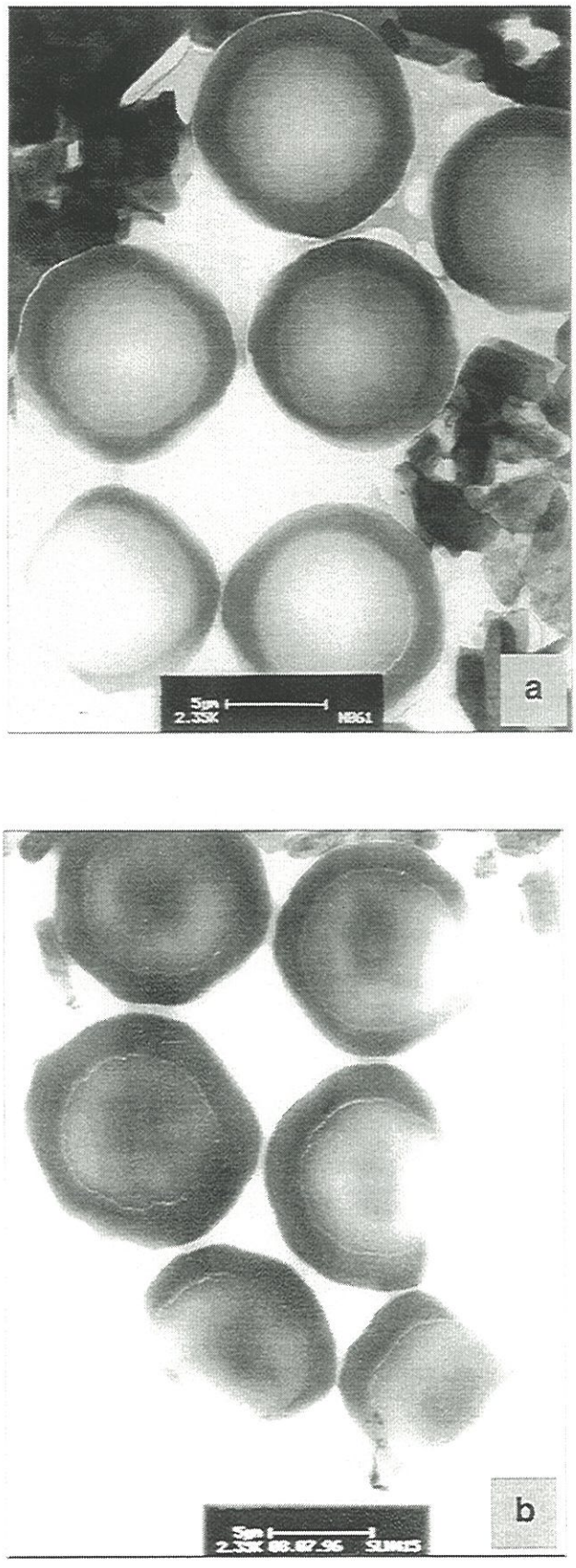

Figure 10: bright field TEM images of
(a)A/M and (b) A-HTT/M

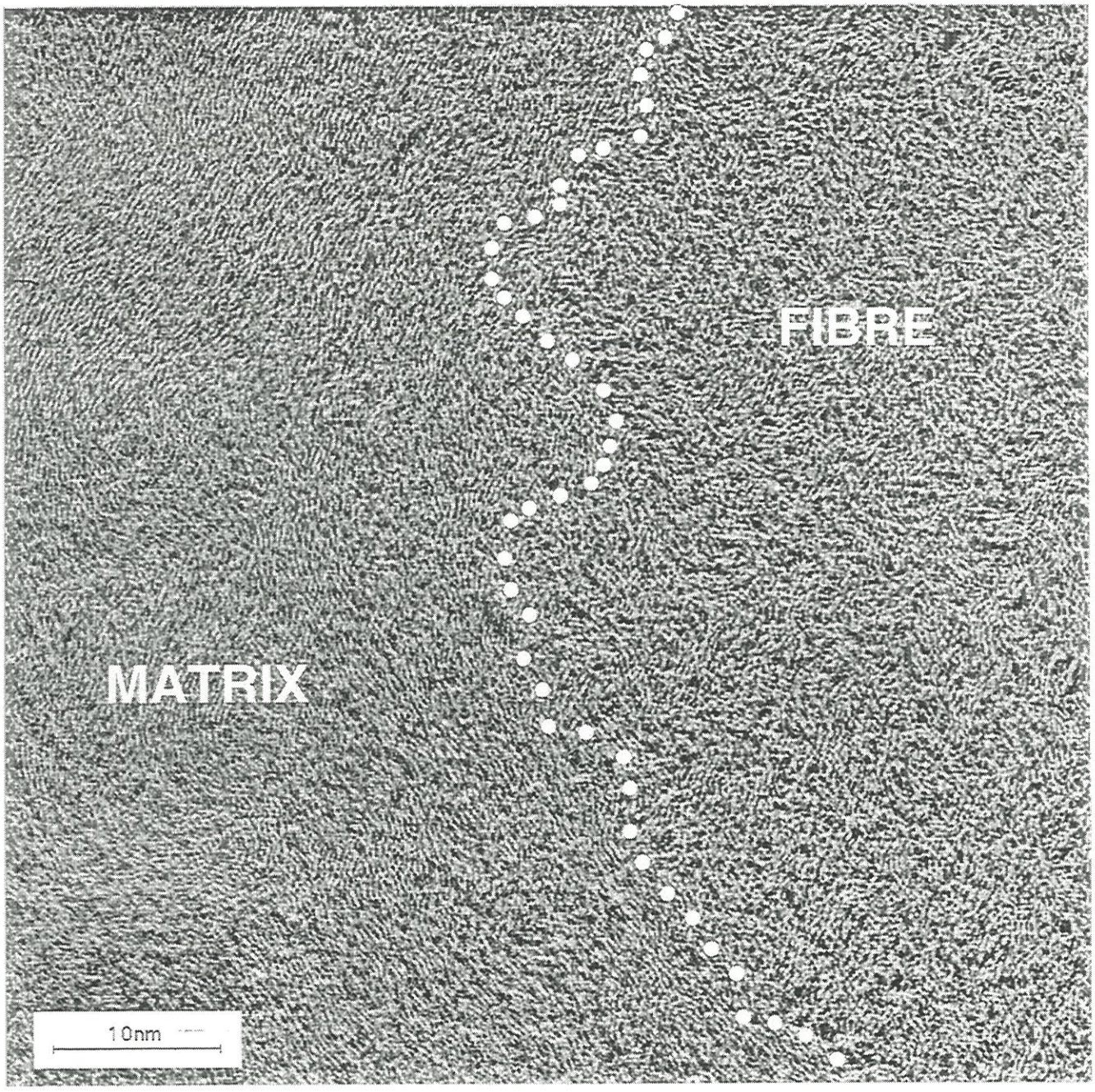

Figure 11: high-resolution image of A/M interface

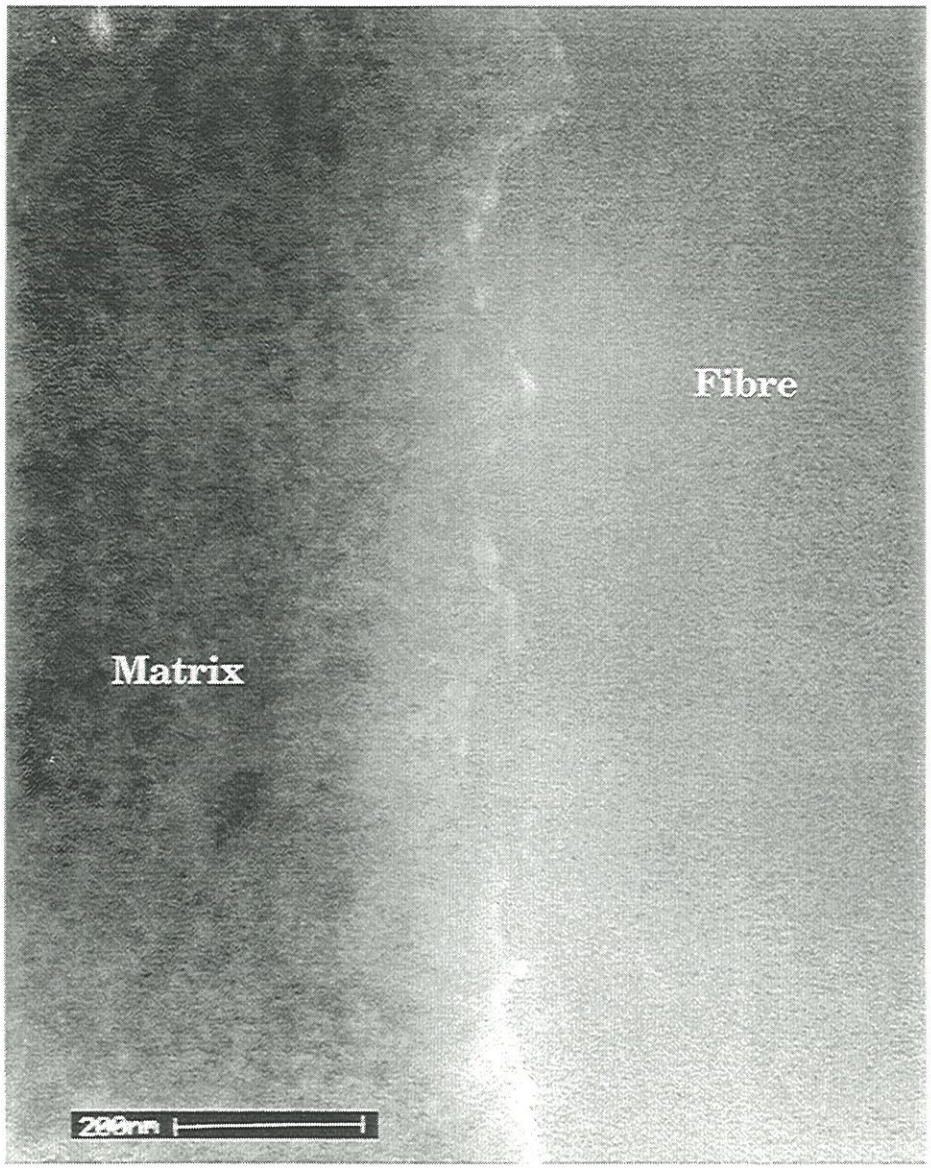

Figure 12: bright field TEM image of A-HTT/M interface

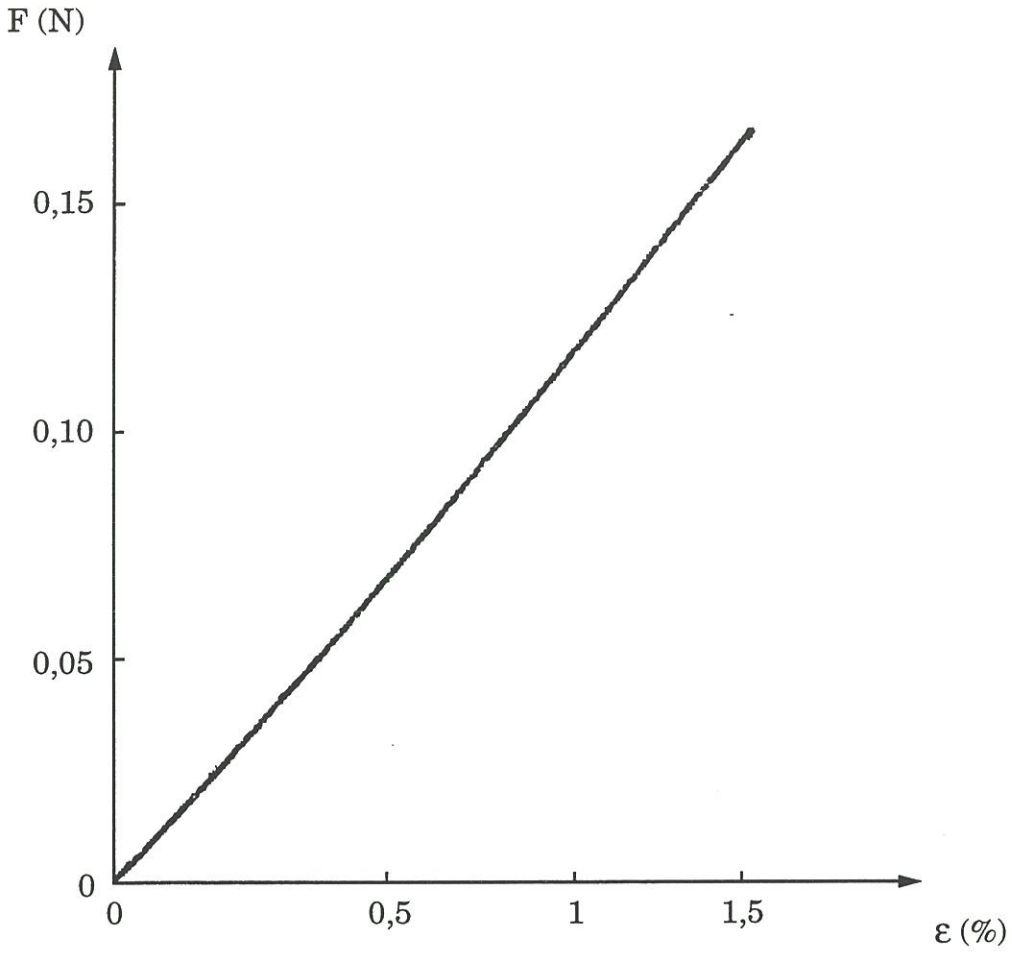

Figure 13: linear tensile load-strain curve
of a C/C microcomposite

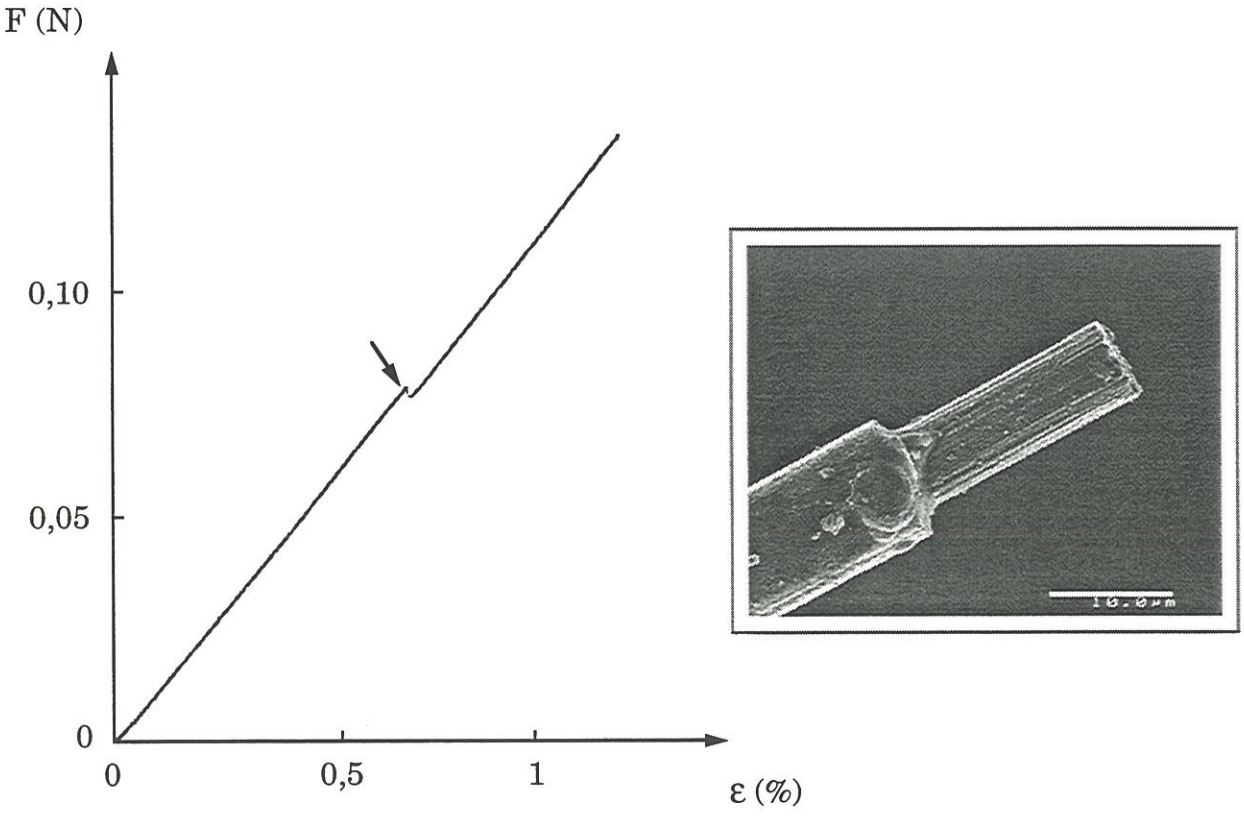

Figure 14: example of tensile load-strain curve with singularity (arrow)
of a C/C microcomposite, and associated fracture surface

- The second type of curves exhibits singularities (arrow in figure 14), which are, most of the time, not associated to a significant change in curve slope. These singularities denote a strength fall, and suggest a probable failure of the matrix.

The 4 sets of microcomposites, prepared with the same matrix and A,B, A-HTT, and B-HTT fibres, present a higher and higher frequency of tensile curves with singularities in the following order :

$$B\ (30\%) < A\ (50\%) < B\text{-}HTT\ (60\%) < A\text{-}HTT\ (\approx 100\%)$$

Thus, fibre heat-treatment leads to a non-brittle behaviour, whereas the increase of fibre surface roughness tends to favour brittle behaviour.

Fibre strength and strain utilisation.

As shown in Table 5, microcomposites tensile properties can be compared to those for the bare fibres (Table 2).

First, fibre controls the ultimate performances of the microcomposite. Strain-to-failure of microcomposites (ε_R), reinforced with heat-treated fibres, is lower than strain-to-failure of microcomposites with A and B fibres. It is the same for the stress-to-failure (σ_R) obtained for A/M and A-HTT/M, higher than the stress-to-failure which characterises B/M and B-HTT/M respectively. The same trend as observed for fibres was evidenced for microcomposites.

Secondly, one noticeable exception was seen for B-HTT fibre: B-HTT/M strain-to-failure is higher than that of the bare fibre (B-HTT), but remains inferior to B fibre strain. Two different reasons can bring about the same effect: healing of fibre surface defects, or a possible axial fibre compression in the material.

Third, for all other microcomposites strain-to-failure is lower than that of the fibre. This is likely related to a fibre residual tension in the microcomposite.

Finally, one particularity of A/M microcomposites is the existence of two (ε_R, σ_R) populations. It involves two different failure strength distributions in

Weibull plot (figure 15.a). Average characteristics of these populations are the following: ε_R=1.45%, σ_R=2400MPa, and ε_R=1.10%, σ_R=1600MPa.

Matrix mechanical properties

Matrix modulus (E_m) can be estimated by the rule of mixture relationship assuming a perfect fibre-matrix bonding:

$$E_C = (E_f.V_f) + (E_m.V_m) \quad (3)$$

where V_f and V_m are the fibre and matrix volume fractions. When Poisson's ratios are the same, this equality is strictly verified. The calculated value of E_m is given for each carbon/carbon materials (Table 5). Values are more confident for B (or A) than for A-HTT (or B-HTT) because a stronger fibre/matrix bonding strength better fulfils the conditions. However, a more accurate determination of E_m was obtained by using the slope of the curve $E.V_f=f(V_m/V_f)$ for different pyrocarbon thicknesses. This way, a matrix modulus of 70 GPa was obtained for different B/M materials (figure 16.a). This value is much higher than those from the literature: 30GPa for high temperature pyrocarbons [29,30], or 35GPa for a smooth laminar [9].

More information on matrix was obtained by tensile testing a A-HTT/M microcomposite, for which fibre contribution was low (V_m=96%) (Table 5). Microcomposite Young modulus is 62GPa, giving E_m=53GPa (eqn 2), assuming a perfect fibre-matrix bonding. It is consistent with the above results. Otherwise, as microcomposite failure is controlled by matrix, strain-to-failure for matrix was estimated to ε_R=1.1%. This value is higher than those usually attributed to low temperature pyrocarbons (0.3%-0.5%). High strains-to-failure up to 2% were only reported for highly graphitised CVD deposits [31]. Weibull statistics were applied to this brittle material (figure 16.b). It gave a Weibull modulus lower than for bare fibres alone (m=4).

Table 5. Mechanical data for carbon/carbon microcomposites

	V_f (%)	E (GPa)	ε_R (%)	σ_R (MPa)	σ_m (MPa)	σ_f (MPa)	σ_f' (MPa)	E_m (GPa)
A/M	45	157 (13)*	1.26 (0.20)	1978 (415)	995	3204	4623	79
B/M	45	158 (12)	1.05 (0.15)	1663 (309)	952	2600	3897	83
A-HTT/M	43	176 (14)	1.15 (0.19)	2031 (432)	636	3626	4304	52
B-HTT/M	45	174 (14)	0.96 (0.20)	1667 (376)	425	3226	3667	49
A-HTT/M	4	62 (6)	1.11 (0.34)	702 (201)	599	3520	19914	53

* standard deviation in brackets

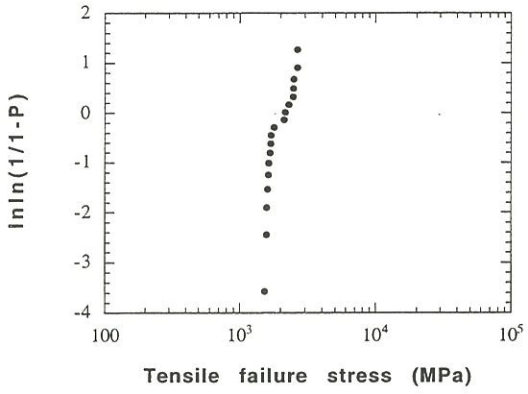

(a) A/M

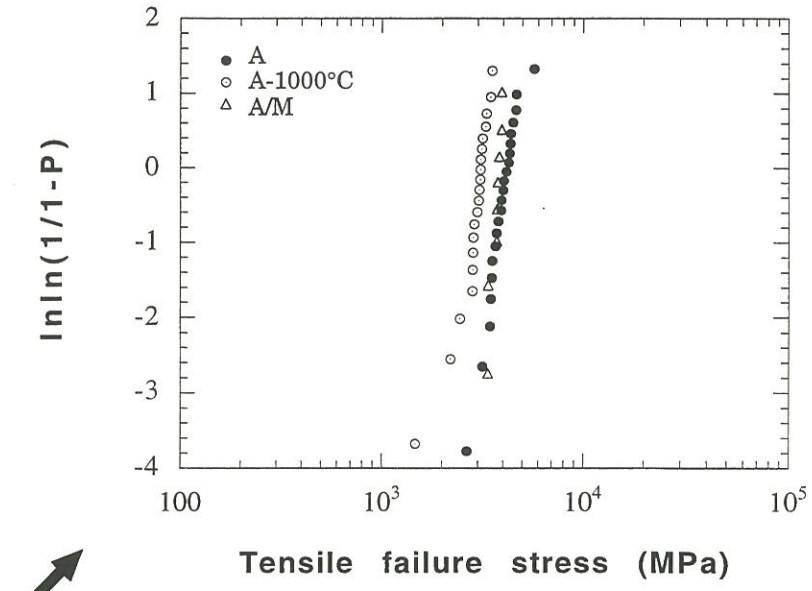

(b) High population σ_R of A/M
(brittle facture, $\sigma_f = E_f.\varepsilon_c$)

(c) Low population σ_R of A/M
(fibre pull-out, $\sigma_f' = F/S_f$)

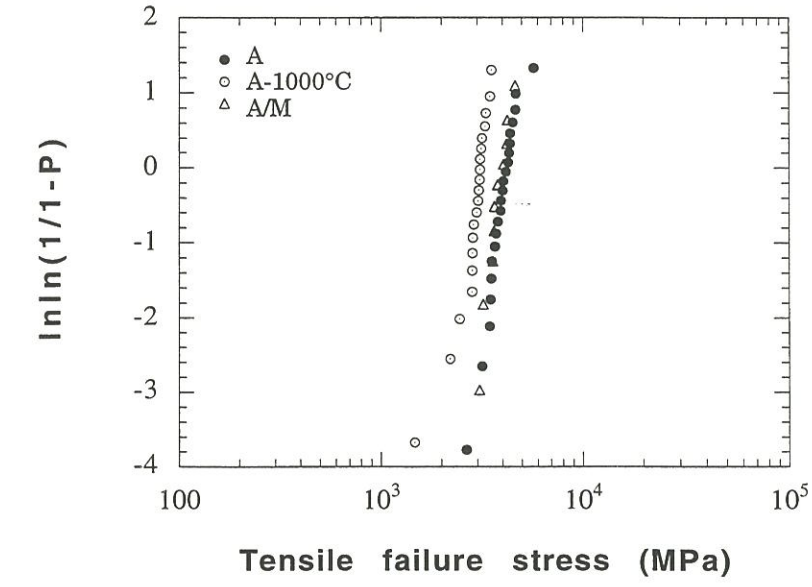

Figure 15: Weibull plots applied to (a) A/M, and to the two populations observed for A/M in (a): (b) high and (c) low population

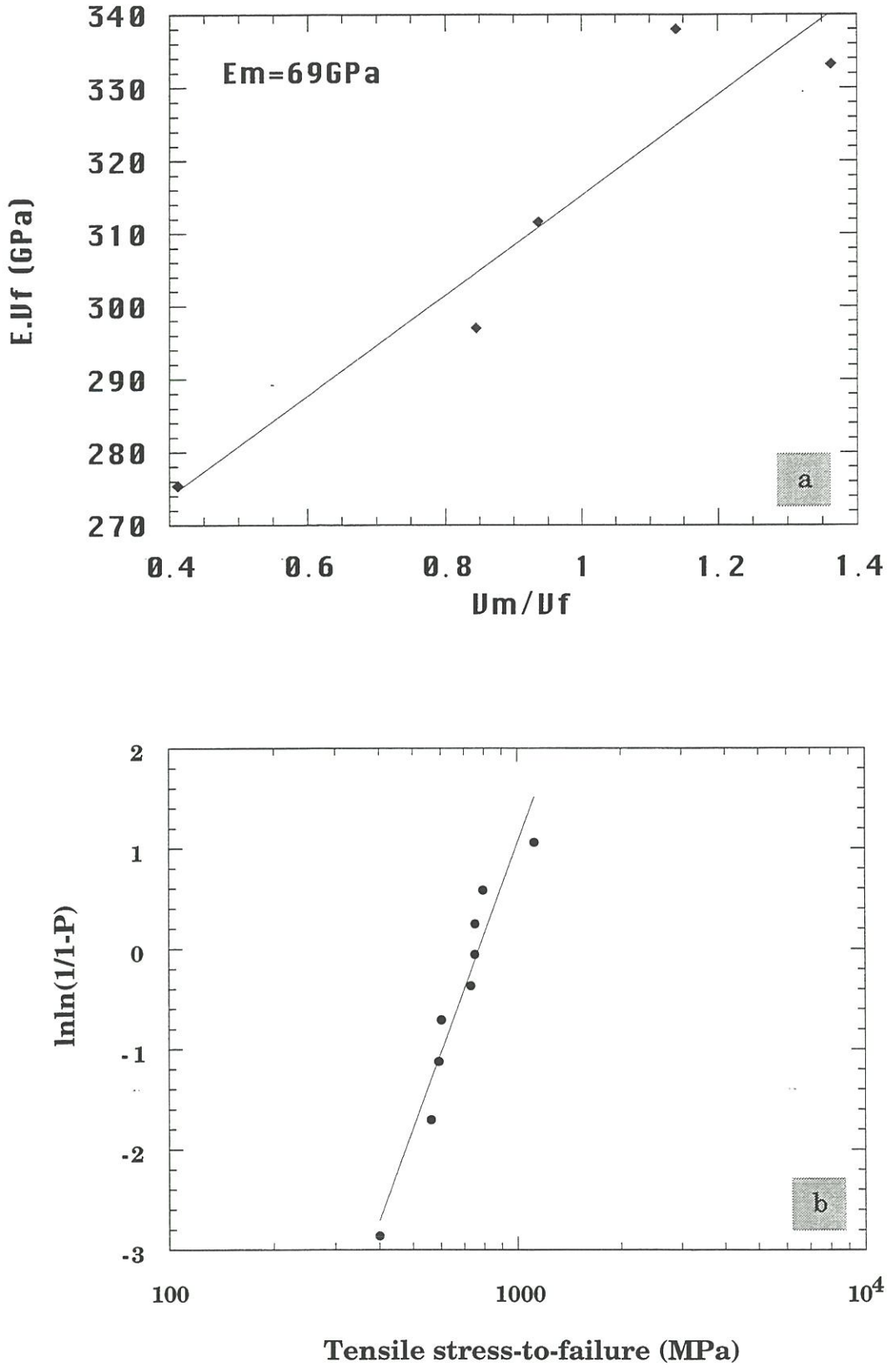

Figure 16: matrix properties
(a) rule of mixture applied for B/M microcomposites with different V_f
(b) Weibull plot of a A-HTT/M microcomposite with V_m=96%

3.2.3 - SEM observations of the fracture surfaces

It is worthy of note that a fracture mirror with mist and hackle markings was systematically observed. That makes the difference between the failure surface among other broken ends, for which the surfaces present bending features as shown in figure 17.

Fracture surfaces exhibited two different features: (1) flat fracture (figure 18.a), and (2) fibre pull-out (figure 18.b). Sometimes the flaw belongs to the matrix, and is responsible for the catastrophic failure of the fibre (notch effect through a strong fibre/matrix bonding) (figure 19).

Flat fracture and fibre pull-out were both encountered for A/M. A-HTT/M microcomposites presented only fibre pull-out, as far as we could see. The very few fracture surfaces observed for B/M and B-HTT/M, were flat surface for B/M, or with a fibre pull-out for B-HTT/M.

A/M fracture surfaces were either of one type or of the other depending on to which (ε_R, σ_R) population they belong (Table 6). Flat surfaces were related to the higher ultimate performances: ε_R=1.45% and σ_R=2400MPa, whereas fibre pull-out was systematically associated to the lower performances: ε_R=1.10% and σ_R=1600MPa. Moreover, the first population (flat surface) is generally characterised by a linear curve to failure, whereas the later (fibre pull-out) presents generally singularities on tensile curves. Fibre stress to failure in microcomposite, determined by the fracture mirror ($\sigma_{fmirror}$), was compared either to fibre stress σ_f, when the load is shared by the fibre and the matrix up to failure assuming that no residual stress exists ($\sigma_f=E_f.\varepsilon_R$), or to the fibre stress σ_f', when load was supported by the fibre alone ($\sigma_f'=F/S_f$). In that case, the matrix is pre-cracked when the fibre fails.

Thus, for low (ε_R, σ_R) population (microcomposites with some fibre pull-out), $\sigma_{fmirror}$ is lower than or equal to σ_f', which assumes that fibre fails respectively with the matrix partially loaded or not, at failure location. On the other hand, if the same comparison is realised with Weibull plots, in applying

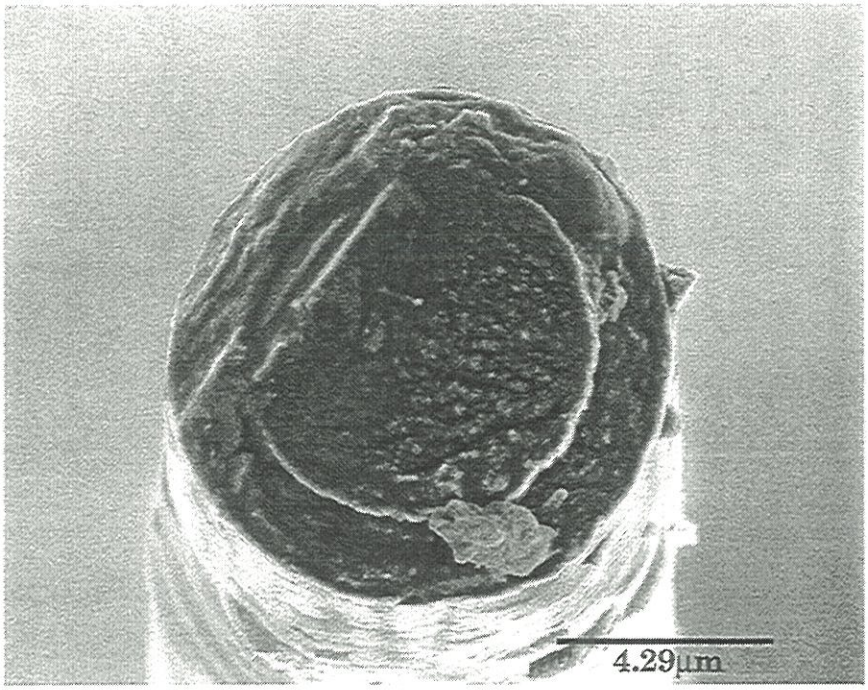

Figure 17: broken end which is not the fracture surface

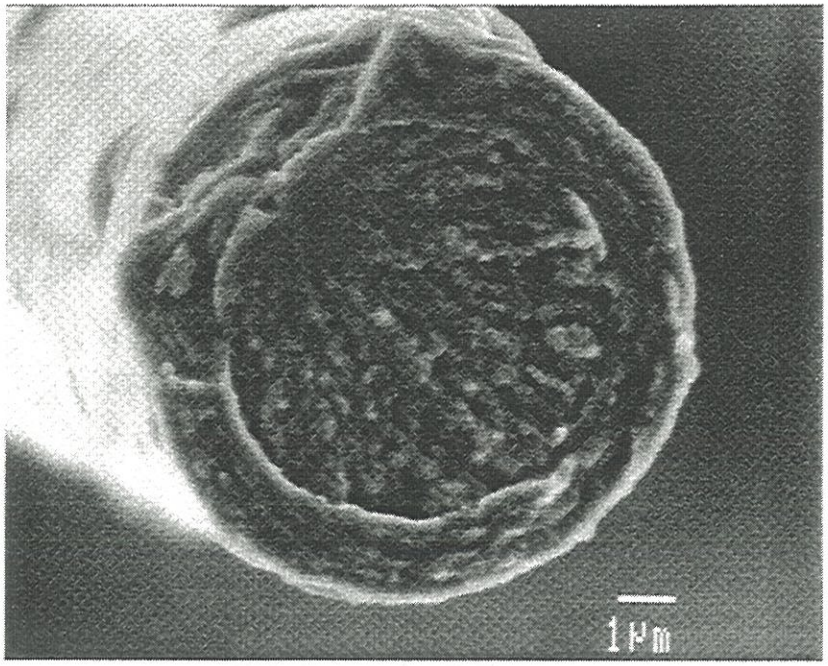

a - flat surface

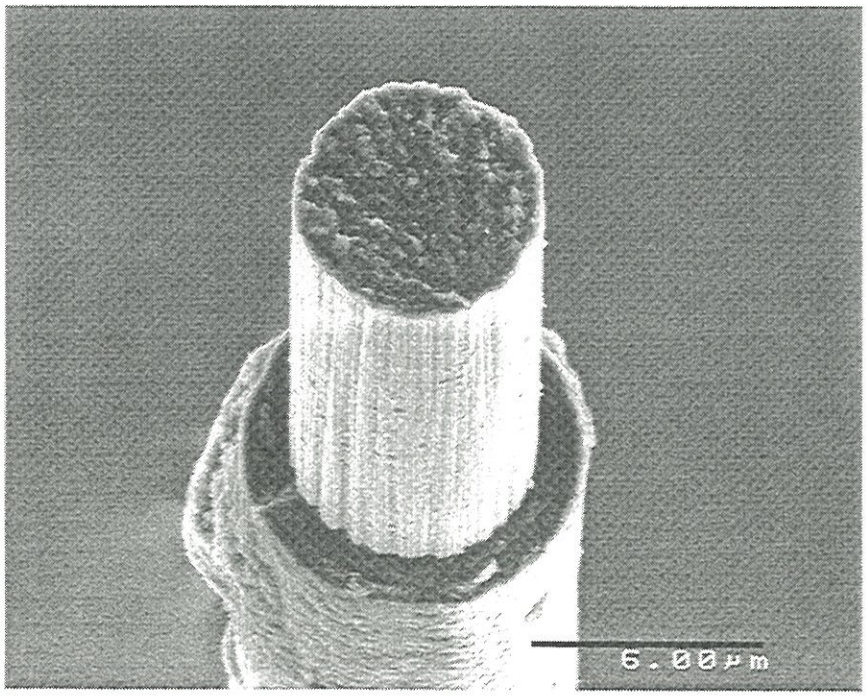

b - fibre pull-out

Figure 18: Fracture surfaces obtained by tensile load
on C/C microcomposites
(a) flat surface, (b) fibre pull-out

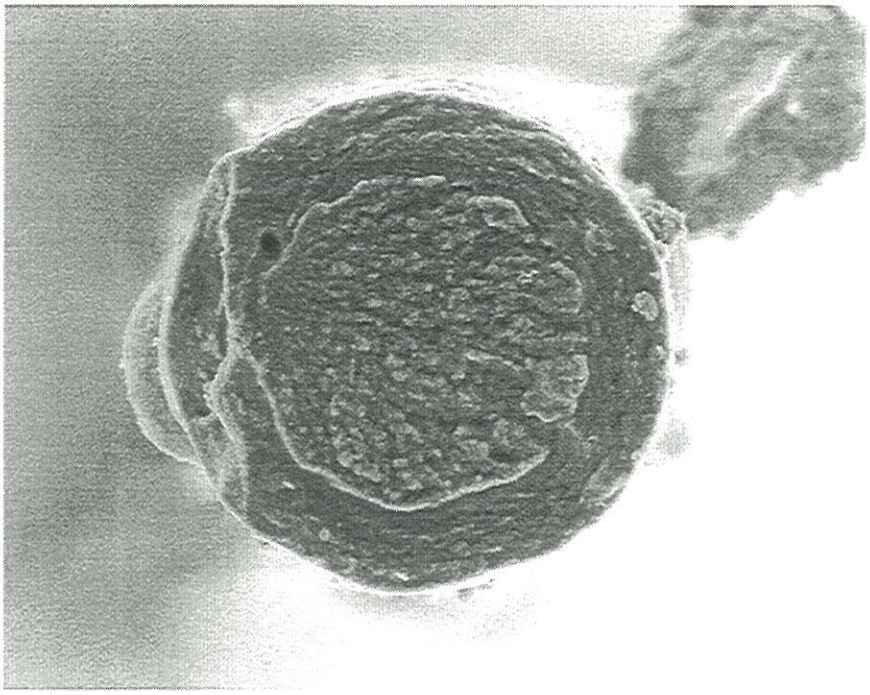

Figure 19: fracture surface initiates by a defect in matrix

Table 6. Analysis of fracture surfaces of A/M microcomposites

Type of fracture	Mechanical properties				Mirror data	
	ε_R (%)	σ_R (MPa)	σ_f (MPa)	σ_f' (MPa)	Rm (μm)	$\sigma_{fmirror}$ (MPa)
Flat surface	1.46	2467	3716	4648	0.483	3739
	1.54	2452	3931	4767	0.388	4171
	1.47	2147	3739	5003	0.522	3597
Fibre pull-out	1.17	1575	2973	3701	0.475	3773
	1.05	1788	2668	4133	0.583	3406
	1.19	1625	3024	3856	0.561	3471

N.B.: $\sigma_f=E_f.\varepsilon_R$ and $\sigma_f'=F/S_f$

Weibull statistics to low strength population (figure 15.c), fibre stress σ_f' in the microcomposite is similar to bare fibre stress to failure. Fibre controls the failure, and is not degraded by the CVD-process.

For high (ε_R, σ_R) population, A/M microcomposites have a flat surface fracture, so fibre and matrix share the load up to failure. As fibre stress to failure ($\sigma_{fmirror}$) is equal to σ_f, fibre is not overloaded in the microcomposite. Weibull plots (figure 15.b) are consistent with these results, obtained from mirror radii.

For A-HTT/M microcomposites, large fibre pull-outs were observed: up to fivetimes the fibre diameter. Fibre-matrix bonding in A-HTT/M must be lower than in A/M microcomposite. Mechanical results are consistent with TEM observations. Only few mirror radii could be measured (Table 7) due to their small diameter. They confirmed that $\sigma_{fmirror}$ is comprised between σ_f and σ_f'.

For B-HTT/M materials, large fibre pull-outs are not observed. So, surface roughness must affect bonding strength by certainly enhancing physical bonding. A slight shrinkage of the fibre, after failure, was observed on a B-HTT/M microcomposite : the two complementary broken ends have each the fibre at a lower level than matrix (figure 20). This confirms observation made on thin foil of B-HTT/M microcomposite (figure 9). Fibre is then in tension in the microcomposite. This is consistent with the hypothesis that surface defects are healed by pyrocarbon deposit.

4 - CONCLUSIONS

When fibre is previously annealed at a temperature superior to the processing temperature, a larger fibre shrinkage is observed in microcomposites (TEM samples). The A-HTT/M interface is thus in transverse tension, without chemical fibre/matrix bonding. As a matter of fact, non-brittle

Table 7. Analysis of fracture surfaces of A-HTT/M microcomposites

Type of fracture	Mechanical properties				Mirror data	
	ε_R (%)	σ_R (MPa)	σ_f (MPa)	σ_f' (MPa)	Rm (μm)	$\sigma_{fmirror}$ (MPa)
Fibre	0.95	1656	2992	3006	0.496	3122
pull-out	1.33	2733	4204	4673	0.268	4253
	1.17	1879	3701	3940	0.298	4031

N.B.: $\sigma_f = E_f.\varepsilon_R$ and $\sigma_f' = F/S_f$

mechanical behaviour is observed with fibre pull-out for this material. On the contrary, the A/M interface is in transverse equilibrium (or even in compression). The interface is too strong, involving an increase of amount of brittle fractures.

Prepared C/C microcomposites are inverse composites: matrix fails before fibre. Matrix Young's modulus was evaluated four to five times lower than that of the fibre: E_m=70GPa and E_f=250-350GPa.

Transition from the brittle regime to the non-brittle one, when shifting from a strong to a weak interface, retains a statistical aspect for the bad control on the residual axial tension in the fibre. In this case, matrix is in compression, enhancing its strain-to-failure (>1.1%), which can be as high as fibre strain-to-failure. So, when matrix failure occurs, fibre is overloaded, and behaviour appears brittle. Fibre in axial tension was evidenced for B-HTT/M, for which strain-to-failure of fibre alone is low (0.78%). However, in this particular case, surface flaws of fibre have to be healed by the pyrocarbon deposit as strain-to-failure is of 1% order.

A higher fibre surface roughness tends to favour brittle behaviour, even with a fibre final heat-treatment. Too few structural observations did not permit to discuss these results. It is supposed that a physical effect can also control the interfacial bonding strength together with the chemical bonding and the residual thermal stresses.

Acknowledgements

This work has been supported by SEP and CNRS through a grant given to B.T. The authors are indebted to J. M. Jouin from SEP and J. Lamon from LCTS, for valuable discussion, and G. Bondieu from SEP and M. Alrivie from LCTS for technical assistance.

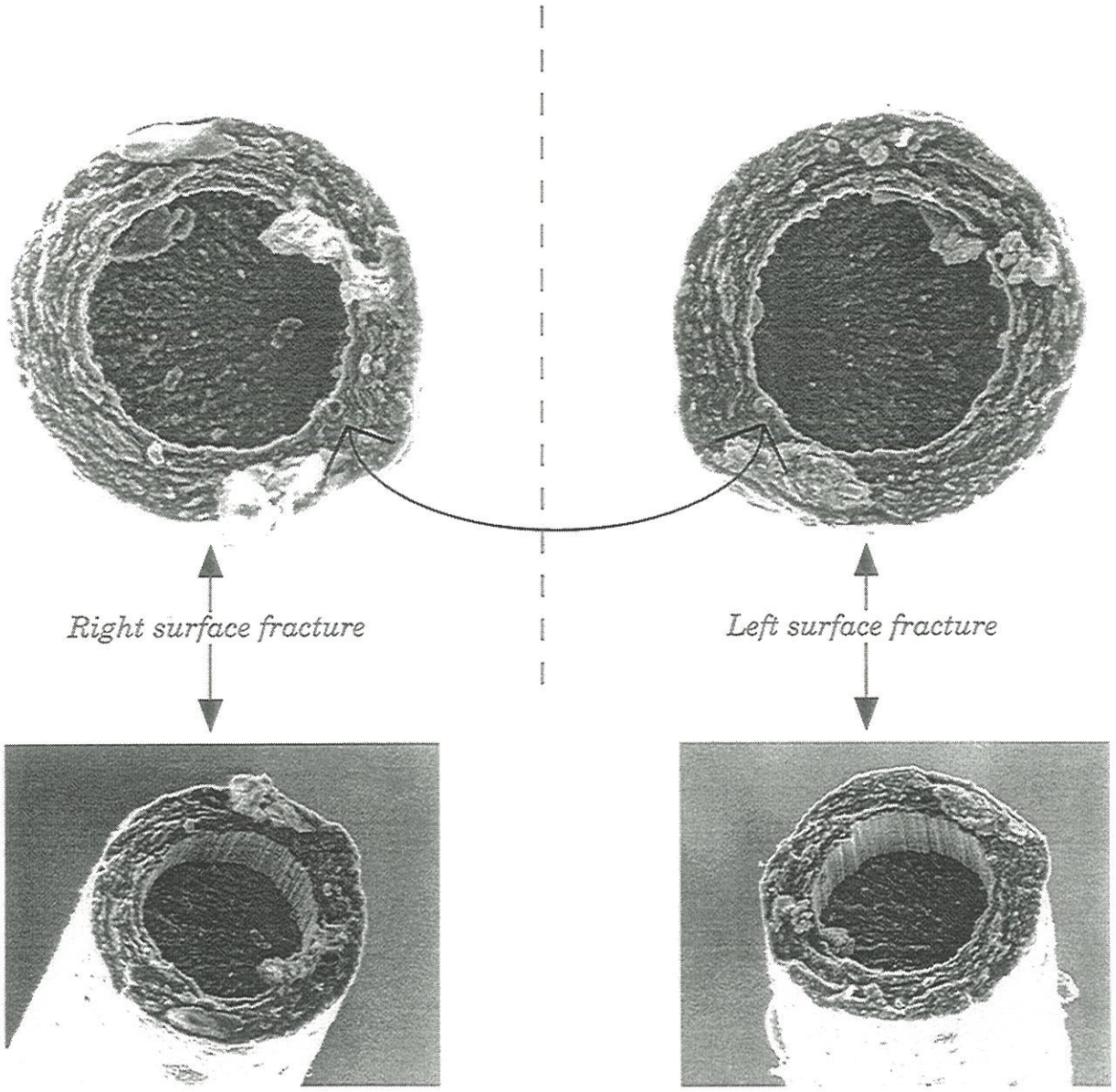

Figure 20: SEM observation of two complementary broken ends
of a tensile tested B-HTT/M microcomposite,
which shows fibre in axial tension in the microcomposite

REFERENCES

[1] C.R. Thomas, E.J. Walker, Effects of PAN carbon fibre surface in carbon-carbon composites, Proceedings 5th Conf. on Industrial Carbon and Graphite, Soc. Cem. Ind. London, **1**, pp.520-531 (1978)

[2] E. Fitzer, K.H. Geigl, W. Hüttner, The influence of carbon fibre surface treatment on the mechanical properties of carbon/carbon composites, Carbon, **18**, pp.265-270 (1980)

[3] R.J. Zaldivar, G.S. Rellick, J.M. Yang, Fibre strength utilization in carbon/carbon composites, J. Mater. Res., **8**, N°3, pp.501-511(1993)

[4] S. Takano, T. Kinjo, T. Uruno, T. Tlomak, C.P. Ju, Investigation of process-structure-performance relationship of unidirectionally reinforced carbon-carbon composites, Ceram. Eng. Sci. Proc., **12** [9-10], pp.1914-1930 (1991)

[5] L.M. Manocha, O.P. Bahl, Y.K. Singh, Mechanical behaviour of carbon-carbon composites made with surface treated carbon fibers, Carbon, **27**, N°3, pp.381-387 (1989)

[6] C. Ahearn, B. Rand, Modification of the fibre-matrix bonding in a brittle carbon-carbon composite by controlled oxidation, Carbon, **34**, N°2, pp.239-249 (1996)

[7] M. Müller, K.-M. Beindorn, K.J. Hüttinger, The significance of the fibre coating in the production of carbon fibre-reinforced carbons from HT carbon fibres and phenolic resin as matrix precursor-II. phenolic resin coatings, Carbon, **33**, N°8, pp.1043-1046 (1995)

[8] K. Hamada, S. Sato, H. Tsunakawa, A. Kohyama, Interfacial microstructure and mechanical properties of C/C composites, Proceedings of the Tenth International Conference on Composite Materials, A. Poursartip and K. Street eds., Whistler, British Columbia, Canada, August , pp.423-430 (1995)

[9] B.L. Butler, D.A. Northrop, T.R. Guess, Interfaces in carbon fiber/pyrolytic-carbon matrix composites, J. Adhesion, **5**, pp.161-178 (1973)

[10] R.G. Schinazi, R.J. Diefendorf, Mechanical properties of single fiber carbon/carbon composites, Proceeding Carbon'94, G.E.C. ed., Granada, Spain, 3-8 july, pp.686-687 (1994)

[11] R. Naslain, J. Lamon, A. Guette, X. Bourrat, F. Langlais, R. Pailler, F. Rebillat, S. Jacques, C. Robin-Brosse, S. Goujard and J.M. Jouin, The microcomposite concept in the field of ceramic matrix composites: advantages

and limits, in Progress in Advanced Materials and Mechanics, Wang Tzuchiang and Tsu-Wei Chou eds., pp.198-208, Peking Univ. Press, Peking, (1996)

[12] F. Heurtevent, Matériaux multicouches nanoséquencés $(PyC/SiC)_n$ Application en tant qu'interphases dans des composites thermostructuraux, PhD Thesis, n°1476, University Bordeaux I (France), March (1996)

[13] S. Jacques, A. Guette, F. Langlais, X. Bourrat, Characterisation of SiC/C(B)/SiC microcomposites by transmission electron microscopy, in PhD Thesis n°1398, University Bordeaux I (France), December (1995)

[14] B. Trouvat, X. Bourrat, R. Naslain, Influence of a carbon interphase with a controlled microtexture on the mechanical properties of single fibre C/C/C microcomposites, to be submitted in Carbon

[15] J.F Villeneuve, D. Mocaer, R. Pailler, R. Naslain, Tensile testing at high temperatures of ex-PCS Si-C-O and ex-PCSZ Si-C-N single filaments, J. of Mater. Sc., **28**, pp.1227-1236 (1993)

[16] M.Guigon, A. Oberlin, and G. Desarmot, Microtexture and structure of some high tensile strength, PAN-base carbon fibres, Fibre Science and technology, **20**, pp.55-72 (1984)

[17] A.R. Bunsell, A. Somer, The tensile and fatigue behaviour of carbon fibres, Plastics, Rubber and Composites Processing and Applications, **18**, pp.263-267 (1992)

[18] X. Bourrat, B. Trouvat, G. Limousin, G. Vignoles, Pyrocarbon anisotropy as measured by electron diffraction and polarized light, to be submitted in Journal of Materials Research

[19] E. Fitzer, M. Heine, Carbon fibre manufacture and surface treatment, in Fiber reinforcement for composite materials, A.R. Bunsell ed., Elsevier, Amsterdam, pp.73-148 (1988)

[20] P.J. Goodhew, A.J. Clarke, J.E. Bailey, A review of the fabrication and properties of carbon fibres, Materials Science and Engineering, **17**, pp.3-30 (1975)

[21] R. Moreton, The effect of gauge length on the tensile strength of R.A.E. carbon fibres, Fibre Sci. Technol., **2**, pp. 273-284 (1969)

[22] Y. Tanabe, E. Yasuda, Change of Weibull modulus in strength of carbon fibres with heat treatment, J. of Mater. Sci. Letters, **10**, pp.756-759 (1991)

[23] J.B. Donnet, R.Y. Qin, Study of carbon fiber surfaces by scanning tunnelling microscopy, part II- PAN-based high strength carbon fibers, Carbon, **31**, N°1, pp.7-12 (1993)

[24] W.P. Hoffman, Scanning probe microscopy of carbon fiber surfaces, Carbon, **30**, N°3, pp.315-331 (1992)

[25] J.B. Barr, Fracture surfaces of carbon filaments, 21st Biennial conference on carbon, Extended Abstracts and Program, American Carbon Society, June 13-18, pp.118-119 (1993)

[26] A.A. Griffith, Phil. Tran. Roy. Soc., **A221**, p.163 (1921)

[27] G.R. Irwin, J. Appl. Mech., **24**, p.361 (1957)

[28] F. Rebillat, J. Crépin-Leblond, S. Mougin, J. Lamon, Experimental determination of the stress field in fibre/matrix interphases of microcomposites, High-Temperature ceramic-matrix composites I: Design, Durability and Performance, Ceramic Transactions **57**, pp.265-270 (1995)

[29] M. Sakaï, R.C. Bradt, D.B. Fischbach, Fracture toughness anisotropy of a pyrolytic carbon, Journal of Materials Science, **21**, pp.1491-1501 (1986)

[30] J. Rappeneau, F. Tombrel, Propriétés physiques des carbones, in Les Carbones, A. Pacault, Groupe Français des carbones ed., pp.839-910

[31] B. Rand, Matrix precursors for carbon-carbon composites, in Essentials of carbon-carbon composites, C.R. Thomas ed., Royal society of chemistry, pp.67-102 (1993)

[32] L. Guillaumat, J. Lamon, Influence of interfacial characteristics on the nonlinear deformations of ceramic matrix composites, Proceedings of the Tenth International Conference on Composite Materials, A. Poursartip and K. Street eds., Whistler, British Columbia, Canada, August , **IV**, pp.649-656

ANNEXE 2

Influence of a carbon interphase with a controlled microtexture on the mechanical properties of a single fibre C/C/C microcomposites

ANNEXE 2

Influence of a carbon interphase with a controlled microtexture on the mechanical properties of single fibre C/C/C microcomposites

1 - INTRODUCTION 2

2 - EXPERIMENTAL 3

2.1 - C/C/C microcomposites preparation 3

2.2 - Mechanical testing 4

2.3 - Structural characterisation 5

3 - RESULTS AND DISCUSSION 7

3.1 - Microcomposites structure 7

3.1.1 - Texture of pyrocarbons 7

3.1.2 - TEM observation of interfaces 7

3.1.3 - SEM observation of polished transverse sections 8

3.2 - Mechanical behaviour 9

3.2.1 - Load-strain curves 9

3.2.2 - Fracture mirrors 10

3.2.3 - Interface and ultimate performances 11

3.3 - Microcomposites heat-treated to HTT2 13

3.3.1 - F/M and F/Ia/M microcomposites 13

3.3.2 - F/Ib/M and F/Ic/M microcomposites 16

4 - CONCLUSIONS 18

REFERENCES

NOMENCLATURE

Ae	extinction angle
OA	orientation angle
d_{002}	interlayer spacing
d	fibre diameter
F	tensile load
σ	applied stress
S_f	fibre section
S_m	matrix section
V	volume submitted to the stress
V_f	fibre volume fraction
V_m	matrix volume fraction
E	Young elastic modulus
E_f	fibre Young modulus
E_m	matrix Young modulus
R_m	fracture mirror radius
$\mathcal{A}$	constant relating mirror radius to fibre stress-to-failure
$\sigma_{f,mirror}$	fibre stress-to-failure deduced from mirror radius
ε_{el}	strain corresponding to the end of the linear domain
ε_R	strain-to-failure
$\varepsilon_{R,f}$	fibre strain-to-failure
$\varepsilon_{R,m}$	matrix strain-to-failure
σ_{el}	stress corresponding to the end of the linear domain
σ_R	stress-to-failure
σ_f	fibre stress-to-failure in the microcomposite such as $\sigma_f = E_f.\varepsilon_R$
σ_f'	fibre stress-to-failure in the microcomposite such as $\sigma_f' = F/S_f$
σ_0	scale parameter in Weibull model
m	Weibull modulus
τ	interfacial shear stress

Influence of a carbon interphase with a controlled microtexture on the mechanical properties of single fibre C/C/C microcomposites

Submitted in Carbon

B. TROUVAT, X. BOURRAT, and R. NASLAIN

Laboratoire des Composites Thermostructuraux

UMR 47 CNRS-SEP-UBI, Université Bordeaux I

3, allée de la Boëtie, 33600 Pessac, France

SUMMARY

The aim of this work was to study the effect of pyrocarbon interphases, with various anisotropies, on the mechanical behaviour of C/C/C microcomposites. A HT PAN-based carbon fibre, with two different surface states, was used as matrix reinforcement, as well as same fibres heat-treated (HTT). Weibull statistics applied to mechanical tensile test data, and electron microscopy observation show the influence of the addition of a more disordered interphase (Ib, Ic), compared to matrix. This interphase type involves a stronger fibre/matrix bonding, and improves mechanical properties (ε_R,σ_R) for microcomposites reinforced with heat-treated fibres: healing of fibre surface defects (created by HTT) by the interphase, and better utilisation of these improved fibres in the material (up to 100% with Ib).

A post heat treatment (HTT2) of these microcomposites show that interphases with a low anisotropy (Ib, Ic) prevent from complete fibre/matrix debonding by accommodation of the difference in coefficients of thermal expansion of fibre and matrix. The resulting microcomposites have a regular behaviour, contrary to microcomposites before HTT2.

1 - INTRODUCTION

Interface has a dominant role on controlling properties of brittle ceramic matrix composites (CMCs). It is essential for improving mechanical performances to assess the relevant parameters using experimental model composites. Most of the researchers, working on the relationship between the interfacial bonding and the mechanical properties in C/C composites, have used liquid-based matrices and studied the influence of fibre surface treatment and post-treatment on performances (matrix shrinkage, matrix stress-graphitization, etc.) [1-5]. More recently, oxidation was also used as a way to weaken the fibre/matrix bonding [6] as it is the case with post-treatments which produce shrinking and debonding of the interface [3].

There is only few papers published on the design of a real interphase in C/C composites [7]. The aim of this work was the material design of a pyrocarbon interphase in C/C/C model microcomposites. This was carried out by changing the microtexture at the fibre surface by controlling the CVD parameters but in the same range of temperature, in order to change the fibre/matrix bonding independently of the residual stresses.

For that purpose, model materials (microcomposites), consisting in coated single fibres, were used to characterise the fibre/matrix interfacial zone and to relate it to mechanical properties. Carbon interphases were deposited on HT PAN-based carbon fibres by Chemical Vapour Deposition (CVD) with different microtextures. Then, the pyrocarbon matrix was deposited, also by CVD. Microtexture and mechanical properties of these C/C/C microcomposites were investigated, and compared to those, reported in a previous work [8] for C/C microcomposites without interphase, and which can be summarised as follow:

Mechanical tensile tests and microscopic observations have shown that carbon/carbon composites [8] are inverse composites : the strain-to-failure of

the matrix ($\varepsilon_{R,m}$) is lower than that of the fibre ($\varepsilon_{R,f}$). Contrary to other CMCs for which $E_m > E_f$, in C/C system, the matrix modulus is very low (e.g. ≈ 70 GPa for thin pyrocarbon coating [8]), four times lower than that of a regular HT-type fibre (250-340 GPa). Depending on fibre treatment, the fibre/matrix interface was seen to switch from weak to strong, and thereafter the mechanical behaviour from non-brittle to brittle, exhibiting fibre pull-out or flat fracture, respectively. The interface was weak and the behaviour non-brittle when the fibre was previously stabilised by annealing (HTT). Transverse coefficient of thermal expansion (CTE) of fibres changed with heat-treatment as carbon planes lined up along fibre axis : a larger shrinkage of heat-treated fibre occurs which creates some debonding at the interface. The interface was strong for non heat-treated fibres.

In this study, the interphase microtexture in C/C/C microcomposites, is an additional parameter, which, combined with surface roughness and heat-treatment of fibre, is expected to increase the range of interfacial bonding strength. The processing conditions for the interphase have to be taken into account, especially temperature, as thermal residual stresses are seen to be important in bonding strength. Influence of composite graphitization was also studied.

2 - EXPERIMENTAL

2.1 - C/C/C microcomposites preparation

Same HT PAN-based carbon fibres[1], with a different surface state, referred to as A and B, were used. A rougher surface characterised B fibre. Some fibres were subjected to a final heat treatment up to a temperature T1

[1] from SEP, Le Haillan, France

Table 1. Mechanical data for HT PAN-based fibres [8]

Fibre		Mechanical data		
Type	d (μm)	E (GPa)	ε_R (%)	σ_R (MPa)
A	6.9 (0.3)*	255 (36)	1.58 (0.22)	3992 (630)
A-HTT	6.7 (0.3)	316 (34)	1.27 (0.24)	3995 (889)
A-HTT2	6.5 (0.3)	398 (13)	0.84 (0.13)	3336 (471)
A 1000°C-2kPa	6.7 (0.3)	252 (8)	1.16 (0.17)	2929 (459)
A-HTT 1000°C-2kPa	6.7 (0.3)	317 (14)	1.12 (0.17)	3569 (597)
B	6.7 (0.3)	247 (28)	1.44 (0.29)	3538 (742)
B-HTT	6.7 (0.4)	336 (30)	0.78 (0.18)	2630 (633)
B-HTT2	6.5 (0.2)	412 (17)	0.64 (0.19)	2607 (732)

* standard deviation in brackets

(HTT) or T2 (HTT2), with T2 higher than T1, and T1 higher than fibre processing temperature. These fibres are referred to respectively as A-HTT, B-HTT, and A-HTT2, B-HTT2. Mechanical properties of these fibres are listed in Table 1. They were determined in a previous work [8]. Fibres can be degraded during the CVD-process. Treatment of A and A-HTT fibres, under conditions close to those for pyrocarbon deposition (1000°C-2kPa-8h) [8], yields a decrease in mechanical properties, especially for A fibres (Table 1). However, the applied treatment must have been more severe as it will be in CVD-process, since it does not take into account the protection of the pyrocarbon as it is deposited.

C/C/C microcomposites, consisting of a single fibre coated with an interphase layer and a matrix shell (figure 1), were made with the above four types of carbon fibres. For that purpose, fibres were mounted on a carbon frame[1]. Pyrocarbon was deposited in a CVD/CVI furnace in isotherm and isobar conditions, with propane or methane as hydrocarbon precursor (Table 2).

Pyrocarbon interphases (Ia, Ib, Ic) , with different microtextures (Table 2), were used. Volume fractions of interphase and matrix were respectively $V_i \approx 13\%$ and $V_M \approx 43\%$.

Some of the microcomposites, with or without an interphase, were subjected to a heat treatment to temperature T2 (HTT2).

2.2 - Mechanical testing

Microcomposites were mechanically characterised with a microtensile device [9], comprising a 0-2N load cell and a straining device driven at constant speed (1%/min). Tensile properties were measured at 10mm gauge length (paper frame). For each sample a set of 15 to 20 specimens was prepared and tested in order to get a statistical population.

---

[1] Papiex®: graphite sheet from Le Carbone Lorraine, France

Table 2. Experimental conditions and characteristics of pyrocarbons

	Experimental conditions				Pyrocarbon characteristic	
	Gas	Gas flow (sccm)	T (°C)	P (kPa)	Ae (°)	Microtexture
M	C_3H_8	2500	1000	2	17	Smooth Laminar
Ia	CH_4	2500	1100	5	15	Smooth Laminar
Ib	C_3H_8	2500	1000	0.5	13	Smooth Laminar
Ic	C_3H_8 H_2	500 2000	1200	2	11	Dark Laminar

N.B.: matrix is designated by M, and interphases by Ia, Ib, and Ic
Ae is the extinction angle (optical measurement in polarised light)

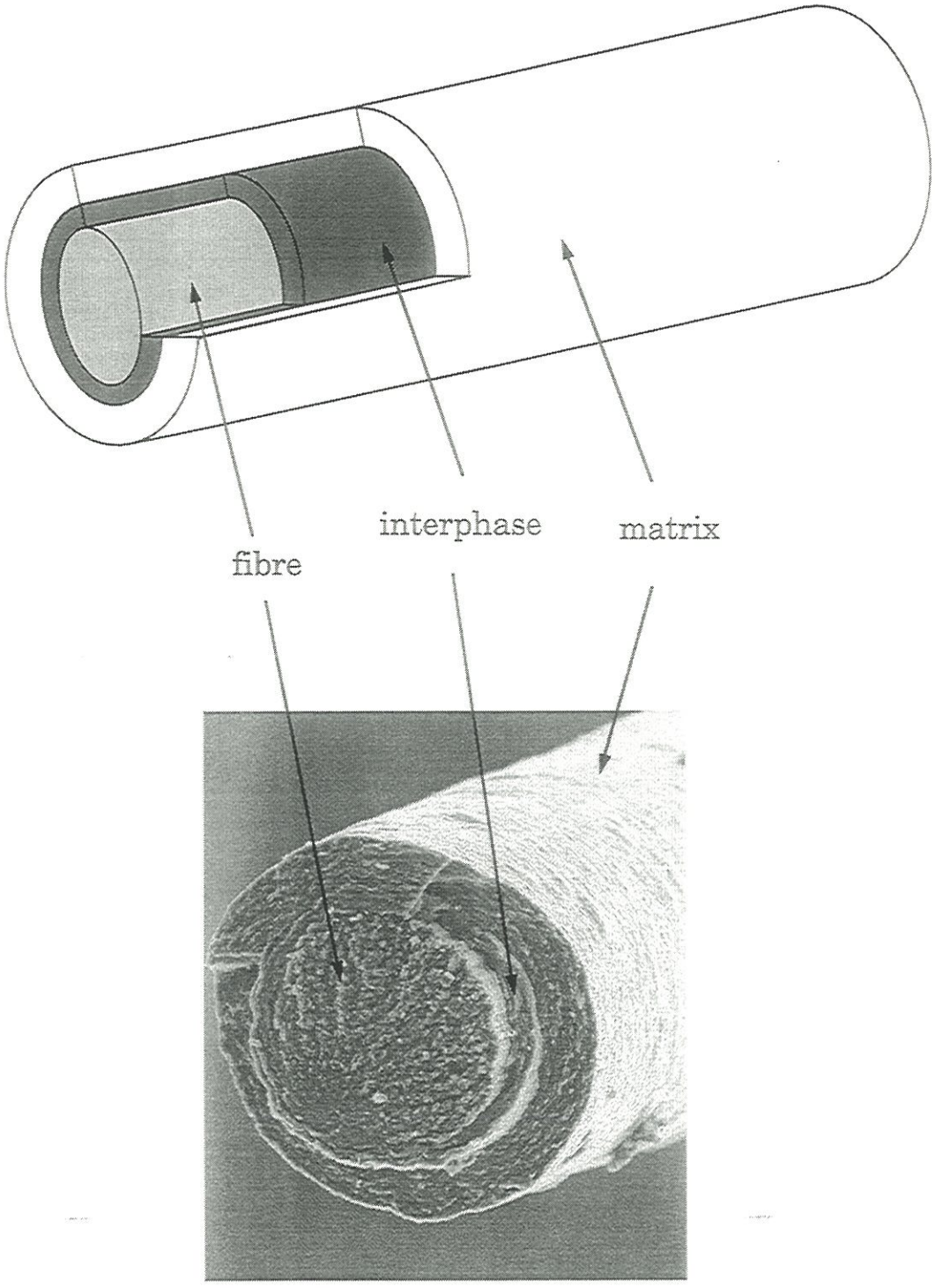

Figure 1: sketch of a C/C/C microcomposite
and the actual material

As already mentioned by other authors for carbon fibres [10,11], stiffening under load is clearly seen in carbon/carbon microcomposites. Different stiffness values could be measured corresponding to the initial, final and tangent moduli. Tangent modulus was only taken into account in this study.

Weibull statistics (weakest link model) were used to analyse the failure of these brittle materials. This approach is the most common technique employed for carbon fibres. The failure probability is expressed as follows:

$$P = 1 - exp\left(-\frac{V}{V_0}\left(\frac{\sigma - \sigma_u}{\sigma_0} \right)^m \right) \quad \text{for stresses} \qquad (1)$$

where

V: volume submitted to the stress, V_0 a reference volume (V_0=1m^3)

σ: applied stress

σ_u: value of stress below which P is zero

σ_0: scale parameter (in stress unit)

m: Weibull modulus which characterises the scatter in strength; slope of the plot lnln(1/(1-P)) against ln(σ)

with the estimator taken as $P = \frac{i - 0,5}{N}$ where N is the number of tested specimens. In this study, σ_u was assumed to be zero.

This relation (eqn 1), established for stresses, can also be applied to strains in the same manner.

2.3 - Structural characterisation

Optical measurement in polarised light was used to characterise pyrocarbon texture by measuring the extinction angle Ae [12]. For that purpose, a deposit at least 1µm thick was made on the fibre for each type of pyrocarbon (matrix (M), Ia, Ib, Ic). Polished cross-sections were realised after embedding these materials in a resin, and used to determine the extinction angle. The larger the angle Ae, the higher the anisotropy: Ae ranges for low

pressure-low temperature pyrocarbons from 0 to 4° for isotropic pyrocarbon, from 4 to 12° for dark-laminar, from 12 to 18° for smooth laminar, and finally 18° and more for rough laminar pyrocarbon for the optical microscope[1] used.

Scanning Electron Microscopy (SEM)[2] observation was made on polished transverse sections of microcomposites, embedded in a resin, and on microcomposite fracture surfaces, obtained by collecting the broken ends after tensile tests. Carbon/carbon microcomposites smashed to fragments on failure due to vibrations caused by the initial fracture, as do carbon fibres. To recover the fracture surface, paraffin oil was used on samples, but it remained difficult to collect them. So, only few fracture surfaces could be examined by SEM. As a result, fracture surface observations could not give statistical results for the studied materials, except for microcomposites with interphase Ic.

Transmission Electron Microscopy (TEM)[3] observations were made on thin foil TEM cross-sections. TEM samples were prepared by embedding microcomposites in alumina cement followed by a mechanical grinding (including dimpling) - ion milling method as described elsewhere [8]. Otherwise, this technique permitted to characterise pyrocarbon interphase texture by measuring the orientation angle (OA), and the interlayer spacing (d_{002}) [12] on electron diffraction pattern micrographs by image analysis. OA is the azimuthal opening of 002 arcs of electron diffraction pattern. It is related to the disorientation of aromatic layers with respect to the anisotropy plane: the lower the anisotropy, the higher the orientation angle.

---

[1] MeF_3 Reichert-Jung microscope

[2] using a JEOL JSM-840A microscope, and a HITACHI S-4500 microscope equipped with a field emission gun

[3] using a CM-30 ST Philips microscope

3 - RESULTS AND DISCUSSION

3.1 - Microcomposites structure

3.1.1 - Texture of pyrocarbons

The extinction angle (Ae) data have permitted to rank the different pyrocarbons (Table 2) in terms of decreasing anisotropy as follows: M>Ia>Ib>Ic. They belong to the "smooth-laminar" class of texture, except Ic, which is a "dark-laminar" pyrocarbon. Corresponding measurements of orientation angle, OA, and inter-basal plane spacing, d_{002}, obtained by TEM are represented in figure 2.

3.1.2 - TEM observation of interfaces

TEM is the only means to control the microtextural features at the fibre-matrix interface. Figures 3.a,b and 3.c,d are the cross-sections of the two references: A/M and A-HTT/M. It was noticed [8] that some interfacial debonding was occurring or not, depending on fibre treatment.

During thinning of TEM samples, residual stresses were seen to be released when the interlaminar shear strength was not too high. This way, fibre axial tensile residual stress in B-HTT/M microcomposite was evidenced [8]: fibre axial shrinking in polished cross-sections.

The same stress release was observed in transverse direction as well. Debonding can occur during thinning due to transverse tensile residual stress across the interface, not counterbalanced by a strong enough chemical bonding. In the reference C/C microcomposites, TEM images have shown that interfacial debondings occurred in A-HTT/M (figure 3.c,d) but not for A/M (figure 3.a,b). Thus, it was assumed that stabilising the fibre with previous heat treatment was essential in order to get transverse tensile residual stress across the interface (highest mechanical performances).

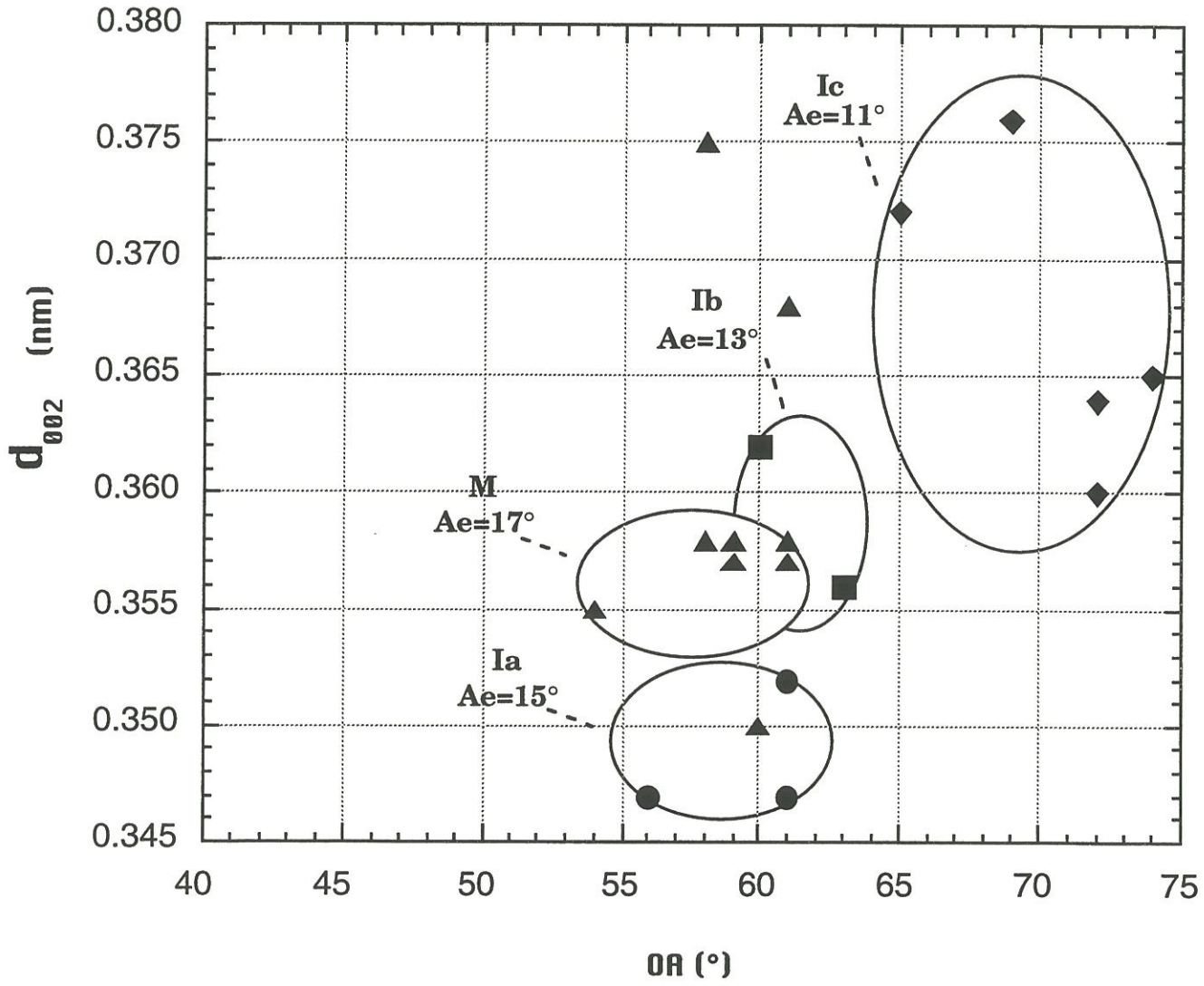

Figure 2: pyrocarbon characteristics:
microtexture (Ae,OA) and interlayer spacing (d_{002}) [12]

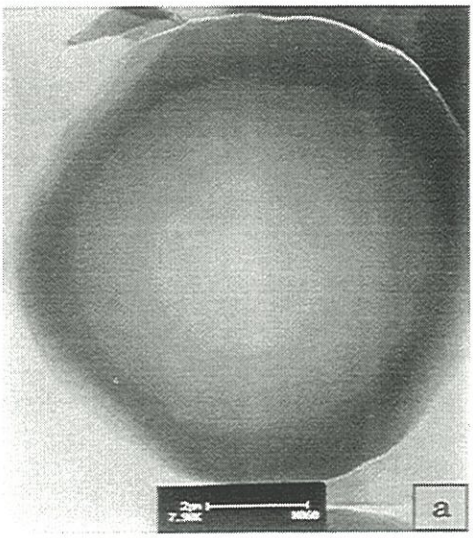

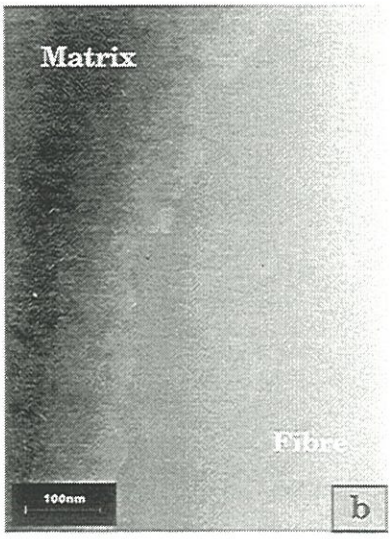

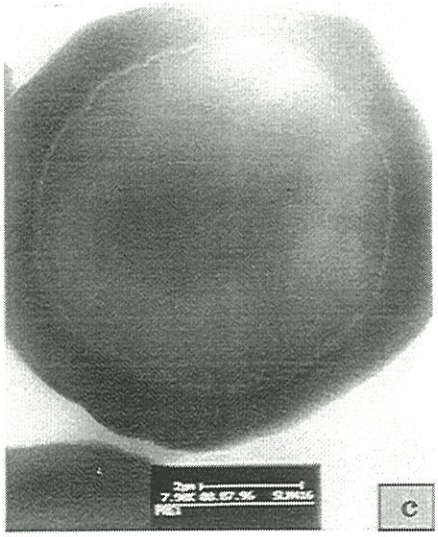

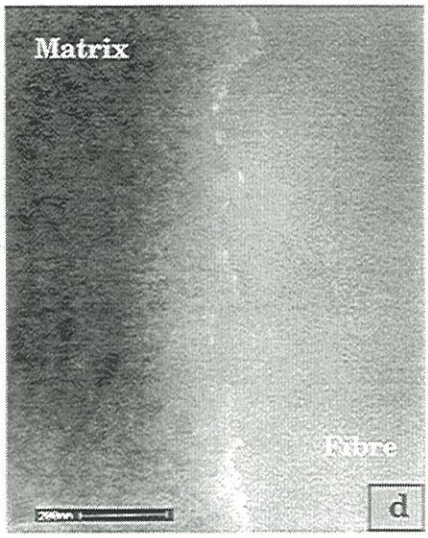

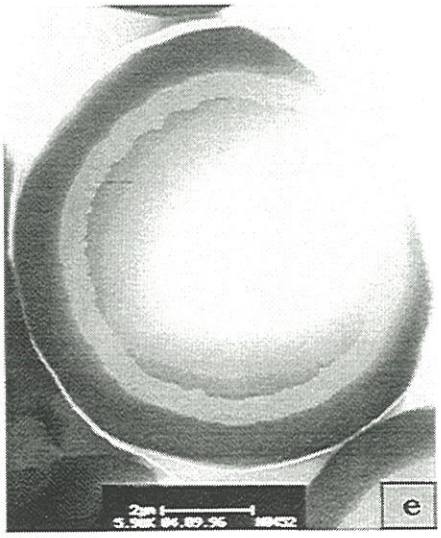

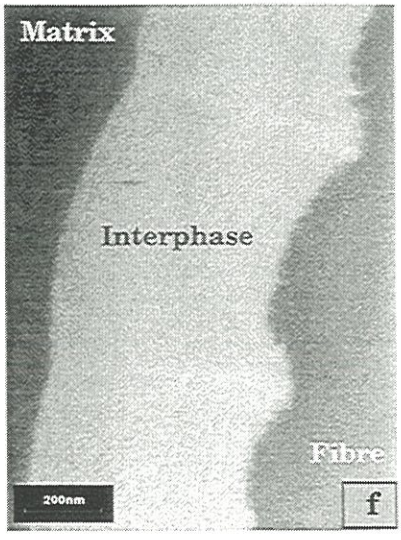

Figure 3: contrasted bright field TEM images of microcomposite and interface region for
(a), (b) A/M; (c),(d) A-HTT/M; (e),(f) A-HTT/Ic/M

For A-HTT-based C/C/C microcomposites, the same debonding phenomenon occurred in TEM samples [12], except for the interphase Ic (figure 3.e,f). In this latter case, interphase layer perfectly coated the fibre roughness, and a strong interface was then achieved. Chemical and/or physical bonding predominate on residual stresses, which are supposed to be equivalent to those for A-HTT/M microcomposite. This is a case where the transverse residual stresses are in tension with a real chemical and/or physical bonding. Moreover, TEM observation confirms the more disorder microtexture of Ic, compare to matrix (figure 2), noticeable by the higher electron density of the interphase in contrasted bright field image (figure 3.f).

Thus interface bonding strength changes according to the nature of the interphase. A-HTT/M microcomposites and corresponding materials, with interphase Ia or Ib, have a weak interface, due to transverse tensile residual stresses, whereas A-HTT/Ic/M microcomposites have a strong interface, due to a strong chemical and/or physical bonding.

3.1.3 - SEM observation of polished transverse sections

Observations were made on thick slices of A-HTT/M microcomposite and corresponding materials, with interphase Ia or Ib, to check if debonding, which was seen in TEM, is representative of the original materials, or due to thermal stress release. SEM micrographs (figure 4) show that debonding is much less important as what is seen by TEM. So it can be likely attributed to thermal stress release by thinning down to very thin slice. SEM and TEM cross checking allows to conclude that A-HTT/M is more debonded than A-HTT/Ia/M and that A-HTT/Ib/M is not; whereas TEM shows that transverse residual stress are in tension in those systems.

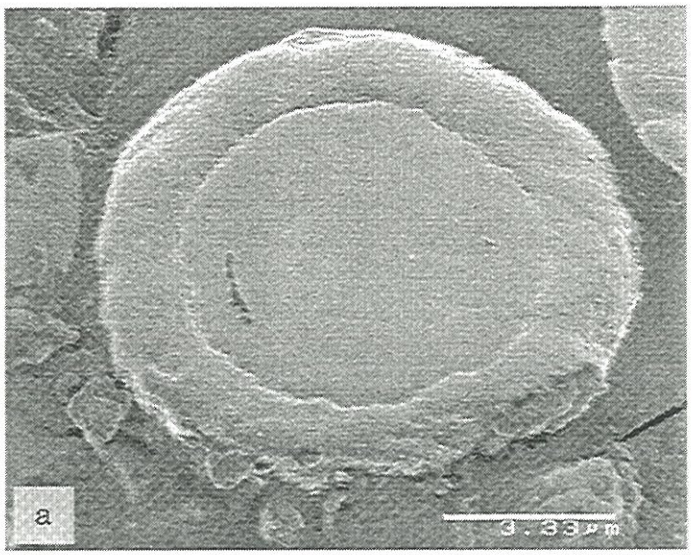

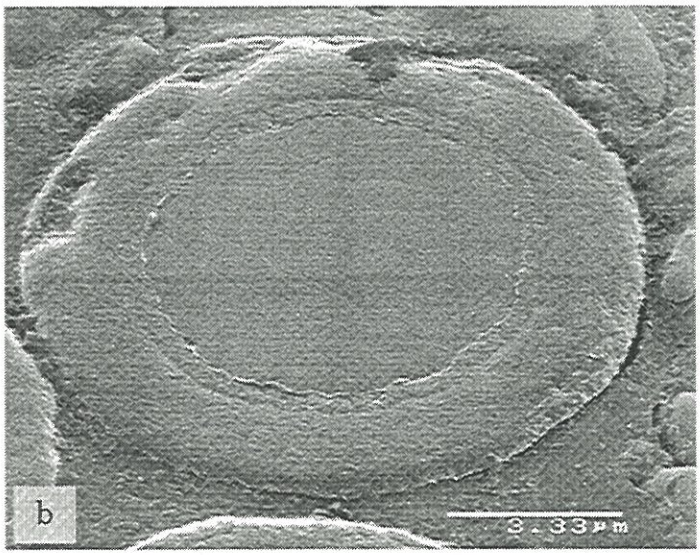

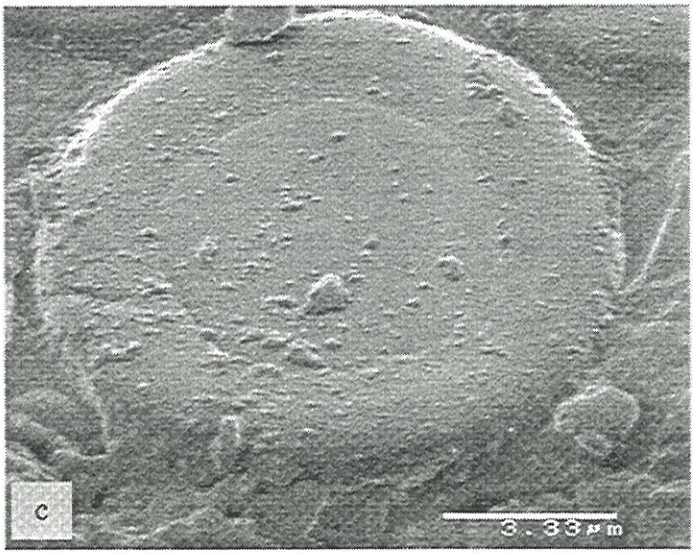

Figure 4: transverse polished sections, observed by SEM, of
(a) A-HTT/M; (b) A-HTT/Ia/M; (c) A-HTT/Ib/M

3.2 - Mechanical behaviour

3.2.1 - Load-strain curves

As previously seen for reference C/C microcomposites [8], two types of tensile curves are encountered for C/C/C microcomposites:

- curves linear up to failure, with some stress stiffening as for carbon fibres (figure 5.a),
- curves with singularities (arrow in figure 5.b), which are, most of the time, not associated with a significant change in curve slope; these singularities denote a load fall : they are supposed to mark the matrix failure.

Comparison with the few collected fracture surfaces showed that curves with singularities were generally connected with fibre pull-out, i.e. evidence of a non-brittle behaviour. On the other hand, linear curves were recorded when flat fracture surfaces were collected, evidencing a brittle fracture.

Two different groups were appearing among the different materials. In one hand, F/M and F/Ia/M microcomposites exhibited both brittle and non-brittle behaviours, depending on the fibre treatment. In an other hand F/Ib/M and F/Ic/M microcomposites exhibited almost exclusively brittle behaviours, whatever the fibre treatment. Details on the different frequencies are emphasised in figure 6:

- *F/M and F/Ia/M* were seen to exhibit the same trend. First, microcomposites reinforced with heat-treated fibres display a higher frequency of non-brittle behaviours. Transverse CTE of fibre changes with heat-treatment as carbon planes lined up along fibre axis : a larger transverse shrinkage of heat-treated fibre occurs, which creates some debonding at the interface (weak interface). Secondly, the interface is stronger when the fibre has been previously surface-treated. The addition of Ia interlayer with a microtexture

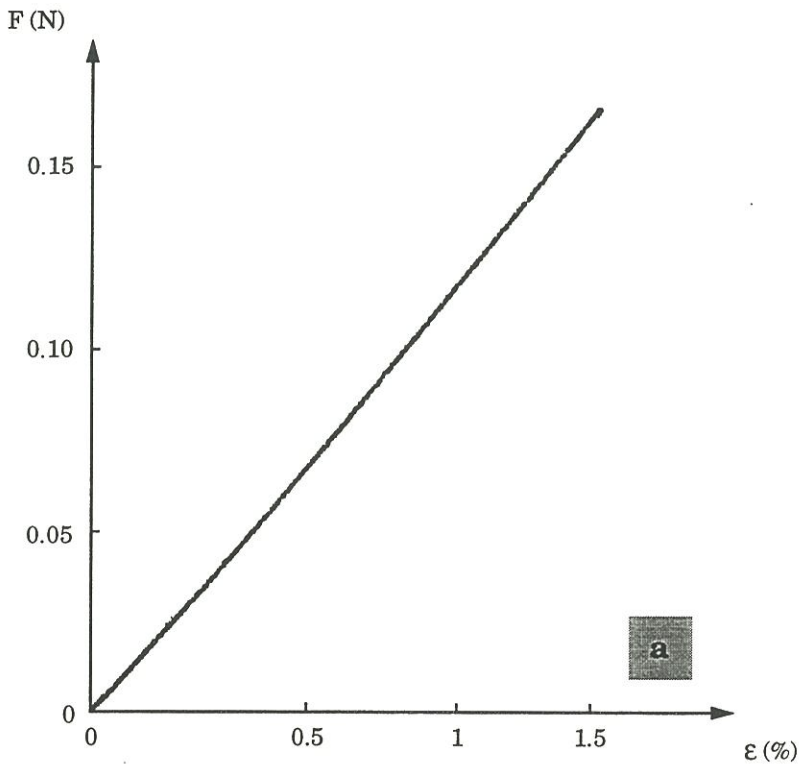

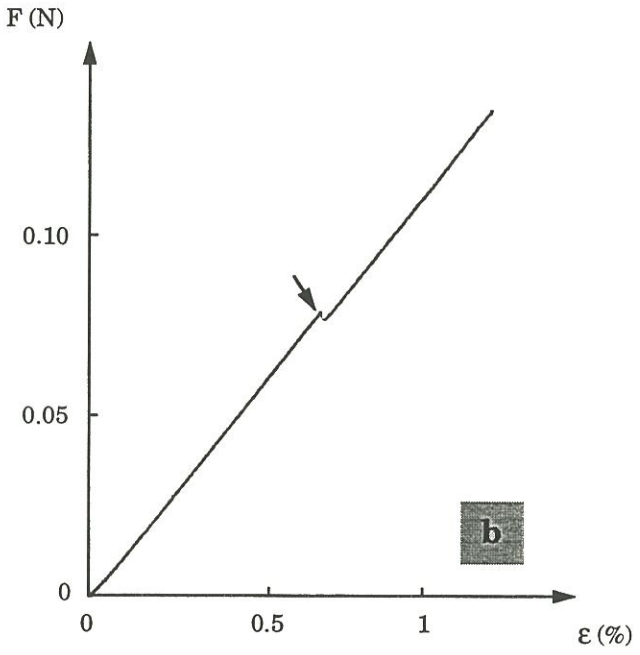

Figure 5: load-strain curves obtained in tension for C/C/C microcomposites
(a) linear curve; (b) curve with singularity (arrow)

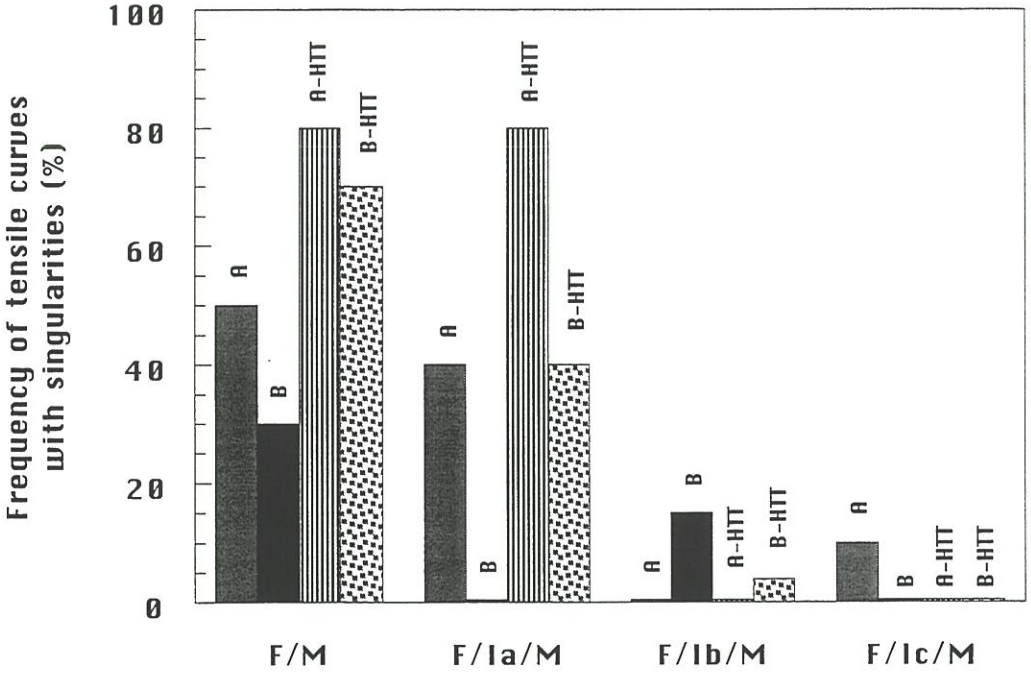

Figure 6: frequency of tensile curves with singularities according to fibre type and interphase

close to that of the matrix (Ae = 15° compared to 17°) did not change the interface so much. It just emphasised the physical bonding effect created by the roughness: B/Ia/M and B-HTT/Ia/M were more frequently brittle.

• *F/Ib/M and F/Ic/M* microcomposites, with Ib or Ic as interphase, are characterised by linear curves whatever the reinforcement. It means that interphases Ib or Ic lead to brittle behaviour, i.e. a stronger interfacial bonding. SEM fracture examinations have shown only brittle fractures in the case of F/Ic/M with a statistical confidence (figure 7). The strong fibre-interphase bonding, seen in TEM (figure 3.c), is then confirmed for F/Ic/M microcomposites whatever the type of fibre. On the contrary F/Ib/M has still a brittle behaviour, but a less strong interphase (lower debond energy) evidenced by the debonding during thinning.

3.2.2 - Fracture mirrors

Fracture surfaces present systematically a mirror pattern (figure 7), as already reported elsewhere [8]. The constant $\mathcal{A}$, which is specific to each material is given by :

$$\sigma = \frac{\mathcal{A}}{\sqrt{R_m}}$$

with σ, the fibre stress-to-failure, and R_m the mirror radius. It has been determined for A and A-HTT fibres (tensile gauge length: L=10mm), and was respectively evaluated to 2.6 and 2.2MPa.m$^{1/2}$ [8]. This way, fibre stress-to-failure in microcomposites can be determined.

Results on A/Ic/M and A-HTT/Ic/M fracture surfaces are listed in Table 3. In this table, $\sigma_{f,mirror}$ is compared to fibre stress σ_f, when load at failure is shared by the fibre and the matrix (for flat fracture) assuming that no residual stress exists ($\sigma_f=E_f.\varepsilon_R$). The data show that $\sigma_{f,mirror}\geq\sigma_f$, i.e. fibres were in axial tension (sometimes close to the equilibrium) in these microcomposites; but never in axial compression as generally found in real C/C composites.

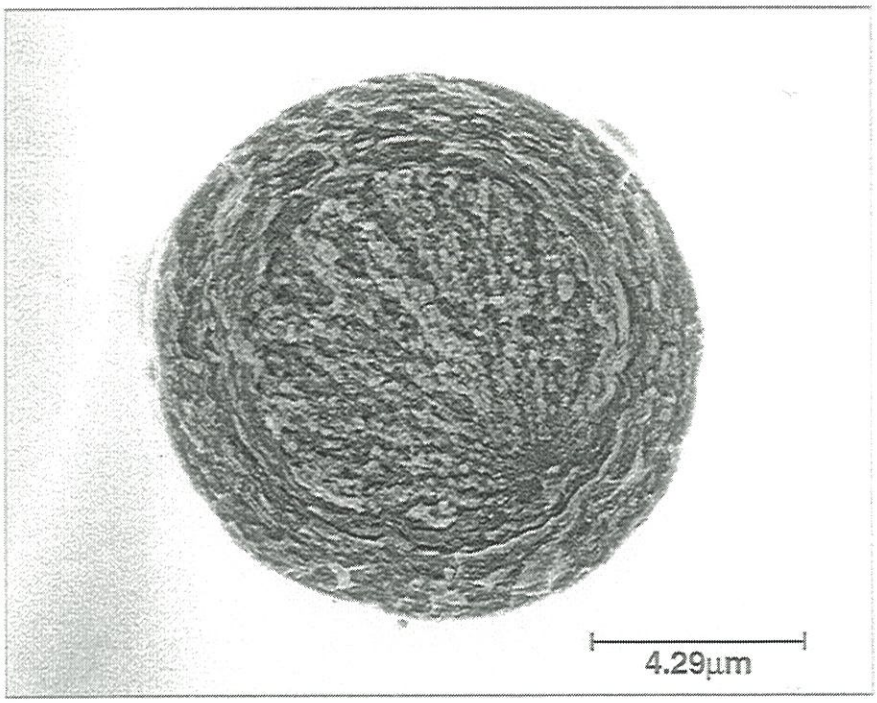

Figure 7: SEM observation of a flat fracture obtained on a tensile tested A-HTT/Ic/M microcomposite

Table 3. Analysis of fracture surfaces of F/Ic/M microcomposites

Material	Mechanical properties			Mirror data	
	ε_R (%)	σ_R (MPa)	σ_f (MPa)	R_m (μm)	$\sigma_{fmirror}$ (MPa)
A/Ic/M	0.79	1400	2010	0.738	3026
	0.96	1553	2436	1.10	2473
	1.06	1917	2699	0.651	3222
	0.77	1251	1969	1.11	2463
	0.95	1396	2424	1.01	2591
	1.47	2325	3750	0.428	3974
	1.13	1801	2871	0.694	3121
	1.11	1756	2841	0.836	2874
A-HTT/Ic/M	1.18	2196	3009	0.691	3127
	1.01	1692	3197	0.450	3279
	1.29	2100	4067	0.222	4659
	1.12	1917	3536	0.364	3646
	0.89	1543	2804	0.536	3005

3.2.3 - Interface and ultimate performances

Ultimate performances of the composites can be improved by controlling carbon anisotropy in the interphase, but only if thermal transverse residual stresses are in tension. This point is evidenced in figure 8, which shows the variations of the stress- and strain-to-failure of the microcomposites versus the microtexture of the carbon deposited at the interface (Ae). These plots show two different groups : microcomposites reinforced with A, and B fibres, and microcomposites reinforced with heat-treated fibres. All the corresponding data are listed in Tables 4 and 5.

Microcomposites reinforced with A, and B fibres .

Mechanical performances of C/C/C microcomposites obtained with B fibres were similar whatever the interphase (figure 8). Even worse, stresses- and strains-to-failure of A fibre-based microcomposites decreased with decreasing the anisotropy of the interphase. As the fibre/matrix bonding in the reference microcomposites is already strong (thermal stress), with a high frequency of brittle behaviours (figure 6), it is evident that the effect of increasing the chemical bonding by decreasing the anisotropy is worse and worse.

Failure strain Weibull plots for the different microcomposites, compared to that of the bare fibre, illustrate that degradation (figure 9). A/M exhibited a double distribution with flat fracture surfaces for the highest (σ_R, ε_R), and pull-outs for the bottom of the distribution [8]. Interphases Ia, Ib and finally Ic gave distributions with lower and lower means values.

Microcomposites reinforced with heat-treated fibres.

For heat-treated fibres, microtexture of the interphase has a great effect on mechanical performances (σ_R, and ε_R), for A-HTT/I/M as well as for B-HTT/I/M (figure 8). As fibre/matrix bonding in the reference microcomposites is weak with mainly a non-brittle behaviour, increasing the chemical bonding

Table 4. Mechanical results for carbon/carbon microcomposites (without carbon interphase)

	E (GPa)	ε_R (%)	σ_R (MPa)
A/M	157 (13)*	1.26 (0.20)	1978 (415)
B/M	158 (12)	1.05 (0.15)	1663 (309)
A-HTT/M	176 (14)	1.15 (0.19)	2031 (432)
B-HTT/M	174 (14)	0.96 (0.20)	1667 (376)

* standard deviation in brackets

Table 5. Mechanical results of C/C/C microcomposites

	E (GPa)	ε_R (%)	σ_R (MPa)
A/Ia/M	154 (13)*	1.19 (0.24)	1824 (380)
B/Ia/M	164 (12)	1.15 (0.20)	1876 (324)
A-HTT/Ia/M	157 (13)	1.11 (0.22)	1732 (351)
B-HTT/Ia/M	162 (14)	0.93 (0.13)	1478 (252)
A/Ib/M	138 (25)	1.20 (0.19)	1637 (245)
B/Ib/M	165 (34)	1.12 (0.25)	1882 (687)
A-HTT/Ib/M	158 (14)	1.60 (0.31)	2513 (505)
B-HTT/Ib/M	178 (19)	1.33 (0.32)	2383 (681)
A/Ic/M	163 (12)	1.06 (0.24)	1732 (444)
B/Ic/M	160 (11)	1.15 (0.20)	1844 (355)
A-HTT/Ic/M	168 (11)	1.38 (0.25)	2317 (453)
B-HTT/Ic/M	170 (15)	1.10 (0.17)	1871 (358)

* standard deviation in brackets

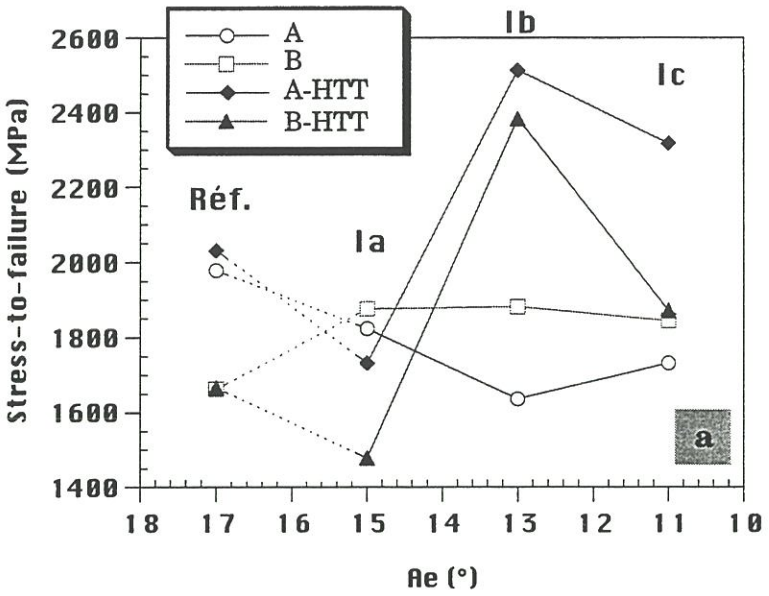

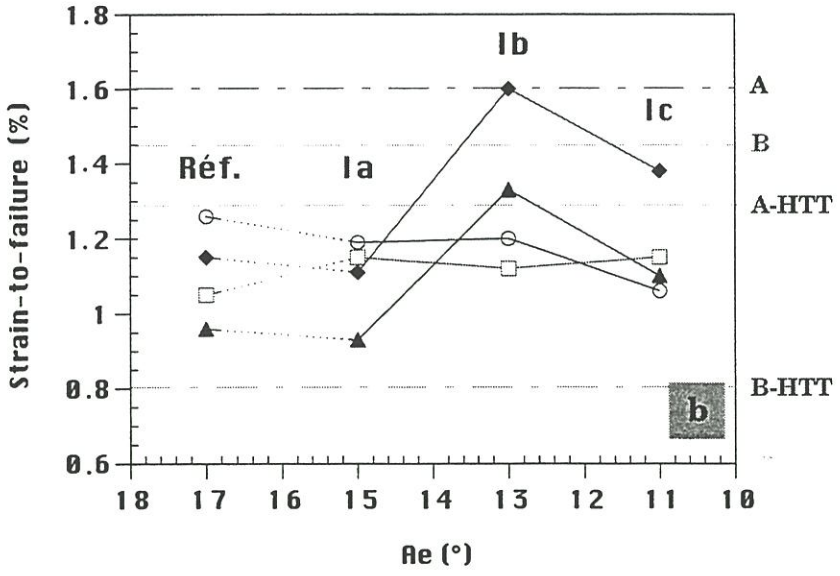

Figure 8: influence of interphase microtexture (Ae) on C/C/C microcomposites mechanical properties: (a) stress- and (b) strain-to-failure

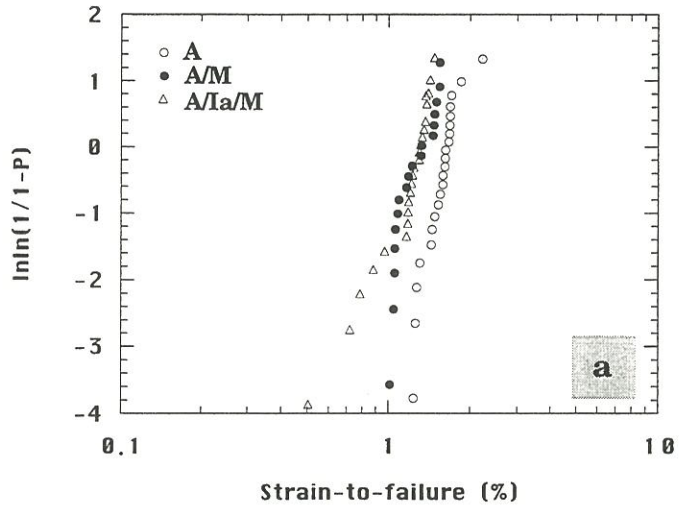

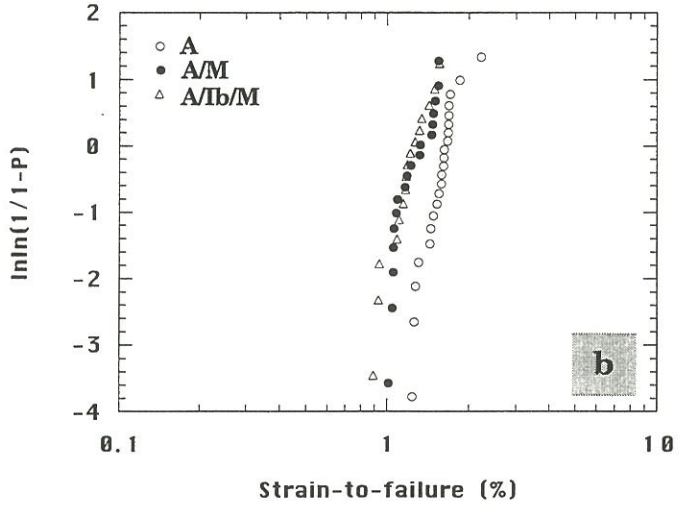

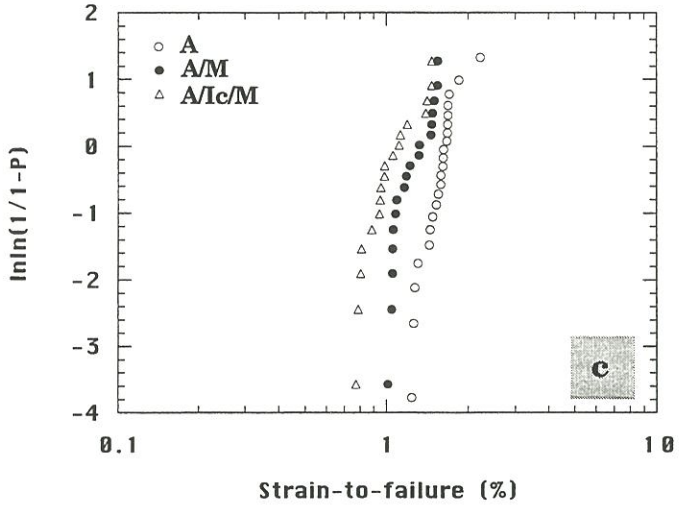

Figure 9: strain Weibull plots for A/I/M microcomposites compared to Weibull plots for A fibre and A/M microcomposite (a) A/Ia/M; (b) A/Ib/M; (c) A/Ic/M

(Ia<Ib<Ic) leads to a brittle behaviour but with an improvement of the performances. It was observed that transverse thermal residual stresses are tensile in A-HTT/M microcomposites. Thus, those improvements are mainly controlled by the chemical bonding strength related to the anisotropy of the pyrocarbon at the fibre surface.

Strain-to-failure attained with Ib (and Ic, in less extent) was much higher than that of the corresponding bare fibre (A-HTT and B-HTT). A-HTT/Ib/M strain-to-failure recovered the optimal values of A fibre. This is clearly demonstrated by the Weibull plots (figure 10 and 11). For many reasons, this improvement of fibre performances in microcomposites can be understood by a healing of surface flaws, created during the annealing of the fibre. First, a similar mechanism has been observed with the reference B-HTT/M microcomposite. Then, SEM observation of a A-HTT/Ic/M fracture surface supports this hypothesis (figure 12): it shows the carbon interphase infiltrated in a surface flaw of the fibre. Finally, the fibre could be in axial compression due to thermal CTE mismatch, but it is not the case :

- fracture mirrors have shown that fibre are either in tension, or in equilibrium in these microcomposites,
- axial residual tensile stresses have been evidenced directly for B-HTT/M [8] by the observation of a shrinkage in each of the two complementary broken ends.

Increase of performances has to be related to the recovery of the highest fibre performances, in a pure elastic mechanism (brittle fracture). These improvements are not due to a dissipating mechanism related to a matrix multicracking damaging.

In the particular case of B-HTT/Ib/M, two populations of failure strain data are observed (figure 11.b). The lower one is close to that observed for B-HTT/M, whereas the higher one is such that strain distribution is the same as

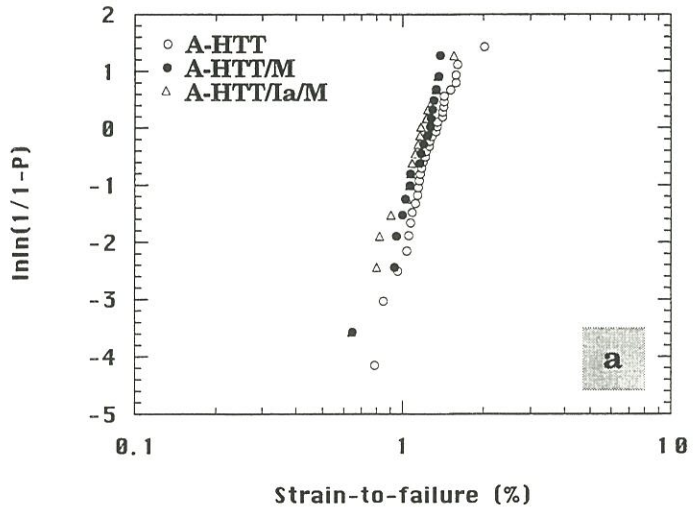

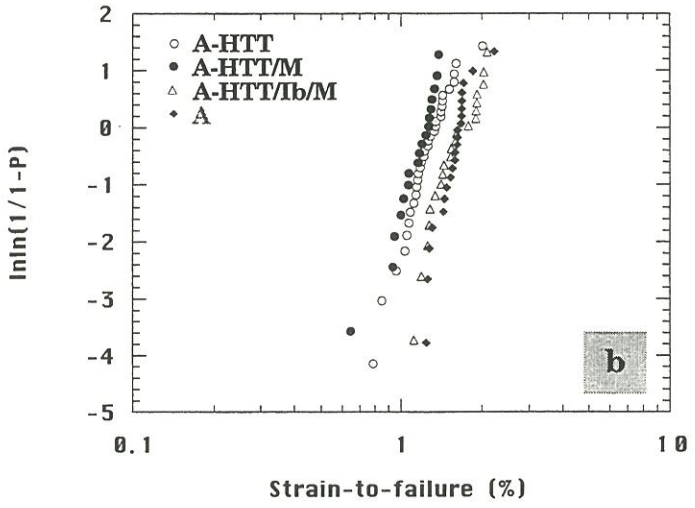

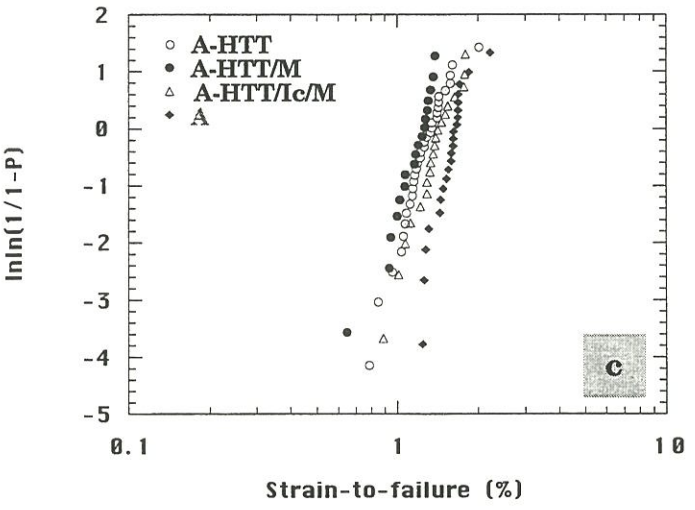

Figure 10: strain Weibull plots for A-HTT/I/M microcomposites compared to Weibull plots for A-HTT and A fibres and A-HTT/M microcomposite
(a) A-HTT/Ia/M; (b) A-HTT/Ib/M; (c) A-HTT/Ic/M

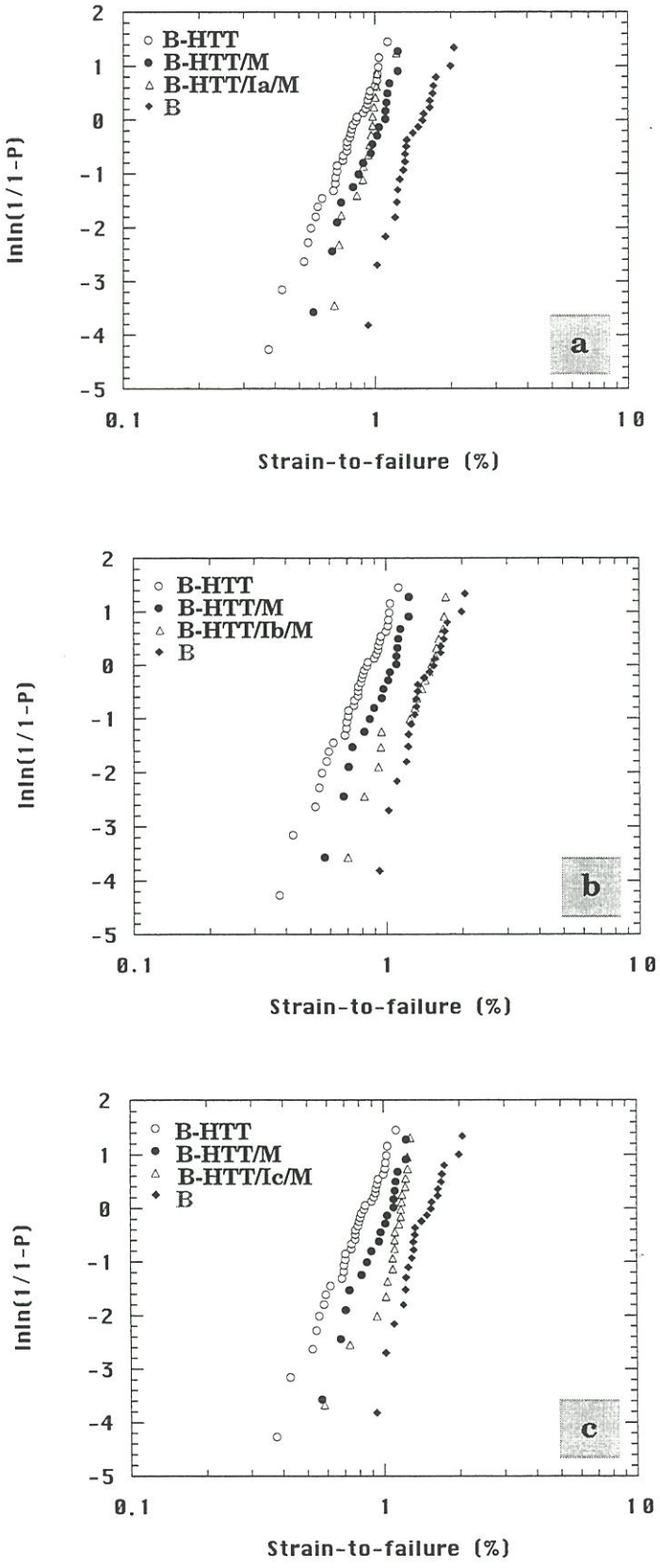

Figure 11: strain Weibull plots for B-HTT/I/M microcomposites compared to Weibull plots for B-HTT and B fibres and B-HTT/M microcomposite
(a) B-HTT/Ia/M; (b) B-HTT/Ib/M; (c) B-HTT/Ic/M

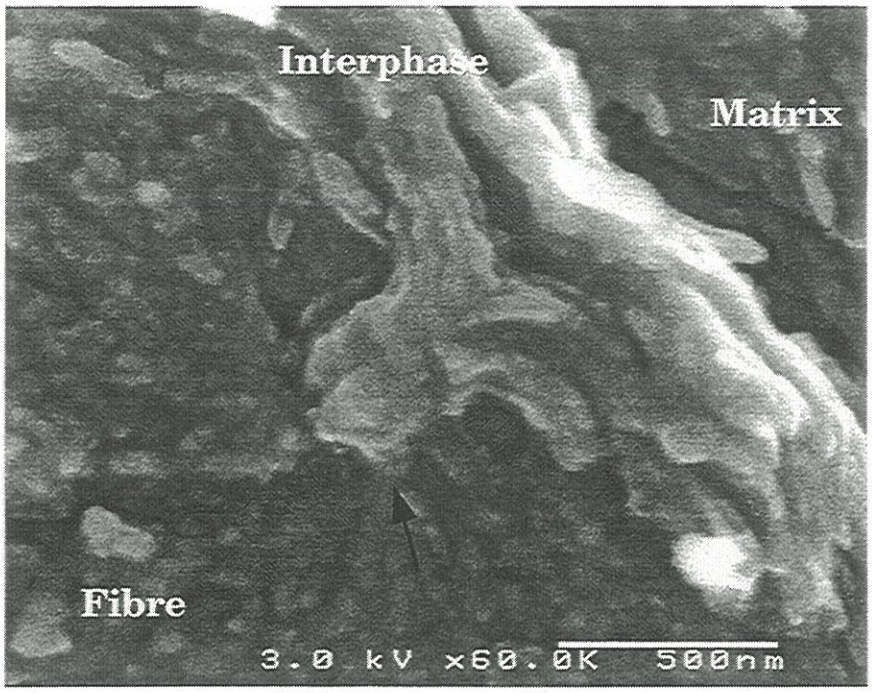

Figure 12: SEM micrograph of an interface region
of a A-HTT/Ic/M microcomposite, showing pyrocabon interphase
which penetrates in a hole at fibre surface (arrow)

that of B fibre. So an improvement is effective only on the last population for this material.

Otherwise, the increase in (ε_R, σ_R) data is such that, except for B-HTT/Ic/M, stresses to failure of these materials are even higher than for microcomposites reinforced with A or B fibre. A better fibre strength utilisation is then obtained with these materials. Difference observed between interphase Ib and Ic could be explained by the stronger interface bonding, generated by interphase Ic, which tends to decrease fibre strength utilisation as it was demonstrated by Zaldivar et al. [3].

A-HTT/Ic/M materials mechanical property data are still higher than those of the references. Here, a more disordered carbon (Ic) can both ensure a strong fibre/matrix chemical bonding, and improved mechanical properties. Oxidation resistance of the interface should be likely improved while retaining high mechanical performances.

3.3 - Microcomposites heat-treated to HTT2

When post-treated to HTT2, materials can be divided in 2 groups: (i) load-strain curves with large fibre pull-out (mm order) (F/M and F/Ia/M), and (ii) those with load strain curves with a catastrophic failure (F/Ib/M, F/Ic/M). Mechanical test data are respectively listed in Tables 6 and 7.

3.3.1 - F/M and F/Ia/M microcomposites

This first group of materials presented 3 different tensile curves depending on the load level of the extraction, i.e. the interfacial shear stress τ when fibre slides in pyrocarbon sheath (figure 13): curves of type (1) for low τ, of type (2) for intermediate τ, and of type (3) for high τ. All these curves presented first a short linear segment, followed by a non-linear curve which ends by a load-fall, and finally, for curves of type (1) and (2), a plateau was occurring at

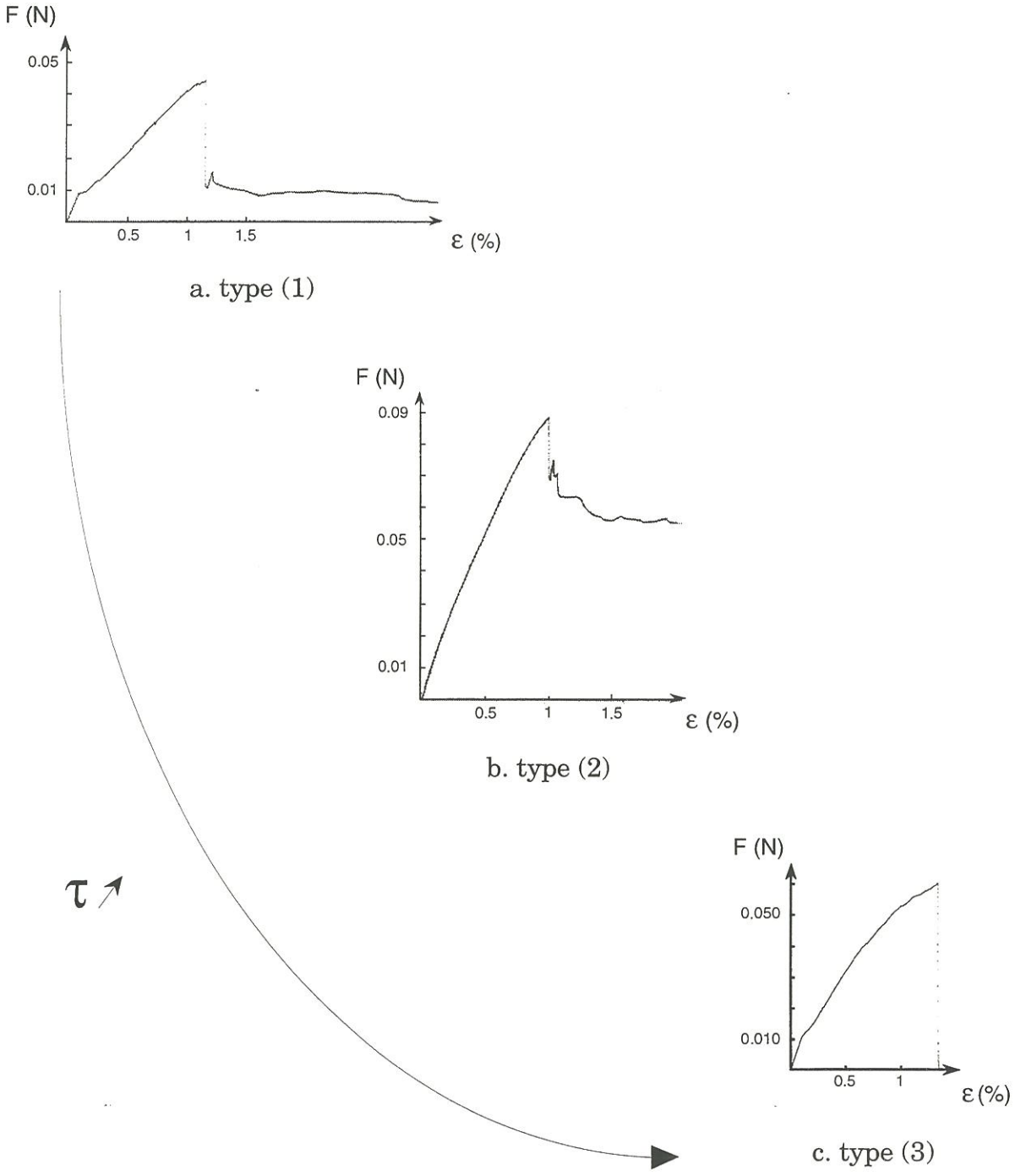

Figure 13: different types of load-strain curves obtained for F/M and F/Ia/M microcomposites after HTT2 according to friction forces (interfacial shear stress τ)

Table 6. Mechanical data for F/M and F/Ia/M microcomposites treated to HTT2

	Mechanical data					Interfacial shear stress		
	ε_R (%)	σ_R (MPa)	E (GPa)	$\varepsilon_{(\sigma max)}$ (%)	σ_{max} (MPa)	Low τ (MPa)	Intermediate τ (MPa)	Percentage of high τ
A/M	0.10	132	118	0.94	423	0.051	-	0
	(0.10)*	(156)	(29)	(0.27)	(120)			
B/M	0.08	95	109	0.94	394	0.026	-	0
	(0.11)	(183)	(22)	(0.2)	(137)			
A-HTT/M	0.06	82	147	1.13	832	0.278	13.5	20
	(0.03)	(40)	(29)	(0.34)	(211)			
B-HTT/M	0.10	135	137	1.21	995	0.190	5.6	40
	(0.09)	(98)	(27)	(0.29)	(254)			
A/Ia/M	0.16	228	143	0.88	656	0.175	1.06	20
	(0.12)	(155)	(23)	(0.30)	(176)			
B/Ia/M	0.22	336	154	0.89	868	0.096	5.42	40
	(0.16)	(267)	(27)	(0.18)	(273)			
A-HTT/Ia/M	0.11	136	119	1.08	637	0.148	-	40
	(0.07)	(85)	(19)	(0.28)	(155)			
B-HTT/Ia/M	0.08	115	138	1.13	815	0.110	-	40
	(0.03)	(43)	(18)	(0.25)	(244)			

* standard deviation in brackets

Table 7. Mechanical data for F/Ib/M and F/Ic/M microcomposites treated to HTT2

	ε_{el} (%)	σ_{el} (MPa)	E (GPa)	ε_R (%)	σ_R (MPa)
A/Ib/M	0.47 (0.12)*	882 (231)	187 (19)	0.53 (0.11)	952 (192)
B/Ib/M	0.52 (0.16)	974 (309)	187 (13)	0.54 (0.12)	1026 (239)
A-HTT/Ib/M	0.39 (0.33)	625 (513)	165 (20)	0.81 (0.13)	1289 (252)
B-HTT/Ib/M	0.34 (0.20)	665 (387)	195 (26)	0.63 (0.17)	1118 (248)
A/Ic/M	0.30 (0.08)	562 (167)	185 (13)	0.32 (0.08)	566 (164)
A-HTT/Ic/M	0.46 (0.13)	879 (257)	189 (14)	0.51 (0.07)	941 (161)

* standard deviation in brackets

constant load. Those features are similar to the features reported for push-out curves.

SEM observation of the loaded samples showed systematically fibre pull-out. Extracted length were generally very large: centimetre order. It could exceed the gauge length, which means that extraction occurred also in jaws. So, fibre/matrix bonding must be very weak. This was confirmed by SEM observations of polished cross-sections of microcomposites before loading, which showed that there was a gap between fibre and pyrocarbon deposit (figures 14.a, 14.b). Heat-treatment to HTT2 has evidenced the difference of shrinkage undergone during the thermal rearrangement of the constituents in the material. This debonding seems to be extended all along the microcomposite. Matrix and fibre bonding would then be limited to the jaws during the tensile test.

Tensile curves can then be explained in accordance with two possibilities:

- contact between fibre and matrix in jaws is connected with a bonding; the end of linearity would indicate the matrix failure (about 0.1% of strain); then, interfacial debonding and sliding of fibre would take place (non-linear part of the curve); a sudden brutal debonding of all the fibre (at jaws) would happen involving the load-fall, followed by pure fibre sliding,
- fibre is solicited by fibre-matrix contact at jaws by shear; the end of linearity would be a threshold strength beyond which fibre sliding would take place. The load-fall would be the result of matrix failure at about 1% of strain (Table 6), followed only by fibre sliding in matrix sheath.

Tensile tests on 25mm gauge length have allowed to extract separately fibre and matrix sheath, with a long enough length to perform tensile test at a 10mm gauge length. This way, fibre and matrix sheath have been characterised separately. Young modulus of extracted fibres: E=410GPa (from

A/M+HTT2 microcomposite) is of same order as that for the A-HTT2 bare fibre (E=400GPa) (Table 1). But stress- and strain-to-failure are much lower: σ_R=2250MPa, ε_R=0.55% (vs.: σ_R=3336MPa, ε_R=0.84% for A-HTT2 bare fibre). This means that fibre is degraded in the microcomposites A/M after the post-treatment HTT2.

Tensile tests, conducted on extracted matrix sheath, have given the following results : E=36GPa, σ_R=449MPa and ε_R=1.23%. Considering literature data for pyrocarbons [13], the value obtained for the elongation is very high compared to the 0.5% of the literature. However, pyrocarbons tested in other works were often bulk pyrocarbons instead of a 2µm-thick tube. In short, strain-to-failure of that post-treated pyrocarbon is of the order, or even higher than the failure elongation of the bare fibres.

The second hypothesis for load-strain curves is validated by these results on extracted matrices. Matrix failure occurs when the load suddenly falls to about 1% of strain. Moreover, this failure mechanism would explain why for some tested microcomposites, load-strain curves finished without any plateau (figure 13.c). In that case, friction must be too high, so matrix failure involves the catastrophic failure of the fibre.

When friction forces are not too high to involve fibre failure, which is the more frequent case (curves 13.a 13.b), fibre slides in the matrix sheath with a constant force F_p. This force allows to determine the interfacial shear stress τ by the following relation:

$$\tau = \frac{F_P}{2\pi r \ell} \qquad (2)$$

where r is the fibre radius, and ℓ the debonding length.

Interfacial shear stresses were then calculated. Two groups were obtained: low τ (inferior to 1MPa), and intermediate τ (1 to few MPa) (Table 6). Considering these values, deduced from curves of types (1) and (2) and percentage of curves of type (3) (Table 6), A/M and B/M materials are characterised by the lowest friction, so it was concluded that fibre-matrix gap is

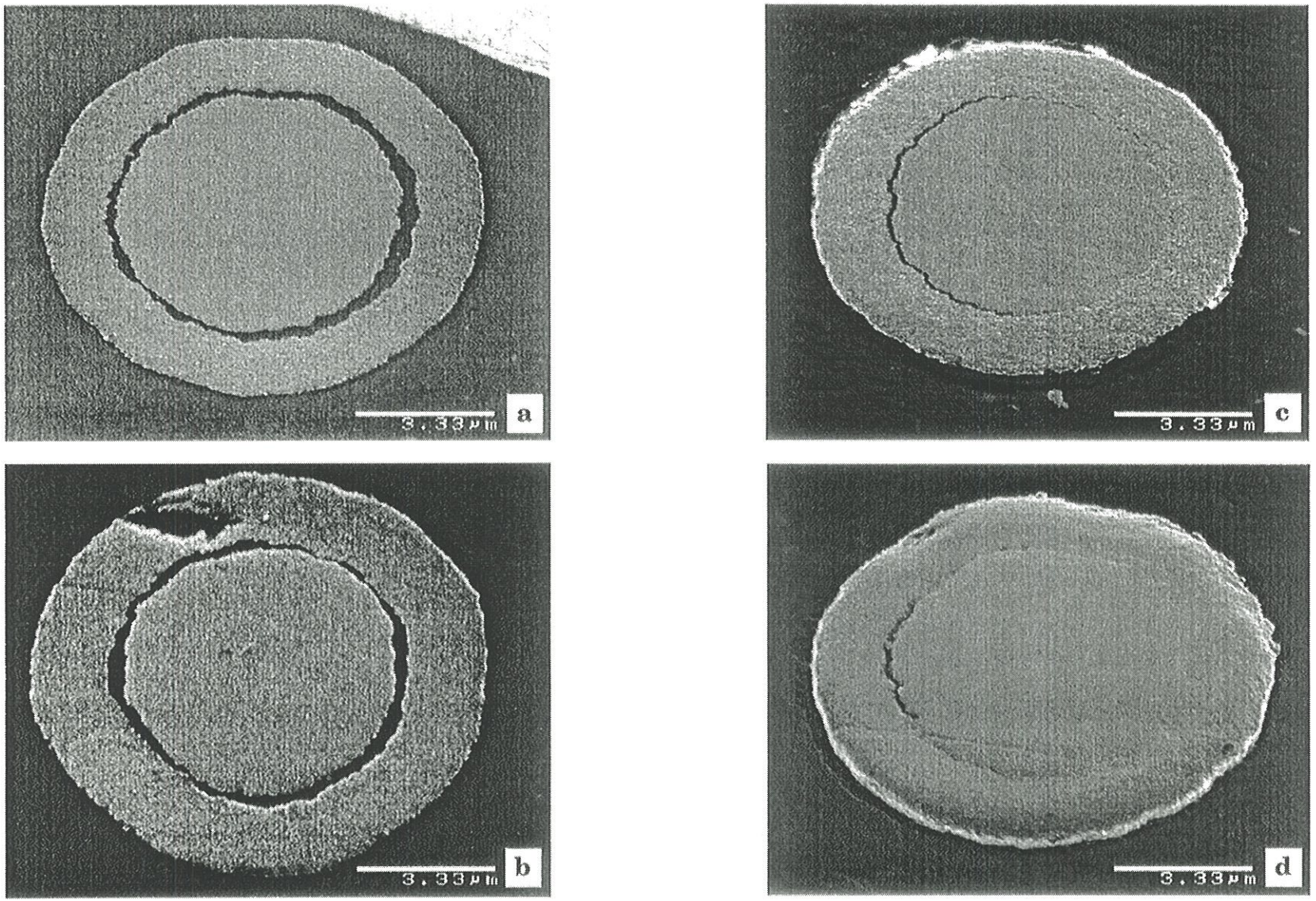

Figure 14: SEM images of polished cross sections of microcomposites after HTT2 showing:

- high fibre-matrix debonding: (a)A/M; (b) A/Ia/M
- low partial fibre-matrix debonding: (c) A/Ib/M; (d) A/Ic/M

the most important for those materials. These results have to be explained not only in term of transverse CTE, but also regarding the irreversible structural changes in fibre regarding pyrocarbon during the different heat-treatments [14]. In short, fibres previously heat-treated (HTT) possess a higher CTE and a lower shrinkage during the HTT2. On the contrary, A and B fibres have a lower CTE and a higher rearrangement, and thereafter a higher shrinkage, during the HTT2. As a result, before the post-treatment, debonding is higher with the stabilised fibres (higher CTE); but after the post-treatment, the shrinkage of A and B fibre is much more important and the gap is now larger for that material.

Otherwise, comparison of τ distribution for A/M+HTT2 and A/Ia/M+HTT2 microcomposites (Table 6) points out the compliance effect of the interphase : debonding is attenuated and τ higher.

3.3.2 - F/Ib/M and F/Ic/M microcomposites

Mechanical test data are listed in Table 6. Load-strain curves of microcomposites, with interphase Ib or Ic, did not show any plateau. But the same features, as for the non-heat-treated materials, are seen in figures 15 and 16. Thus, F/Ib/M and F/Ic/M materials, treated to HTT2, were characterised by a stronger bonding than F/M and F/Ia/M microcomposites. This is corroborated by SEM observation (figure 14): the large gap noticed between fibre and matrix for the former materials did not appear for F/Ib/M and F/Ic/M microcomposites, which have shown only partial debonding.

F/Ib/M+HTT2 microcomposites, reinforced with A and B fibres, mainly showed a brittle tensile behaviour (figure 17). On the contrary, microcomposites, reinforced with heat-treated fibres, exhibited, for the most part, tensile curves with singularities. These singularities mark limited debonding and sliding, linearity keeping on after that. Then, a lower bonding characterises these materials compared to A/Ib/M or B/Ib/M.

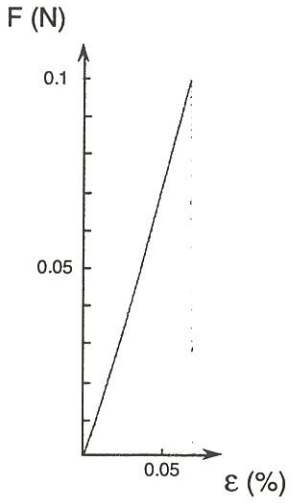

Figure 15: brittle linear behaviour obtained for
F/Ib/M microcomposites after HTT2

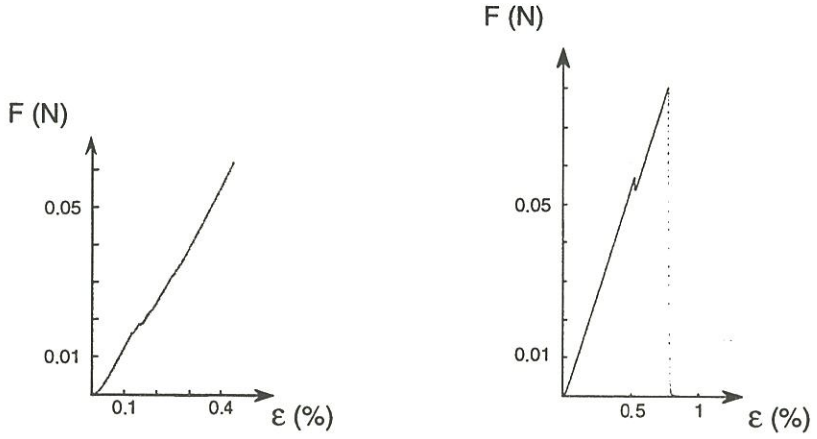

Figure 16: load-strain curves observed for F/Ib/M microcomposites
after HTT2, containing some singularities,
which disturb momentarily the linearity

For A/Ic/M+HTT2 and A-HTT/Ic/M+HTT2 microcomposites, less tensile curves with singularities were observed compare to interphase Ib, especially for A-HTT fibre (figure 17). A stronger bonding interface is then achieved with interphase Ic.

As a result interphases Ib and Ic are seen to accommodate the shrinkage mismatching between fibre and matrix when a post-treatment is necessary. It is likely that a non-debonding interface can be managed regarding to post-treatment.

Strains-to-failure of microcomposites, constituted with A or B fibre and interphase Ib, are the same (0,5%). Strains-to-failure for heat-treated fibre microcomposites are higher and equal to values of bare fibres treated alone to HTT2. Considering properties of degraded fibres in A/M+HTT2 microcomposite, if the same degradation has occurred in A/Ib/M+HTT2 and B/Ib/M+HTT2, strain to failure of these materials would be the same as the degraded fibre one. So, fibre controls the failure of F/Ib/M+HTT2 materials with a probable degradation of A and B fibres, and intact mechanical properties for A-HTT and B-HTT fibres.

Lower mechanical properties are obtained for F/Ic/M+HTT2. Fibre would be either degraded, compared to preceding materials, due to the stronger interface bonding before HTT2, or in residual axial tension in the microcomposite.

Considering the strains-to-failure of matrix sheath, extracted from a A/M+HTT2 material (1.2%), and of HTT2 fibres ($\leq$0.8%), a case, inverse to what was observed for non-heat-treated microcomposites, results: $\varepsilon_{R,m} > \varepsilon_{R,f}$. Fibre failure occurs first, followed immediately after by matrix failure.

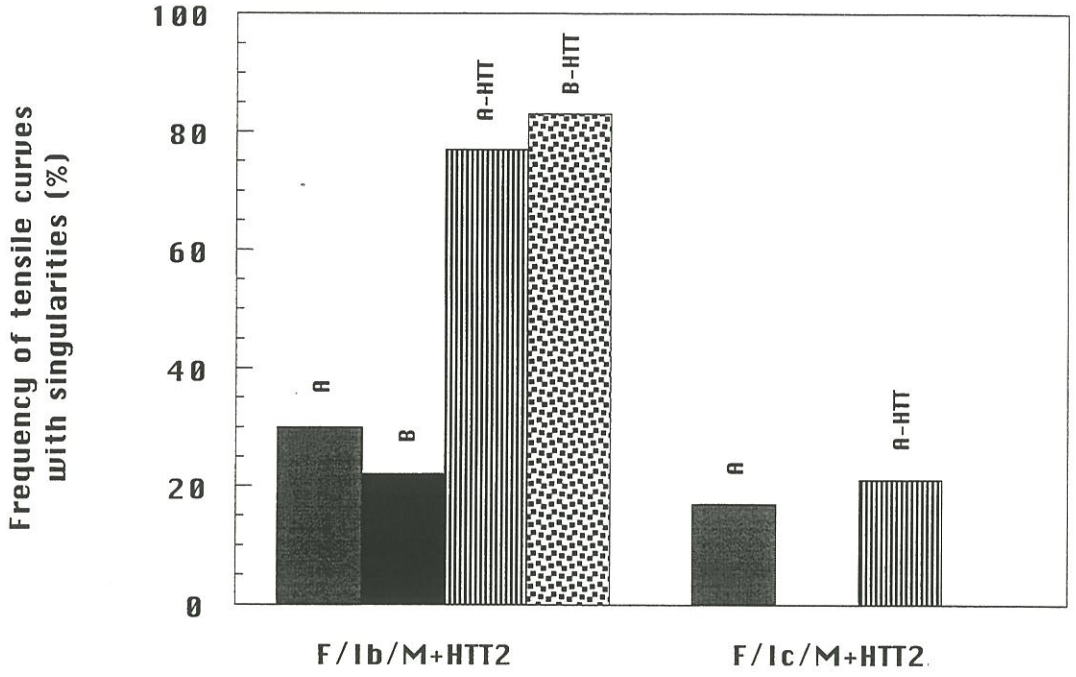

Figure 17: frequency of tensile curves with singularities according to fibre type and interphase for F/Ib/M and F/Ic/M treated to HTT2

4 - CONCLUSIONS

Carbon/carbon microcomposites, before HTT2, are **inverse composites**: $\varepsilon_{R,m} < \varepsilon_{R,f}$ whereas carbon/carbon microcomposites, after post-treatment, are **regular**: $\varepsilon_{R,m} > \varepsilon_{R,f}$ as fibre strain-to-failure is very degraded by the annealing.

For both of them, bonding strength controls the mechanical behaviour. So, transverse residual stresses at interface are of prime importance, as well as strong chemical and/or physical bonding.

Microcomposites before HTT2.

Fibre/matrix interface switches from strong to weak, and thereafter the mechanical behaviour from brittle to non-brittle (figure 18.a, 18.b), when fibre is previously stabilised by annealing (HTT). A larger shrinkage is observed for heat-treated fibres during cooling-down, which involves a transverse residual tension at the interface. But, that fibre did not allow to test the debonding ability (low $\varepsilon_{R,f}$, axial residual tension in the fibre, etc.).

On the other hand, when a strong interface is achieved by using a more disordered interphase microtexture (Ic), which overwhelms residual stresses, all microcomposites are characterised by a brittle behaviour.

A compromise is obtained with the interphase Ib, with a microtexture intermediate between that of matrix and that of interphase Ic. Ib and Ic interphases involve an improvement of mechanical properties (ε_R,σ_R) for microcomposites reinforced with heat-treated fibres. For non-heat-treated fibres, the fibre/matrix bonding is initially strong, and is stronger with the pyrocarbon deposits used for the interphase, favouring brittle fracture. Otherwise, Ib and Ic interphases lead to a healing of fibre surface defects, created by the HTT, and to the utilisation of these improved fibres in the material up to 100% of their perfomances with Ib interphase. For Ic, fibres fail before, by notch effect, because of a strong resulting chemical bonding due to its more disordered microtexture.

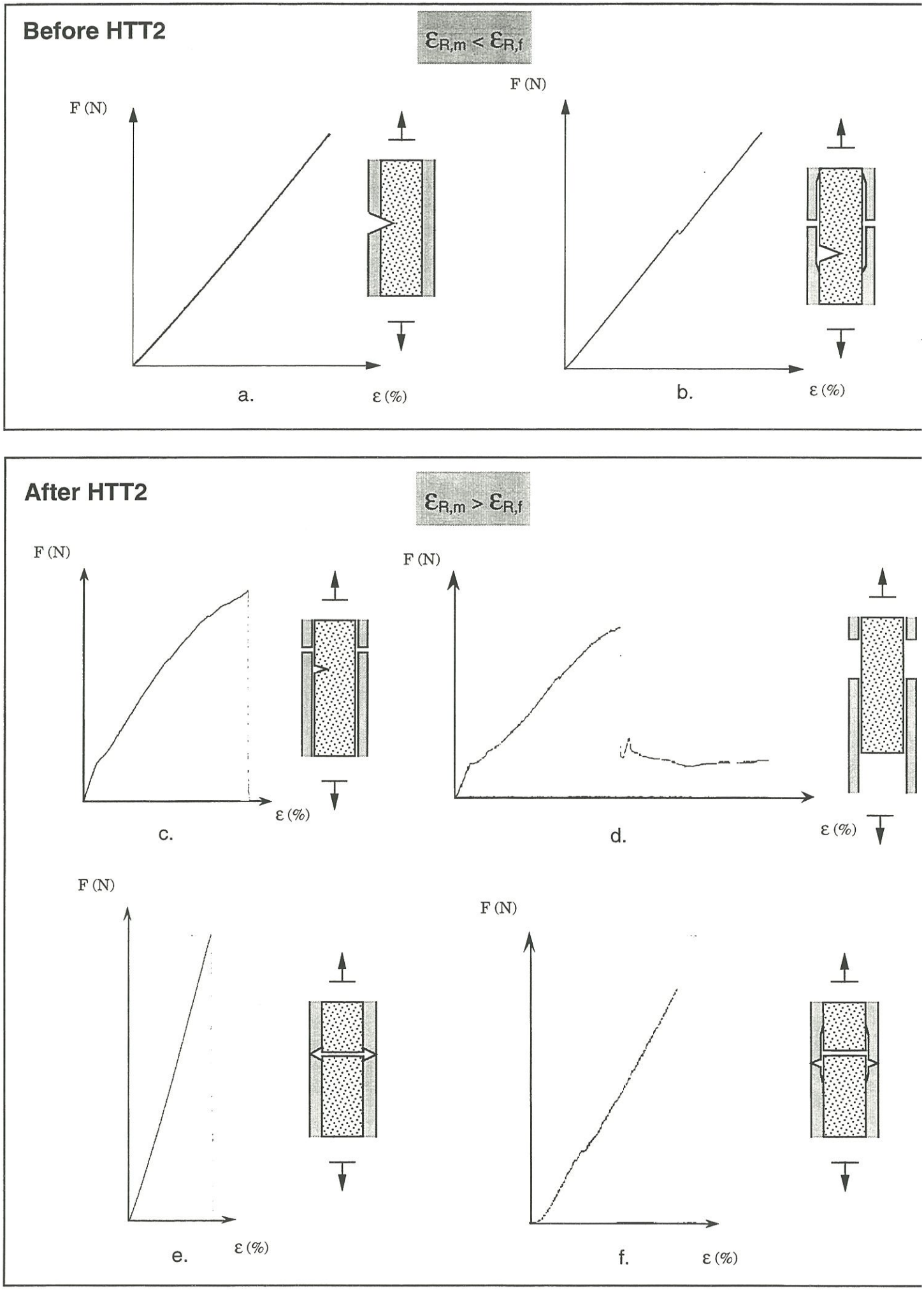

Figure 18: mechanical behaviours observed for microcomposites

Microcomposites after HTT2.

Mechanical behaviour of these materials depend on interphase microtexture. Fibre heat-treatment is of minor importance, constituting sub-groups of the two principal mechanical behaviours observed. These behaviours are the following:

- curves with fibre extraction (figure 18.c,d), which yield a plateau for low and intermediate τ. Complete fibre-matrix debonding characterises these materials, for which failure (or ε_{max}, σ_{max}) is controlled by matrix failure as fibre is very little solicited;
- curves with catastrophic failure (figure 18.e,f) resulting from relatively strong interface even after HTT2 due to the accommodation of difference in thermal expansion of constituents by the interphase (Ib,Ic). These materials are then controlled by fibre, which has a strain-to-failure inferior to the matrix one.

This work points out the importance of the use of a carbon interphase of controlled microtexture in carbon/carbon composites. Moreover, it shows that the more disordered interphases (Ib,Ic), are giving the higher mechanical properties before HTT2, and are well behaving towards HTT2 (interface still well bonded).

Acknowledgements

This work has been supported by SEP and CNRS through a grant given to B.T. The authors are indebted to J. M. Jouin from SEP and J. Lamon from LCTS, for valuable discussion, and G. Bondieu from SEP and M. Alrivie from LCTS for technical assistance.

REFERENCES

[1] C.R. Thomas, E.J. Walker, Effects of PAN carbon fibre surface in carbon-carbon composites, Proceedings 5th Conf. on Industrial Carbon and Graphite, Soc. Cem. Ind. London, **1**, pp.520-531 (1978)

[2] E. Fitzer, K.H. Geigl, W. Hüttner, The influence of carbon fibre surface treatment on the mechanical properties of carbon/carbon composites, Carbon, **18**, pp.265-270 (1980)

[3] R.J. Zaldivar, G.S. Rellick, J.M. Yang, Fibre strength utilization in carbon/carbon composites, J. Mater. Res., **8**, N°3, pp.501-511(1993)

[4] L.M. Manocha, O.P. Bahl, Y.K. Singh, Mechanical behaviour of carbon-carbon composites made with surface treated carbon fibers, Carbon, **27**, N°3, pp.381-387 (1989)

[5] S. Takano, T. Kinjo, T. Uruno, T. Tlomak, C.P. Ju, Investigation of process-structure-performance relationship of unidirectionally reinforced carbon-carbon composites, Ceram. Eng. Sci. Proc., **12** [9-10], pp.1914-1930 (1991)

[6] C. Ahearn, B. Rand, Modification of the fibre-matrix bonding in a brittle carbon-carbon composite by controlled oxidation, Carbon, **34**, N°2, pp.239-249 (1996)

[7] M. Müller, K.-M. Beindorn, K.J. Hüttinger, The significance of the fibre coating in the production of carbon fibre-reinforced carbons from HT carbon fibres and phenolic resin as matrix precursor-II. phenolic resin coatings, Carbon, **33**, N°8, pp.1043-1046 (1995)

[8] B. Trouvat, X. Bourrat, R. Naslain, Fibre-matrix bonding in carbon/carbon microcomposites: role of HTT and surface roughness of fibre, to be submitted in Carbon

[9] J.F Villeneuve, D. Mocaer, R. Pailler, R. Naslain, Tensile testing at high temperatures of ex-PCS Si-C-O and ex-PCSZ Si-C-N single filaments, J. of Mater. Sc., **28**, pp.1227-1236 (1993)

[10] M.Guigon, A. Oberlin, and G. Desarmot, Microtexture and structure of some high tensile strength, PAN-base carbon fibres, Fibre Science and technology, **20**, pp.55-72 (1984)

[11] A.R. Bunsell, A. Somer, The tensile and fatigue behaviour of carbon fibres, Plastics, Rubber and Composites Processing and Applications, **18**, pp.263-267 (1992)

[12] X. Bourrat, B. Trouvat, G. Limousin, G. Vignoles, Pyrocarbon anisotropy as measured by electron diffraction and polarized light, to be submitted in Journal of Materials Research

[13] B. Rand, Matrix precursors for carbon-carbon composites, in Essentials of carbon-carbon composites, C.R. Thomas ed., Royal society of chemistry, pp.67-102 (1993)

[14] P. Delhaès, M. Trinquecoste, J.L. Carlier, A. Derré, P. Chadeyron, High temperature thermal and mechanical properties of high tensile carbon single filaments, Carbon'95, 22nd Biennial Conference on Carbon, American Carbon Society, 16-21 July, pp.16-17 (1995)

ANNEXE 3

Toughening mechanisms in carbon/carbon minicomposites with interface control

ANNEXE 3

Toughening mechanisms in carbon/carbon minicomposites with fibre/matrix interface control

1 - INTRODUCTION 2

2 - EXPERIMENTAL 3

2.1 - C/C minicomposites preparation 3

2.2 - Mechanical testing 4

2.3 - Structural characterisation 4

3 - RESULTS AND DISCUSSION 5

3.1 - Bare tows 5

3.1.1 - Non-heat-treated tow (A) *6*

3.1.2 - Heat-treated tow (A-HTT) *7*

3.2 - Carbon/carbon minicomposites 8

3.2.1 - Minicomposites structure *8*

3.2.2 - Tensile behaviour *9*

3.2.2.1 - Brittle behaviour with A tows: A/M 9

3.2.2.2 - Non-brittle behaviour with heat-treated tows: 9

A-HTT/M, A-HTT/I/M 9

3.3 - Modelling 14

3.3.1 - Interfacial shear stress measurement: τ *15*

3.3.2 - Coefficient of thermal expansion (CTE) mismatch *15*

3.3.3 - Matrix-multiple-cracking mode *17*

4 - CONCLUSION 20

REFERENCES

NOMENCLATURE

V_f	fibre volume fraction*
V_m	matrix volume fraction*
$e_{int.PyC}$	pyrocarbon thickness inside the composite
$e_{ext.PyC}$	pyrocarbon thickness at the composite surface
γ	percentage of failed fibres before the tensile test
α	percentage of previous fibre failures (fibres failed before the tow failure)
α_c	critical percentage of failed fibres which involves the failure of the tow
S_{tow}	tow cross section area
$S_{tow,corr}$	tow cross section area, corrected from the cross section area of fibres failed before the tensile test, and of fibres failed before the tow failure
$S_{f,corr}$	bare tow cross section area, corrected from that of fibres failed before the tensile test
S_f	single fibre cross section
E_f	fibre Young modulus
E_{tow}	tow Young modulus
E_m	matrix Young modulus
E_c	Young modulus of the minicomposite
ε_1	strain corresponding to the first fibre failure in the minicomposite
σ_1	stress corresponding to the first fibre failure in the minicomposite
ε_{el}	strain corresponding to the end of the linear domain
σ_{el}	stress corresponding to the end of the linear domain
ε_R	strain-to-failure
σ_R	stress-to-failure

* closed porosity volume fraction is supposed to be zero

$\sigma_{R,f}$	fibre stress-to-failure, assuming that fibres support the load alone
m	Weibull modulus
ε_0	strain scale factor
$\Gamma(x)$	gamma function
F	load force
L_i	intercrack length, determined for a crack i by the mean of the distances of this crack to the crack (i-1), and to the crack (i+1)
ℓ	ineffective length, defined as the half-length related to the debonded domain on both sides of crack
M_0	term related to the axial coefficient of thermal expansion mismatching such as $M_0 = \int_{T_0}^{T_e} (\alpha_m - \alpha_f).dT$, with T_0 the ambient temperature, T_e the processing temperature, α_m and α_f the thermal expansion coefficients of matrix and fibre
u_0	crack opening under no load
u(F)	crack opening under load F
c_f	fibre stiffness $c_f=1/(E_f.S_f)$
τ	interfacial shear stress
L	gauge length
N	number of cracks
Δ	elongation
σ_p	maximum stress of the unload/reload loop
R	fibre radius
a_1 and b_2	Hutchinson coefficients

Toughening mechanisms in carbon/carbon minicomposites with fibre/matrix interface control

Submitted in Journal of the American Ceramic Society

B. TROUVAT, X. BOURRAT, and R. NASLAIN

Laboratoire des Composites Thermostructuraux

UMR 47 CNRS-SEP-UBI, Université Bordeaux I

3, allée de la Boëtie, 33600 Pessac, France

SUMMARY

This study deals with the toughening mechanisms in C/C composites. It was conducted on model minicomposites, consisting of 3000-filaments-tows of HT PAN-based carbon fibre, and pyrocarbon matrix. Control on interfacial parameters was obtained by stabilising the fibre (thermal residual stress), and by depositing an interphase between the fibre and the matrix with various microtextures (chemical bonding). It was shown, this way, that tensile behaviour switches from brittle to non-brittle behaviour with multiple matrix cracking. In this latter case, two toughening mechanisms were observed as previously reported for other ceramic matrix composites (e.g. SiC/SiC). When the interface is weak (low τ (<1MPa)), debond/sliding occurs with a high crack spacing, and a high residual strain. When the interface is stronger ($\tau \approx 7$MPa), it is more likely a matrix-multiple-cracking-based toughening mechanism which occurs: low crack spacing, and low residual strain.

1 - INTRODUCTION

Mechanical properties of carbon/carbon composites are sensitive to interface strength. This was shown in numerous works [1-8], relating fibre/matrix bonding to flexural load-strain curves and fracture surfaces. A strong interface leads to a brittle tensile behaviour, whereas a weak interface permits fibre/matrix debonding and sliding generating a non-linear mechanical behaviour and fracture surface with fibre pull-out. In these previous studies, liquid matrix precursors were preferred, as modification of fibre/matrix bonding was easily achieved by changing carbon fibre type, fibre surface treatment [1-5], and composite post-heat-treatment (matrix shrinkage, matrix stress-graphitization, etc.) [4,6,7]. More recently, oxidation was also used as a way to weaken the fibre-matrix bonding strength [8].

In all these previous works, toughness of unidirectional C/C composites was then achieved by a debonding/sliding mechanism with matrix crack deflection. Toughening process in other brittle matrix composites (ceramic matrix (CMCs)) is different in that multiple matrix cracking occurs [9,10]. The more classical one (debond/sliding based toughening) is induced by energy dissipation through fibres sliding along the debonded interfaces. It requires extensive initial debonding which necessitates weak interface and an adhésive fibre/matrix failure (low interfacial shear stress, high crack spacing). The other one (matrix-multiple-cracking-based toughening) was evidenced by Droillard et al. [10], and indicates that a strong interface can also involve toughening by favouring matrix cracking as mechanism of energy dissipation (high interfacial shear stress, low crack spacing). This latter mechanism has the advantage to be compatible with high strength requirements (good load transfer). Here, crack deflection is no more at fibre surface, but within the interphase itself (cohesive failure of the fibre/matrix interface).

Promoting multiple matrix cracking in C/C composites by interface control would considerably improve their mechanical performances. To our

knowledge, only Zaldivar et al [7] have seen this phenomenon during in-situ flexural test of a polished 2150°C HTT C/C composite (E130/based-PAA carbon).

In the present paper, the influence of fibre stabilisation on damaging mode and mechanical performances was studied in tensile loading of C/C minicomposites. Control of the interface was obtained by inserting a controlled-microtexture carbon interphase in-between fibre and matrix.

2 - EXPERIMENTAL

2.1 - C/C minicomposites preparation

Fibres used were HT PAN-based carbon fibres referred to as A fibres. Fibre tows contained 3000 filaments. Some of them were subjected to a temperature T1 (HTT) with T1 higher than fibre processing temperature, and referred to as A-HTT.

First, two reference C/C composites (minicomposites F/M) were prepared by rolling single tows around a graphite frame, and by depositing a pyrocarbon matrix in a CVD/CVI (Chemical Vapour Deposition/Infiltration) furnace. Isothermal and isobaric conditions were used (ICVI mode), and propane was chosen as precursor (Table 1). Secondly, minicomposites were prepared with a pyrocarbon interphase, with different microtextures, referred to as I1,I2,I3, on A-HTT tows (A-HTT/I/M samples). Interphase deposition preceded the matrix deposit in the same heating cycle.

Inner depositing rates (CVI) were lower than those measured at the surface (CVD) (Table 1). Experiment durations were controlled in order to get an interphase thickness of about 0.1µm inside the tows.

Table 1. Experimental conditions and pyrocarbon characteristics

Pyrocarbon	Experimental conditions		Deposit rate (μm/h)		Extinction angle Ae (°)		Interphase thickness (μm)	
	T (°C)	P (kPa)	CVD	CVI	CVD	CVI	CVD	CVI
Matrix	1000	2	0.23	0.17	16	18		
I1	1000	1	0.10	0.05	17	20	0.2	0.1
I2	1100	2	0.86	0.17	14	14	0.8	0.15
I3	900	2	0.03	0.01	14	-*	0.2	0.1

* The interphase pyrocarbon thickness (<1μm) did not permit the optical measurement (Ae). However, the optical activity (brightness) seemed to be lower, compared to that of a similar thickness of pyrocarbon matrix.

2.2 - Mechanical testing

Minicomposite tensile tests were conducted with a tensile device, comprising a 0-500N load cell, and two strain cells (capacity: 1mm), symmetrically placed on the frame. Displacement was carried out at constant speed (0.085%/min). Tensile properties were measured at 50mm gauge length, with tow extremities fixed on steel supports with a structural cement[1]. The alignment of tows towards steel supports was achieved with help of a devised equipment. For bare tows, sizing was taken off before tensile test.

A set of five specimens were tested for each type of minicomposites.

2.3 - Structural characterisation

Optical measurement in polarised light was used to characterise pyrocarbon texture by measuring the extinction angle Ae [11]. For that purpose, a deposit at least 1µm thick was specially made on tows for each type of pyrocarbon (M, I1, I2, I3). Polished cross-sections were realised after embedding these materials in resin, following the classical procedure. The larger the angle Ae, the higher the anisotropy: Ae ranges from 0 to 4° for isotropic pyrocarbon, from 4 to 12° for dark-laminar, from 12 to 18° for smooth laminar, and finally 18° and more for rough laminar pyrocarbon on the optical microscope[2] used.

Optical microscopy observation was also made on polished minicomposites cross-sections. Longitudinal sections of tested minicomposites permitted to characterise the damaging of the material (crack opening, crack spacing, ...).

---

[1] Scotch-Weld 9323 B/A, Scotch 3M

[2] MeF_3 Reichert-Jung microscope

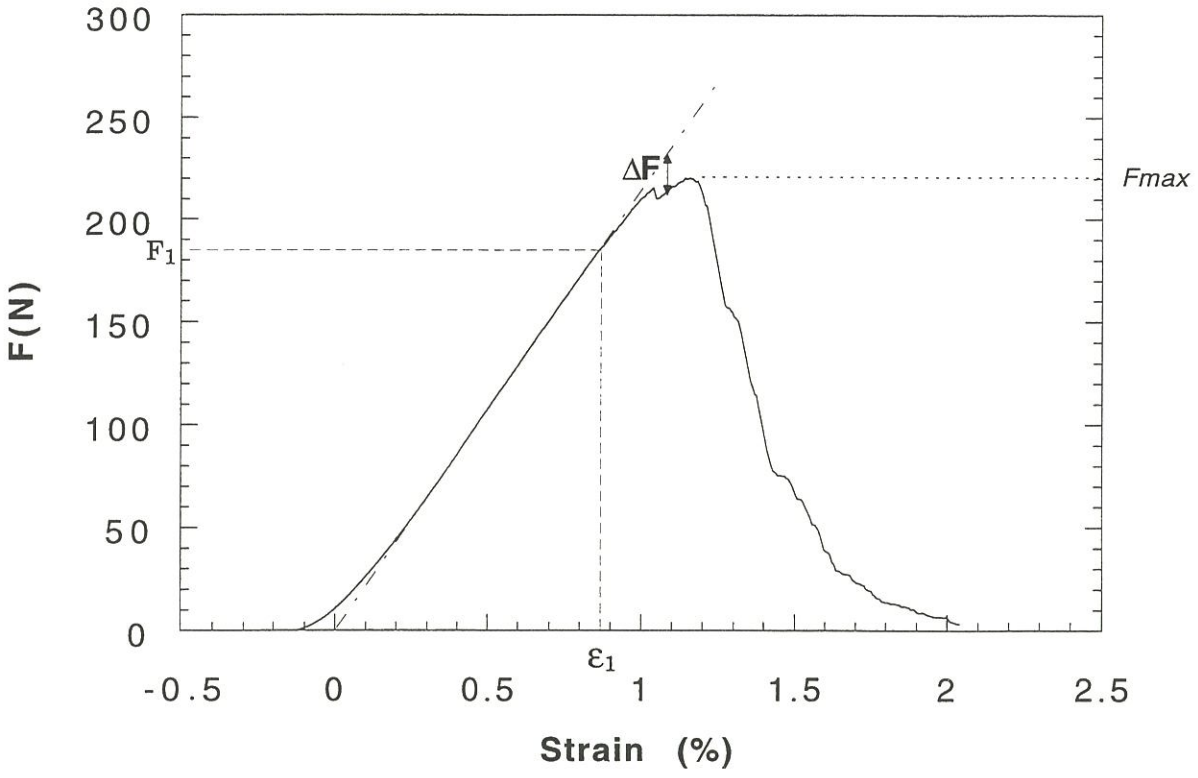

Figure 1: load-strain curve of a bare A tow

Scanning Electron Microscopy (SEM)[1] was used to study fracture surfaces, and damaging of tested minicomposites. Otherwise, some tensile tests were performed in a SEM microscope[2] equipped with a tensile stage, provided with a straining device and a 0-200N load cell. In situ damaging could then be studied for A-HTT/M minicomposites.

3 - RESULTS AND DISCUSSION

3.1 - Bare tows

Tensile load-strain curve (figure 1) has a first linear part, which ends when the first fibre failures happen (F_1,ε_1). When a critical percentage of failed fibres is attained, tow failure occurs (F_{max}).

Data on bare tows were analysed according to a method exposed by Lissart [12]. Results are listed in Table 2. Percentage of failed fibres before tensile test, γ, is determined with tow Young modulus deduced from the first linear part of the tensile curve:

$$\gamma = 1 - \frac{E_{tow}}{E_f} \tag{2}$$

Calculation of tow stress beyond linearity needs first the determination of the percentage α of fibres previously failed. α is defined as follows:

$$\alpha = \frac{\Delta F}{F + \Delta F} \tag{3}$$

where F is the load supported by the tow, and ΔF is defined in figure 1.

---

[1] using a HITACHI S-4500 microscope equipped with a field emission gun

[2] JEOL JSM-840A microscope

The critical percentage α_c corresponds to the maximum force, observed on the tensile curves. It is related to Weibull modulus[1] m:

$$\alpha_c = 1 - e^{-1/m} \tag{4}$$

α is directly related to the fibre failure probability in the tow:

$$\alpha = 1 - exp\left(-\frac{S_f . L}{V_0} . \left(\frac{\varepsilon_f}{\varepsilon_0} \right)^m \right) \tag{5}$$

where S_f is the fibre cross section area; L, the gauge length; m, the Weibull modulus; ε_0 a scale factor in strain unit in using a reference volume V_0 (V_0=1mm^3).

This way, the statistical parameters (m, ε_0) of fibre are deduced from $\ln\ln(1/(1-\alpha))$-$\ln\varepsilon$ curves. Moreover, mean strain-to-failure of fibres are determined by the relation:

$$\bar{\varepsilon}_{R,f} = \varepsilon_0 . \left(\frac{S_f . L}{V_0} \right)^{-1/m} . \Gamma\left(1 + \frac{1}{m} \right) \tag{6}$$

where $\Gamma(x)$ is the gamma function.

3.1.1 - Non-heat-treated tow (A)

Statistical parameters of A tow, and mean fibre strain-to-failure, determined with above analysis, show results similar to those obtained on single fibres [13].

The first fibre failures, associated to the end of linearity, are seen at ε_1=0.70% and σ_1=1455MPa on tensile curves. Then, tow failure occurs for ε_R=1.03% and σ_R=2587MPa. Tow Young modulus indicates a percentage of 17% of fibres failed before the tensile test (eqn 2).

---

[1] Weibull statistics are commonly used to analyse the failure of carbon fibres. The failure probability P to the applied strain ε is expressed as follows: $P = 1 - exp\left(-\frac{V}{V_0} \left(\frac{\varepsilon - \varepsilon_u}{\varepsilon_0} \right)^m \right)$

where V: volume submitted to the strain, V_0 a reference volume (V_0=1mm^3), ε_u value of strain below which P is zero (ε_u=0), ε_0 scale factor, and m Weibull modulus.

Table 2. Tensile mechanical data for bare tows

	S_{tow} (mm^2)	E_c (GPa)	$\varepsilon_{el}=\varepsilon_1$ (%)	$\sigma_{el}=\sigma_1$ (MPa)	γ (%)	α_c (%)	$\varepsilon_{(Fmax)}$ (%)	F_{max} (N)	σ_{max}** (MPa)	m	ε_0 (%/mm^3)
A	0.109	209 (9)*	0.70 (0.06)	1455 (162)	17 (4)	6 (4)	1.03 (0.11)	219 (18)	2587 (258)	9 (1)	0.669 (0.173)
A-HTT	0.104	237 (10)	0.55 (0.10)	1297 (274)	25 (3)	14 (6)	0.77 (0.03)	163 (20)	2429 (93)	6 (2)	0.279 (0.106)

* standard deviation in brackets

** $\sigma_{max}=F_{max}/(S.(1-\gamma).(1-\alpha_c))$. corrected section from failed fibres

Table 3. Theoritical and experimental data for A fibre (gauge lengths of 10 and 25mm)

Fibre	Theoritical* $\overline{\varepsilon}_{R,f}$ (%)		Experimental** $\overline{\varepsilon}_{R,f}$ (%)	
	L=10mm	*L=25mm*	*L=10mm*	*L=25mm*
A	1.52	1.37	1.58	1.40
A-HTT	0.98	0.84	1.27	1.30

* from equation (6) with tow data
** from single filament tensile tests

The scattering of α_c (Table 2) does not permit to determine a Weibull modulus from equation 4. But, statistical parameters can be deduced from $\ln\ln(1/(1-\alpha))$-$\ln\varepsilon$ curves: m=9, and ε_0=0.669% for a volume of 1mm^3. Application of equation (5) to $\alpha_c(m=9)$=10% gives $\varepsilon_{calc}(F_{max})$=1.05%, which is similar to experimental value ($\varepsilon_{mes}(F_{max})$=1.03%).

Mean failure characteristics can then be deduced from above statistical parameters for a gauge length of 50mm: $\overline{\varepsilon}_{R,f}$=1.27%, and $\overline{\sigma}_{R,f}$=3175MPa.

Results, obtained on monofilaments with gauge lengths of 10 and 25mm, are consistent with preceding results. On one hand, strain Weibull curves, corrected from the volume influence ($\ln\ln(1/(1-\alpha))$-$\ln V=f(\ln\varepsilon)$), are superimposed (figure 2.a). On the other hand, application of equation (6) to 10 and 25mm gauge lengths gives the same values for mean strains-to-failure than the experimental ones obtained on monofilament tensile tests (Table 3).

3.1.2 - Heat-treated tow (A-HTT)

Failure occurs for ε_R=0.77% and σ_R=2429MPa. Thus, A-HTT tow has the same stress, but a lower strain-to-failure than A tow. Heat-treatment of tows created surface defects on fibres. Otherwise, A-HTT tow has more fibres failed before the tensile test (25% against 17%). It is due to a more delicate handling of A-HTT tow, for which sizing is eliminated by the HTT. First fibre failures occur before (ε_1=0.55%, σ_1=1297MPa) than those observed for A tow. It is supposed that large defects must be created by HTT.

A higher critical percentage is found for A-HTT tow: α_c=14%, associated to a Weibull modulus m=7 (eqn 5). The other m value, deduced from the $\ln\ln(1/(1-\alpha))$-$\ln\varepsilon$ plots, is similar: m=6. The scale factor ε_0 is equal to 0.279% for a volume of 1mm^3. Application of equation (5) to $\alpha_c(m=6)$=15% gives $\varepsilon_{calc}(F_{max})$=0.59%, which is less than experimental value ($\varepsilon_{mes}(F_{max})$=0.77%).

As for A, statistical parameters are the same as those deduced from tensile tests on single fibres: for L=10mm, m=6 and ε_0=0.264% ; for L=25mm, m=6 and ε_0=0,257%. Strain Weibull curves, corrected from the volume

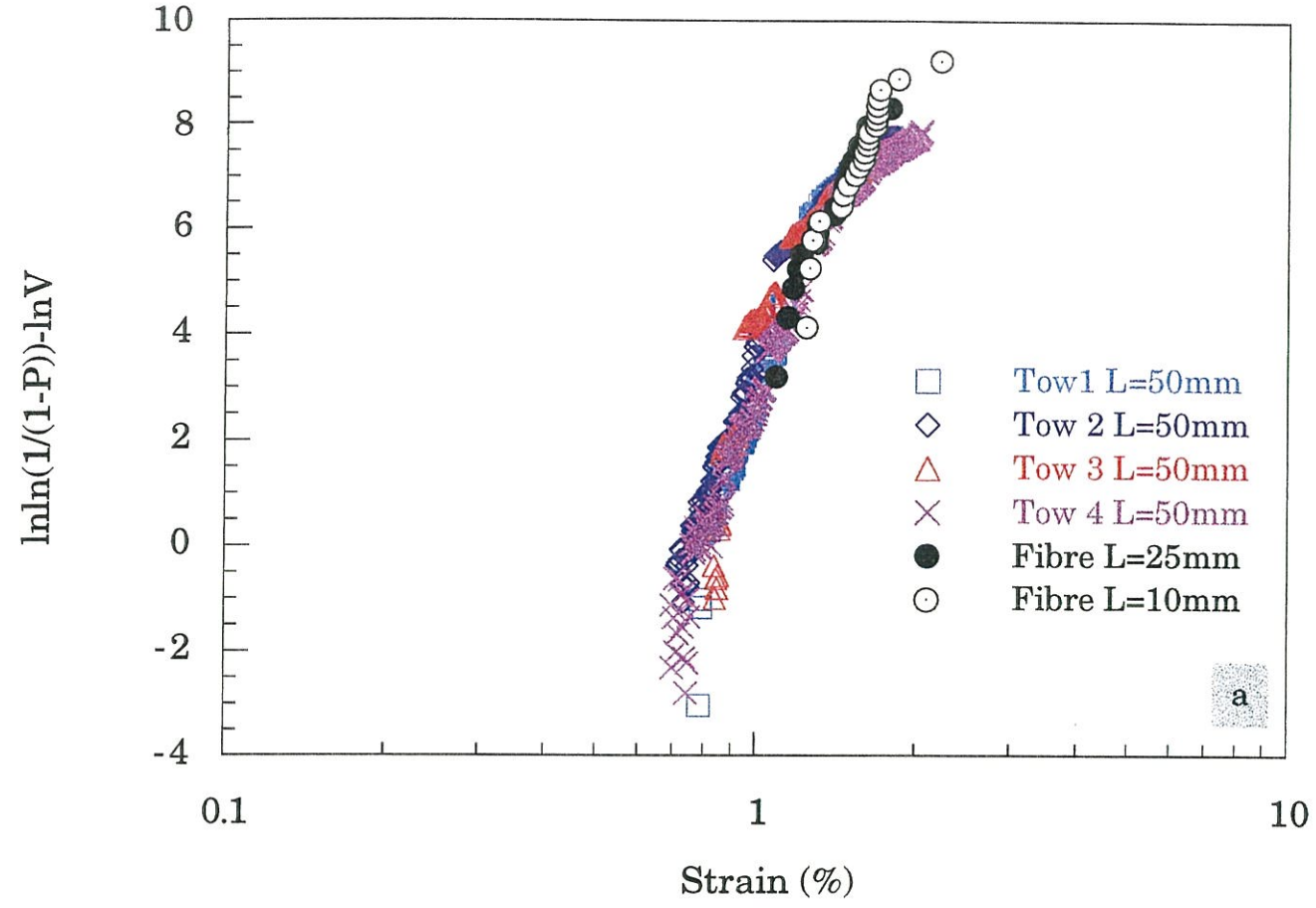

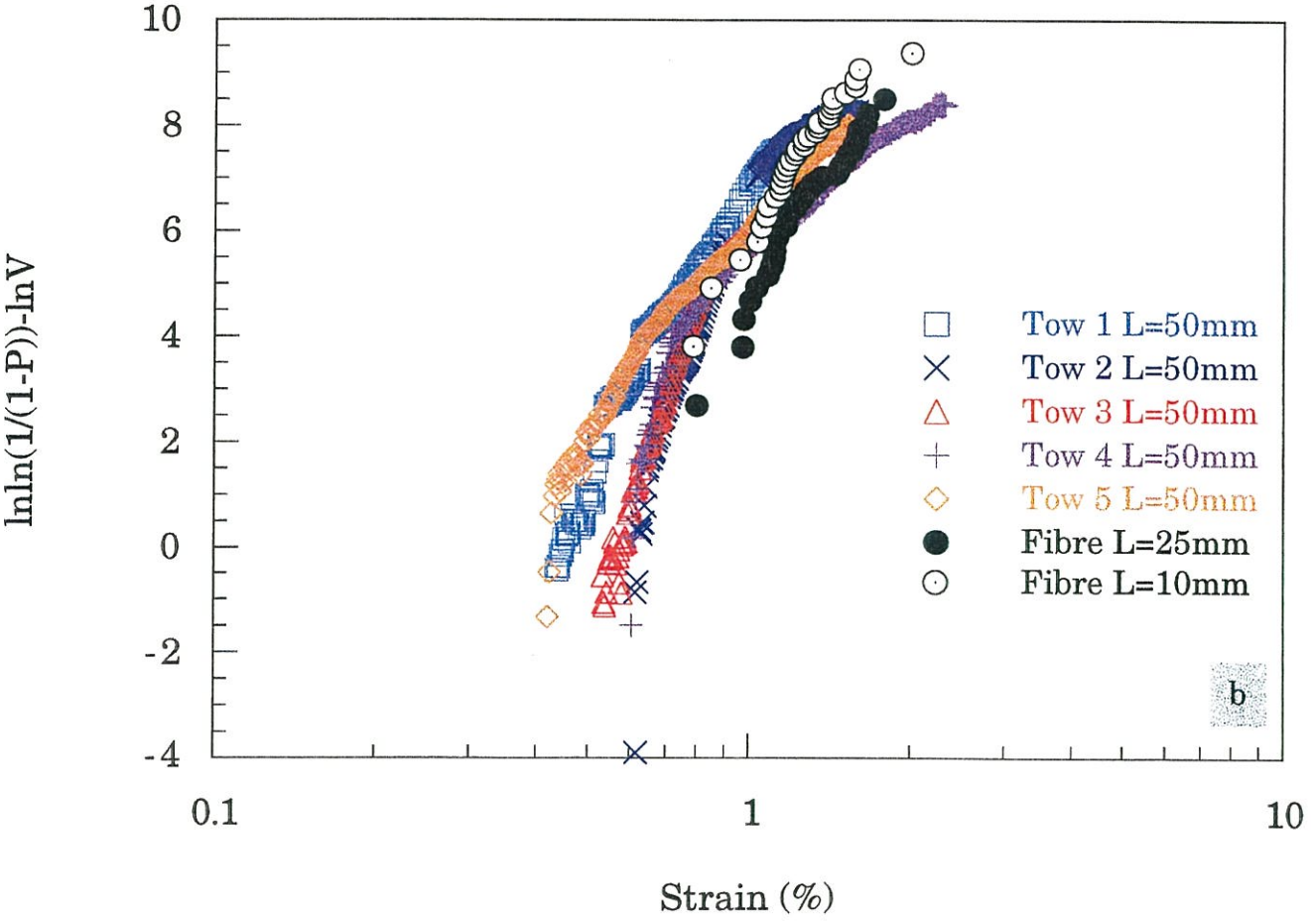

Figure 2: Weibull plots, corrected from volume, of bare fibres and bare tows
(a) A, (b) A-HTT

influence ($\ln\ln(1/(1-\alpha))$-$\ln V=f(\ln\varepsilon)$), are close for fibres and tows (figure 2.b), though more dispersed than for A fibre. Nevertheless, application of equation (6) for gauge lengths of 10 and 25mm does not give similar results as for A fibre. Lower values are expected with tow data (Table 3). It can be due to an unavoidable selection effect of fibres during the single-fibre mechanical testing.

3.2 - Carbon/carbon minicomposites

3.2.1 - Minicomposites structure

Optical texture of pyrocarbon.

Pyrocarbon texture can be different at the surface and inside the composite due to different pyrocarbon deposit rate. Residence time and composition of the gas phase in the inner region of the tow are not similar to those at the material surface. In this study, deposition conditions were varied in order to change the pyrocarbon texture inside the minicomposite ($I1_{int}$, $I2_{int}$, $I3_{int}$). The extinction angle data are listed in Table 1. The different pyrocarbons belong to the "smooth-laminar" textural class, except $I1_{int}$, which is a "rough laminar" pyrocarbon. Outer pyrocarbon is similar for matrix and interphase $I1_{ext}$, whereas $I2_{ext}$ and $I3_{ext}$, interphases characterised by the same texture, are a little less ordered.

Optical and SEM observations of polished cross sections.

Minicomposites (figure 3.a) did not exhibit any apparent fibre/matrix debonding before loading (figure 3.b). However, in polished sections performed near the minicomposite cut ends, some debonding could be observed. This is indicative of interface strength. This way, weak fibre/matrix interfaces were observed in the inner part of A-HTT/I1/M and A-HTT/I3/M minicomposites. For A-HTT/I2/M, debonding was essentially observed in the outer zone, in-between matrix and I2 interphase (arrow on figure 4).

Table 4. Data for non-infiltrated tows and carbon/carbon minicomposites

Tow	Mechanical data											Multiple cracking data	
	S_{tow} (mm^2)	V_f (%)	ε_{el} (%)	σ_{el} (MPa)	E_c (GPa)	$S_{tow,corr}$ (mm^2)	ε_R (%)	σ_R (1) (MPa)	$S_{f,corr}$ (mm^2)	E_f (2) (GPa)	$\sigma_{R,f}$ (3) (MPa)	L_i (µm)	u_0 (µm)
A/M	0.168	65	0.57 (0.05)*	992 (58)	177 (4)	0.168	0.57 (0.05)	992 (58)					
A-HTT/M	0.198	52	0.38 (0.02)	701 (35)	186 (7)	0.149	1.02 (0.08)	1872 (62)	0.078	288	3576	376	1.6
A-HTT/I1/M	0.211	49	0.33 (0.01)	578 (49)	175 (9)	0.158	1.04 (0.04)	1818 (170)	0.078	322	3683	521	2.3
A-HTT/I3/M	0.203	51	0.30 (0.03)	532 (76)	177 (11)	0.152	1.02 (0.17)	1810 (226)	0.078	320	3527	575	2.4
A-HTT/I2/M	0.221	47	0.45 (0.02)	766 (23)	173 (9)	0.161	0.79 (0.07)	1665 (116)	0.078	382	3437	251	0.355

* standard deviation in brackets

(1) $\sigma_R = \dfrac{F}{S_{tow,corr}}$ with $S_{tow,corr} = S_{tow}(1-\gamma)$

(2) E_f is the slope of the linear part III of the curve, in taking $S_{f,corr}$

(3) $\sigma_{R,f} = \dfrac{F}{S_{f,corr}}$ with $S_{f,corr} = S_{baretow}.(1-\gamma)$

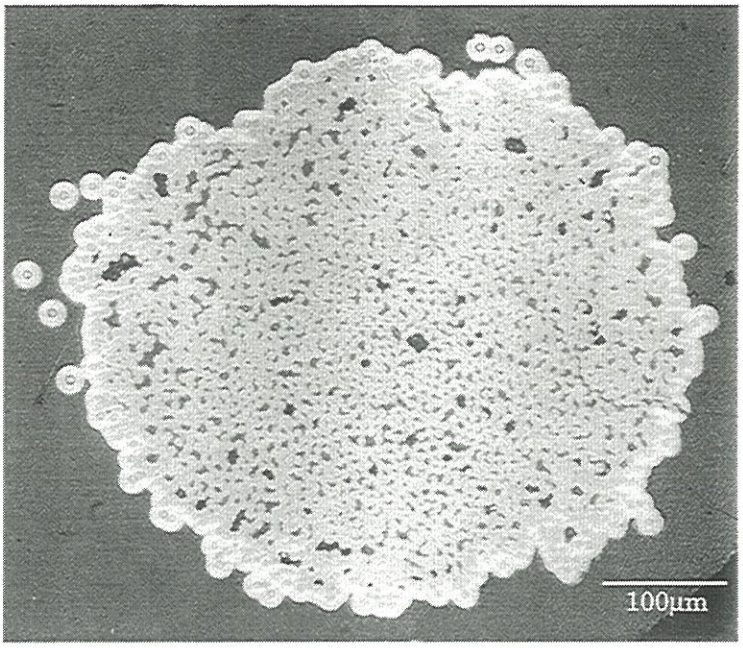

(a)

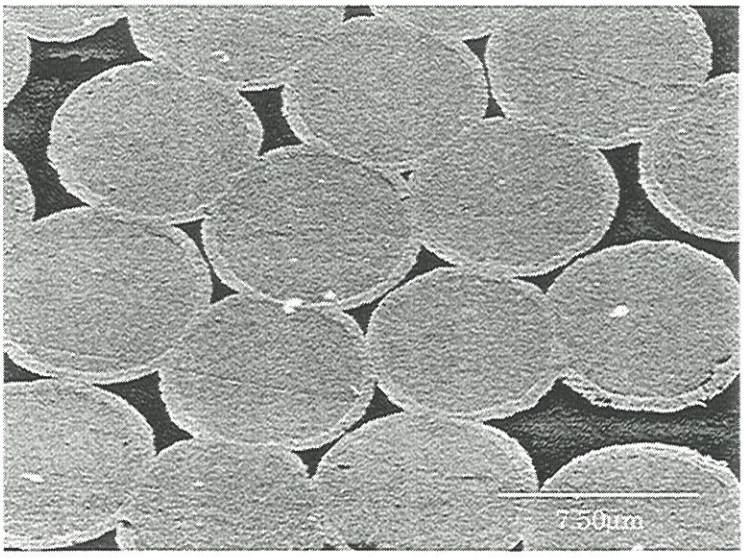

(b)

Figure 3: observation of polished cross-section of a A-HTT/I3/M minicomposite
(a) a whole view in optical microscopy, (b) view at a higher magnification in SEM

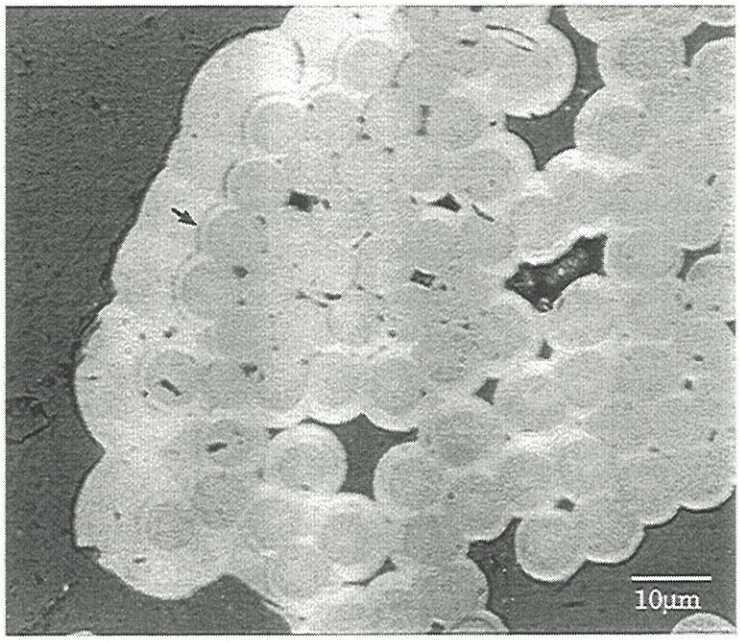

Figure 4: polished cross-section of A-HTT/I2/M minicomposite
at location closed to cutting ends
(arrow: crack deflection at pyrocarbon-interphase interface)

3.2.2 - Tensile behaviour

Tensile tests showed two groups of materials: brittle composites with A tows, and **non-brittle composites with heat-treated tows** (Table 4). The last group is of great interest as a **multiple matrix cracking was observed** as for other Ceramic Matrix Composites (e.g. SiC/SiC composites).

Models, developed for CMCs, could then be applied to these non-brittle C/C minicomposites.

3.2.2.1 - Brittle behaviour with A tows: A/M

A/M minicomposite (V_m=35%) displays a linear tensile curve up to failure (figure 5). Strain-to-failure (ε_R=0.57%) is lower than the strain of first fibre failures in the bare tow (ε_1=0.70%).

SEM observation after failure showed no matrix crack (mode I), and a flat fracture surface, without fibre pull-out (figure 6). Thus, A/M tow is characterised by a catastrophic failure, which follows the weakest link model. This brittle tensile behaviour is the common one encountered for C/C composites. This corresponds to a strong fibre/matrix bonding. Crack, initiated in the matrix, progresses through fibres in mode I, involving the catastrophic failure of the minicomposite.

The Young modulus of the minicomposite is ≈177GPa. The rule of mixture gives a matrix Young modulus equal to 40GPa, assuming that all fibres participates in material stiffness and a **strong fibre/matrix bonding**. However, the uncertainty on this E_m value is high: 145%.

3.2.2.2 - Non-brittle behaviour with heat-treated tows: A-HTT/M, A-HTT/I/M

Two subgroups appear among these materials. The most encountered is characterised by the existence of a domain of high damaging on tensile curves

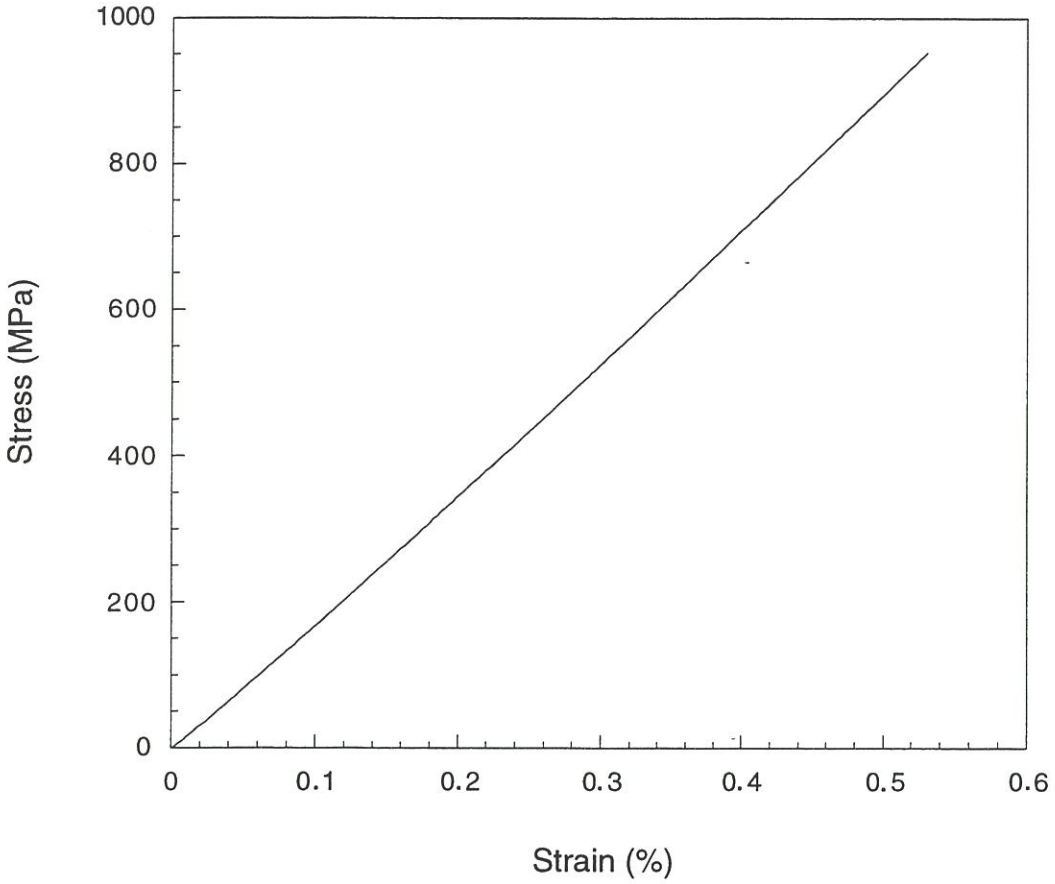

Figure 5: tensile stress-strain curve of A/M minicomposite (brittle behaviour)

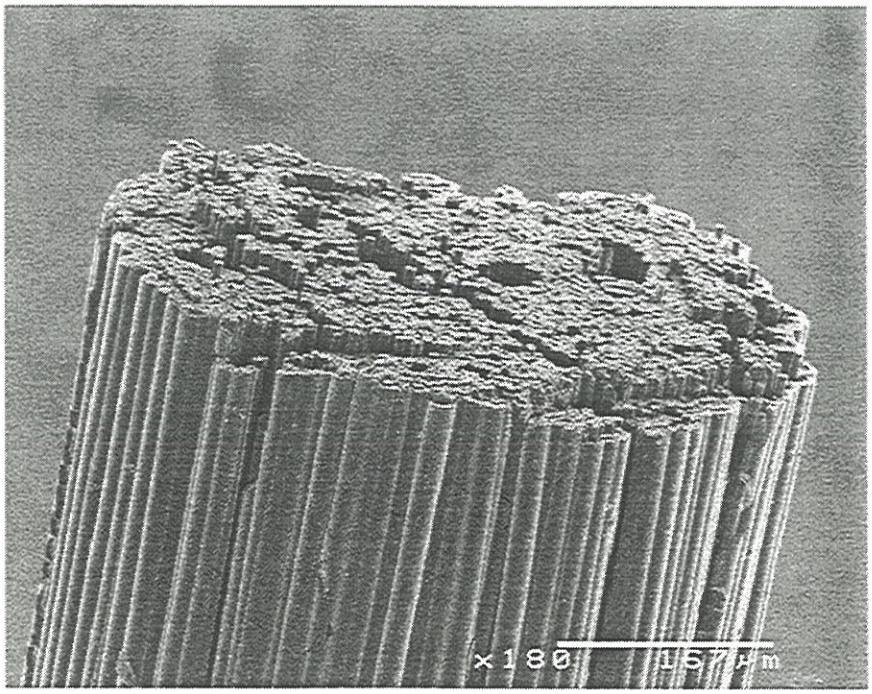

Figure 6: flat fracture surface of A/M brittle minicomposite

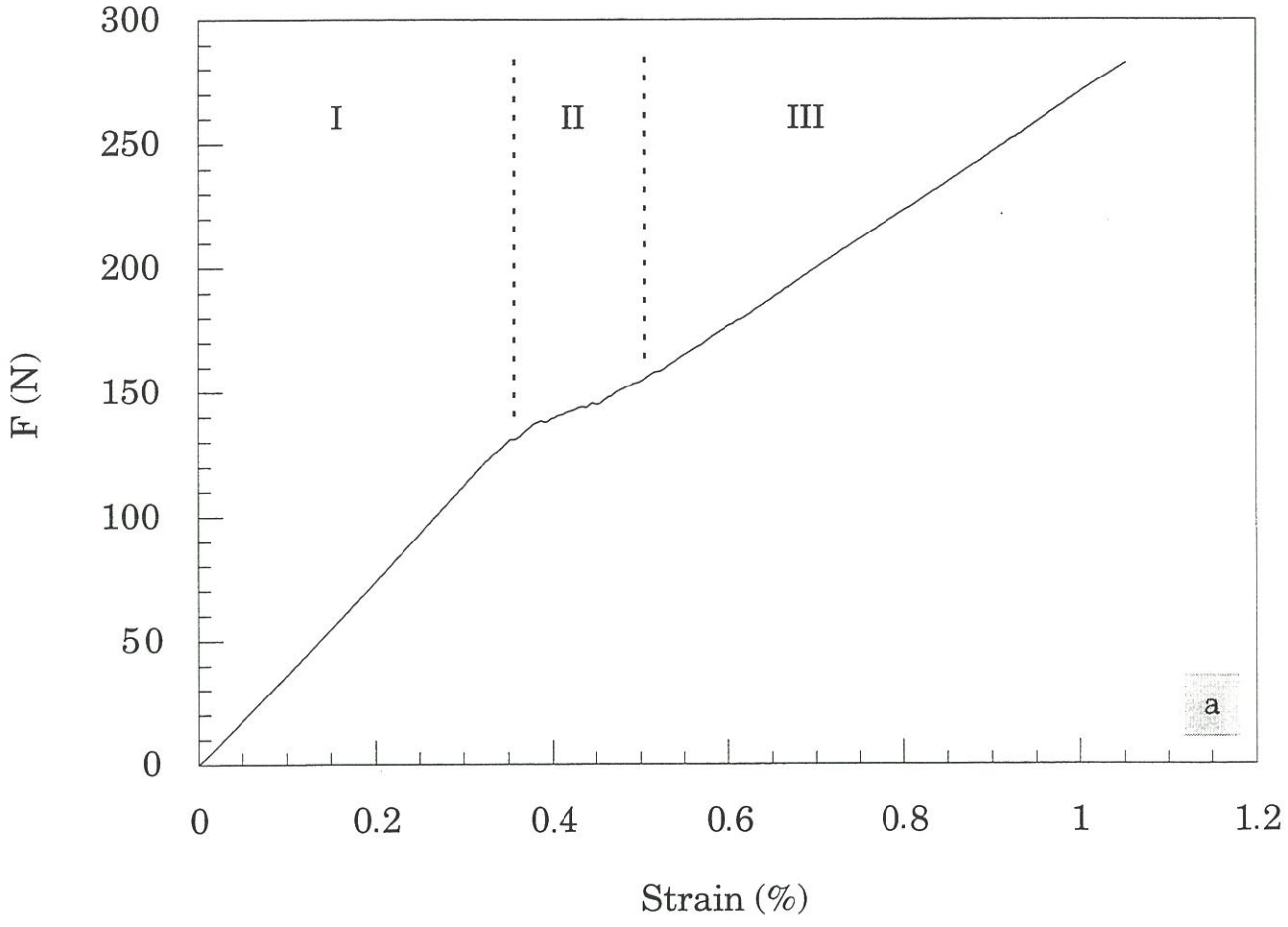

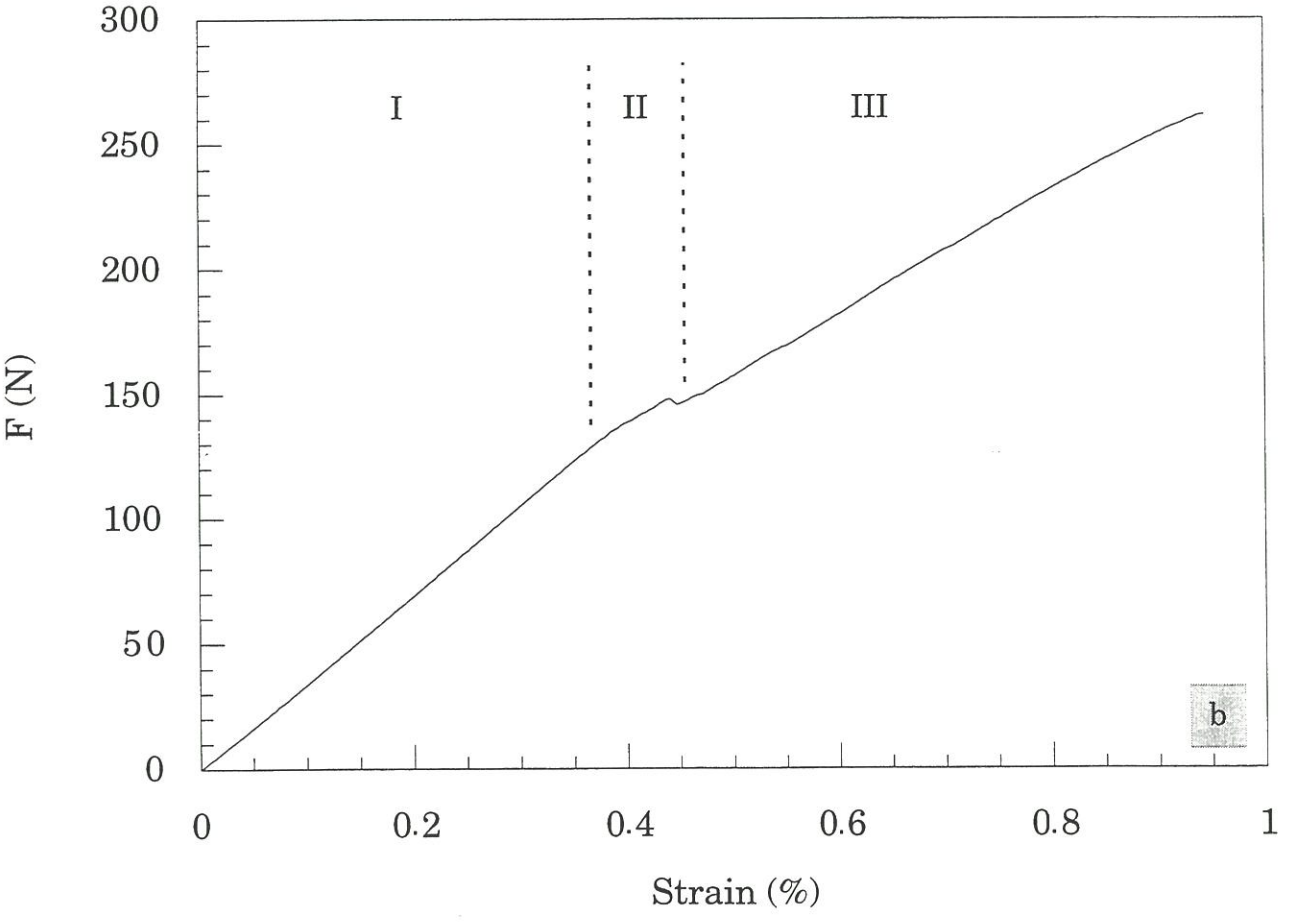

Figure 7: tensile load-strain curves of A-HTT/M with
(a) a linear, or (b) a convex-up part III

(A-HTT/M, A-HTT/I1/M, A-HTT/I3/M); whereas, for A-HTT/I2/M, this domain is not seen, there is only a change in the slope of the curve.

A-HTT/M reference minicomposite.

A-HTT/M minicomposite (V_m=52%) has a non-linear mechanical behaviour as most CMCs (figure 7). The first part of the plot is linear up to ε_{el}=0.37% and σ_{el}=700MPa (Part I). It is followed by a domain (ε=0.37-0.50%) where the material is highly damaged (load falls, large strains at constant load) (Part II). Then, two different cases can happen (Part III): (1) the curve is linear again (figure 7.a), which would be associated to the end of damaging and sliding; (2) the curve has a slightly convex-up shape (figure 7.b), which would indicate that damaging and/or sliding is going on, but in a much less extent than previously. This last case is encountered for minicomposites with a part II less perturbed, i.e. less damaging. In this case, damaging would progress all along the test.

Failure of A-HTT/M minicomposite occurs at ε_R=1%, i.e. with an increase of 34% compared to strain-to-failure of bare tow (in-situ strain-to-failure of fibres in A-HTT/M is higher than bare tow one). Pyrocarbon matrix enhances the fibre tow failure: α_c increases.

SEM observation of failed samples showed multiple matrix cracking (figure 8). Non-linear mechanical behaviour is then attributed to matrix cracking as for most CMCs. For curves with a linear part III, cracking saturation should be attained. Matrix is probably no more solicited, fibres then supporting alone the applied load. This is consistent with Young modulus, deduced from linear part III, considering only the fibre section, which is evaluated to be 290GPa, a value close to fibre modulus (316GPa). The crack spacing was estimated to be about 380µm with a mean crack opening of 1.6µm.

Optical observation of longitudinal sections (figure 9) showed the crack going through the minicomposite without fibre failure (figure 9.a,b). There is crack deflection at fibre-matrix interface (figure 9.c), and crack bridging by fibres. Damaging features similar to those for other CMCs then characterise

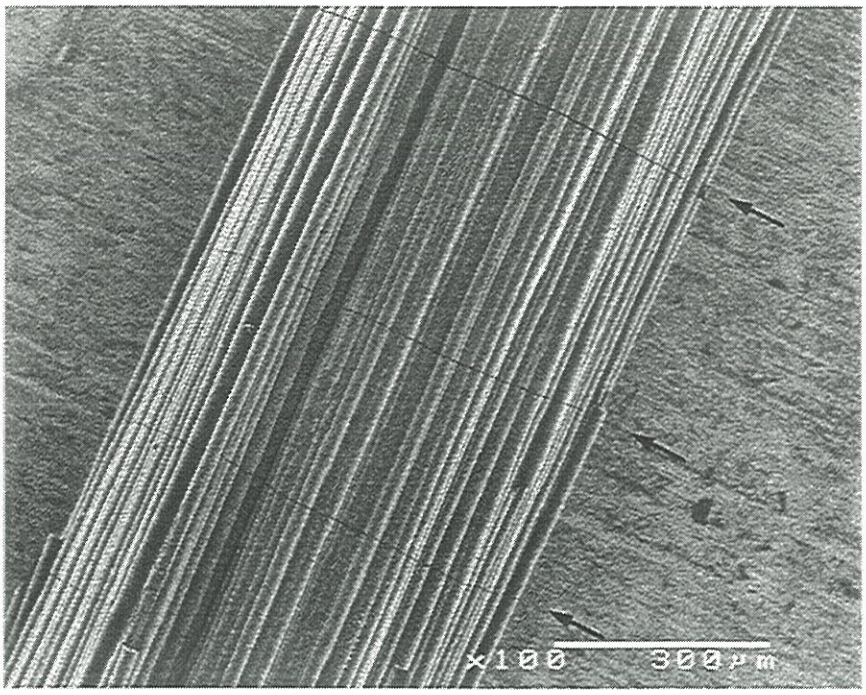

Figure 8: multiple matrix cracking: A-HTT/M loaded to failure
(SEM after tensile test; arrows: matrix cracks)

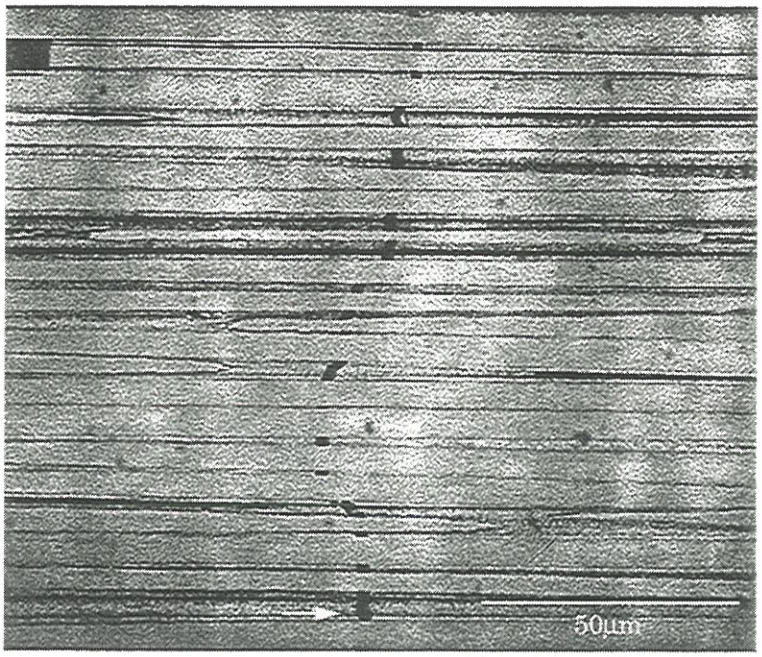

(a)

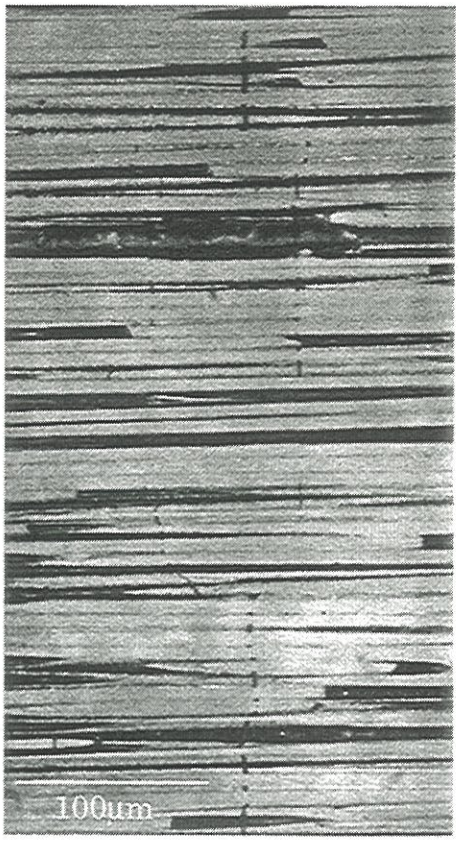

(b)

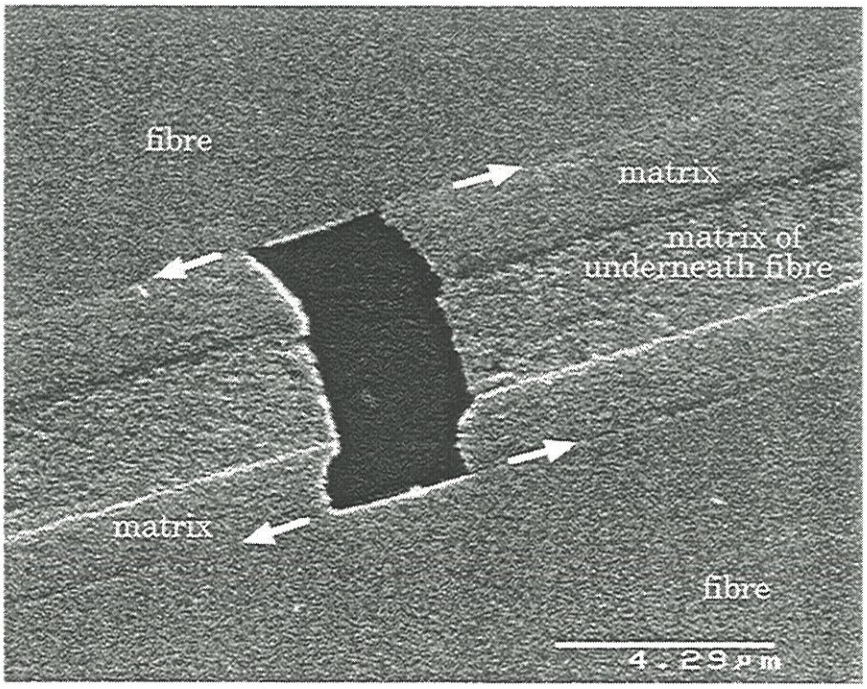

(c)

Figure 9: optical micrographs of a longitudinal section of A-HTT/M loaded to failure (a) matrix crack (arrow) bridged by the fibres; (b) matrix crack divided in two branches inside the minicomposite; (c) crack deflection at fibre-matrix interface (arrows)

the reference, A-HTT/M. So, the same debond/sliding-based toughening occurs for this non-brittle C/C minicomposite. Otherwise, cracks sometimes divide in branches, permitting more energy dissipation. Figure 9.b shows example of a main crack, which at a certain location divides in two secondary branches, and then takes back its main way.

First matrix failures happen for ε_{el}=0.37%. Commonly encountered strain-to-failure of low temperature pyrocarbons is in the range of about 0.3-0.5% [14,15], but this rises to as high as 2% for highly graphitized CVD deposits [15]. Now, previous works on microcomposites [13,16] have shown that pyrocarbon matrix has a mean strain-to-failure as high as 1%. It is concluded that matrix is in tension in minicomposite. To be complete, matrix strain-to-failure, measured for A/M (assimilated to minicomposite strain-to-failure), is higher (0.57%) than for A-HTT/M (0.37-0.46%). So, matrix failure characteristics in these materials are seen to be dependent on residual stresses, i.e. in tension in minicomposites, but lower for A/M than for A-HTT/M. Real failure characteristics of matrix can then not be deduced from minicomposites data unless to quantify all stresses in the material.

SEM observation of fracture surfaces (figure 10.a) reveals a failure at different levels: so, failure occurs in different blocks. Some regions are characterised by little or no fibre pull-out (figure 10.b), whereas others are characterised by important fibre pull-out (figure 10.c), especially at composite surface, where local V_m is higher. Fibre pull-out lengths can be as high as tentimes the fibre diameter (a hundred micrometers).

A-HTT/I/M minicomposites.

Load-strain curves of these minicomposites are plotted in figure 11 with that of the reference, A-HTT/M.

Materials, with interphases I1 or I3 (figures 12, 13), behave like the reference (A-HTT/M). Three domains characterise the tensile curve: a linear part I, an eventful part II, and a linear or convex part III according to the

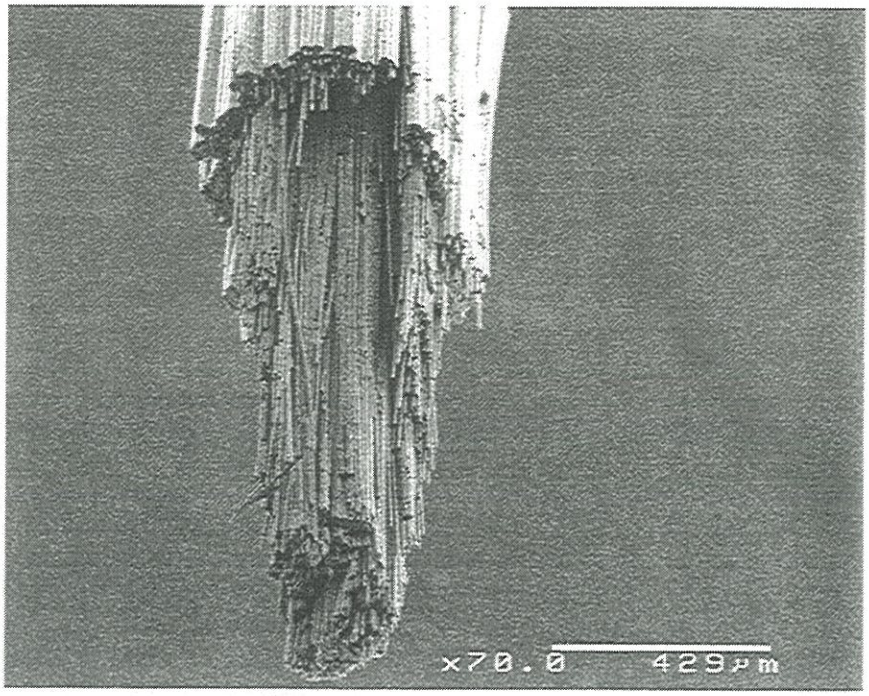

(a)

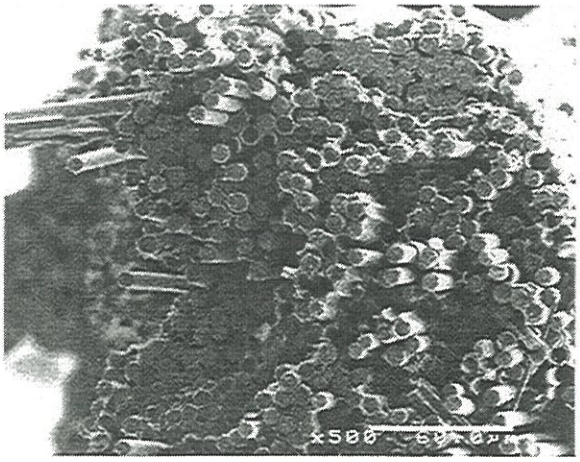

(b)

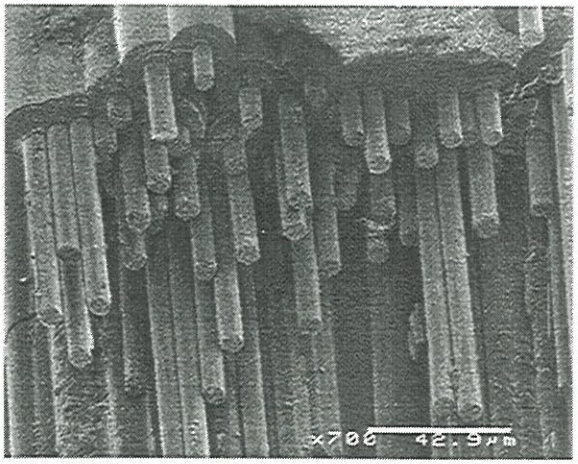

(c)

Figure 10: fracture surface of a A-HTT/M minicomposite
(a) whole surface and regions of (b) little pull-out, and (c) larger pull-out

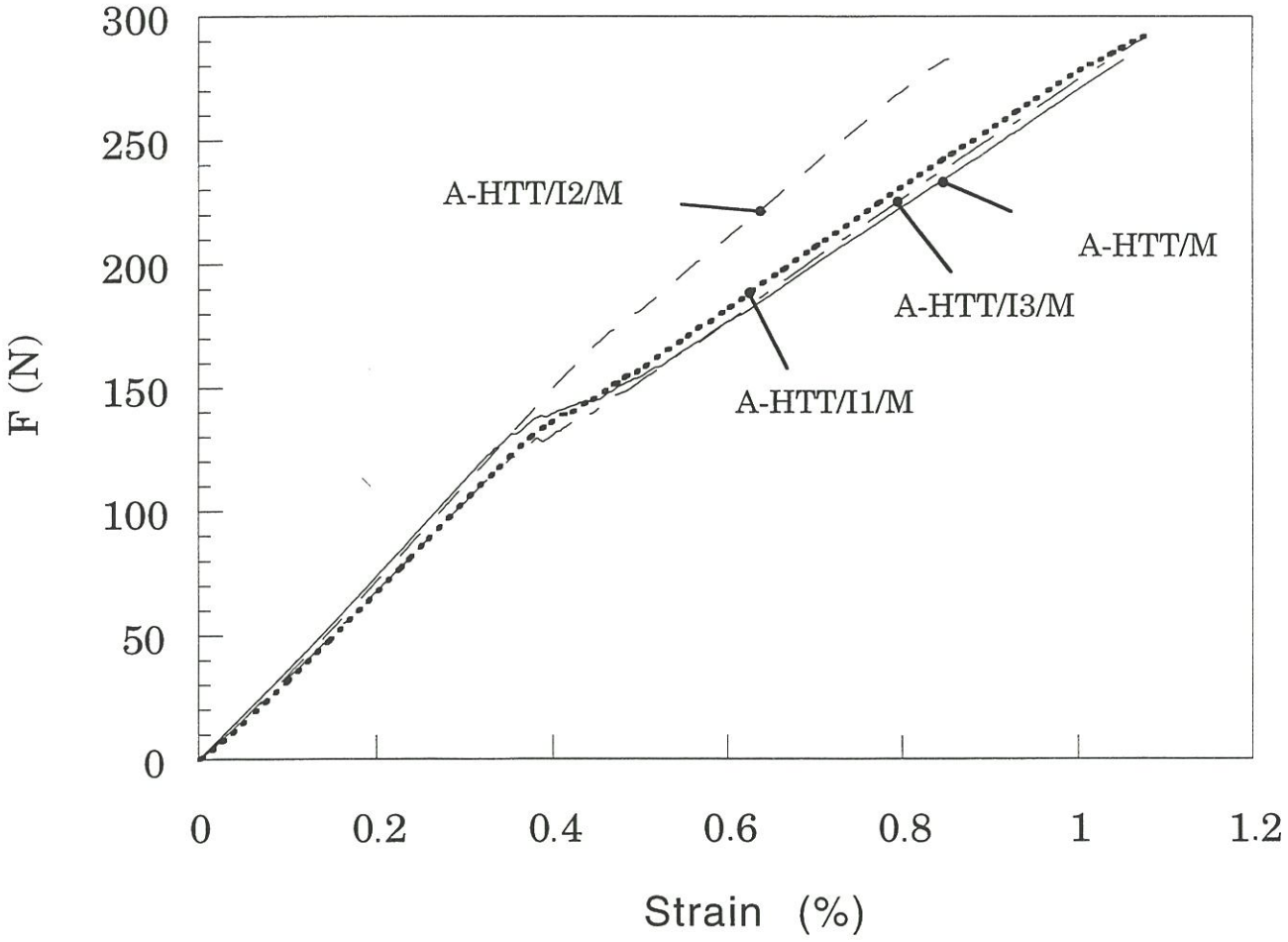

Figure 11: tensile load-strain curves of
A-HTT/M and A-HTT/I/M minicomposites

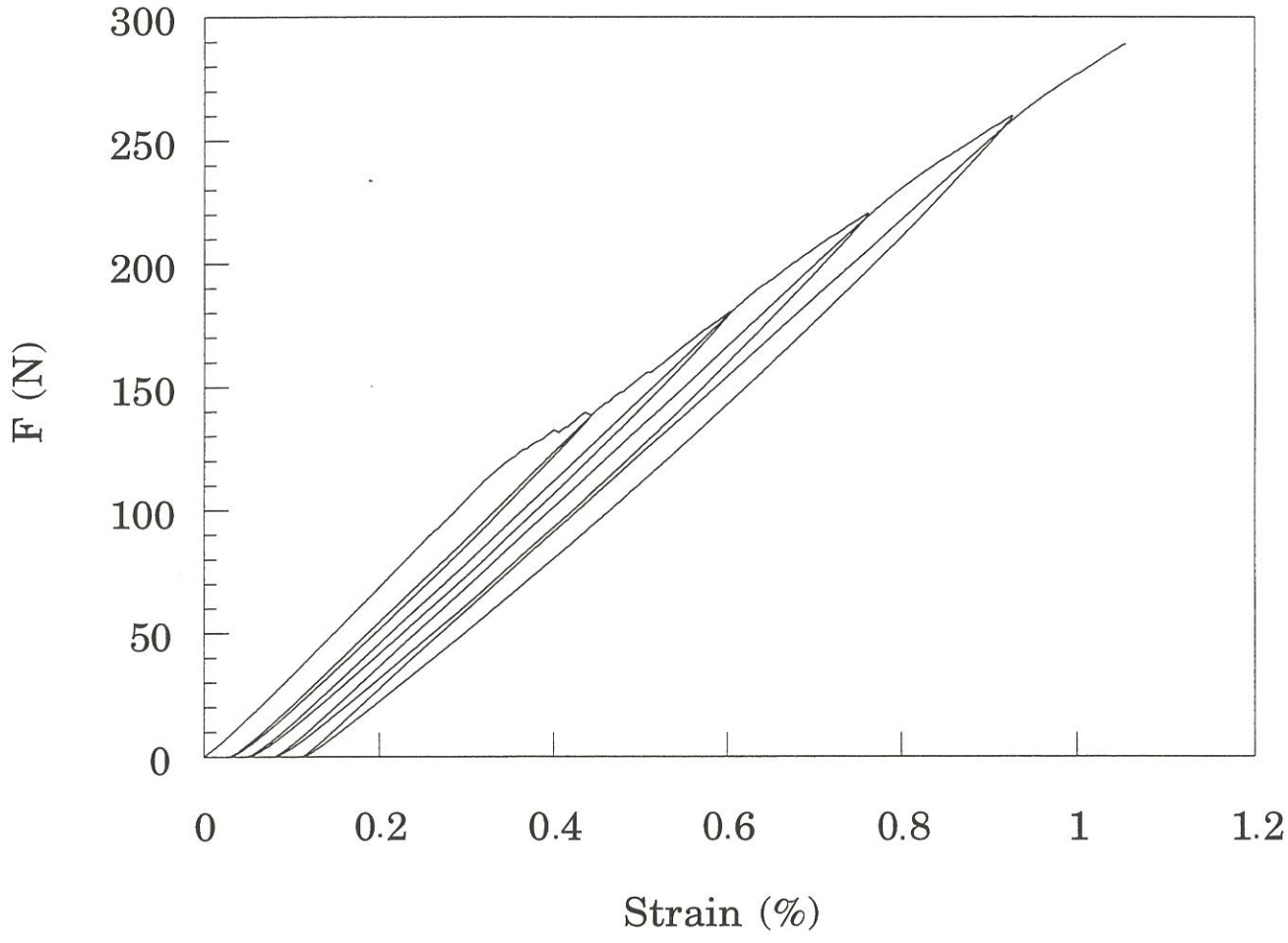

Figure 12: tensile load-strain curve of A-HTT/I1/M minicomposite with unload/reload cycles

damaging mode in part II. However, the end of the linearity (part I) occurs sooner than in the reference: $\varepsilon_{el}\approx0.30\%$, $\sigma_{el}\approx500MPa$ (Table 4) versus $\varepsilon_{el}=0.37\%$, $\sigma_{el}=700MPa$ for the reference. The first matrix failures happen at a lower strain, but the end of part II is similar.

In order to confirm limits of linear domains, acoustic emission measurements were made during tensile testings of A-HTT/I3/M and A-HTT/M minicomposites (figures 13,14). This measurement takes into account all events, such as cracking, sliding (friction). Beginning of acoustic emission on curves tends to the same conclusions on limits of linear domains. Otherwise, the observed abrupt increase of emission acoustic is attributed to a high matrix damaging, as observations, made in a SEM in-situ tensile testing of a A-HTT/M minicomposite, showed the simultaneous appearance of major part of matrix cracks. On the other hand, absence of an increase of acoustic emission during unload/reload cycle shows that sliding does not involve a significant acoustic emission. Moreover, a more eventful part II for tensile curve (figure 13 compared to figure 14) is associated to a more abrupt increase of acoustic emission, so attribution previously made to a higher damaging is right.

SEM observation has shown the same features as for the reference: multiple matrix cracking, with crack deflection at fibre surface, and fibre crack bridging (figure 15). For the plots with a linear part III, the corresponding Young modulus (based on fibre cross section area) is closed to that of the fibre (Table 4). It confirms that fibres retake the load due to the complete damaging of matrix. Crack spacing was evaluated to be 521µm for A-HTT/I1/M, and 573µm for A-HTT/I3/M, with a similar crack opening (2.3µm). So, damaging is similar for minicomposites, with interphase I1 or I3, and with higher values than A-HTT/M.

Mechanical performances, about 1% of elongation, and 1800MPa for the stress, are identical to those of the reference. This is in agreement with the fact that fibres control the failure as matrix is completely damaged and unloaded.

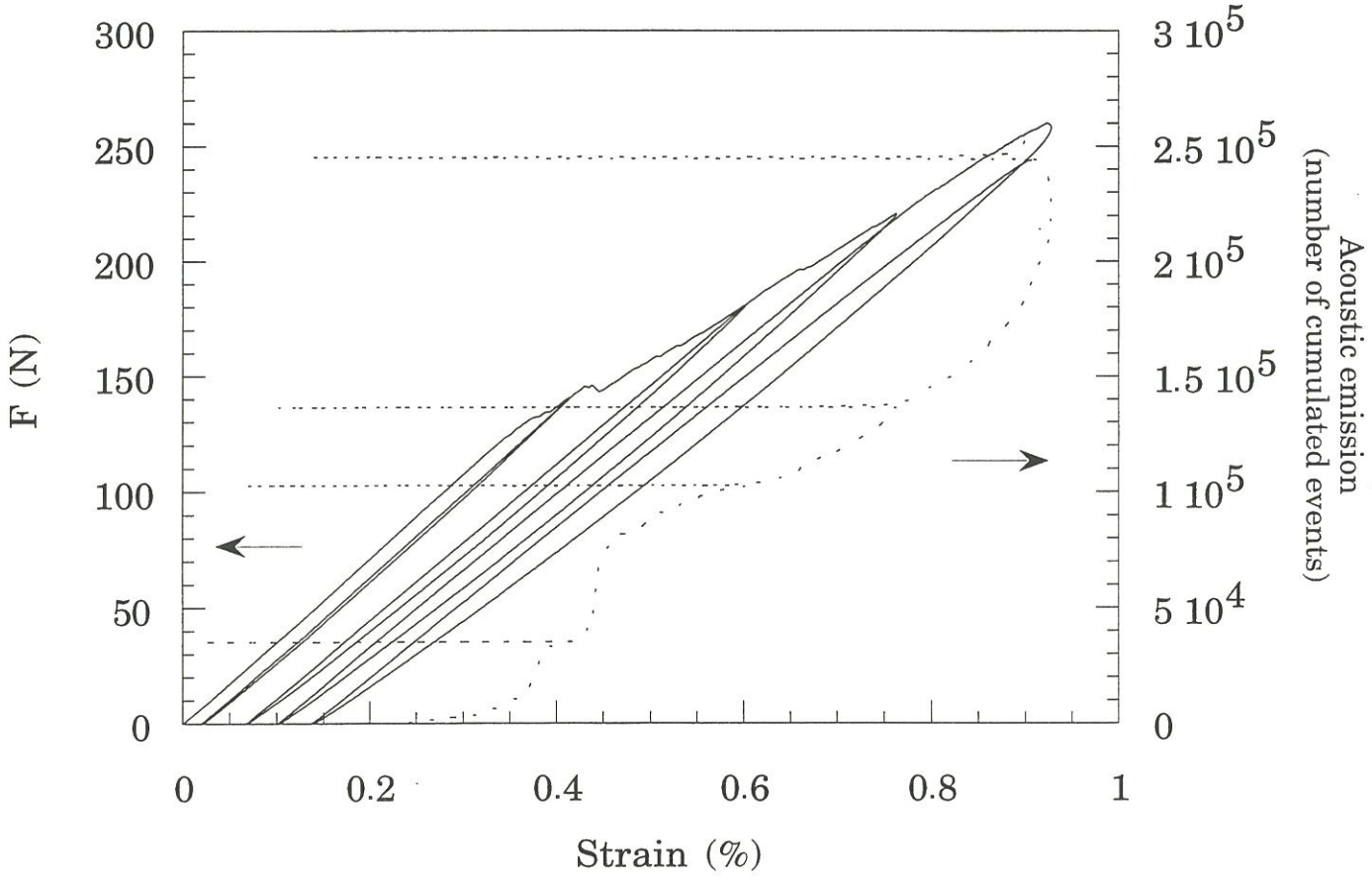

Figure 13: tensile load-strain curve of a A-HTT/I3/M minicomposite with associated acoustic emission; unload/reload cycles were performed

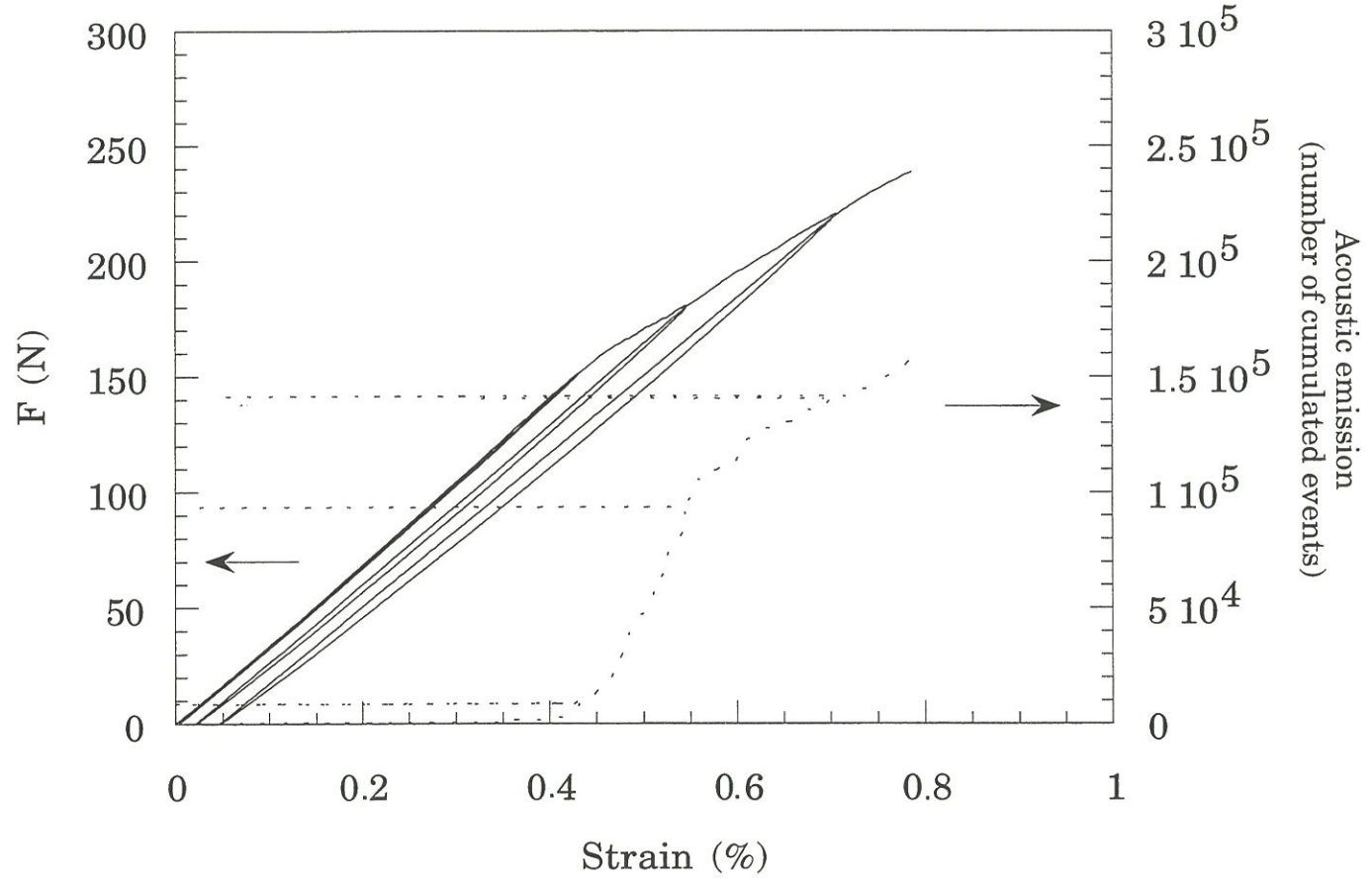

Figure 14: tensile load-strain curve of a A-HTT/M minicomposite with associated acoustic emission; unload/reload cycles were performed

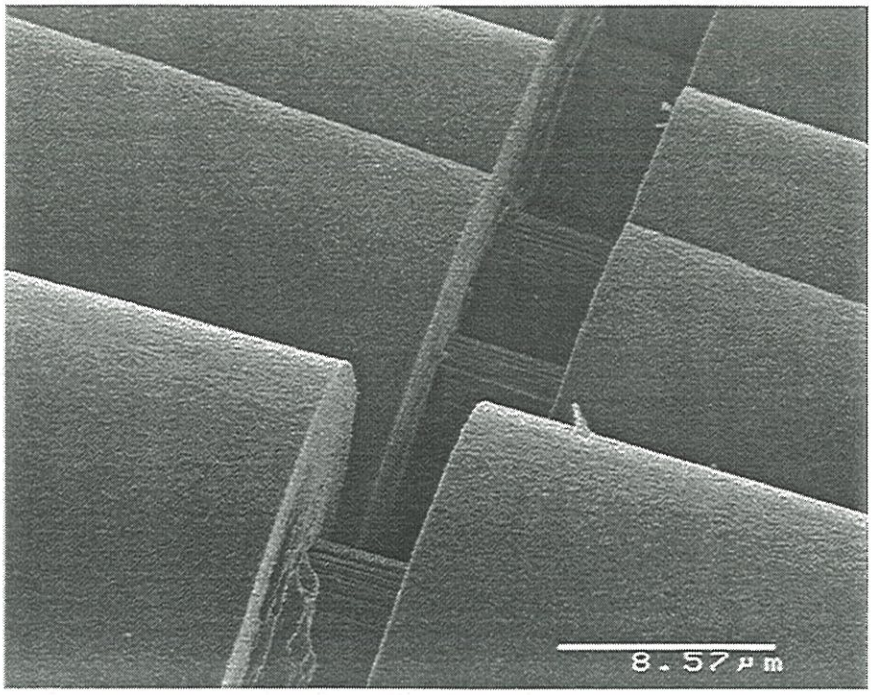

Figure 15: SEM micrograph of a tensile tested A-HTT/I1/M minicomposite showing a crack bridging by fibres

A-HTT / I2 / M minicomposite.

A different mechanical behaviour is encountered for minicomposites with interphase I2 (figure 11). The domain of high damaging (part II), observed for other materials, does not exist anymore. Only, a change in the slope curve occurs for ε_{el}=0.45%. This value is similar to those observed for the preceding materials, when damaging is less important, and with a convex-up part III (figure 7.b). But, after the linear domain, A-HTT/I2/M minicomposite is characterised by a higher load, for a given strain, than those of the other materials. Final slope of the curve (part III) gives a higher Young modulus than that expected for the fibres alone (Table 4). So, for this minicomposite, fibres do not support the load alone up to failure. Matrix remains at least partially loaded up to failure.

Acoustic emission measurements during tensile test (figure 16) showed an abrupt increase of events at $\varepsilon \approx 0.45\%$, and no change of signal during unload/reload cycle. So, A-HTT/I2/M is highly damaged when curve slope changed. Multiple matrix cracking occurs.

SEM observation confirms the multiple matrix cracking (figure 17), but with characteristics far different from what was observed until now. A lower crack spacing was obtained, more than twotimes lower (251µm), associated with a crack opening fivetimes lower than the preceding ones (0.355µm) (figure 17.b). Moreover, optical observation of polished longitudinal sections of failed sample show no apparent crack propagation in the inner part of the material (figure 18.a). There is either crack deflection, or eventually crack closing due to residual stresses. In both cases, residual stresses are not completely relaxed: there are still regions where debonding has not occurred. These observations explain why matrix still participates in a non negligible manner to the load applied up to failure.

Moreover, it is shown that crack deflection occurs in-between the matrix and the interphase (figure 18.c), whereas for other materials it takes place at

fibre surface (figure 9.c). Otherwise, SEM micrographs of a fracture surface (figure 19) shows the same features: fracture of fibre blocks at different levels. Figure 19.b evidences again that crack deflection occurs at matrix/interphase interface in the outer sheath of the minicomposite. This is consistent with the observations on the interface strength deduced from materials behaviour on cutting (§3.2.1).

Thus, a different mechanism of crack propagation is induced by intercalating I2 interphase. The lower crack spacing, and the crack deflection before crack reached fibre surface, remind characteristics of other CMCs matrix-multiple-cracking-based toughening [10]. Difference resides in a crack deflection in-between matrix and interphase, instead of crack branching in the interphase for CMCs with strong interface.

3.3 - Modelling

In order to determine interfacial characteristics of the non-brittle C/C minicomposites, modelling approaches developed for other CMCs were applied to these materials. They show that outer matrix sheath is in tension and the entity, constituted of fibres and the intra-tow matrix, was in compression. Except A-HTT/I2/M, minicomposites have similar characteristics with however an interfacial shear stress slightly higher for the reference (A-HTT/M). A-HTT/I2/M differs from the others by a different damaging mode associated with a relatively high interfacial shear stress.

Intercrack lengths, L_i, measurements permitted to rank minicomposites in terms of decreasing friction, or decreasing interfacial shear stresses, as follows:

A-HTT/I2/M>A-HTT/M>A-HTT/I1/M,A-HTT/I3/M.

Determination of τ values were consistent with this above classification.

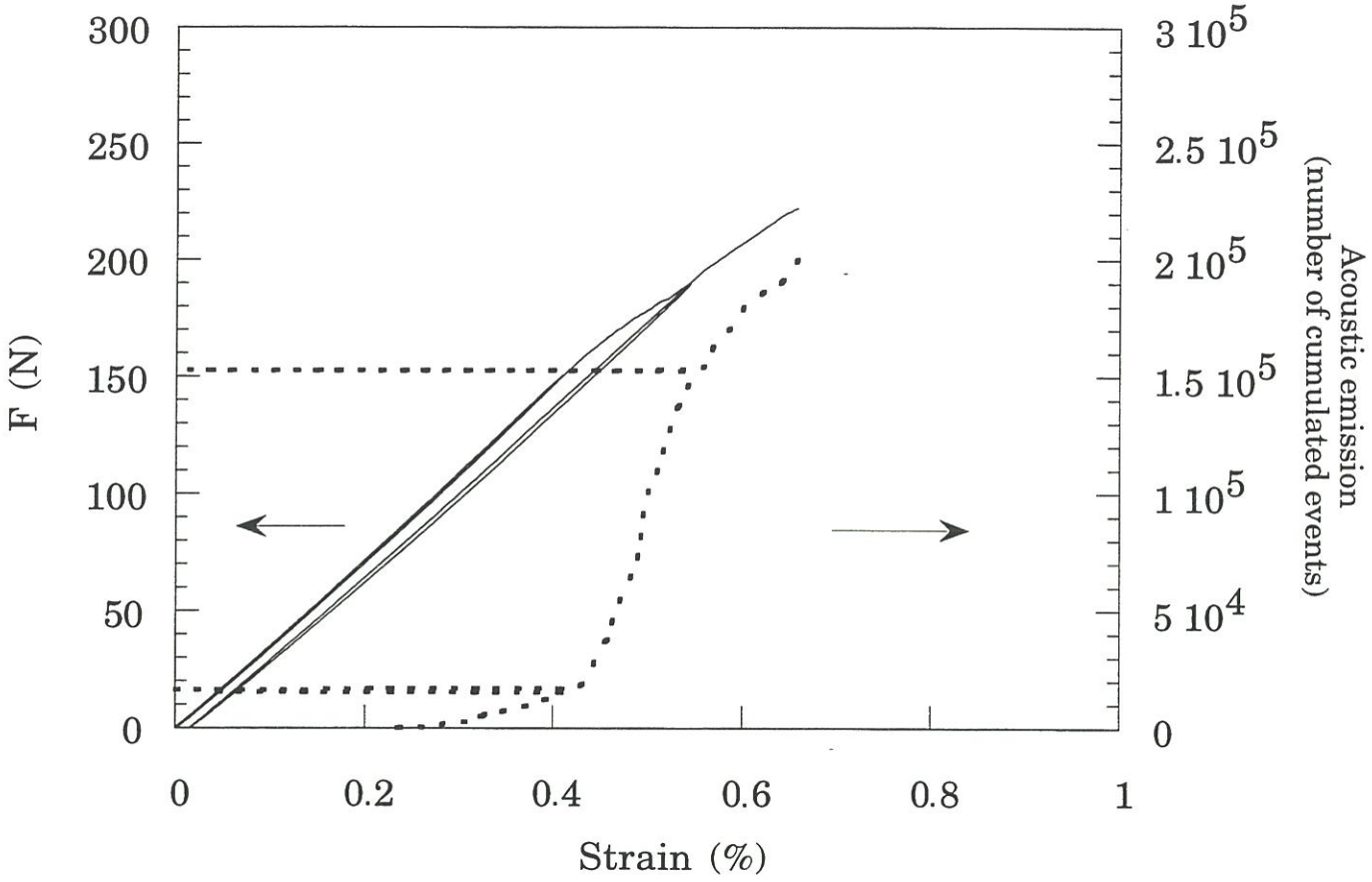

Figure 16: tensile load-strain curve of a A-HTT/I2/M minicomposite with associated acoustic emission, and unload/reload cycles (tensile test was not conducted up to failure)

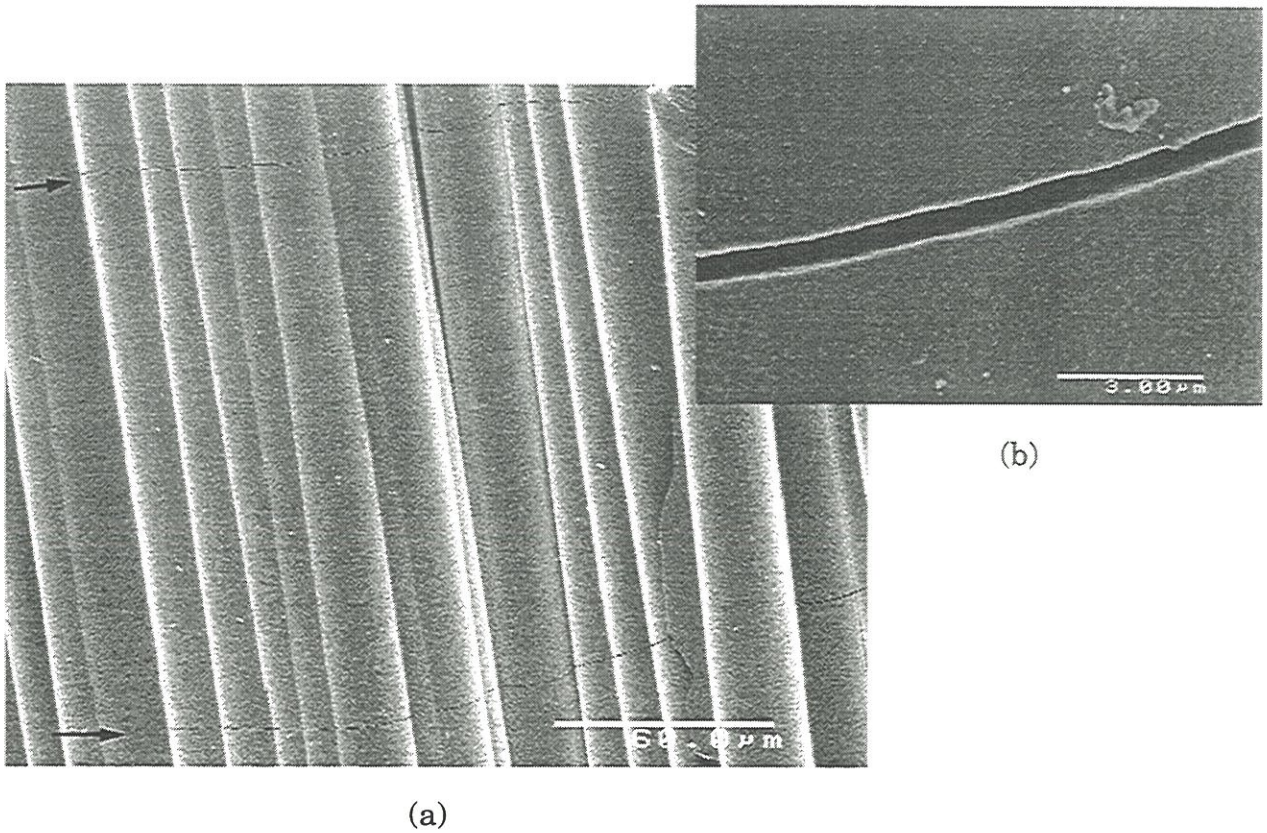

Figure 17: SEM micrograph of a tensile tested A-HTT/I2/M minicomposite showing (a) multiple matrix cracking; (b) magnification of a crack

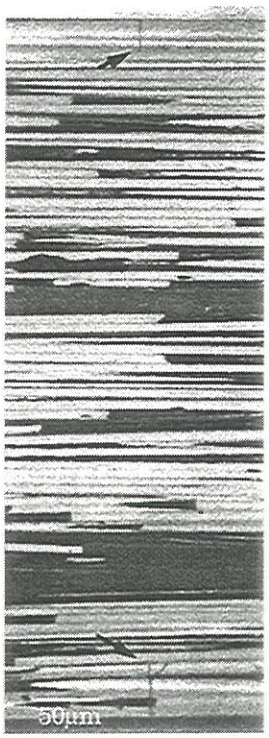

(a)

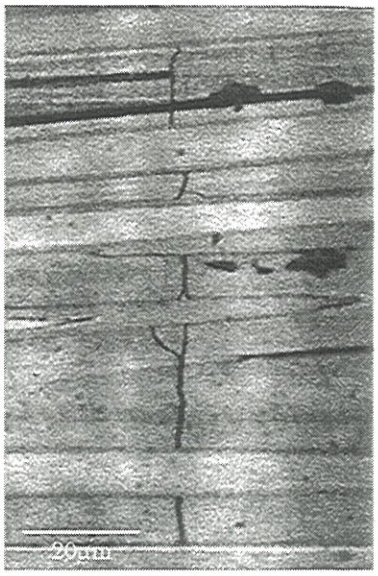

(b)

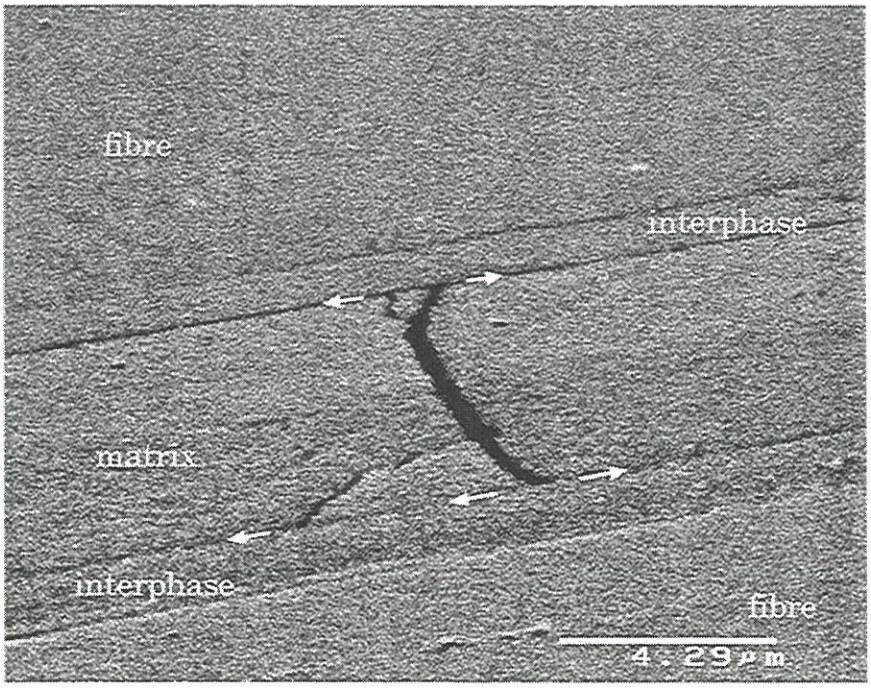

(c)

Figure 18: optical micrographs of a longitudinal section of A-HTT/I2/M loaded to failure (a) whole view showing matrix crack limited to the outer sheath (arrows); (b) high magnification of a crack, (c) showing crack deflection at matrix/interphase interface (arrows) (a and b: optics, c: SEM)

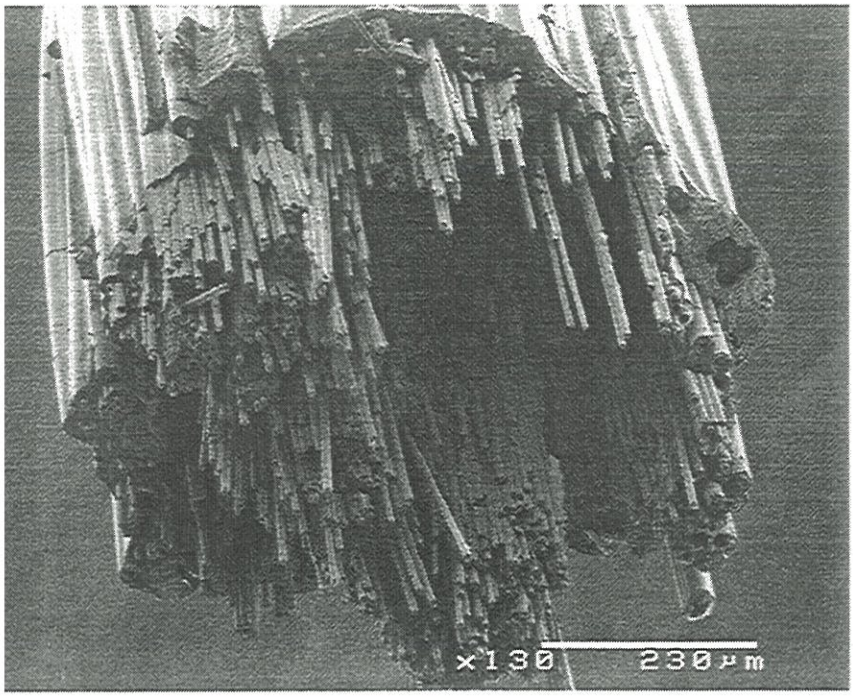

(a)

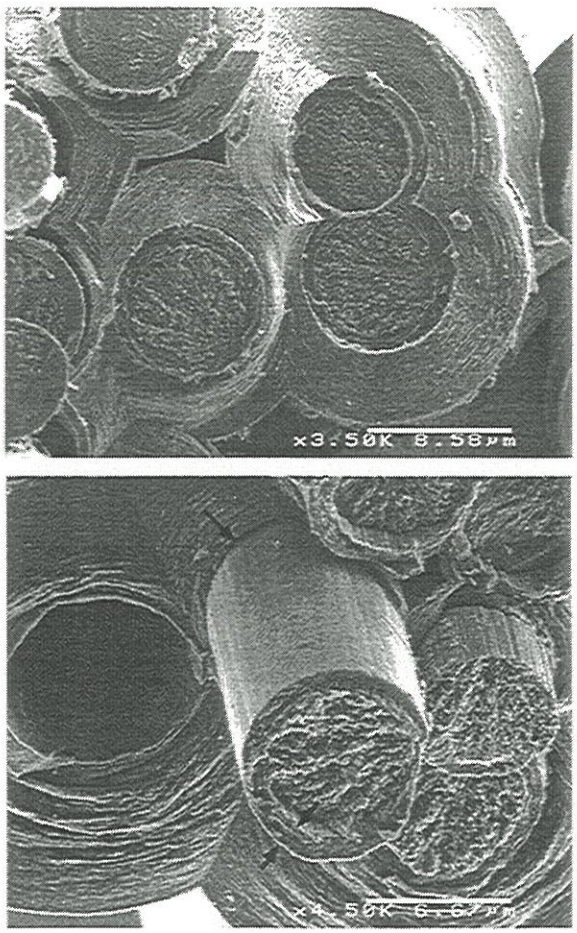

(b)

Figure 19: fracture surface of a A-HTT/I2/M minicomposite
(a) whole surface, and (b) surface regions showing the crack deflection
at matrix/interphase interface

3.3.1 - Interfacial shear stress measurement: τ

The method used to determine τ has been developed for microcomposites (single fibre model composite) [17]. τ was assumed to be constant along the debonded length. Applied to minicomposites, this model gives an apparent interfacial shear stress. For this measurement, unload/reload cycles were performed during tensile testing. The width of the hysteresis loop (figure 20), δΔ, is related to the shear stress and to the applied stress σ during cycling by the equation:

$$\frac{\delta\Delta}{\sigma_p^{\,2}} = \frac{b_2.\left(1-a_1.V_f\right)^2.R.N}{2.E_m.V_f^{\,2}}.\frac{1}{\tau}.\left(\frac{\sigma}{\sigma_p}.\left(1-\frac{\sigma}{\sigma_p}\right)\right) \qquad (7)$$

where σ_p, the maximum stress of the cycle; a_1 and b_2 the Hutchinson coefficients [18] defined for Poisson coefficients equal to 0.4 for fibre and matrix; R, the fibre radius; N the number of matrix cracks.

τ is determined by plotting $\delta\Delta/\sigma_p^{\,2}$ against $(\sigma/\sigma_p.(1-\sigma/\sigma_p))$ (figure 21). For that purpose, the number of cracks at a given stress σ_p has to be known. This number N is estimated, assuming that saturation state is reached. In this case:

$$N = \frac{L}{L_i} - 1 \qquad (8)$$

with L, the gauge length.

Determined values (table 5) show low interfacial shear stresses (<1MPa) for minicomposites, with interphase I1 or I3, and a slightly higher value (1MPa) for the reference minicomposite. On the other hand, A-HTT/I2/M has a relatively high interfacial shear stress (7MPa). In all cases, τ remains low compared to values obtained for brittle C/C composites by microindentation (≈70MPa) [19].

3.3.2 - Coefficient of thermal expansion (CTE) mismatch

An axisymmetric model, developed for C/C/SiC minicomposite [20], was used to calculate the axial residual stresses related to the CTE mismatch.

Table 5. Interfacial shear stresses τ deduced from unload/reload cycles for A-HTT minicomposites

	A(THT)/M	A(THT)/I1/M	A(THT)/I3/M	A(THT)/I2/M
τ (MPa)	1.1	0.73	0.63	6.8

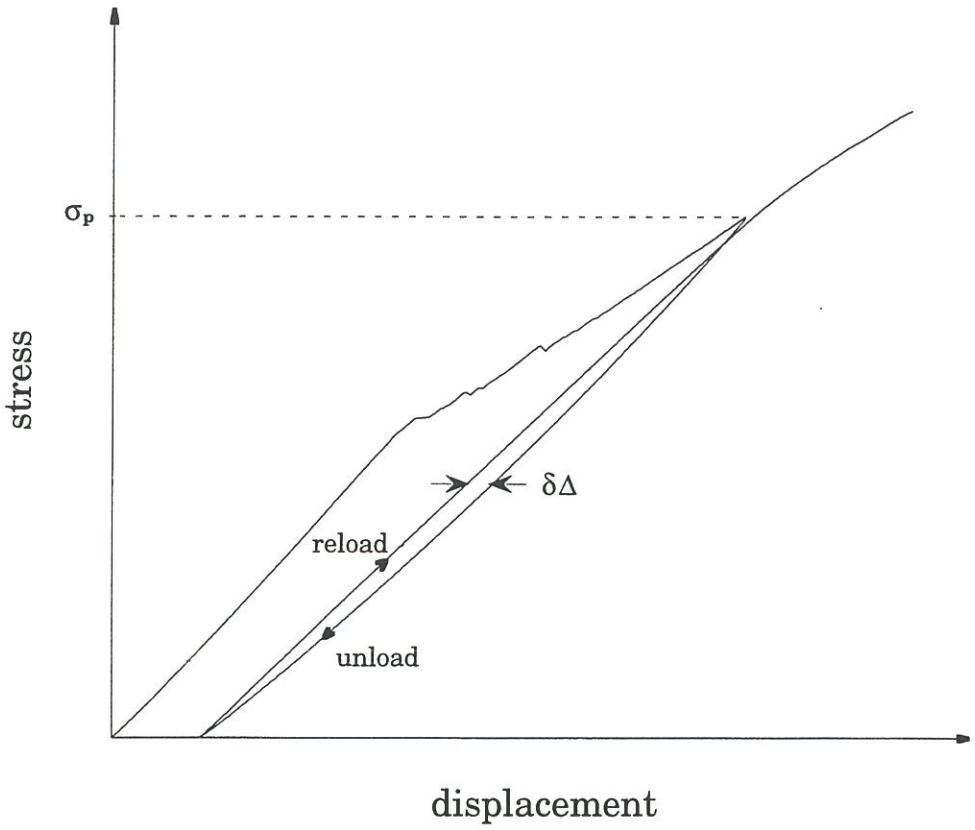

Figure 20: sketch of a unload/reload cycle [18]

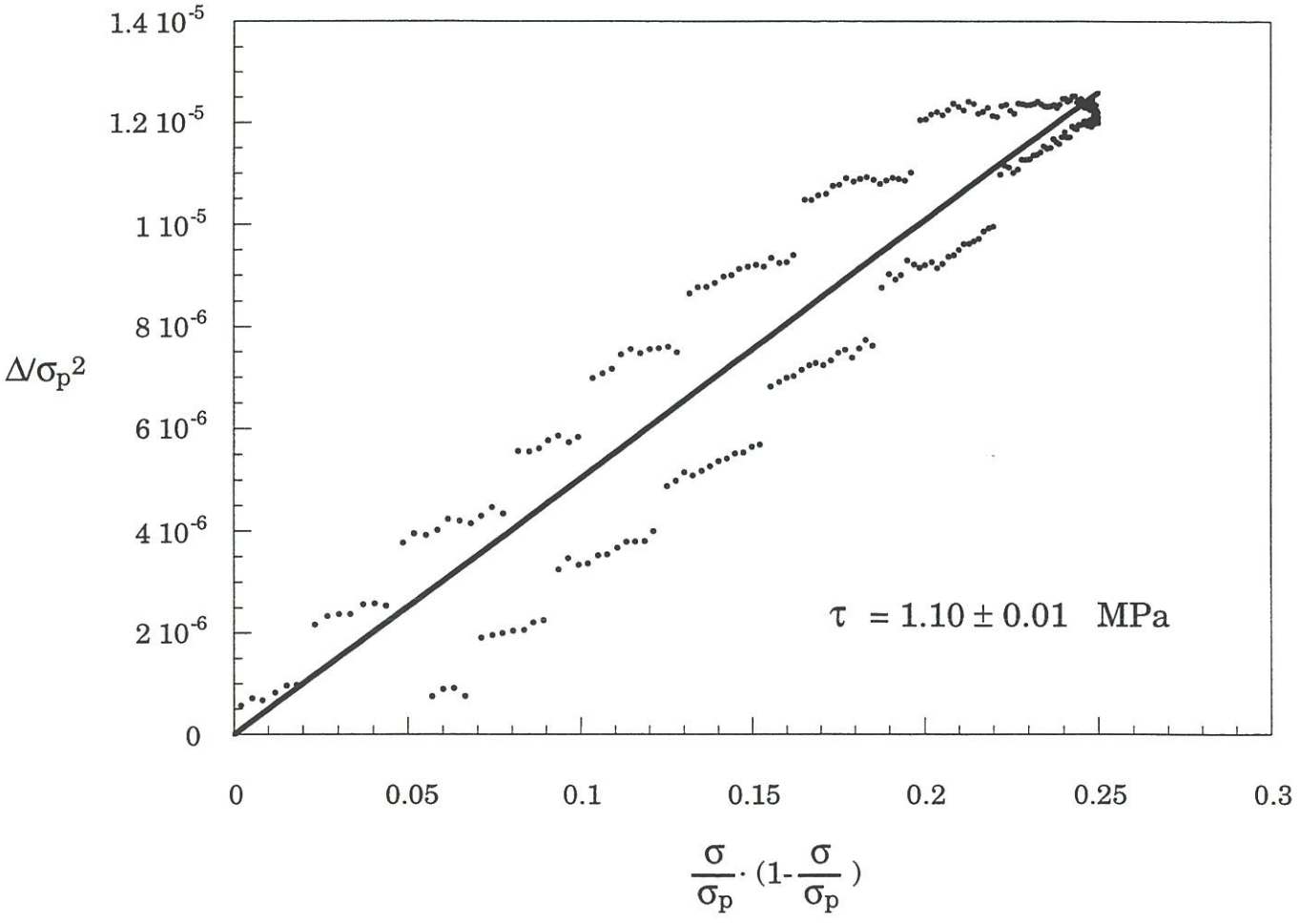

Figure 21: determination of the interfacial stress τ for A-HTT/M minicomposite

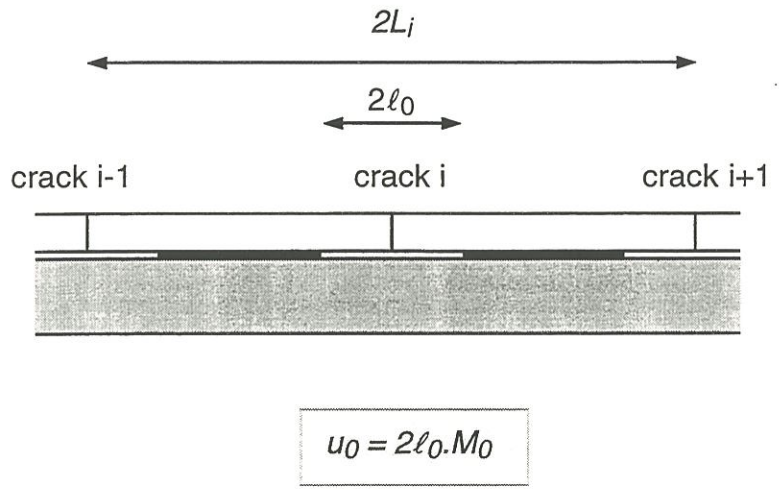

a.

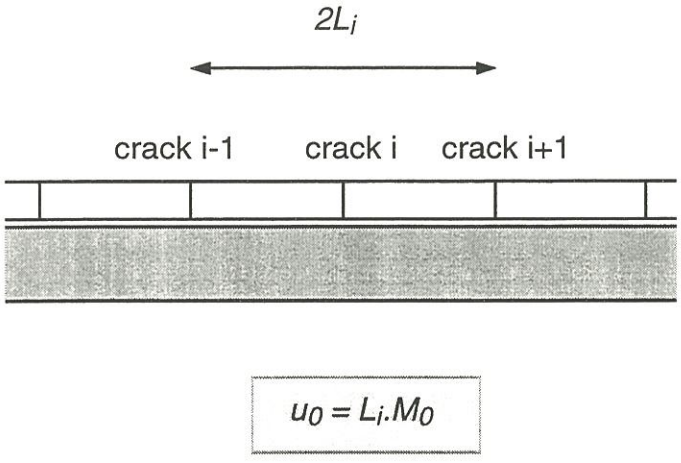

b.

Figure 22: minicomposite damaging [20]
(a) before, and (b) at cracking saturation state

Radial residual stresses, Poisson's effect, and sliding along debonded interfaces (mode II cracks) are neglected in this approach.

The residual crack opening after tensile test (u_0) is related to intercrack length (L_i) at cracking saturation (figure 22.b) by the relation:

$$u_0 = M_0 . L_i \tag{9}$$

where $M_0 = \int_{T_0}^{T_e} (\alpha_m - \alpha_f).dT$, with T_0 the ambient temperature, T_e the processing temperature, α_m and α_f the thermal expansion coefficients of matrix and fibre. For materials, which have not reached the cracking saturation state, the crack opening is independent of intercrack spacing. The ineffective length, ℓ, defined as the half-length related to the debonded domain on both sides of the crack, is identical for each crack ($\ell=\ell_0$) (figure 22.a): $u_0 = M_0 . 2\ell = M_0 . 2\ell_0$ (10)

Otherwise, another value of M_0 can be deduced from measurements of crack opening under load. Crack opening is related to the load F by adding to equation (10) displacement induced by load:

$$u = 2.\ell . (c_f . F + M_0) \tag{11}$$

where $C_f=1/(E_f.S_{f,corr})$.

As $u_0=2.\ell.M_0$,

$$\frac{du}{dF} = 2.\ell . c_f = \frac{c_f}{M_0} . u_0 \tag{12}$$

M_0 is then deduced from the slope of du/dF-u_0 plot.

u_0-L_i plots are represented in figure 23. For A-HTT/I2/M minicomposite, a relatively constant crack opening is observed, which does not permit to determine a M_0 value: independence of L_i towards u_0 means that this material has not attained the cracking saturation state, but the low scattering of the obtained low L_i values can be misleading. u_0-L_i data are consistent with determined interfacial shear stresses. The lower the crack spacing, the higher the interfacial shear stress.

Scattered but rather large intercrack lengths, L_i, and crack openings, u_0, are observed for materials with interphase I1 and I3, and in a less extent for the reference. All points fall on a same straight line characterised by a slope of 0.007. Otherwise, determination of M_0 by crack opening method was conducted

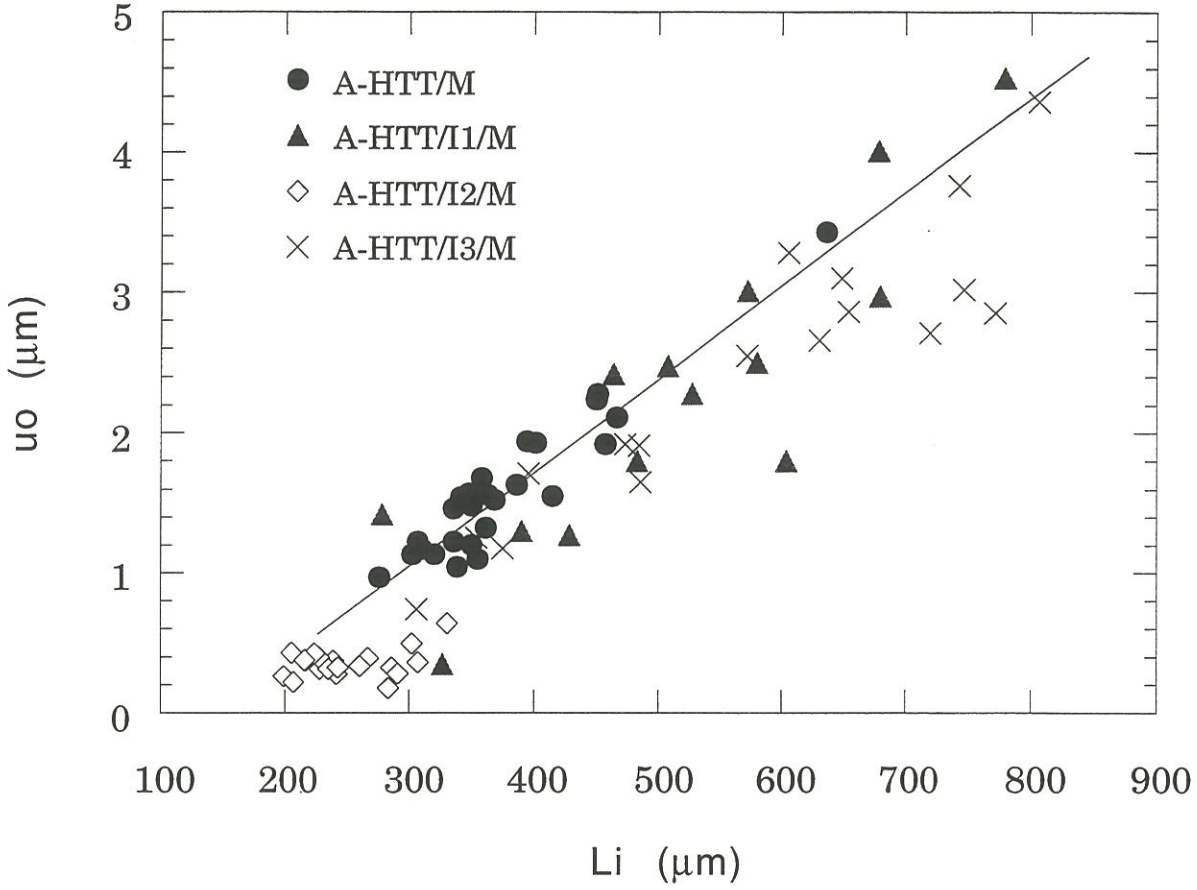

Figure 23: u_0-L_i plots for A-HTT/M and A-HTT/I/M minicomposites

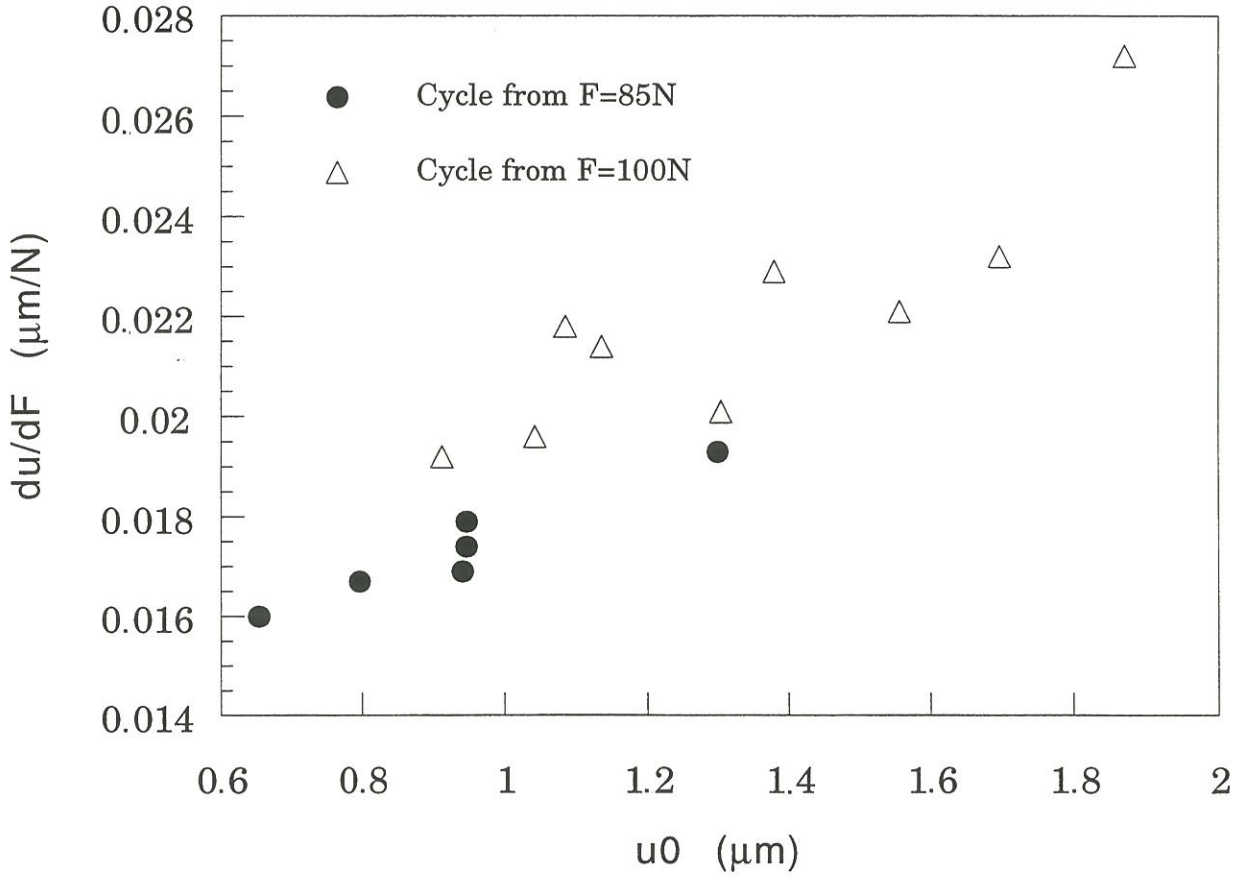

Figure 24: du/dF plots obtained by unload/reload cycles performed on a A-HTT/M tensile tested in a SEM
(each points corresponded to a crack)

on a A-HTT/M minicomposite, tensile tested in a SEM. du/dF-u_0 plots(figure 24) give similar values (0.006; 0.008). But, for du/dF-u_0 plots, as well as for u_0-L_i plots, straight lines, defined by the experimental points do not pass through the origin. Moreover, the associated difference in axial coefficients of thermal expansion, α_{PyC}-α_f, equal to $7.10^{-6}°C^{-1}$, is too high compared to $\alpha_{//}$ cited in literature for same type of carbon fibre (T300: $\alpha_{//}$=-0.5+3.2.10^{-3}.T [21]) and some pyrocarbons ($\alpha_{//(0°C)}$=-1.2.10$^{-6}°C^{-1}$, $\alpha_{//(1000°C)}$=-0.8.10$^{-6}°C^{-1}$ [22]). So, the modelling has to be adapted to carbon/carbon minicomposites in that some stress factors, neglected in above analysis, appear to have more importance than in C/C/SiC minicomposites. However, these results show that reference and minicomposites, with interphase I1 and I3, do have the same characteristics (same slope), so similar axial residual stresses. On the other hand, sign of determined M_0 gives the following information: $\alpha_{PyC}>\alpha_f$, so fibre is in compression and matrix in tension in the minicomposite. Then, for minicomposites, outer matrix sheath is in tension, and the entity, constituted of fibres and intra-tow matrix, is, in the lump, in compression. Strains-to-failure of matrix on tensile curves, as deduced from the onset of non-linearity (0.3 and 0.5%) , are then underestimated.

For A-HTT/I2/M, such axial residual stresses of compression should exist on outer matrix sheath as cracks appear for similar strains (0.4%). Moreover, small L_i value indicates that matrix is reloaded on smaller distances. That fits with a high τ value (§3.3.1). Consequently as L_i decreases, crack opening decreases too, as it corresponds to stress relaxation associated to smaller lengths. So, for the reference and materials with interphase I1 and I3, when matrix crack occurs, a large crack opening happens, associated to a large debonding length.

3.3.3 - Matrix-multiple-cracking mode

By stabilising the fibre and adding an interphase, the damaging mode of the materials is changed: from single to multiple-cracking mode.

Single fracture.

For A/M minicomposite, with $\varepsilon_{R,f}(1.6\%)>\varepsilon_{R,m}(\approx 1\%)$ [13], a single fracture occurs. The brittle behaviour is related to a very strong fibre/matrix bonding: matrix failure involves fibre failure, even though fibre strain-to-failure is higher than that of the matrix. A load-strain curve linear up to failure, and a flat fracture, without fibre pull-out, then characterise A/M, which is schematically resumed in figure 25 (curve (a)). Otherwise, the low strain-to-failure, obtained for this minicomposite (0.57%), indicates that matrix is in axial residual tension in the material. The high interface strength is the result of a good chemical and/or physical bonding, and radial CTE mismatching.

Stabilising fibre (A-HTT) involves decrease of the fibre strain-to-failure, so, a lower difference in strains-to-failure of fibre and matrix, but in the same time a change in CTE mismatch. A weaker fibre/matrix interface is then induced (interface in radial residual tension), with a matrix in slightly higher axial residual tension (first matrix failures at about 0.3%). It results a multiple-matrix-cracking for the A-HTT/M minicomposite.

Multiple fracture.

Debond / sliding mechanism. In this classical model of multiple failure fracture, Aveston, Cooper and Kelly (ACK [23]) have introduced a sliding stress (τ) to better quantify the fibre/matrix load transfer in the debonded region. In this model, the major contribution to toughness involves sliding of the fibres along the debonded interfaces [24,25]. Toughening thus requires extensive initial debonding which necessitates weak interfaces. Behaviour obtained with the stabilised fibre (A-HTT/M) exhibits the typical features described by this model, as schematically represented in figure 26.a and 26.b (low τ). It corresponds to an elastic loading up to the first matrix crack[1]. Then, if the fibres are able to sustain the additional load thrown upon them, multiple

[1] As shown by White et al. [26], low pressure CVI produces laminar pyrocarbon free of cracks. For other carbon matrices, this first part is more likely an extension of pre-cracks.

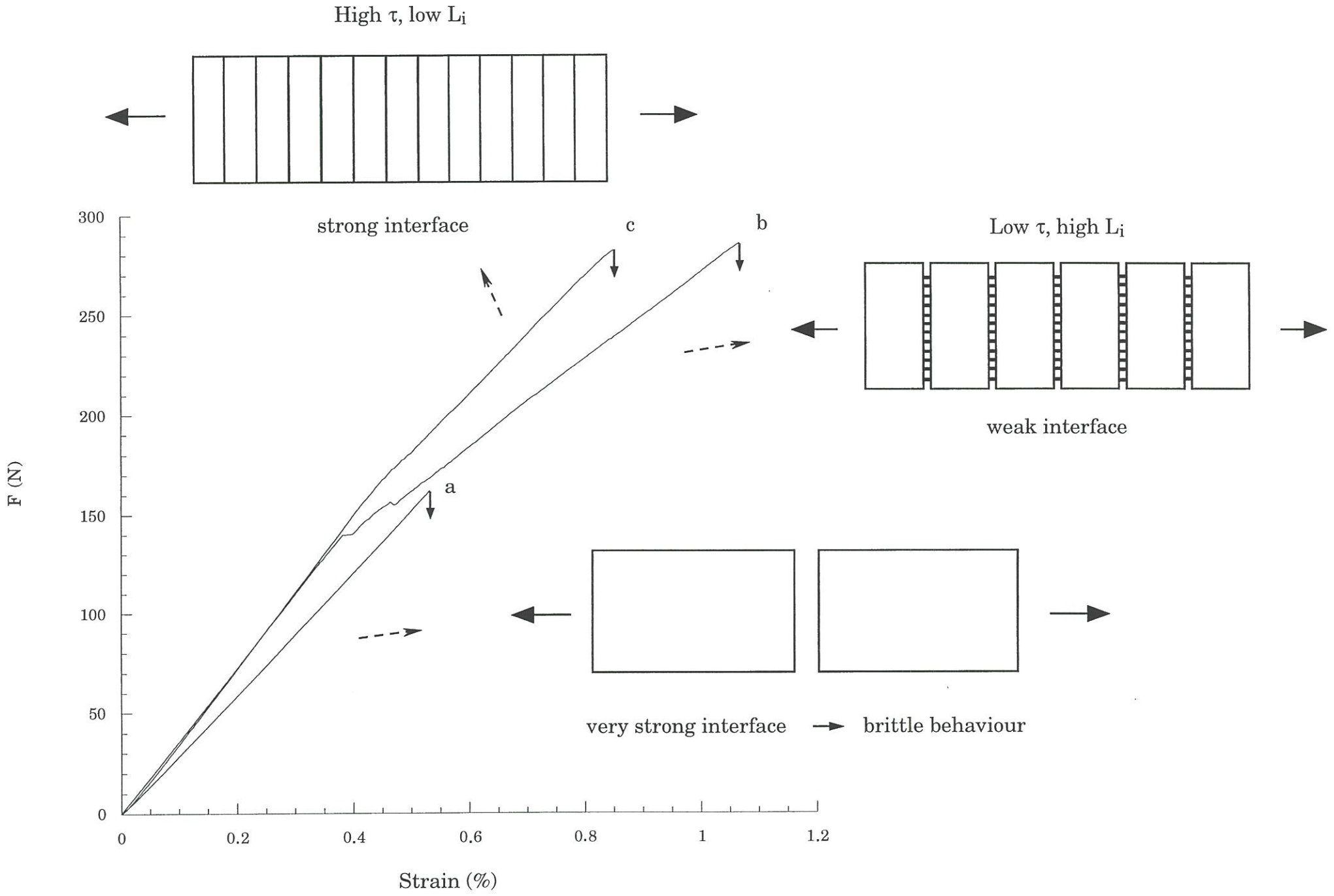

Figure 25: typical tensile curves obtained on C/C minicomposites according to interface strength, and associated schematic damaging mode

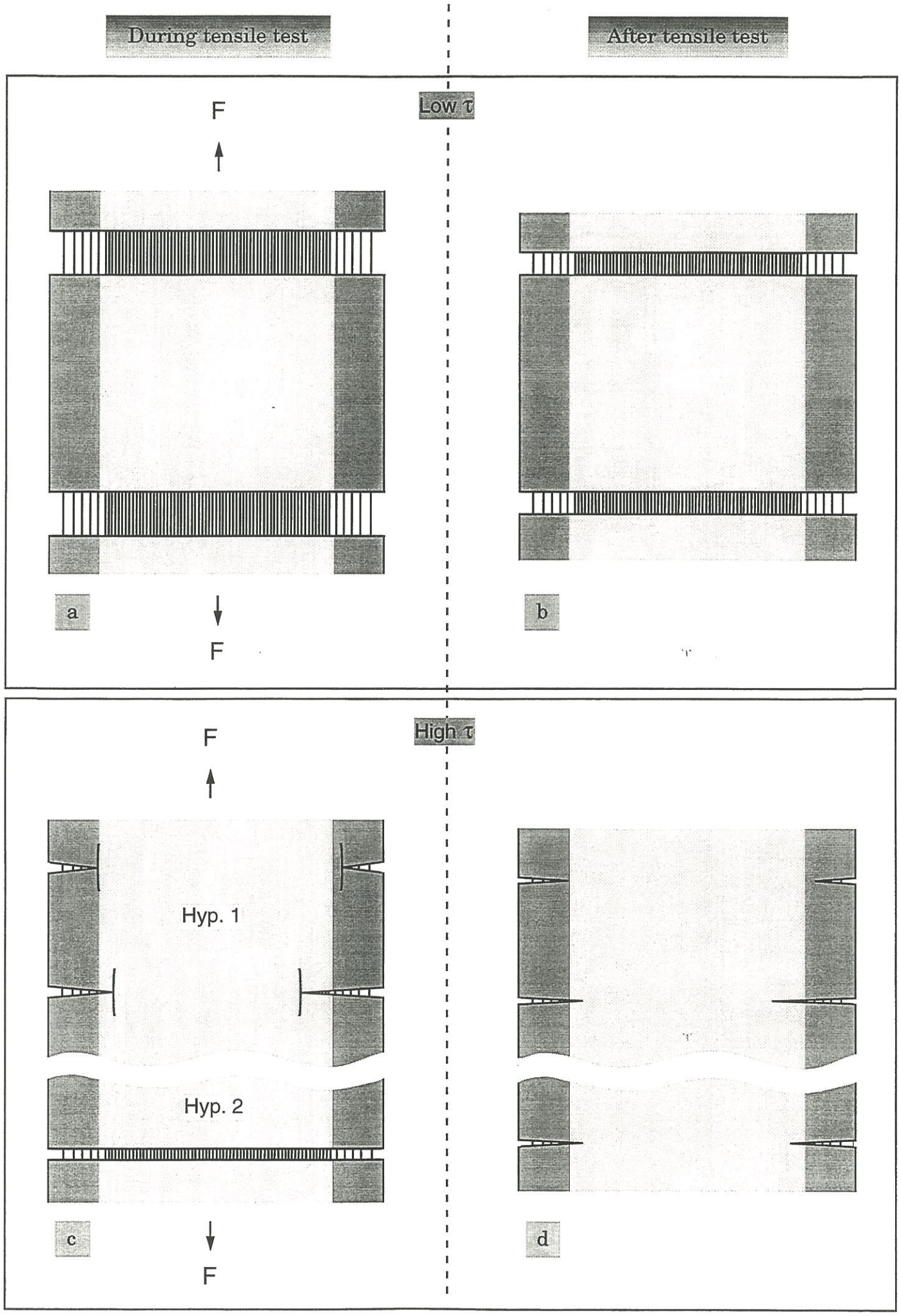

Figure 26: damaging mode according to interfacial shear stress (shematics)

fracture occurs (part II of the load strain curve). The load borne by the matrix is taken up by the fibres: first, residual axial compression is released, and secondly the overload creates an extra extension. A displacement of fibre and matrix in reverse direction is occurring during the test (figure 26.a). After the test, the failed sample exhibits residual strain (figure 26.b). As τ is low, the volume of matrix unloaded is high, as well as the debond length 2ℓ. As a result, the crack spacing observed in the failed sample is high [27], and so is the crack opening. This behaviour is represented in figure 25 (curve (b)).

Multiple-cracking-based toughening. When the fibre has been previously stabilised, and when the interlayer deposition (interphase I2) produces a high τ, multiple fracture appears different. Experimental observations have shown very fine cracks with a low spacing, only visible in the outer zone with a high V_m (dark grey in figure 26.d). Two different hypotheses can be formulated, whereas to the damaging mode in that material: (1) cracks are really limited to the outer zone; (2) cracks are crossing the whole minicomposite but close back by unloading.

In the first hypothesis (figure 26.c,d Hyp.1), the minicomposite behaves as a large single-fibre composite because of the large V_m variations: in the outer zone V_m is 85%, and less than 10% in the inner zone. It can be supposed that elastic modulus and residual stress are homogenised. As a result, the sheath is in tension (dark grey in figure 26.c) and the inner part in compression. Matrix cracking is thus limited to the external zone, and deflection at the tip of the cracks occurs at the first fibres of the inner zone.

Fracture surfaces observation has shown that the catastrophic failure is occurring at different levels in sheath and core. That fits quite well with that assumption.

In the second hypothesis, it is supposed that cracks are passing through the whole minicomposite (figure 26.c,d Hyp.2). But as τ is high, the debond length is reduced, and matrix remains partially loaded up to failure. When

unloading, cracks closure occurs (figure 26.d Hyp.2), due to an incomplete relaxation of residual stresses in the core of the minicomposite.

For either one or the other assumptions, the increase of τ and the decrease of ℓ, as well as the residual strain (unload test) are the same features as those encountered in CMCs [28] related to an alternative toughening mechanism. Indeed, toughening is not based on low debond energy and sliding, but rather on a good load transfer to the matrix with an increase of the work of fracture by increasing the matrix cracking. This work suggests that this mechanism is controlled by tensile radial residual stress, and a strong chemical bonding (interphase). This damaging mode generates the third mechanical behaviour observed for C/C minicomposites (figure 25 curve (c)).

4 - CONCLUSION

Non-heat-treated fibre (A) gives a brittle carbon/carbon minicomposite, whereas stabilised fibre (A-HTT) leads to a non-brittle behaviour with multiple matrix cracking. Rearrangement of carbon planes along fibre axis with HTT, leads to a higher transverse thermal expansion coefficient for the stabilised fibre. As a result, a fibre/matrix interface is in higher residual tension, so, easily debonded, and thus preventing a catastrophic failure through the fibres by deflecting the cracks. In that case, toughness is based on the **debond/sliding mechanism** of the weak interface: low τ (a few MPa), high crack spacing (a hundred μm), and high residual elongation. This behaviour is featured by a load-strain curve with a non-linear domain with a plateau-like feature (zone II in figure 7).

Addition of a carbon interphase (I2) **between fibre and matrix permits to toughen C/C minicomposites by a matrix-multiple-cracking-based mechanism**. The different mechanical behaviour induced by this interphase is attributed to an enhanced chemical bonding combined with tensile thermal

residual stresses. Matrix-multiple-cracking-based mechanism is known with strong interface [11]: high τ (a few hundred MPa), low crack spacing (a few ten μm) and low residual elongation. The load-strain curve exhibits a non-linear convex-up domain.

As a result, with stabilising a HT PAN-based fibre and adding a carbon interphase, toughness of unidirectional C/C composites was successfully obtained with similar energy dissipation processes than for other CMCs.

Acknowledgements

This work has been supported by SEP and CNRS through a grant given to B.T. The authors thank F. Rebillat for his contribution in hysteresis loop analysis, G.-A. Lebrun for helpful suggestions and comments, and B. Humez from LCTS, for technical assistance.

REFERENCES

[1] C.R. Thomas, E.J. Walker, Effects of PAN carbon fibre surface in carbon-carbon composites, Proceedings 5th Conf. on Industrial Carbon and Graphite, Soc. Cem. Ind. London, **1**, pp. 520-531 (1978)

[2] E. Fitzer, K.H. Geigl, W. Hüttner, The influence of carbon fibre surface treatment on the mechanical properties of carbon/carbon composites, Carbon, **18**, pp. 265-270 (1980)

[3] L.M. Manocha, O.P. Bahl, Y.K. Singh, Mechanical behaviour of carbon-carbon composites made with surface treated carbon fibers, Carbon, **27**, N°3, pp.381-387 (1989)

[4] S. Takano, T. Uruno, T. Kinjo, P. Tlomak, C.P. Ju, Structure and properties of unidirectionally reinforced PAN-resin based carbon-carbon composites, Journal of Materials Science, **28** , pp. 5610-5619 (1993)

[5] W. Kowbell, C.H. Shan, The mechanism of fiber-matrix interactions in carbon-carbon composites, Carbon, **28**, N°2/3, pp.287-299 (1990)

[6] R.J. Zaldivar, G.S. Rellick, J.M. Yang, Fibre strength utilization in carbon/carbon composites, J. Mater. Res., **8**, N°3, pp.501-511 (1993)

[7] R.J. Zaldivar, G.S. Rellick, J.M. Yang, Microstructural observations on the failure modes of unidirectional carbon/carbon composites, in Extended Abstracts of the 21st Biennal Conference on Carbon, American Carbon Society, Buffalo, June 13-18, (1993)

[8] C. Ahearn, B. Rand, Modification of the fibre-matrix bonding in a brittle carbon-carbon composite by controlled oxidation, Carbon, **34**, N°2, pp.239-249 (1996)

[9] A.G. Evans, F.W. Zok, J. Davis, The role of interfaces in fiber-reinforced brittle matrix composites, Comp. Sci. Technol., **42**, pp.3-24 (1991)

[10] C. Droillard, J. Lamon, X. Bourrat, Strong interface in CMCs, a condition for efficient multilayered interphases, Mat. Res. Symp. Proc., **365**, pp.371-375 (1995)

[11] X. Bourrat, B. Trouvat, G. Limousin, G. Vignoles, Pyrocarbon anisotropy as measured by electron diffraction and polarized light, to be submitted in Journal of Materials Research

[12] N. Lissart, Probabilités de rupture et fiabilité des composites à matrice céramique, PhD Thesis, University of Bordeaux, n°1207, 8 December (1994)

[13] B. Trouvat, X. Bourrat, R. Naslain, Fibre-matrix bonding in carbon/carbon microcomposites: role of HTT and surface roughness of the fibre, to be submitted in Carbon

[14] J. Rappeneau, F. Tombrel, Propriétés physiques des carbones, in Les Carbones, A. Pacault, Groupe Français des carbones ed., pp.839-910 (1965)

[15] B. Rand, Matrix precursors for carbon-carbon composites, in Essentials of carbon-carbon composites, C.R. Thomas ed., Royal society of chemistry, pp.67-102 (1993)

[16] B. Trouvat, X. Bourrat, R. Naslain, Influence of a carbon interphase with a controlled microtexture on mechanical properties of single fibre C/C/C microcomposites, to be submitted in Carbon

[17] J. Lamon, F. Rebillat, Microcomposite test procedure for evaluating the interface properties of ceramic matrix composites, J. Am. Ceram. Soc., **78** [2], pp.401-405 (1995)

[18] J.W. Hutchinson, H.M. Jenson, Models of fiber debonding and pull-out in brittle composites with frictions, Mechanical of Materials, **9**, pp.139-163 (1990)

[19] K. Hamada, S. Sato, H. Tsunakawa, A. Kohyama, Interfacial microstructure and mechanical properties of C/C composites, Proceedings of ICCM-10, Whistler, B.C., Canada, August, **VI**: Microstructure, Degradation, and Design, pp.423-430 (1995)

[20] G.-A. Lebrun, Comportement thermomécanique et durée de vie de composites à matrice céramique: théorie et expérience, PhD Thesis, University of Bordeaux, n°1606, 30 November (1996)

[21] E. Yasuda, Y. Tanabe, H. Machino, S. Kimura, Correlation between thermal expansion coefficient and orientation function of various types of carbon fibers, 18th Biennal Conference on Carbon (1987) p.30, Tanso (1988) [N°132] 3

[22] B.T. Kelly, Physics of graphite, Applied Science Publishers (1981)

[23] J. Aveston, G.A. Cooper, A. Kelly, Single and multiple fracture, in "The properties of fiber composites" conference Proceedings of the National Physical Laboratory, IPC Science and Technology Press, Surrey, England, pp.15-26 (1971)

[24] A.G. Evans, Perspective on the development of high-toughness ceramics, J. Am. Ceram. Soc., **73**, pp.187-206 (1990)

[25] R.J. Kerans, R.S. Hays, J. Pagano, T.A. Parthasarathy, The role of the fiber-matrix interface in ceramic composites, Ceramic Bulletin, **68**, [2], pp.429-442 (1989)

[26] J. Dubois, C. Agache, J.L. White, Metallography, **3**, p.337 (1970)

[27] J. Lamon, Interfaces and interfacial mechanics: influence on the mechanical behavior of ceramic matrix composites (CMC), Journal de Physique IV, colloque C7, supplement au journal de Physique III, **3**, November, pp.1607-1616 (1993)

[28] R. Naslain, Fiber-matrix interphases and interfaces in ceramic matrix composites processed by CVI, Composites Interfaces, **1**, n°3, pp.253-286 (1993)

ANNEXE 4

Pyrocarbon anisotropy as measured by electron diffraction and polarised light

ANNEXE 4

Pyrocarbon anisotropy as measured by electron diffraction and polarised light

1 - INTRODUCTION 2

2 - EXPERIMENTAL 3

2.1 - Optical microscopy 3

2.2 - Transmission electron microscopy (TEM) 4

2.3 - Image Analysis (IA) 4

3 - RESULTS AND DISCUSSION 5

3.1 - Optical measurement of the anisotropy 5

3.1.1 - Fundamentals of the technique *5*

3.1.2 - Measurements *9*

3.2 - Pyrocarbon anisotropy as measured by electron diffraction 10

3.2.1 - Pyrocarbon diffraction and anisotropy *10*

3.2.2 - Measurement procedure *11*

3.2.3 - Results *12*

3.2.3.1 - Anisotropy of interface pyrocarbon in C/C composites 12

3.2.3.2 - Comparative variation of anisotropy, OA, and d_{002} interlayer spacing 14

4 - DISCUSSION 16

5 - CONCLUDING REMARKS 17

REFERENCES

Pyrocarbon anisotropy as measured by electron diffraction and polarised light

Submitted in Journal of Materials Research

X. BOURRAT, B.TROUVAT, G. LIMOUSIN and G. VIGNOLES

Laboratoire des Composites Thermostructuraux

UMR 47 CNRS-SEP-UBI, Université Bordeaux I

3, allée de la Boëtie, 33600 Pessac, France

F. DOUX

Société Européenne de Propulsion - Le Haillan

BP37 - 33165 Saint Médard-en-Jalles, France

SUMMARY

This work is dealing with the measurement of the anisotropy of pyrocarbon by electron diffraction on very thin fibre-coatings used to control the interfacial behaviour in carbon/carbon composites. It is proposed to differentiate the various pyrocarbons on the basis of the disorientation of the coherent domains with respect to the anisotropy plane. This was realised by image analysis of the electron diffraction pattern micrographs, by measuring the azimuthal opening of the carbon 002 diffraction arcs. A computer program records then fits the intensity along the Debye-Scherrer 002 ring by a gaussian law, and the full width at half height is named the Orientation Angle (OA). This angle increases with the loss of anisotropy when the texture switches from rough-laminar to smooth- or dark-laminar. Comparisons are made between this technique and more classical optical measurements made by means of polarised light, which are more rapid and only semi-quantitative. The two techniques are complementary since they deal with different scales.

1 - INTRODUCTION

In the field of carbon/carbon composites, the relationship between structure and mechanical properties is of prime interest. That is mainly due to the high anisotropy of the graphitic form of carbon involved in these materials, especially in the different forms used in carbon/carbon composites (C/C). A good example is the carbon fibre itself, the modulus of which was shown to be directly related to the orientation angle of the basal planes along the fibre axis [1].

For pyrocarbons, it is already known that most of the physical properties change with their structure. It is demonstrated in companion papers [2,3] that changing the structure of pyrocarbon between the fibre and matrix by depositing an interphase, enables to switch the tensile behaviour from brittle to non-brittle. So, it is especially important to measure and control the anisotropy in order to monitor the interface, e.g. fibre/matrix chemical bonding strength, CTE, etc. [2-4].

Different methods have been developed to measure the carbon anisotropy. Most of them are based on X-ray diffraction (XRD) [1, 5-7], whereas the other ones involve optical methods [8-12] measurement of the reflecting power anisotropy. Bomar et al. [9] have introduced an "optical anisotropy factor" which is defined as the ratio of maximum-to-minimum intensity of the reflected light by rotating the stage on a 15µm-large field. This is done with a micro-photometer and was latter developed by Koizlik and Grübmeier [11] on a smaller target : from 10µm down to 5µm. This factor is well related to the X-ray "Bacon factor of anisotropy" [7]. Different setups have been developed. For example, Stevens has used a synchronous micropolarimeter [10] to approach the bireflectance (Re-Ro).

However, the reflectance anisotropy level (Ro/Re) can be very easily approached on a regular polarising microscope. According to Diefendorf and

Tokarsky [8], the technique has a good spatial resolution (> 2μm) and is very accurate to distinguish low-pressure and low temperature CVD/CVI pyrocarbons [e.g.13]. It will be regarded in this work as a reference. For that reason it will be precisely described in the first part of paragraph 3.

The optical texture of pyrocarbons is indeed well related in many situations, but it was seen in a previous work [14] that the scale of the relevant phenomenon, for example at the interface of a C/C, was far below the optical resolution: indeed, it lies at the nanometer scale of few carbon layers. In this work, a procedure based on TEM image analysis was developed to extract some quantitative structural data.

2 - EXPERIMENTAL

A series of model carbon/carbon composites, constituted by a single filament or a bundle of the same fibres were prepared by a CVD process in a hot-wall furnace described elsewhere [2] and reported in Table 1. Propane but also methane were used to manage the two successive pyrocarbon coatings. First, a thin layer (0.5μm) was deposited with various microtextures. This coating has a mechanical role and is called interphase as in other ceramic composites [15]. Then, the matrix was deposited systematically under the same CVD conditions.

2.1 - Optical microscopy

For optical measurements, the same deposit conditions were used, but only one type of pyrocarbon was deposited as a thick coating to perform the measurement. Polishing was made, following a classical protocol. The finishing was obtained with a alumina polishing suspension (0.05 μm).

Table 1. Characteristics of pyrocarbons

	Pyrocarbon characteristic	
	Ae (°)	Microtexture
M	17	Smooth Laminar
M_{int}	18	Rough Laminar
Ia	15	Smooth Laminar
Ib	13	Smooth Laminar
Ic	11	Dark Laminar

N.B.: matrix is designated by M, and interphases by Ia, Ib, and Ic
Ae is the extinction angle (optical measurement in polarised light)

All the measurements were made in this study on a MeF3 REICHERT-JUNG™ apparatus. It is an inverse microscope equipped with a polariser and a rotatable analyser.

Sample are polished sections of the deposit with the basal plane edge-on (maximum bireflectance). The orientation of the anisotropy plane on the stage of the optical microscope is either set at 45° or, for uniaxial deposits, measurement have to be done in the same diagonal position as shown in figure 1. In this situation the incident light is plane polarised and has its vibration direction parallel to the polariser. Originally, the analyser is crossed : a Maltese cross appears with the extinguished branches parallel to the Nicols.

2.2 - Transmission electron microscopy (TEM)

Samples were obtained by mechanical thinning and ion-milling with a Gatan DuoMill™ at room temperature. The details of the procedure were described previously [4]. Electron diffraction was conducted in a Philips CM30ST. The selected area diffraction technique (SAD) was preferred for its high angular resolution, with an aperture of 110nm in diameter. The illumination is set up with a high emission, C_1-lens moderately excited (spot size "3"), a 100µm condenser aperture is used, and the C_2-lens is defocused in order to keep a high signal intensity with a negligible α angle. A selected area of 110nm in diameter was systematically used, with a 5 mm selection aperture. The camera length on the plate was L=1.35m in order to get a high resolution diffraction pattern. Two or three exposure times were necessary in order to get the right optical density on the 002 ring, in the range of 5 to 10s. The film was a Scientia™ film from Agfa.

2.3 - Image Analysis (IA)

The TEM micrographs were digitised on an Arcus II™ scanner from Agfa equipped with a transmission back and with a resolution of 2400 dpi in

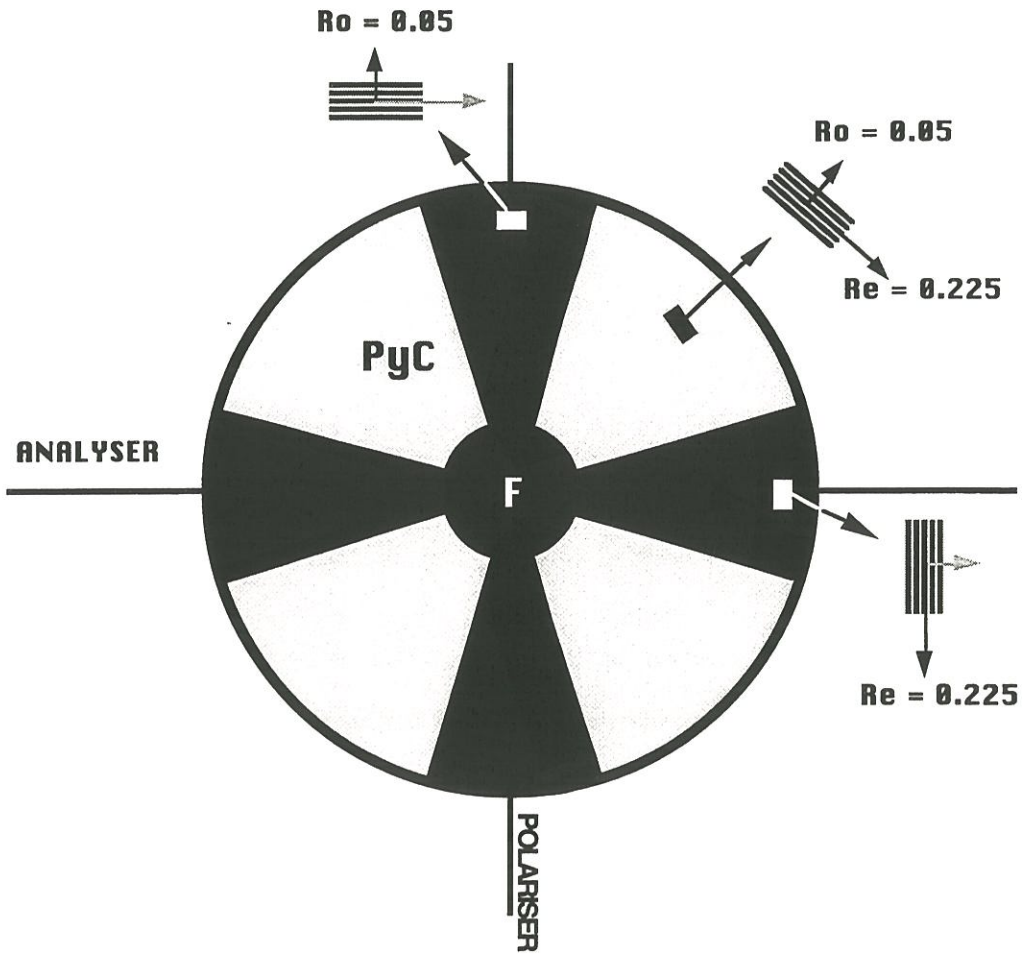

Figure 1: Observation of a cross-section of a microcomposite (single fibre coated with pyrocarbon) in optical microscopy under cross-polars

grey level. The optical density accessible with that scanner is much better than that of the emulsion : 0.08 < DO < 3.30. The pattern was recorded with the absolute density scale, by means of the automatic control. A squared size (1600 x 1600 pixel) image was obtained.

The image processing algorithms were developed on a Power Mac 7100/66 (RAM : 72Mo and an CPU : 66 MHz) with the Labview™ software from National Instruments (Austin, TX USA), provided with the Concept Vi™ image analysis virtual instrument library from Graftek (France). This software enables developing dedicated image processing applications in the LabView™ context.

3 - RESULTS AND DISCUSSION

3.1 - Optical measurement of the anisotropy

3.1.1 - Fundamentals of the technique

The measurement of the optical properties of opaque materials as pyrocarbon can be performed by means of reflected polarised light. Optical properties depend on three basic phenomena : reflection, refraction and absorption of light. Light vibration has an electromagnetic nature. On the ray path, an electric field and a magnetic field are propagating in phase and perpendicularly. The plane which contains the electric field to which the human eye is sensitive is considered as the light vibration plane in this paragraph. The electric field variations E represents the amplitude. The velocity of an electromagnetic wave is given by the relation :

$$c = c_0(1/\varepsilon\mu)^{-1/2} \quad (1)$$

$$\text{with } (\varepsilon\mu)^{-1/2} = n \quad \text{then : } c = c_0/n \quad (2)$$

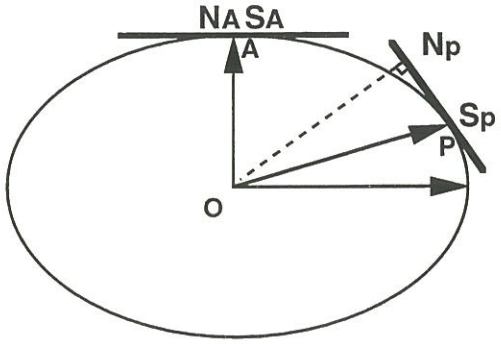

Figure 2: Ellipsoidal wave surface at time t, in the case of a punctual source in an anisotropic crystal : the speed along the normal Np is different than that along the radius Sp, except along the axes (like in A)

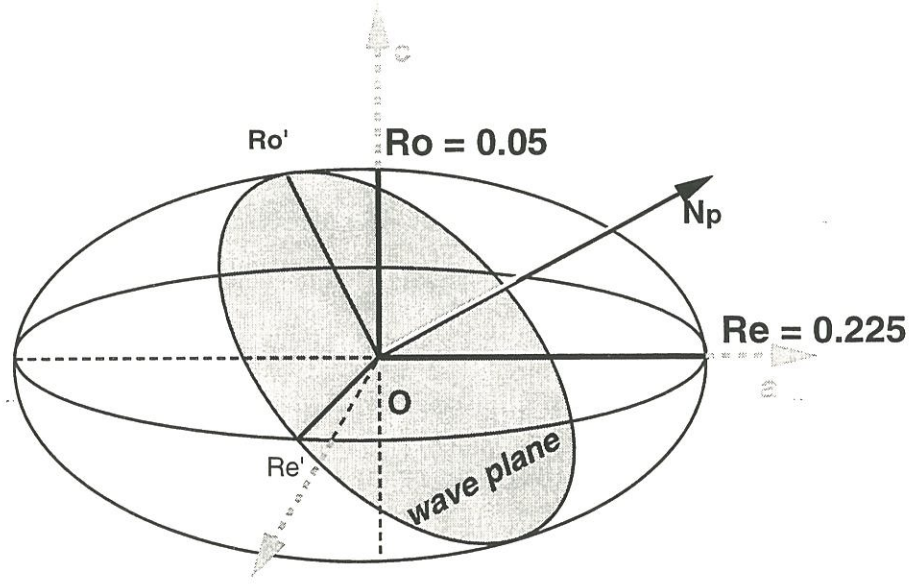

Figure 3: Reflectance indicatrix of graphite : negative uniax

where c_0 is the velocity in vacuum, ε the dielectric constant of the medium, μ the magnetic permeability ($\mu \approx 1$ for most of metals) and n, the refractive index. As wave propagation in anisotropic crystals is concerned, directions, speeds and refractive indices are always related to the normal to the wave, as a convention (figure 2). Let us consider a wave plane with a given orientation centred at the origin of the indicatrix. The intersection of this plane with the ellipsoid is an ellipse, the axes of which indicate the vibration planes which can propagate in this plane without deformation : they are the preferential directions associated to the wave plane as shown in figure 3.

A vibration with any direction is always transmitted in an isotropic medium for any direction of this medium. For anisotropic media, propagation in a given direction occurs following two orthogonal polarised waves with different speeds depending on their refractive index. For a plane light wave parallel to the crystal face (figure 4a and b) the ordinary rays (spherical) are transmitted without refraction whereas the extraordinary rays (ellipsoidal) are propagating regarding to the optical axis and do not follow Descartes' law (also known as Snell's law). Two refractive indices as well as two absorbing coefficients are related to these two vibrations inside the graphite crystal (i.e. birefringence and dichroism, respectively).

The situation of interest in this study is represented in figure 4b : the polished surface of the graphite crystal through which the plane wave is penetrating contains the optical axis. This surface is perpendicular to the basal planes. The ordinary and extraordinary rays are intermingled. Waves propagate in the crystal following the same path, but still polarised at 90° and with the maximum speed difference v_o-v_e. Out of the crystal, vibrations are out of phase :

$$\Phi = 2\pi(n_e - n_o)\, \ell / \lambda \qquad (3)$$

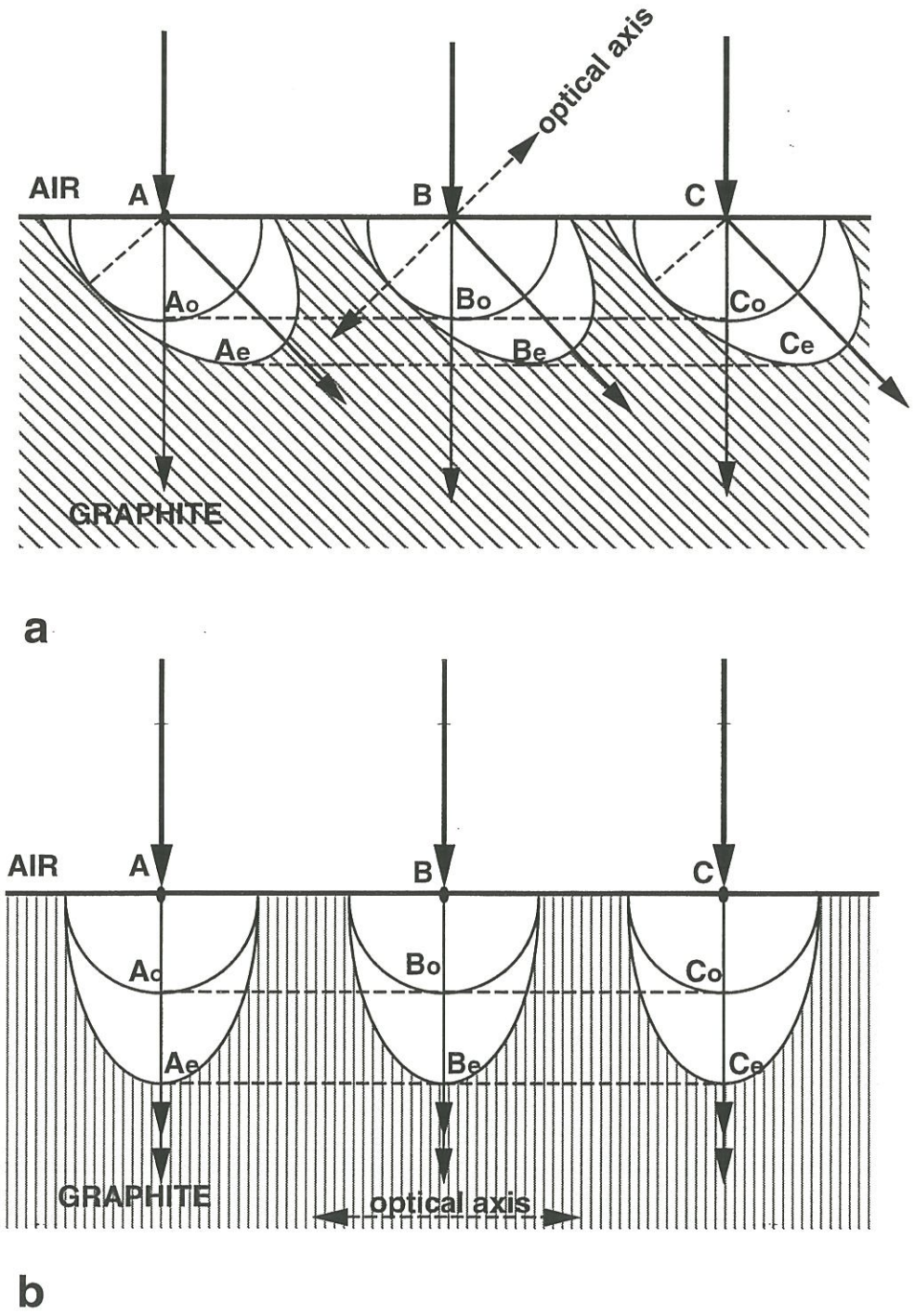

Figure 4: Wave propagation in graphite : (a) optical axis in any orientation (b) parallel to the optical axis. Ao, Bo, Co the ordinary wave surface and Ae, Be, Ce the extraordinary wave surface

Whereas to the amplitude, it is necessary to take absorption into account. It is convenient to define the reflectance of the graphite crystal for the different directions. Reflectance is given by Fresnel's equation :

$$R = \frac{(n-N)^2 + k^2}{(n+N)^2 + k^2} \qquad (4)$$

with N, the index of the embedding medium (in air N=1), n the refractive index and k, the extinction coefficient. Experimental measurements of the graphite reflectance in air, were reported by Ramdhor [16] and Ergun [17] :

Ramdhor :	Ro=0.225	Re=0.050
Ergun :	Ro=0.280	Re=0.080

The situation described in figure 4b is the case where the highest bireflectance can be measured : Ro/Re = 4.5 (3.5 following Ergun).

In-between crossed polars, in the optical microscope, this situation is schematically represented in figure 5. The graphite planes are oriented in the diagonal position at α=45° from the normal position. Entering the crystal, the polarised wave is then resolved into two equal components projected with the same magnitude into the ordinary (OC) and the extraordinary direction (OA). Then, the wave amplitude reflected in the same directions, are proportional to the square root of the ordinary and extraordinary reflectance : Ro and Re respectively. If the intensity transmitted by the polariser is considered to be 1, the amplitude of the two refracted beams emerging from the crystal can be vectorially written:

$$OC_1 = 1 \text{ x } (Ro)^{1/2} \sin\alpha \cos(\omega t) \qquad (5)$$

$$OA_1 = 1 \text{ x } (Re)^{1/2} \cos\alpha \cos(\omega t - \Phi) \qquad (6)$$

and using Ramdhor's values :

$$OC_1 = 0.47 \sin 45 \cos(wt) = 0.16 \cos(\omega t) \qquad (7)$$

$$OA_1 = 0.22 \cos 45 \cos(\omega t - \Phi) = 0.33 \cos(\omega t - \Phi) \qquad (8)$$

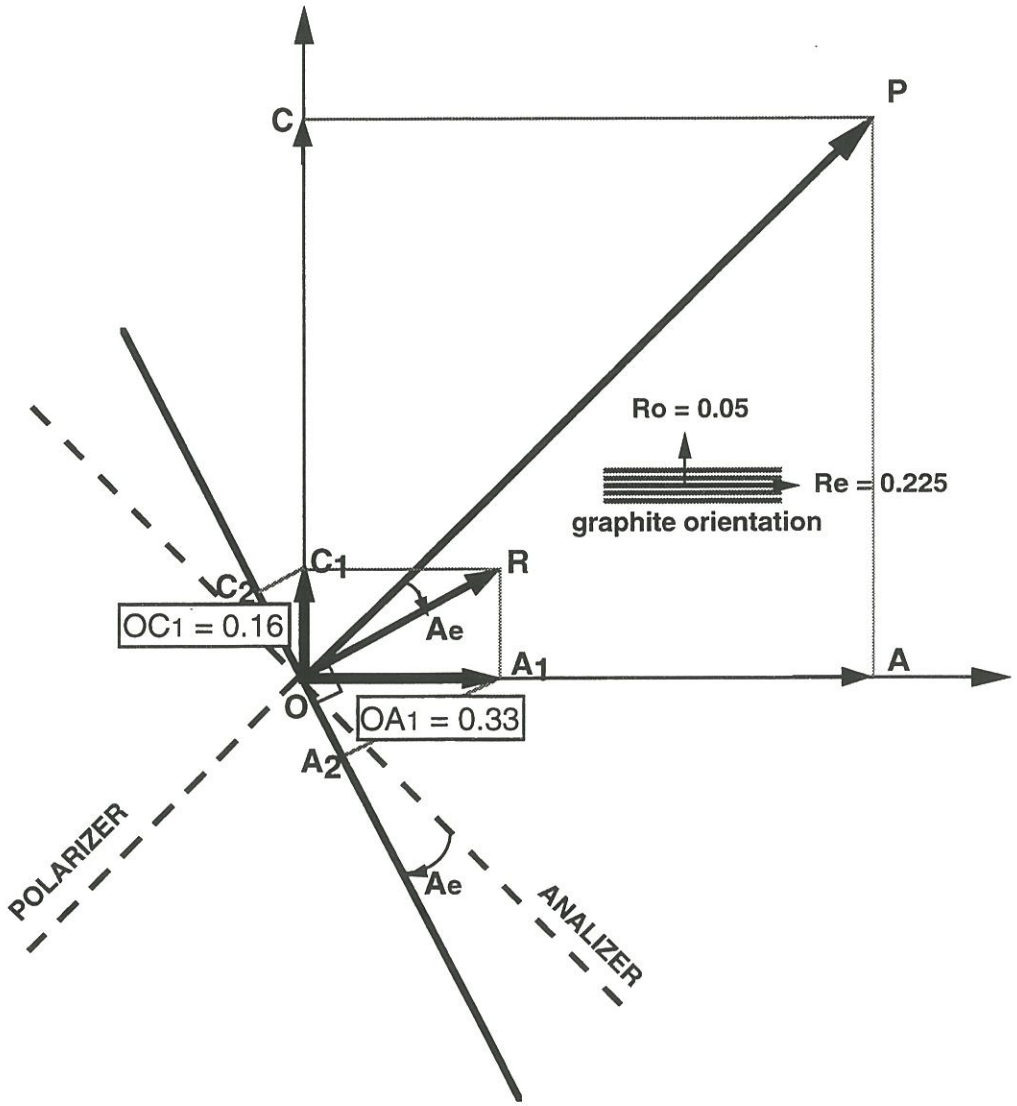

Figure 5: Measurement of the extinction angle, Ae, in polarized light
Crystal in the diagonal position

The resultant in the case of graphite is the vector OR. The polarisation plane of this vector has been rotated by an angle Ae, regarding OP. If the analyser is uncrossed by the same angle, the crystal completely extinguishes (Ae ≈ 19,5°). Physically in the analyser, both rays are deflected into the transmission direction of the analyser. The resultant amplitudes are:

$$OC_2 = 1 \times (Ro)^{1/2} \sin\alpha \cos(\omega t) \cos(45\text{-}Ae) \quad (9)$$

$$OA_2 = 1 \times (Re)^{1/2} \cos\alpha \cos(\omega t\text{-}\Phi) \cos(45\text{+}Ae) \quad (10)$$

as $OC_2 = OA_2$ in the extinction conditions, and after simplification :

$$(Ro)^{1/2}/(Re)^{1/2} = \tan(45+Ae) \quad (11)$$

where Ae is expressed in degree. The analysis introduced by Diefendorf and Tokarsky [8] gives a good approximation of the reflectance anisotropy ratio Ro/Re :

$$Ro/Re = \tan^2(45+Ae) \quad (12)$$

This should be completely true if the two refracted beams, OC_1 and OA_1 are still in phase. But the phase difference is faint and can be neglected :

$$\Phi_e\text{-}\Phi_o \approx 179.1 - 153.3 \approx 25° \quad (13)$$

for λ = 550 nm, the phase difference is < 40 nm (with $k_e = 0.01$)
This small difference corresponds to the first order "iron grey" of the Michel-Lévy chart, that is to say a dark grey extinction, sufficient to obtain the ratio Ro/Re in the pyrocarbons described in this work. Diefendorf et al [8] recommend to use a Nakamura plate to increase the ability to detect the position of the minimum light intensity.

For pyrocarbons, bireflectance is produced by a "pseudo crystal", the turbostratic stacking of carbon layers. First, the intrinsic bireflectance of that turbostratic pile increases with increasing order of the stacking [18,19]. Secondly, because the measurement is obtained by means of an optical

Table 2. Domains of extinction angle (Ae) associated to microtextures of pyrocarbons

Microtexture	Domain of extinction angle
rough laminar	Ae>18°
smooth laminar	12°<Ae<18°
dark laminar	4°<Ae<12°
isotropic	Ae<4°

microscope, the response is averaged on a large volume depending on the resolving power of the objective (about 0.5 μm). Because of the disorientation of the turbostratic stackings (i.e. the microtexture), only the average contribution is accessible. The larger the disorientation, the lower the apparent bireflectance. As a result, this technique integrates a structural and a textural variation. Anisotropy of carbon is the textural aspect. Fortunately, both are varying in the same way and are taken in account to range the different pyrocarbons. For that reason it was preferred to speak about **apparent reflectance anisotropy ratio Ro/Re**. For the same reason it is best to consider the Ae angle value and not the Ro/Re ratio.

It is very convenient to classify the pyrocarbons following the well known optical scale : rough laminar (RL), smooth laminar (SL), dark laminar (DL) and isotropic pyrocarbon (I). The extensive use of this technique has shown in the case of LP-CVD/CVI, that a good connection exists between the classical optical scale and the Ae values. These relationships are reported in Table 2.

3.1.2 - Measurements

An example of an optical measurement is provided in figure 6. A fibre with a thick coating is selected in order to get an accurate value. When the two Nicols are crossed a Maltese cross appears. By rotating the analyser the first quadrant (dashed line) extinguishes, then get bright again. The value of the rotation angle for the maximum extinction is called extinction angle, Ae. If the two polars are of good quality the value of Ae ranges from 0° to 22° for pur pyrolytic carbons.

The different CVD conditions were selected in order to scan a broad range of Ae values from rough- to dark-laminar in-between 18° > Ae > 11°. Optical measurements are reported on Table 1.

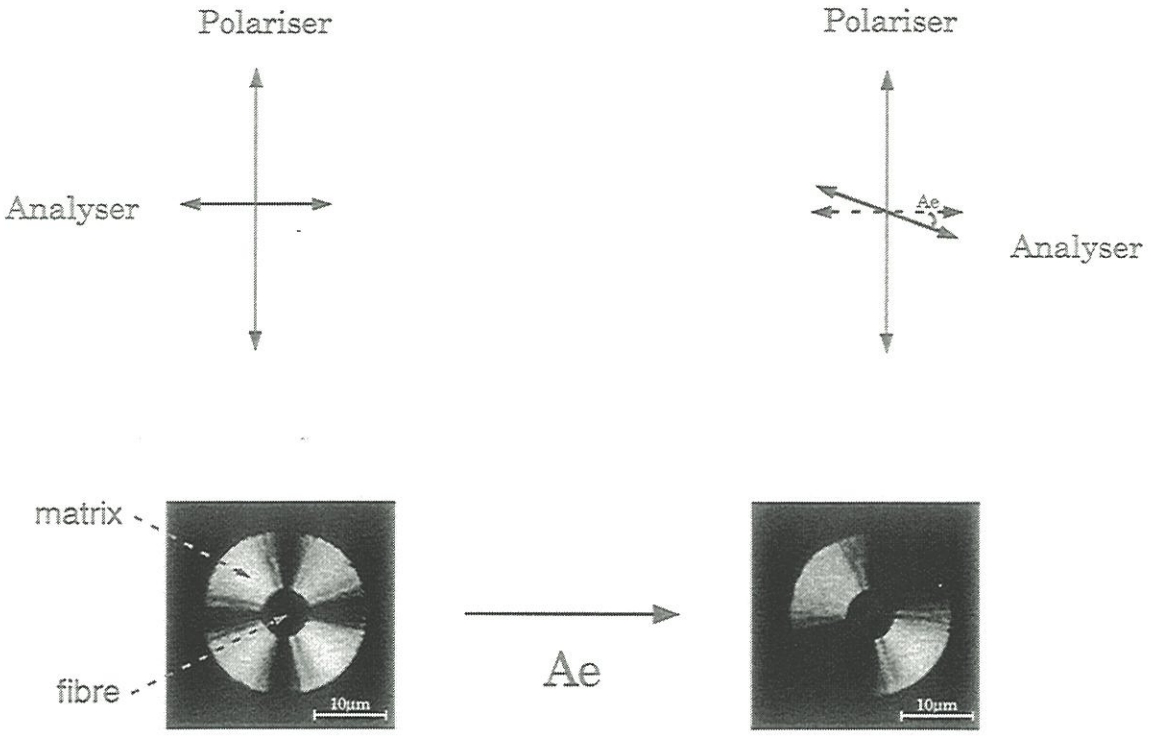

Figure 6: Measurement of the extinction angle (Ae) in polarised light (example of a coated fibre)

First, in the same conditions, the matrix has a higher Ae value when measured inside the tow (M int) as compared to the surface or on the single fibre composite (M). The increase is faint but reproducible (18° vs 17°). This effect can be related to the higher residence time of gaseous precursors involved in CVI and thereafter the progress of the homogeneous reactions, within the tow as shown in a previous work [13].

Secondly, the conditions selected to get a disorganised pyrocarbon for the interphase Ic gives a value of 11°. This is already a dark-laminar pyrocarbon regarding the chart of Table 2.

Finally, the intermediate microtextures were reached by changing the mother molecule and using specific pressure/temperature conditions. Interphase Ia gave Ae = 15°, and Ae = 13° for Ib.

3.2 - Pyrocarbon anisotropy as measured by electron diffraction

3.2.1 - Pyrocarbon diffraction and anisotropy

Pyrocarbons crystallise in the hexagonal form of carbon. Unlike graphite, their structure is limited to two dimensions : the hexagonal lattice of the aromatic layer. This has been known as the **turbostratic structure** since its discovery by Warren in 1941 [20]. The layers are stacked one on each other with a rotational disorder. These small stacks form domains (also called crystallites). As these domains are very small, some coherent scattering exists in-between the layers even if not perfectly parallel. The diffracted spots observed in the reciprocal space are not the 00.ℓ graphite spots, but the so-called 00ℓ turbostratic interlayer interference.

The different pyrocarbon can be described by the size of these domains or stacks of layers as represented on figure 7 : the layer diameter approached by the coherent length ℓ_a (or the defect-free part of the layer involved in a stack), and the number **N** of layers coherently stacked together (or the length ℓ_c). The

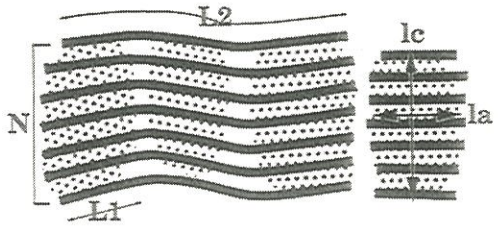

Figure 7: Model of turbostratic piles of carbon layers

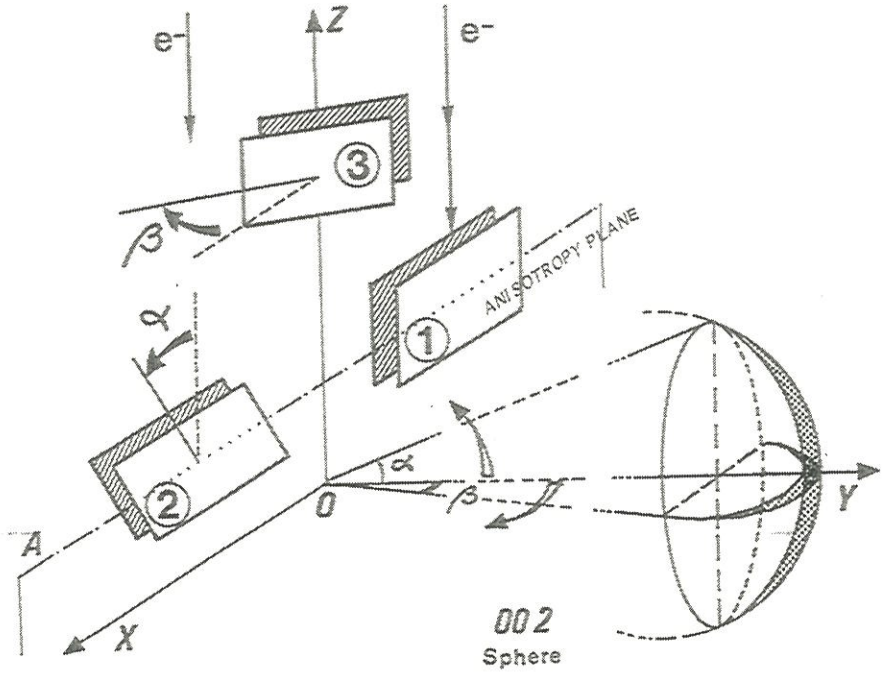

Figure 8: Schematic of anisotropy in the real and reciprocal space

interlayer distance in-between the layers is $\mathbf{d_{002}}$ **spacing**. Again, this notation is preferred to c/2, provided that this is not a 3D graphitic parameter. With high resolution TEM, the lattice fringes technique gives very easily access to the real layer size diameter $\mathbf{L_2}$ and the defect-free part of the layer $\mathbf{L_1}$).

In addition to the domain structure, the different pyrocarbons differ by their anisotropy. When they are highly anisotropic, all the domains (layers) are parallel to the anisotropy plane. As this anisotropy decreases, more and more domains are misaligned with respect to the anisotropy plane. In the reciprocal space E*, this gives rise to the polar distribution of the 002 spots as represented in figure 8 following Oberlin [21]. Layers aligned parallel to the anisotropy plane (1) can be either tilted by an angle α regarding the z axis (or incident direction) as represented by the domain (2) or twisted by an angle β as represented in (3). In the reciprocal space, this disorientation with respect to the anisotropy plane gives rise to the distribution of the intensity on the 00ℓ sphere (of $1/d_{00\ell}$ radius). The electron diffraction pattern is a plane section of the reciprocal space E*, xOy in figure 8, where two 002 arcs appear perpendicularly to the anisotropy plane. The electron diffraction pattern gives directly access to the β-angle distribution, because the wave length of the electron beam is very short (λ = 1.969 pm), thus the Ewald sphere radius ($1/\lambda$) is large and can be considered as a plane in the analysed region.

The measurement of the azimuthal opening of these arcs along the Debye-Scherrer ring is proposed in this work as a quantification of the anisotropy. The value of the interlayer spacing (d_{002}) is obtained as well by a previous standardisation with a graphite pattern, obtained in similar conditions.

3.2.2 - Measurement procedure

The first step is to correct the optical density of the film in order to retrieve the real diffracted intensity on the whole peak which is to be measured.

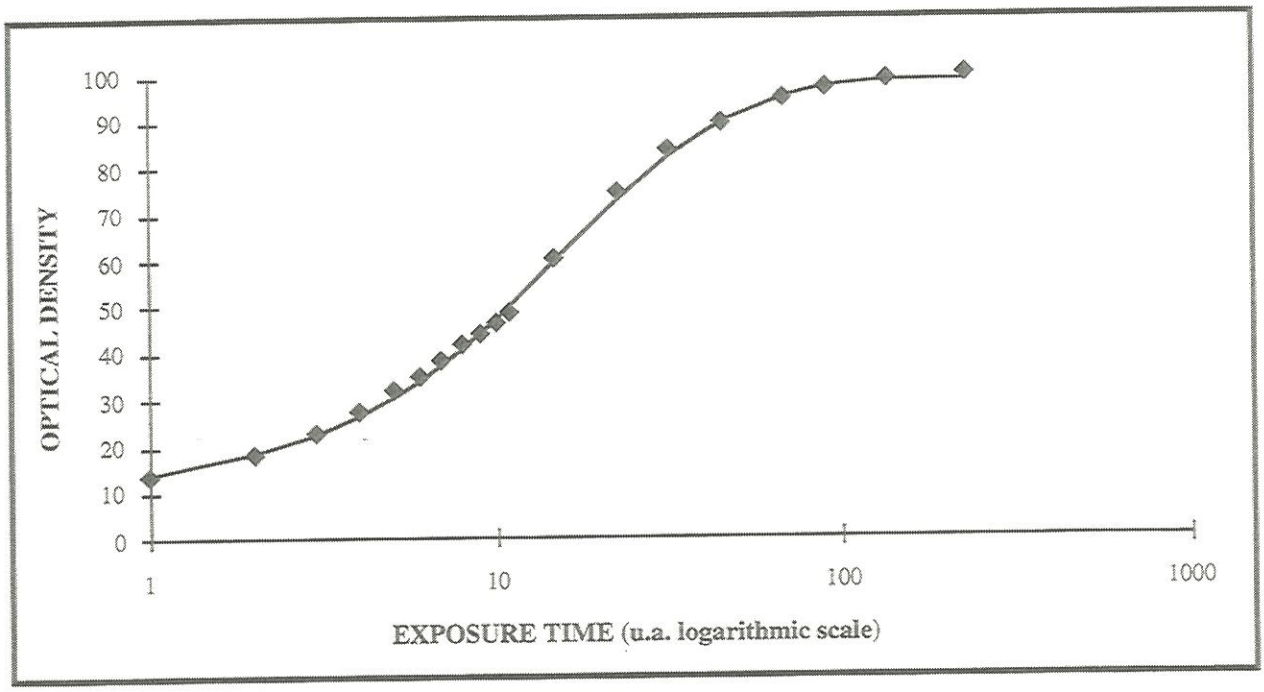

Figure 9: Experimental darkening curve of Scientia emulsion

The response of a CCD camera might be the best solution. With a film, first, the pattern has to be strictly recorded in the linear domain of the emulsion. Most of the central peak is out of this domain. Then, the standardisation of the emulsion is necessary. For that purpose, a few series of increasing exposure times are realised with increasing beam intensities in order to plot the curve of figure 9 : the optical density as a function of the exposure time. This way, every digitised pattern is corrected by means of this transfer function in order to recover the real dynamic. Finally, a linear anamorphose is realised in order to map the dynamic of the 255 grey levels from the foot to the top of the 002 peaks.

At this stage, a tool is provided to scan the intensity across the diagram (figure 10) passing through the centre. The centre of the diagram was previously found automatically, provided that the central spot is systematically saturated by the anamorphose. The program finds out the two 002 maxima, so the "Debye-Scherrer" ring is drawn, superimposed on the pattern and the intensity is thus extracted versus the azimuthal angle (figure 11).The program fits those peaks to two gaussian curves and the anisotropy is given as the mean value of the two widths at half height.

3.2.3 - Results

3.2.3.1 - Anisotropy of interface pyrocarbon in C/C composites

The opening angle OA and the interlayer spacing d_{002} have been measured on the different interphases. Unfortunately, it was not possible to get both optical and diffraction measurements on exactly the same sample. Figure 12 is a 002-darkfield image of a cross-section of a microcomposite with an interface Ia (inset). The three different carbons can be easily identified: fibre (F), Ia interphase and matrix (M).

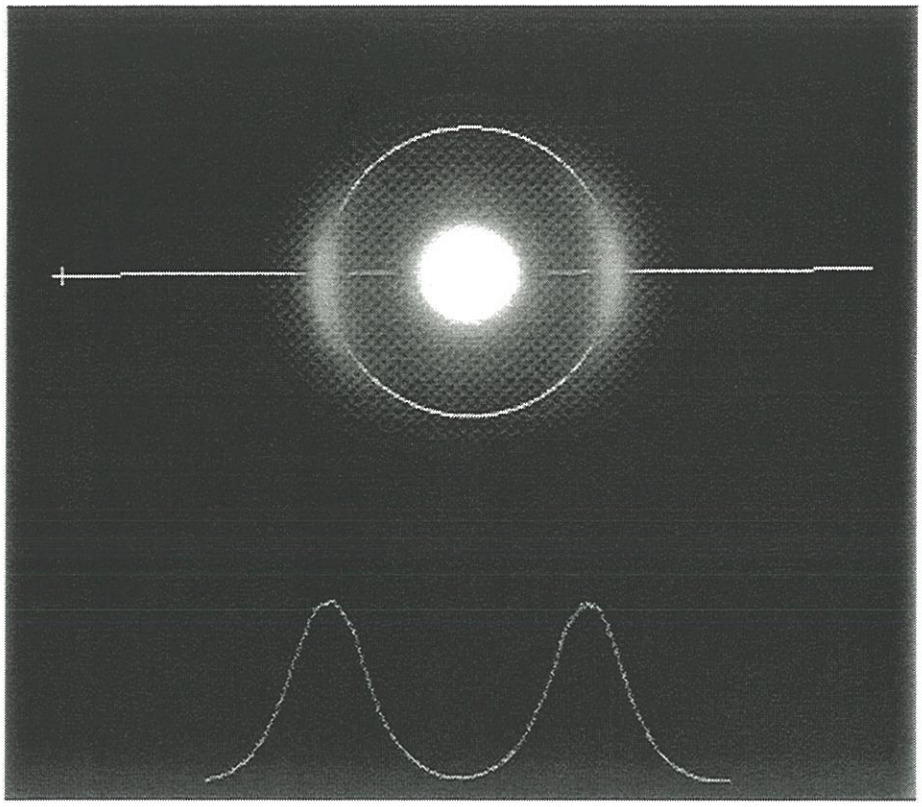

Figure 10: a) Scan across the diffraction pattern and draw of the 002 ring, and b) record of the intensity versus the azimuthal angle

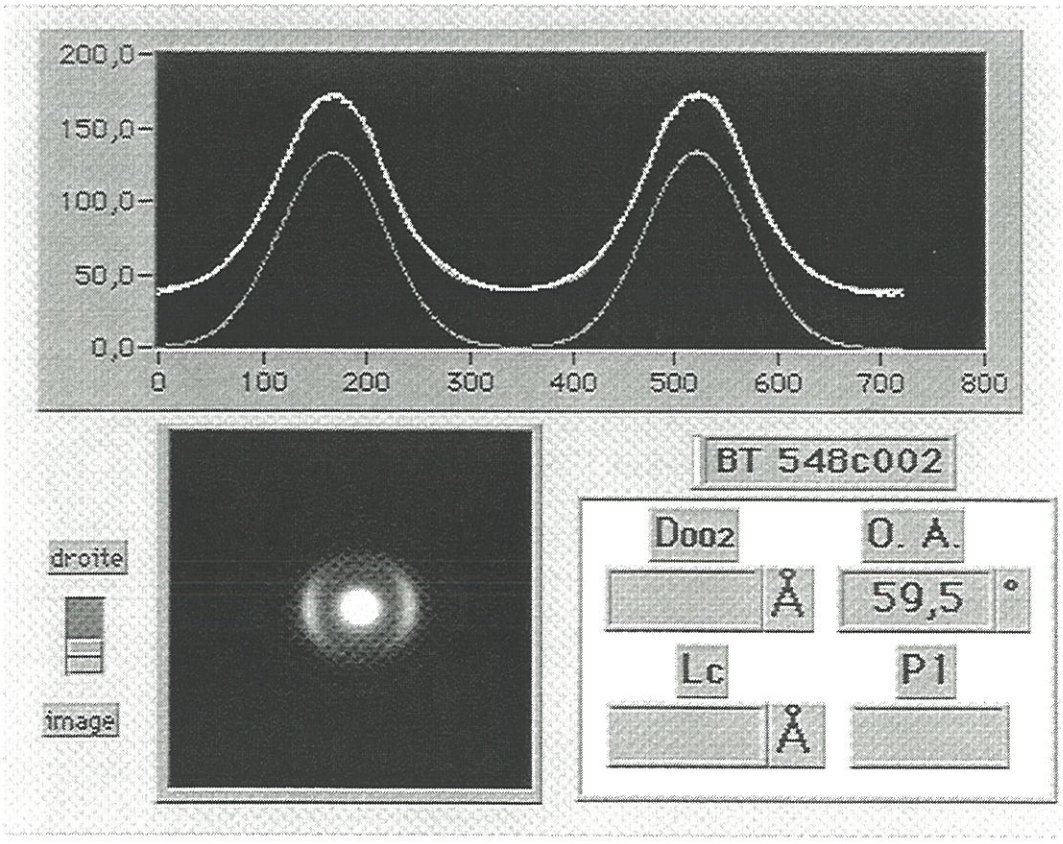

Figure 11: Front panel of the software. Pattern to be analysed (white), and plot obtained in figure 10b. Gaussien fit (down) of the experimental intensity measured versus the azimuthal angle. OA is the mean width at half height of the two gaussiens

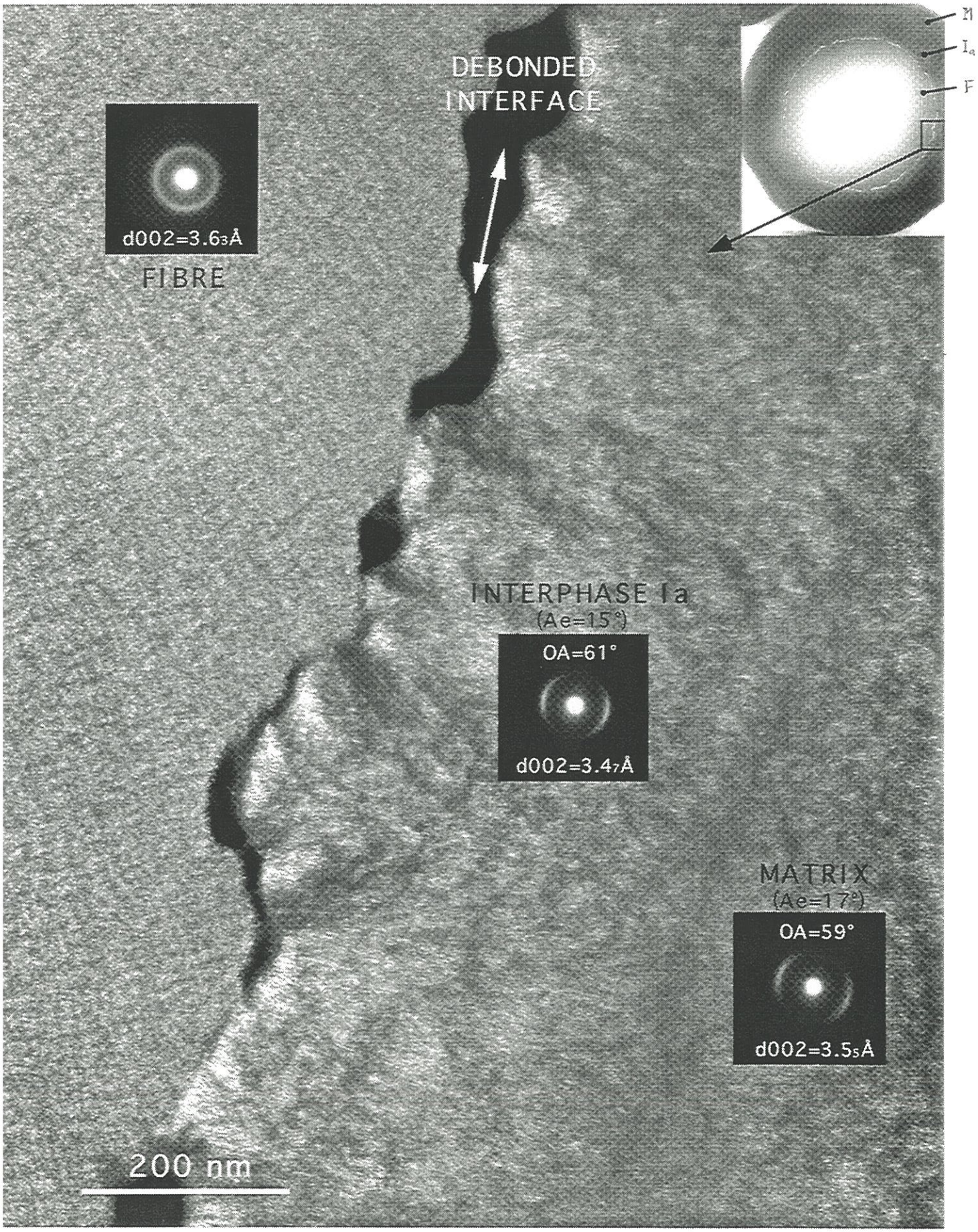

Figure 12: Microcomposite with interface Ia. Inset is a low magnification of the microcomposite

The fibre is characterised by small coherent domains with an isotropic microtexture. A high resolution micrograph (figure 13) shows that isotropic microtexture. The layers are defective with a fairly low coherent stacking : Lc = 11Å which gives an average of $Lc/d_{002} \approx 3$ layers per domain.

The interphase is decohesive. Except on rare places, the interphase is debonded from the fibre surface. This debonding is already there in the original composite but amplified during thinning [2, 3]. The electron diffraction shows that this pyrocarbon is well organised (OA = 61°) with a d_{002} spacing lower than that of the matrix. The darkfield technique reveals that the first layers on the fibre surface are more organised. Domains are more contrasted exhibiting a columnar shape. However, this was not quantified.

Matrix was deposited with a different procedure. Optical measurements were found close, but different from that of the interphase : Ae = 17° versus 15° in the Ia interphase. Again, it is to note that Ae is not directly measured on the same sample, but on a sample with a thicker pyrocarbon coating deposited in the same CVD conditions. With diffraction, the OA values for the matrix and the interphase belong to the same range : $59° < OA < 61°$. Only the d_{002} spacing was seen systematically lower in the interphase than what it is in the matrix : in the example of figure 12 it is 3.47 vs 3.55Å for the matrix.

The same analysis was conducted in the three materials obtained with the three different interphases Ia, Ib and Ic. Figures 14 and 15 give the example of the materials constituted with the same fibre, the same matrix but interphase Ib and Ic deposited in conditions known for giving lower anisotropic carbon: Ae = 13 and 11°, respectively.

- ***Interphase Ib*** has the same adhesive behaviour as interphase Ia. The interface is nearly completely debonded from the fibre surface. It was verified by SEM on the bulk material that this debonding is not an artefact, but was pre-existing and amplified by sampling [2]. Otherwise, it appears very different

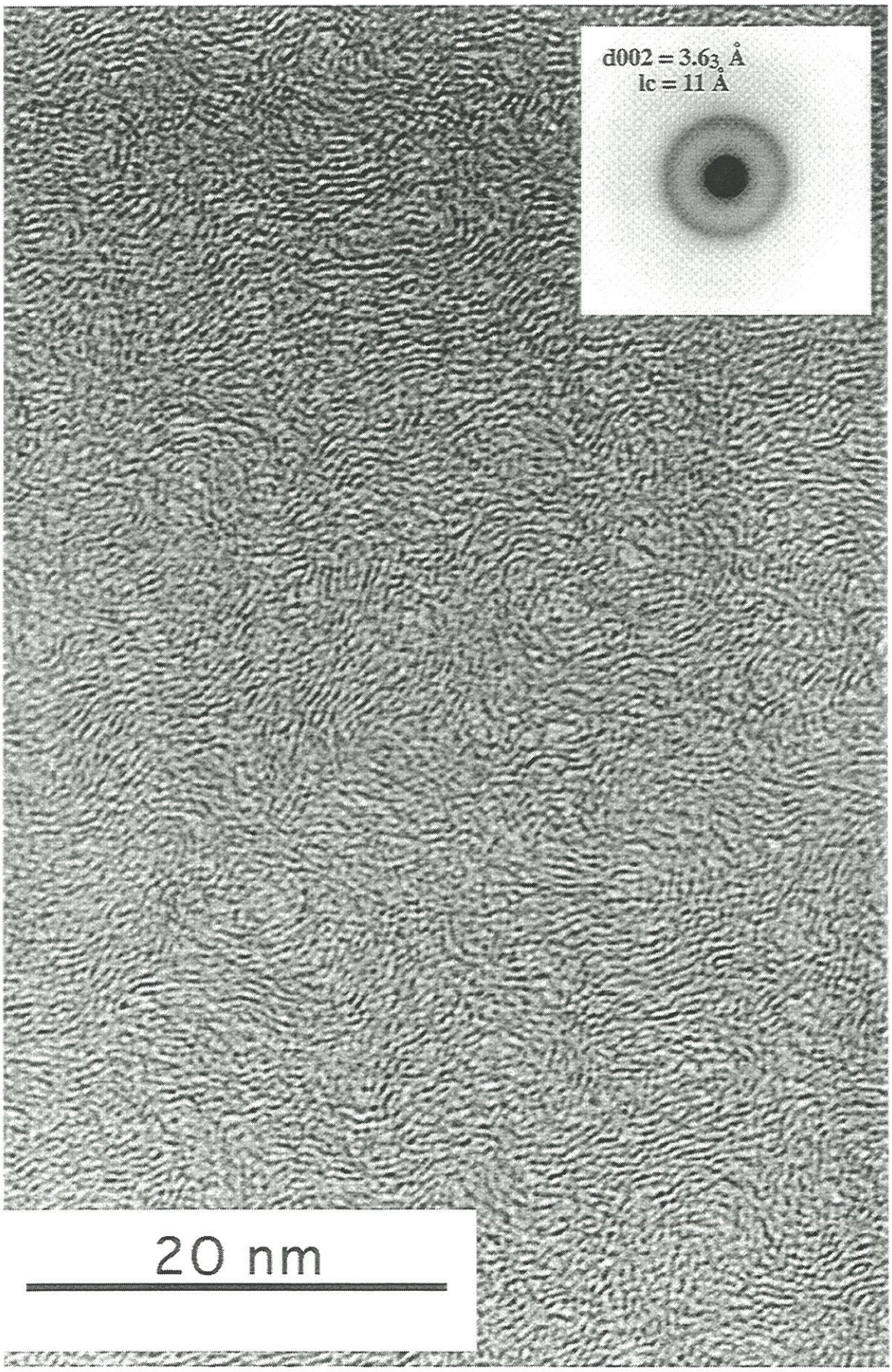

Figure 13: lattice fringe image of the fibre (HT PAN-based carbon fibre)
(inset: electron diffraction pattern)

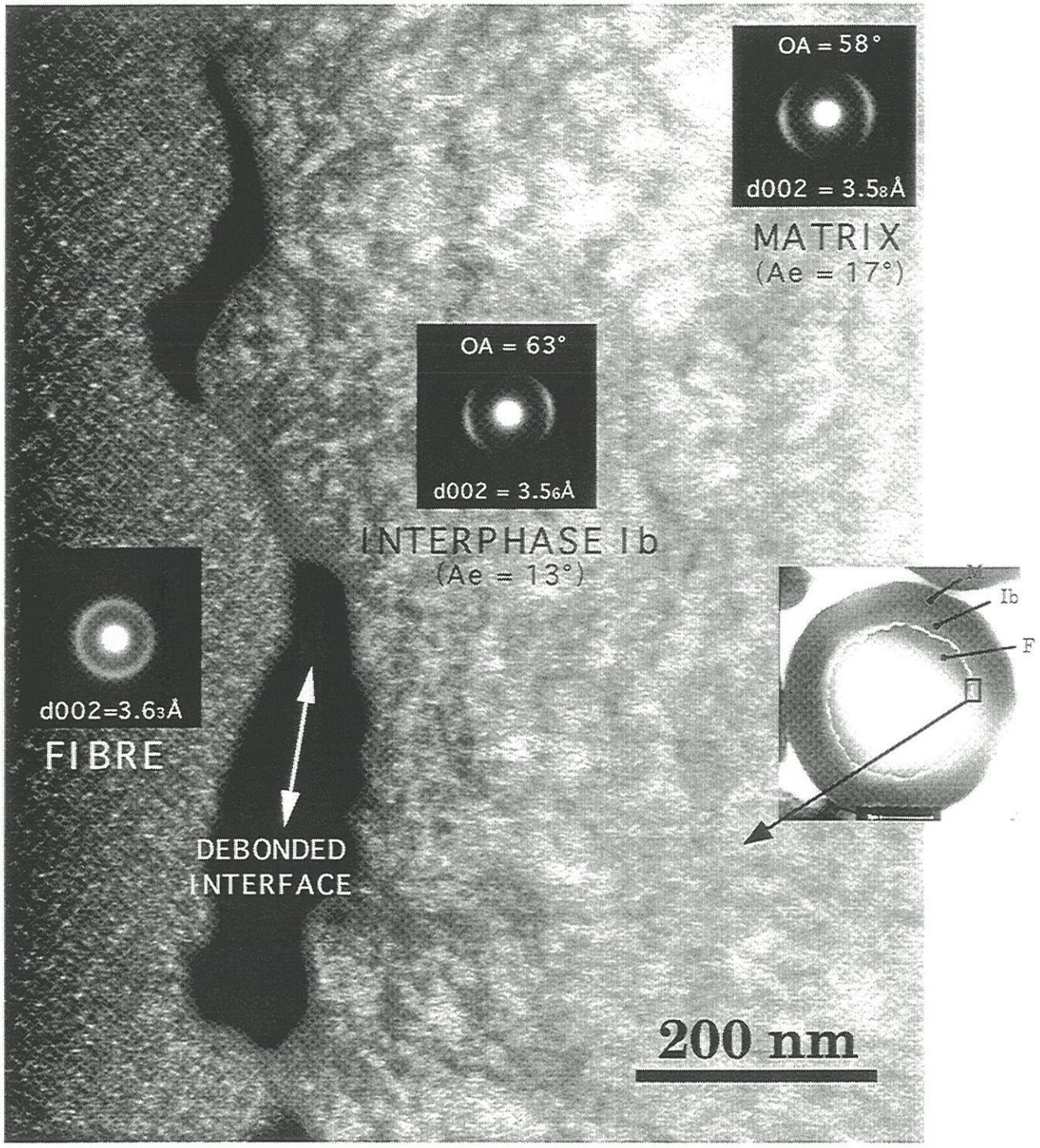

Figure 14: Microcomposite with interface Ib. Inset is a low magnification of the microcomposite

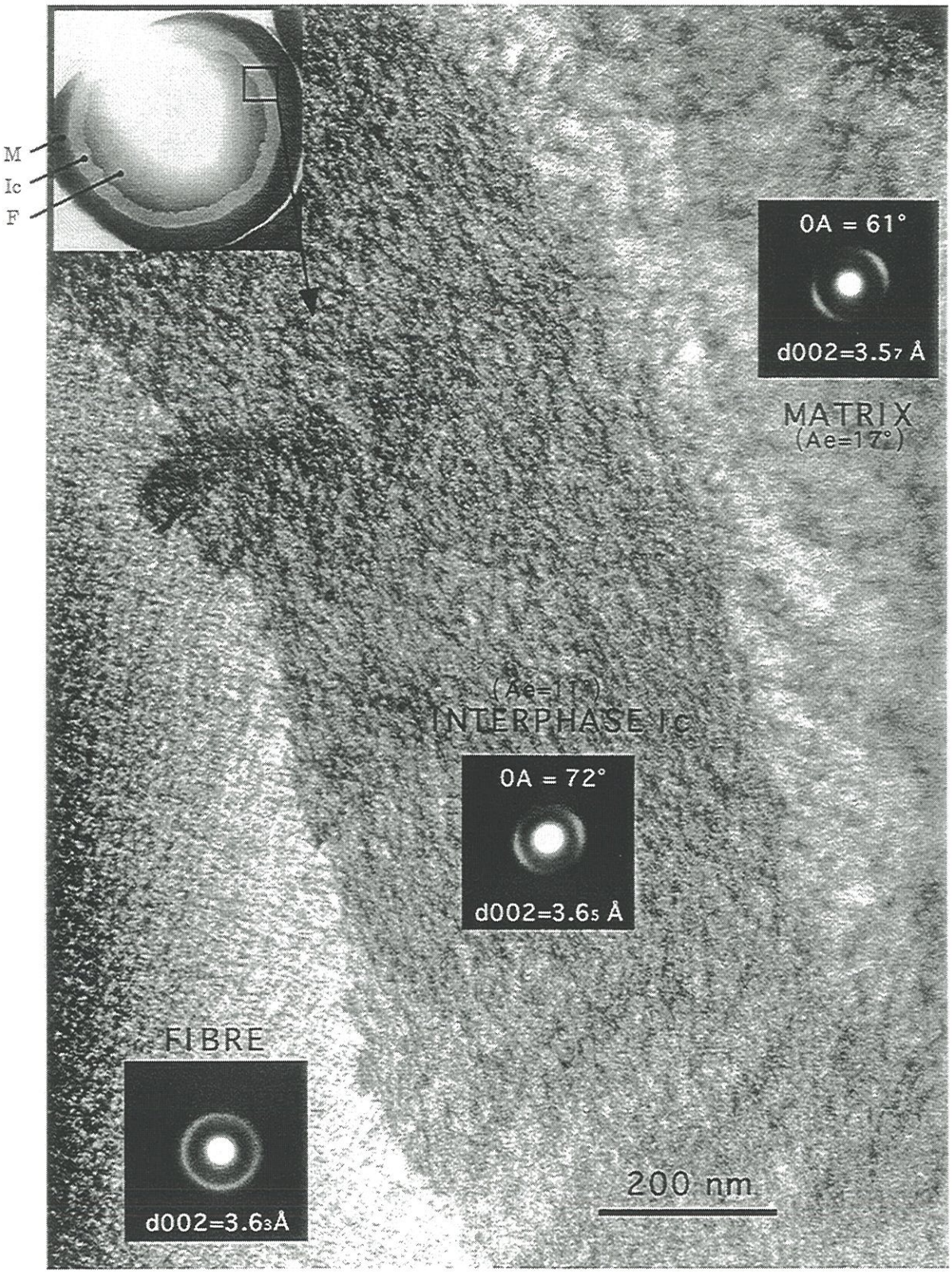

Figure 15: Microcomposite with interphase Ic. Inset is the low magnification

from interphase Ia. Structure and microtexture of Ib, give values very close from those of the matrix, but only two measurements were available : interlayer spacing were 3.56 and 3.62Å, and OA 60 and 61°.

- With ***interphase Ic*** the interface is not debonded (figure 15, inset). This point is very important on the point of view of the interface mechanics. That was not the case with interphase Ia and Ib or without interphase. It is assumed that the chemical bonding with the fibre is stronger. The microtexture of Ic is clearly less ordered: 65° < OA < 74°. The interlayer spacings are measured in a broad range from 3.6 to 3.75Å, higher than the other pyrocarbons. Those values distinguish themselves from the previous ones. They correspond to a dark laminar pyrocarbon as asserted by optical analysis. The 002 darkfield technique shows that this layer is homogeneous.

3.2.3.2 - Comparative variation of anisotropy, OA, and d_{002} interlayer spacing

Figure 16 plots the interlayer spacing d_{002} versus the orientation angle 0A for the different pyrocarbons. Despite of the data spreading, the various pyrocarbons can be distinguished on this plot. On the whole, when the reflectance ratio or Ae decreases, the orientation angle OA and the d_{002} spacing increase. But in details, the linear decrease of Ae does not correspond to an equivalent linear decrease of OA value. Only Ic or M_{int} can be clearly distinguished with OA as a single variable. The same thing occurs with d_{002}-spacing. The decrease of the reflectance ratio can occur without any decrease of d_{002}-spacing : that is the case of pyrocarbon Ia with the same spacing as the rough laminar pyrocarbon M_{int} ($d_{002} \approx 3.49$Å), but with a lower anisotropy (OA = 59°). It can be seen this way that the various optical properties of the pyrocarbon (as reflectance ratio, Ae) are probably not linearly related to the structural parameters (OA at long range, or d002-spacing at the level of the turbostratic structure). Meanwhile, it is to note that the optical measurement is

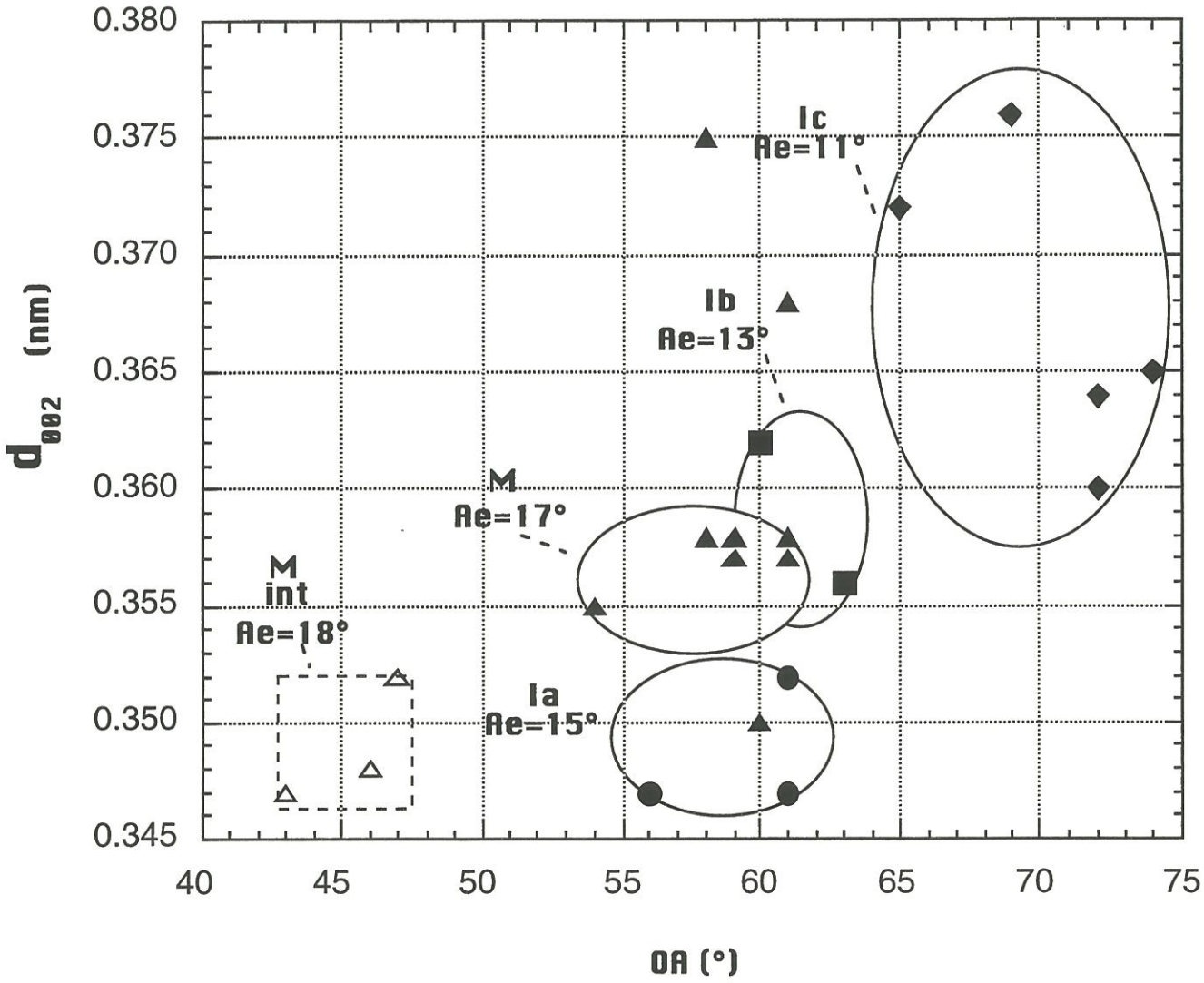

Figure 16: Plot of the electron diffraction data : d_{002} spacing vs 0rientation Angle

not strictly obtained on the same materials, but on thicker coatings deposited in the same conditions.

Figure 16 shows interesting results about the matrix. First, when the matrix is infiltrated (M_{int}) in the core of the bundle (3000 filaments) the optical measurement shows a small but perceptible increase from 17° (for M) to 18° (for M_{int} , empty triangles). This CVI/CVD relationship is well known. The point here is that diffraction data are much more sensitive to that increasing order of M_{int} with respect to M : OA drops down by 15 degrees and the d_{002}-spacing gets close to 3.44Å, the value of the turbostratic carbon.

When the matrix is deposited on the single fibres (solid triangles) figure 16 shows that the plots are highly spread along the ordinate. For a mean OA value of 59°, d_{002} can considerably vary : $3.5 < d_{002} < 3.7_5$Å. A direct examination in TEM high resolution of this pyrocarbon is not easy to perform in the very same areas where the diffraction patterns are realised. However, on a statistical point of view, high resolution has revealed some heterogeneity at the scale of 100 nm, the scale of the diffraction technique. Figure 17 shows the ordering of the smooth laminar pyrocarbon (Ae = 17°) in the best areas. Layer size could be measured : L2 ≈ 6nm, L1 ≈ 1nm and N ≈ 6 for that pyrocarbon. In other places, this laminar deposition can be disturbed by some "growth centres", supposed to grow in gas phase (figure 18). These growth centres induce the rotation of the layers which are subsequently deposited, inducing an Ω-like shape. Unlike in the classical mechanisms controlling the decreasing anisotropy, a complete rotation of the layers, (perpendicularly to the anisotropy plane), is occurring here in the disturbed areas of the smooth laminar pyrocarbon.

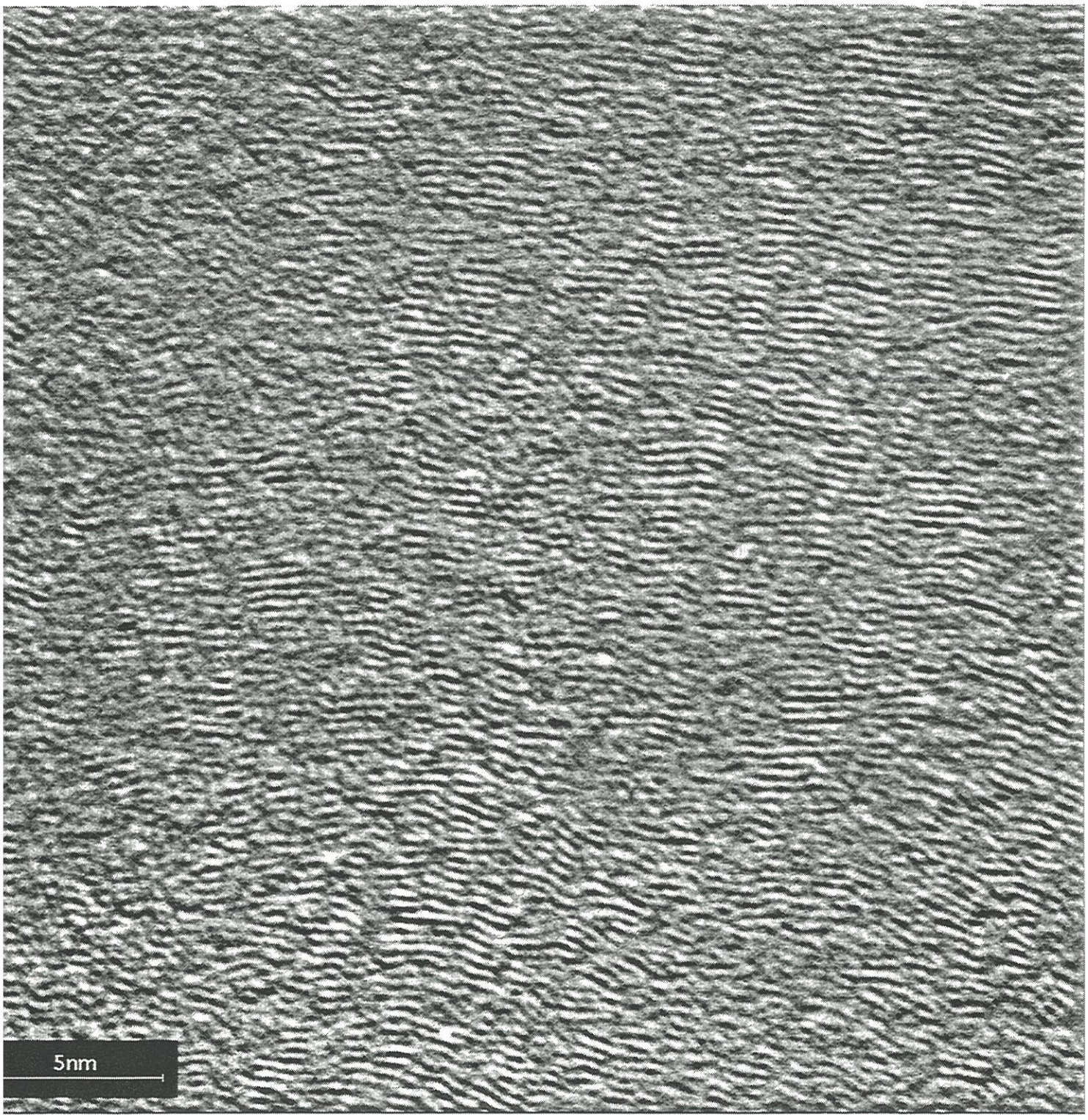

Figure 17: Matrix microtexture : regular smooth laminar microtexture
(lattice fringes TEM technique)

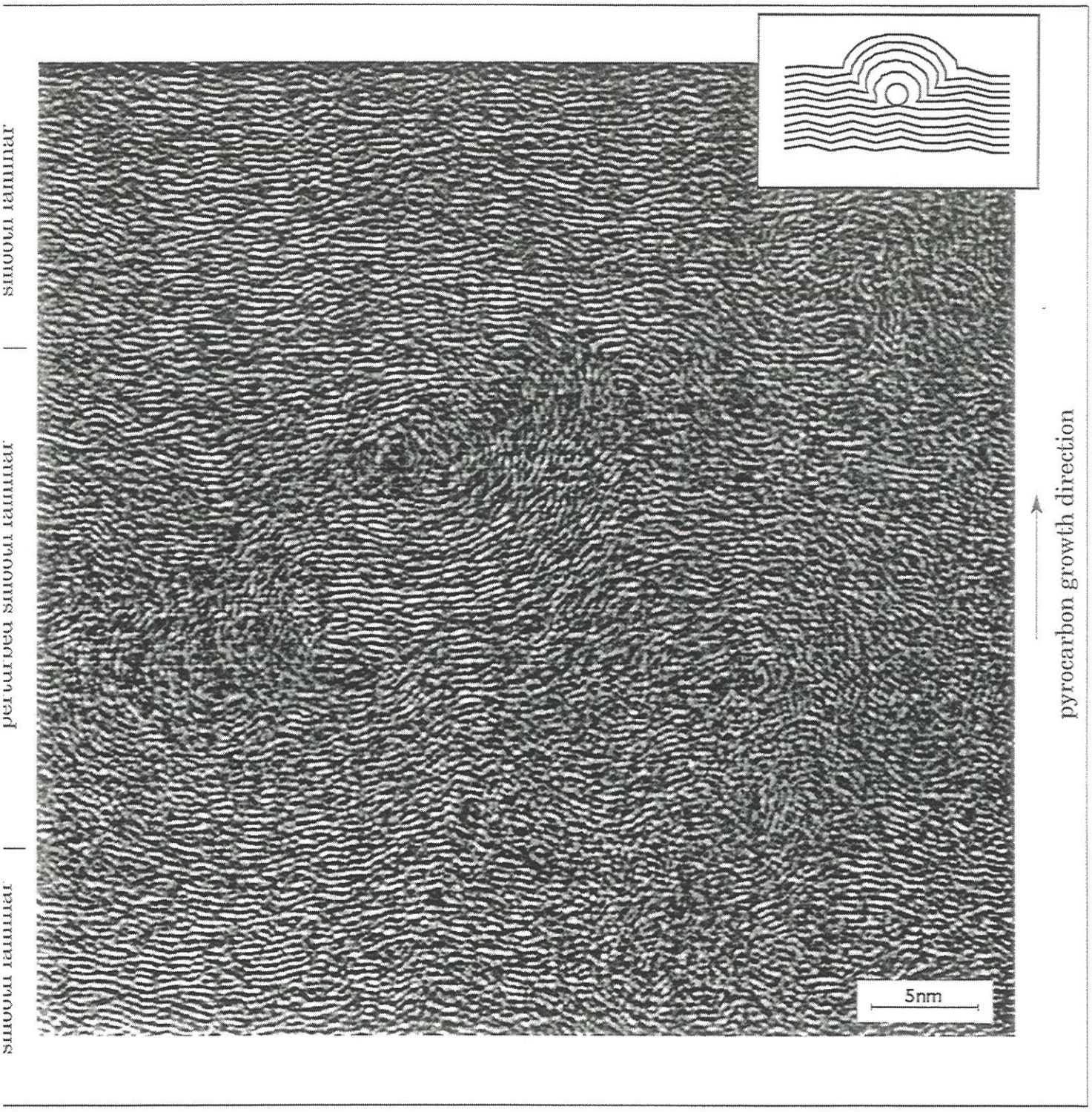

Figure 18: Matrix microtexture : disturbed area (lattice fringes TEM technique)
Inset: schematic of a pyrocarbon growth with a Ω-like shape

4 - DISCUSSION

The CVD conditions (T, P, gas flow, or mother molecule) were optimised in this work, in relation with the optical scale : from Ae = 17° for the matrix to Ae = 11° for Ic. The diffraction data have clearly demonstrated that the optical scale might not be linearly related to the anisotropy as defined by the orientation angle of the coherent domains. The question is to better understand what relationships exist between the two scales.

Figure 19 shows the scale at which these two techniques are applied: optical measurement integrates volumes at micrometer scale, whereas electron diffraction applies to volumes ten times smaller. When the anisotropy decreases for the different types of pyrocarbons, La and Lc, the coherent lengths, are known to decrease. In the mean time, the amount of lattice defects increases, mainly sp3 hybridisation and hydrogen content. In other words, some disturbance of the electronic structure occurs which is likely to control the absolute values of the reflectance. For that reason, the physical meaning of Ae is somewhat complex, since this measurement is only a function of the reflectance ratio Ae = f(Ro/Re). So, in addition to the disorientation of the carbon layer, Ae sums up different effects, but varying as the anisotropy. As for OA measurement, the volume of 110nm selected by a very small aperture was chosen for being optimum [14]: large enough to be representative, and small enough to ignore the curvature produced by the fibre. Finally, data obtained by diffraction were seen to be widely scattered as compared to the optical measure. This is mainly due to the occurence of disturbed areas (see figure 18) at the same scale as the selected area itself (110nm).

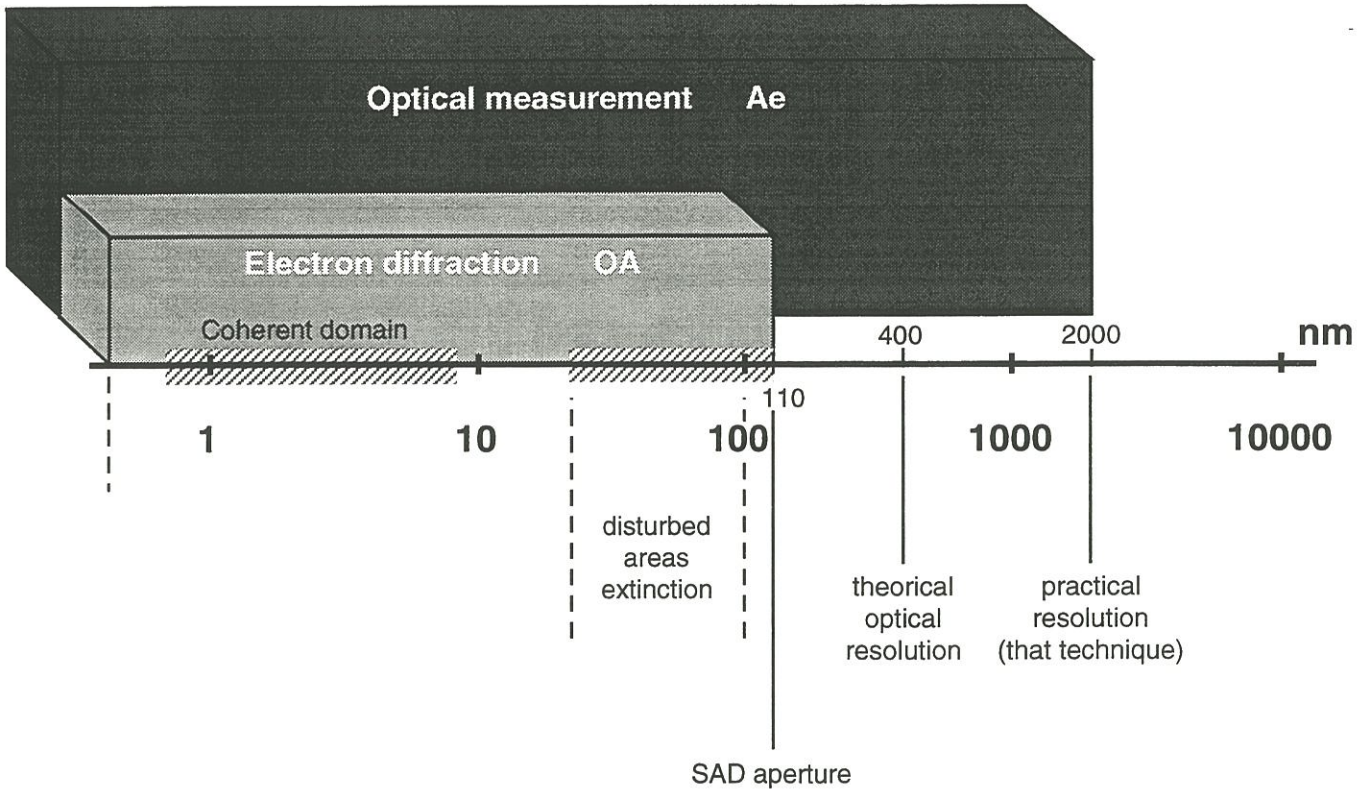

Figure 19: Scale effect between optical microscopy (Ae) and electron diffraction (OA) measurement

5 - CONCLUDING REMARKS

The comparison of the two techniques : optical measurement on one hand, and the electron diffraction OA and d_{002} spacing in the other hand, have shown a good correlation, in the whole, and a useful complementarity.

- Both gave the same variations among the first samples studied in this work (LP-CVD smooth laminar pyrocarbon). The two scales appear to be not linear, but these results are not obtained strictly on the same samples.
- Depending on the needed spatial resolution and the nature of the parameters required, one or the other technique will be equivalent and in the same time complementary. Indeed, optical measurements integrate all scales up to the µm, while electron diffraction gives information from nanometer to micrometer scale depending on the area selected.

The optical method is based on the measurement of the apparent reflectance ratio of the pyrocarbon. This ratio is decreasing with a structural order decrease (intrinsic), defects and also with the increasing texture disorder (anisotropy). Instead of using a photo-multiplication (PM), this method involves the rotation of the analyser of a regular polarisation device. It has the advantage to be easily performed. However, it requires a deposit at least 2 µm-thick and an optical polishing of high quality. Finally, it requires to scale the rotation with standards mainly for the polarisation device. This measurement is only semi-quantiative but it enables to separate the different pyrocarbons of a same family. This was demonstrated in this work on various smooth laminar pyrocarbons obtained by LP-CVD.

The electron diffraction technique is irreplaceable to analyse coatings as thin as 0.5 µm and lower. Coupled to an image analysis software, it gives the following structure parameters : (i) the orientation angle, OA, of the scattering domains, which is a measurement of the "geometric" anisotropy (microtexture); (ii) the interlayer spacing d_{002} which is a basic measurement of the short distance ordering of carbon (i.e. turbostratic structure of scattering

domains). Other pieces of information can be extracted in the diffraction pattern. More work is required to extract them with accuracy : e.g. Lc, the turbostratic pile thickness, La, the size of the carbon layer, and P1, the ratio of graphite staking in the turbostratic pile.

ACKNOWLEDGEMENT

Authors wishes to thank SEP for grant given to B. Trouvat.

REFERENCES

[1] W. Ruland, Appl. Polymer Symp., 9, p 285 (1969)

[2] B. Trouvat, X. Bourrat and R. Naslain, Influence of a carbon interphase with a controlled microtexture on the mechanical properties of single fibre C/C/C microcomposites, to be submitted in Carbon

[3] B. Trouvat, X. Bourrat and R. Naslain, Toughening mechanisms in carbon/carbon minicomposites with interface control, to be submitted in Journal of the American Ceramic Society

[4] B. Trouvat, X. Bourrat and R. Naslain, Fibre/matrix bonding in carbon/carbon microcomposites: role of HTT and surface roughness of the fibre, to be submitted in Carbon

[5] D.B. Fiscbach, Preferred orientation parameters for pyrolytic carbons, J. Appl. Phys., **37,** (5), pp.2202-2203, (1966).

[6] W. Ruland, J. Appl. Phys., **38**, 3585 (1967)

[7] G.E. Bacon, A method for determining the degree of orientation of graphite, J. Appl. Chem., **6**, pp.477-481 (1956).

[8] R.J. Diefendorf and E. W. Tokarsky, The relationships of structure to properties in graphite fibers, Air Force report AF 33(615)-70-C-1530 (1971)

[9] E.S. Bomar, R.J. Gray and W.P. Eatherly, A Technique for measuring preferred orientation in pyrolytic-carbon coatings using plane-polarized light,

[10] D.W. Stevens, A micropolarimeter for the determination of optical anisotropy and preferred orientation in nearly isotropic pyrocarbons, Proceed. 6RD Int. Materials Symposium, Univ. of California at Berkeley, pp 129-141 (1976)

[11] K. Koizlik and H.B. Grübmeier, Ein optisches Verfahren zur Messung der Orientierungsanisotropie von Pyrokohlenstoffhüllschichten beschichter Kernbrennstoffteilchen, Leitz-Mitt. Wiss. u. Techn. Bd. **VI**, Nr 4, pp. 121-126 (1974).

[12] T. Hirai and S. Yajima, Structural features of pyrolytic graphite, J. Mat. Sc., **2**, 18-27 (1967)

[13] P. Dupel, X. Bourrat and R. Pailler, Structure of Pyrocarbon infiltrated by Pulse-CVI, Carbon, **33**, 9, pp 1193-1204 (1995)

[14] X. Bourrat, R. Pailler and P. Hanusse, Quantitative analysis of carbon coating anisotropy for CMC interfaces, Proceed. of the 21st Biennial Conf. on

Carbon, Buffalo June 13-18, State Univ. of N.Y. at Buffalo, ACS ed., pp.94-95 (1993)

[15] R.Naslain, Interface et interphase in SiC/SiC composites, HTCMCII (1992)

[16] P. Ramdhor, "Mikroskopische Beabachtungen auf Graphiten und Koksen.", Arch. Eisenhüttenwes Dtsch, **25 A** (1928)

[17] S. Ergun, "Determination of longitudinal and transverse optical constantes of absorbing uniaxial crystals. Optical anisotropy of graphite" Nature, **14**, 135-136 (1967)

[18] R.A Forest, H. Forest, H. Marsh, C. Cornford and B.T. Kelly, "Optical Properties of Anisotropic Carbon in "Chemistry and Physics of Carbon", P. Thrower ed., Elsevier,New York, NY, 19, (1984). Diefendorf & Tokarsky 75

[19] J.N. Rouzaud, A. Oberlin, Carbon films: structure and microtexture (optical and electron microscopy and Raman spectroscopy), Thin solids films, **105**, pp. 75-96 (1983)

[20] B.E. Warren, X-Ray diffraction in random layer lattices, Phys. Rev., **59**, pp.693-699 (1941)

[21] A. Oberlin, Carbon, **22**, pp.521-541 (1984)

Résumé

Dans les matériaux composites carbone/carbone (C/C), les interfaces entre constituants jouent un rôle essentiel dans le comportement mécanique. Ce travail a porté sur la modification des caractéristiques interfaciales fibre/matrice de ces matériaux par l'interposition d'une interphase de carbone de microtexture contrôlée. Des expériences ont été menées sur des composites modèles (micro et minicomposites) préparés par dépôt chimique en phase vapeur (CVD/CVI). Leur caractérisation microstructurale et leur comportement mécanique en traction à l'ambiante ont été étudiés en parallèle afin de mieux comprendre le rôle de l'interphase. L'influence de traitements thermiques a également été mise en évidence. Les résultats ont montré que, selon les caractéristiques interfaciales, il est possible d'avoir, pour les composites carbone/carbone, les différents comportements mécaniques observés pour les autres composites à matrice céramique (CMCs), à savoir la rupture fragile et le comportement tenace présentant de la multifissuration matricielle.

Mots Clés

Composite C/C - interphase carbone - CVD/CVI - microcomposite - minicomposite - microtexture (MO,MET) - propriétés mécaniques - traction - multifissuration matricielle - traitement thermique

Abstract

Interfaces in carbon/carbon composites (C/C) are dominant in controlling the mechanical behaviour. The present work dealt with the modification of the fibre/matrix interfacial characteristics of these materials in adding a controlled-microtexture carbon interphase. Experiments were conducted on model composites (micro and minicomposites) prepared by chemical vapour deposition (CVD/CVI). Microstructural characterisation and tensile mechanical behaviour at room temperature were studied in parallel in order to better understand the role of the interphase. The heat-treatment influence was also evidenced. Results showed that, according to the interfacial characteristics, carbon/carbon composites can display the different mechanical behaviours observed for the other ceramic matrix composites (CMCs) i.e. catastrophic failure, or toughening behaviour with matrix-multiple-cracking.

Key-Words

Composite C/C - carbon interphase - CVD/CVI - microcomposite - minicomposite - microtexture (OM,TEM) - mechanical properties - tension - matrix-multiple-cracking - heat treatment